



Universität Stuttgart

# NMR spectroscopy with single shallow NV centers

Von der Fakultät Mathematik und Physik der Universität Stuttgart zur  
Erlangung der Würde einer Doktorin der Naturwissenschaften (Dr. rer. nat.)  
genehmigte Abhandlung

Vorgelegt von  
Farida Shagieva  
aus Kasan

**Hauptberichter:** Prof. Dr. Jörg Wrachtrup

**Mitberichter:** Prof. Dr. Peter Michler

**Tag der mündlichen Prüfung:** 19. July 2019

3. Physikalisches Institut  
Universität Stuttgart

2019



# SUMMARY

Nuclear Magnetic Resonance (NMR) is an analytical method which has the most widespread application in modern science and technology. It is a commonly used tool in physics, chemistry, biology and medicine. NMR spectroscopy and Magnetic Resonance Imaging (MRI) are invaluable for studying structure, dynamics and interactions of biomolecules, performing chemical analysis, drug screening and design, medical diagnosis, to name a few most prominent areas of application. We owe the discovery of NMR to Felix Bloch and Edward Purcell, who were awarded the 1952 Nobel Prize in Physics "for their development of new methods for nuclear magnetic precision measurements and discoveries in connection therewith".

In essence, NMR is the measurement of the weak oscillating magnetic field created by the Larmor precession of nuclear spins in an external magnetic field. The external field induces magnetization of the sample in accordance with the Boltzmann distribution. The rotation of spins is triggered by a radiofrequency electromagnetic pulse which changes their direction, and the field oscillations are measured by Faraday pickup coils. Conventional NMR measurements scheme imposes restraints on the experiment parameters, specifically on the sample size. Namely, one needs a large enough amount of substance to provide a sufficient number of nuclear spins in order to have a detectable signal. In other words, high enough sample magnetization is

required. For the same reason, a strong magnetic field must be created in the sample volume to provide high magnetization and, hence, increase the signal-to-noise ratio.

At the same time, NMR imaging and detection techniques follow the overall trend in science which drives research from the comprehensively studied processes at the macroscale, to the insufficiently explored nanoworld where the smallest basic components of living matter reside. For instance, the characteristic diameter of hemoglobin, the protein responsible for the oxygen transport in the human body, is about 5 nanometers. A strand of DNA, the repository of genetic information, is roughly 2-3 nanometers across. The most fundamental life processes related to inheritance and evolution take place at the nanoscale, where nature has been perfecting its art over millennia. The nanoscale study of chemical reactions and biological processes can unveil new approaches to develop technologies for medicine, and for production of materials, electronics, and drugs.

Conventional (macroscale) NMR measurements are not applicable to nanometer objects because of the aforementioned requirement of sufficient sample size, and because the pickup coil cannot be scaled down to such a small size. To overcome these impediments, several improvements of the method have been developed. The common strategies comprise application of extreme magnetic fields, cryogenic technologies, and hyperpolarization techniques, which however all require high-tech equipment that come with enormous costs.

In an ideal hyperpolarized state all the nuclear spins occupy the same energy level, i.e. they are polarized in the same direction. Therefore, if the sample's state approaches the hyperpolarized one, the NMR signal increases drastically. The first hyperpolarization method was invented by Albert Overhauser in 1953, who observed that the saturation of electron spin resonances in metals was accompanied by the growth of the nuclear polarization as a result of relaxation processes. This gave rise to the development of numerous approaches for increasing the nuclear spin polarization beyond the value determined by the Boltzmann distribution.

One of them, the dynamic nuclear polarization (DNP) is based on the polar-

ization transfer from the highly polarized electron spin reservoir to nuclear spins. The most advanced strategies to increase the sensitivity include the combination of DNP with the utilization of small NMR coils. Even without applying hyperpolarization, one can analyse nano- and picomole quantities of biomolecules at low temperatures ( $\sim 100$  mK) with the help of waveguide NMR probes with characteristic size of 100 microns.

However, the ultimate sensitivity limit of a single nuclear spin still remains a challenge for NMR measurements. The magnetic moment of a single electron, which is 660 times larger than the one of proton, can be detected by means of magnetic resonance force microscopy (MRFM). MRFM is a well-established technique which was first described in 1991. It is a combination of atomic force microscopy (AFM), laser interferometry and MRI techniques. Having the spatial resolution of less than 10 nm, this method is ten billion times more sensitive than conventional MRI used for medical applications. The main source of signal noise in the MRFM measurements are the thermal fluctuations of AFM cantilever, that is why the experiments are carried out at cryogenic temperatures.

The aforementioned powerful nano NMR techniques are unfortunately not applicable for *in vivo* studies because MRFM requires ultralow temperatures, and hyperpolarization sometimes requires chemical modification of the sample.

In the last decade, another promising method came into play, in which the Nitrogen-Vacancy (NV) centers in diamond are used for nanoscale NMR measurements to achieve the sensitivities close to the ones required for single-proton detection with chemical shift resolution, i.e. for reconstructing the chemical bonds of the proton from the NMR signal. The NV center NMR measurements can be performed at room temperature, therefore they are ideally suited for ultrasensitive medical and biological studies. In the present work, the possibility to polarize external nuclear spins using NV center has been demonstrated. The proposed approach, combining the ultrasensitive NV center NMR measurements with DNP, has the potential to be developed into a unique stand-alone method for imaging of single proteins and for noninvasive study of cellular intermediates in enzyme-catalyzed reactions

and of entire metabolic pathways in an intact living cell.

In the **present work** single shallow (near-surface) NV centers in diamond were used as sensors for nano NMR spectroscopy. The main research directions were focused on the improvement of the dynamical decoupling noise spectroscopy technique (DDNS) by means of combining it with DNP schemes, in which the NV center's electron spin was used as the source of polarization, and finding new applications for this method. It has been demonstrated that using the NV centers one can detect various substances which are in a close contact with the diamond surface.

DDNS is the method of acquisition of NMR signal via the application of a microwave pulse sequence to a single shallow ( $< 10$  nm deep) NV center, i.e. without active manipulation of nuclear spins. The investigated substance containing the target nuclei is brought in contact with diamond interface. The sample is placed into the confocal microscope equipped with the system for the microwave manipulation of the NV center's electron spin under a weak ( $\sim 10^1 - 10^3$  G) static magnetic field. The precession of nuclear spins creates a fluctuating magnetic field at the location of the NV center. The closer a nuclear spin is to the NV center, the larger magnetic field it creates. Therefore the contribution from the distant nuclei can be neglected. Due to thermal fluctuations, the total magnetic moment of the nuclei in the vicinity of the NV center is never equal to zero, i.e. a net magnetization is always present, which oscillates with the Larmor frequency and produces the NMR signal, referred to as spin noise. The detection volume of an NV center is usually defined as the size of the domain, occupied by the nuclei closest to the NV center, which constitutes  $\sim 70\%$  of the detected signal. Physically it usually corresponds to a volume of several  $nm^3$ , depending on the NV depth, and therefore DDNS with single NV center is a nano-NMR technique. The application of the dynamical decoupling pulse sequence allows to the NV center spin state acquire a phase due to interaction with the spins confined within the nanoscopic volume of the material. Dynamical decoupling protocols consists of sequential microwave pulses, separated by time windows. If the noise period is equal to the doubled period of the pulses, the NV center

accumulates the phase. The other frequencies are filtered out. The NMR signal is the projection of the acquired phase to the  $\hat{S}_z$  component of the NV center's spin as a function of pulse separation.

The microwave pulses can be considered as gate operations on the Bloch sphere. As a rule, the  $|0\rangle \leftrightarrow |-1\rangle$  transition is used as a qubit. Pulse imperfections and nonzero microwave detuning affect the quality of the acquired signal. Geometric or more generally holonomic quantum computation has attracted a lot of attention in the last few years due to the robustness of geometric quantum gates against these types of noise. An advantage of using non-adiabatic holonomic quantum gates (HQGs) is that their implementation requires much less time than that of the dynamic gates. Such gates can be realized in the ground state of the NV center's electron spin, utilizing the  $\{|1\rangle, |-1\rangle\}$  states as a qubit basis and the  $|0\rangle$  as an ancillary state. In this work, the performance of holonomic quantum gates (HQG) in comparison with the standard gate operations has been studied in the presence of different kinds of noise. When the dynamical decoupling pulse sequence is composed of holonomic gates, the errors are being accumulated in the ancillary state and do not affect the qubit manifold. This repopulation between the qubit and the non-computational basis leads to compression of the Bloch sphere, reducing the contrast of the NMR signal. Thus, HQGs are inappropriate for the NMR sensing techniques where sequential application of a large amount of pulses is required, despite the fact that their fidelity is higher than that of the dynamical gates.

Introduction of the idle time between two consecutive implementations of the detection protocol converts the DDNS into the scheme for the correlation spectroscopy. The decay time of the phase correlations acquired within the two applications of dynamical decoupling pulse sequences allows one to gain an insight into the molecular dynamics of the material applied to the diamond surface, as it was recently demonstrated for simple organic materials. Interestingly, it is one of the few methods which enables one to measure the diffusion inhomogeneity on the nanoscale. This is common

for example, in organic molecules in the living cell membranes due to the presence of lipid rafts. Here the correlation protocol was used to study a translational diffusion of the phospholipids in the artificial cell membranes as a first step the investigation of non-uniformity of diffusion in spatially contiguous lipid clusters. The characteristic time scale of the diffusion process ( $D \sim 0.1 - 2 \mu\text{m}^2/\text{s}$ ) is ideally suited for the correlation measurement scheme, leading to the correlation decay times in the order of tens of microseconds, which is shorter than the relaxation time of the NV center itself. The average value of the coefficient of translational diffusion was measured to be  $0.17 \pm 0.04 \mu\text{m}^2/\text{s}$  for the semi-solid lipid bilayer.

The ability of shallow NV centers to sense the nuclear spins confined within the nanoscopic detection volume suggests the possibility of pushing the existing sensing limits towards the detection of 2D materials. This would open the whole new branch of applications in electronics and quantum computing, including the potential realization of a room-temperature quantum simulator. In this thesis nuclear quadrupole resonance spectroscopy of  $^{11}\text{B}$  ( $I = 3/2$ ) in the bulk hexagonal boron nitride (hBN) has been performed with the aim of realizing this application.

To obtain as much information about the system as possible, each nuclear spin should contribute to the acquired signal. This can be achieved by hyperpolarization of a sample. The source of polarization in this work is the electron spin of the NV center, which can be optically repolarized after each procedure of the polarization transfer. The mechanism of the polarizing protocol is based on the electron-nuclear double resonance at the Hartmann-Hahn condition, when the Rabi frequency of the dressed states of the NV center spin becomes equal to the Larmor frequency of the target nuclear spins. The rate of polarization transfer is set by the strength of dipolar couplings between them: the closer the nuclear spin is, the faster it can be polarized. Thus, the hyperpolarization  $^{13}\text{C}$  nuclear spins, which are intrinsic to diamond, has been successfully realized in this way whereas the polarization of external nuclei still remains challenging. In this thesis,

the room-temperature DNP of  $^1\text{H}$  spins in an organic liquid (immersion oil Fluka Analytical 10976) at 544 G has been demonstrated. The polarization transfer from the NV center to nuclear spins was observed as a reduction of the  $T_{1\rho}$  decay time, when applying the Hartmann-Hahn protocol on- and off-resonant. For instance, if the NV center is 7.7 nm deep, it takes 150  $\mu\text{s}$  to transfer 19% of its polarization to the nuclear spins in the detection volume during each repetition of the polarizing sequence. Introducing the idle times after the polarization transfer we were able to catch the fine effects in its dynamics. Namely, the speed of polarization increased with increment of the idle time. This suggests slower molecular diffusion near the diamond surface in comparison with the bulk liquid, because it is attributed to an effect caused by the polarized nuclear spins in an adsorption layer leaving the detection volume and being substituted by the unpolarized nuclei.

To yield benefits from the successful hyperpolarization of nuclear spins the created polarization excess should be detected by NMR means. Due to presence of the molecular diffusion in the liquid, the polarized nuclei diffuse out of the detection volume of the NV center. Therefore, the NMR enhancement in our case can only be detected from the hyperpolarized solid sample. In this work we demonstrate the polarization transfer from the NV center to the  $^{19}\text{F}$  ( $I = 1/2$ ) nuclear spins in  $\text{CaF}_2$  using Hartmann-Hahn protocol. Nevertheless even in this case the signal is a precious resource that is rapidly and irreversibly decays due to the spin diffusion and nuclear spin relaxations. The created polarization excess must withstand several repetitions of the detection scheme which lasts tens of microseconds. In the case of DDNS, this time is limited by  $T_2^{\text{nucl}} \sim 10 \mu\text{s}$ . Homonuclear decoupling of the nuclear spins during the detection does not help here due to the resonance properties of the radiofrequency pulses on nuclei, which will result in the phase acquisition not only due to the spin noise, but also because of the oscillating radiofrequency field.

Another approach to use the full potential of the hyperpolarized spin system is to implement an another acquisition scheme. There is a recently developed detection mechanism based on the sensing of  $A_{zz}$  component of the hyperfine

coupling between NV center and nuclear spins, which means that polarization must be preserved along  $z$ -axis. This results in the  $T_1$ -time limited polarization decay time, which has the lower limit of  $\sim 1$  s for  $^{19}\text{F}$  in  $\text{CaF}_2$ . In this scenario the utilization of the hybrid spin register combining the use of the quantum memory (intrinsic nitrogen nuclear spin) with NV sensing at high ( $\gtrsim 2000$  G) magnetic fields even allows one to resolve the chemical shift. The hyperpolarization routine used in this work is limited only by the strength of the microwave field, required to fulfil the Hartmann-Hahn condition for target nuclear spins, the experiments with the hyperpolarized NMR spectroscopy at high magnetic fields are the most promising strategy to detect the enhanced signal.

### Thesis outline

This thesis is divided into six chapters.

[Chapter 1](#) contains the basic theory concerning the NV center: physical properties and growth procedure of diamond, a formation of NV centers, its electron spin energy levels, basic spin manipulation techniques and the description of the experimental setup.

A comparison between the performance of detection sequences composed of standard and geometric quantum gates realized in the ground state of NV center is presented in [Chapter 2](#).

[Chapter 3](#) demonstrates the experiments on the measurements of the lateral diffusion of phospholipids in the artificial cell membranes using correlation spectroscopy.

In [Chapter 4](#) the experimental results of the dynamical decoupling noise spectroscopy of the bulk hexagonal Boron Nitride (hBN) are shown.

[Chapter 5](#) gives an overview of the possible realizations of nuclear spin polarization using NV center in diamond. The dynamics of the polarization transfer from the NV centers electron spin to the nuclear spin bath in an organic liquid is studied.

Preliminary experiments towards the detection of hyperpolarized nuclear spins in a solid  $\text{CaF}_2$  sample is described in [Chapter 6](#).

# ZUSAMMENFASSUNG

Die Kernspinresonanz (NMR) ist ein physikalisches Phänomen, welche zu den wichtigsten Anwendungen in der modernen Wissenschaft und Technologie gehört. Sie ist ein weit verbreitetes Werkzeug in den Disziplinen Physik, Chemie, Biologie und Medizin. Die Kernspinresonanzspektroskopie (NMR-Spektroskopie) und die Magnetresonanztomographie (MRT) sind unersetzbar in der Erforschung der Struktur, Dynamik und Wechselwirkungen von Biomolekülen, die Durchführung chemischer Analysen, die Untersuchung von Medikamenten und deren Wirkstoffdesign, die medizinische Diagnose und vieles mehr. Die Entdeckung der NMR verdanken wir Felix Bloch und Edward Purcell, die 1952 mit dem Nobelpreis für Physik "für die Entwicklung neuer Methoden für magnetische Präzisionsmessungen im Kern und damit verbundene Entdeckungen" ausgezeichnet wurden.

Im Wesentlichen ist NMR die Messung des schwachen, oszillierenden Magnetfelds, welches durch die Larmorpräzession von Kernspins in einem äußeren Magnetfeld erzeugt wird. Dieses äußere Magnetfeld induziert eine Magnetisierung der Probe gemäß der Boltzmann-Verteilung. Die Rotation der Spins wird durch einen Hochfrequenzimpuls ausgelöst, der ihre Ausrichtung ändert und die Feldschwingungen werden mit Faraday-Spulen detektiert. Dieses herkömmliche NMR-Messschema schränkt die Experimentparameter, vor allem die Probengröße, ein. Es wird eine ausreichend große Substanzmenge

benötigt, damit genügend viele Kernspins zum erfassten Signal beitragen. Anders gesagt, ist eine ausreichend hohe Magnetisierung der Probe erforderlich. Aus diesem Grund muss im Probenvolumen ein starkes Magnetfeld erzeugt werden, um eine hohe Magnetisierung zu erhalten und das Signal-Rausch-Verhältnis zu erhöhen.

Gleichzeitig folgen MRT und andere Detektionsmethoden dem allgemeinen wissenschaftlichen Trend, der das Interesse von den umfassend untersuchten Prozessen auf der Makroskala hin zur ungenügend erforschten Nanowelt verlagert, in welcher sich die kleinsten Grundkomponenten lebender Materie befinden. Beispielsweise beträgt der charakteristische Durchmesser von Hämoglobin, welches ein Protein für den Sauerstofftransport im menschlichen Körper ist, etwa 5 Nanometer. Weitere Beispiele sind ein DNA-Strang usw. Die grundlegendsten Lebensprozesse im Zusammenhang mit Vererbung und Evolution finden auf der Nanoskala statt, wo die Natur ihre Kunst über Jahrtausende perfektioniert hat. Die Untersuchung chemischer Reaktionen und biologischer Prozesse auf dieser Nanoskala, kann neue Ansätze für die Entwicklung von Technologien in der Medizin, sowie für die Herstellung von Materialien, Elektronik und Medikamenten eröffnen.

Das herkömmliche (makroskopische) NMR-Messschema ist nicht auf Nanometerobjekte anwendbar, weil eine ausreichende Probengröße erforderlich ist und somit können die Nanometerstruktur nicht direkt aufgelöst werden. Um diese Hindernisse zu überwinden, wurden verschiedene Verbesserungen des Verfahrens entwickelt. Die gängigen Strategien umfassen die Anwendung extremer Magnetfelder, Tieftemperaturtechnik und Hyperpolarisierungstechnik, die jedoch alle Hochtechnologie-Geräte erfordern und mit enormen Kosten einhergehen.

In einem idealen, hyperpolarisierten Zustand besetzen alle Kernspins das gleiche Energieniveau, d.h. sie sind in die gleiche Richtung polarisiert. Deshalb steigt das NMR-Signal drastisch an, wenn der Zustand der Probe sich dem hyperpolarisierten annähert. Die erste Hyperpolarisierungsmethode wurde 1953 von Albert Overhauser entdeckt, der beobachtete, dass die Sättigung von Elektronenspinresonanzen in Metallen mit dem Anwachsen der Kernpolarisation infolge von Relaxationsprozessen einhergeht. Dies führte

zur Entwicklung zahlreicher Ansätze, um die Kernspinpolarisation über den durch die Boltzmann-Verteilung bestimmten Wert zu steigern.

Eine davon, die dynamische Kernpolarisation (DNP, Abkürzung für engl. 'Dynamical Nuclear Polarization'), basiert auf der Polarisationsübertragung eines hochpolarisierten Elektronenspinreservoirs auf die Kernspins. Die fortschrittlichsten Strategien zur Erhöhung der Empfindlichkeit umfassen die Kombination von DNP mit der Verwendung kleiner NMR-Spulen. Selbst ohne Anwendung der Hyperpolarisierung kann man Biomoleküle in Mengen von Nano- und Pikomol bei niedrigen Temperaturen ( $\sim 100$  mK) mit Hilfe von Wellenleiter-NMR-Sonden mit einer charakteristischen Größe von 100 Mikrometern analysieren.

Die ultimative Empfindlichkeitsgrenze eines einzelnen Kernspins ist allerdings immer noch eine Herausforderung für NMR-Messungen. Das magnetische Moment eines einzelnen Elektronenspins, welches 660-mal größer als das eines Protons ist, kann mittels der Magnetresonanz-Kraftmikroskopie (MRFM) erfasst werden. MRFM ist eine bewährte Technik, die erstmals 1991 beschrieben wurde. Sie ist eine Kombination aus Rasterkraftmikroskopie (AFM), Laserinterferometrie und MRI-Techniken. Mit einer räumlichen Auflösung von weniger als 10 nm ist diese Methode zehn Milliarden Mal empfindlicher als die konventionelle MRI für medizinische Anwendungen. Die Hauptquelle des Signalrauschens bei den MRFM-Messungen sind die thermischen Schwankungen des AFM-Hebelarms, weshalb die Experimente bei kryogenen Temperaturen durchgeführt werden.

Die oben genannten, leistungsstarken Nano-NMR-Techniken sind für In-vivo-Untersuchungen leider nicht geeignet, weil MRFM niedrigste Temperaturen benötigt und die Hyperpolarisierung unter Umständen die Probe chemisch modifiziert. Im letzten Jahrzehnt kam eine weitere, vielversprechende Methode ins Spiel, bei welcher Stickstoff-Fehlstellen (NV) Zentren in Diamant für NMR-Messungen im Nanomaßstab verwendet werden. Dabei wird eine Empfindlichkeit erreicht, die nahe derjenigen liegt, welche zur Auflösung der chemischen Linienverschiebung eines einzelnen Protonenspins erforderlich ist, um damit zum Beispiel die chemischen Bindungen des Protons aus dem NMR-Signal zu rekonstruieren. Die NMR Messungen mit NV-Zentren können

bei Raumtemperatur durchgeführt werden und eignen sich daher ideal für hochempfindliche medizinische und biologische Untersuchungen. In der vorliegenden Arbeit wurde die Möglichkeit demonstriert, externe Kernspins unter Verwendung eines NV-Zentrums zu polarisieren. Der vorgeschlagene Ansatz, hochempfindliche, NV-basierte NMR-Messungen mit DNP Methoden zu vereinigen, hat das Potential zu einem einzigartigen, eigenständigen Verfahren entwickelt zu werden, welches die zerstörungsfreie Abbildung einzelner Proteine, die nichtinvasive Untersuchung von Zwischenprodukten in enzymkatalysierten Reaktionen und die vollständigen Stoffwechselwege einer intakt lebenden Zelle, ermöglicht.

In **der vorliegenden Arbeit** wurden einzelne, oberflächennahe NV-Zentren in Diamant als Sensoren für Nano-NMR-Spektroskopie verwendet. Das Hauptaugenmerk der Forschung konzentrierten sich dabei auf die Verbesserung der dynamisch-entkoppelten Rauschspektroskopietechnik (DDNS, Abkürzung für engl. 'Dynamical Decoupling Noise Spectroscopy') durch Kombination mit DNP-Schemata, bei welcher der Elektronenspin des NV-Zentrums als Quelle der Polarisation verwendet wird. Es wurde gezeigt, dass mit Hilfe von NV-Zentren verschiedene Stoffe, die nah an der Diamantoberfläche sind, detektiert werden können.

DDNS ist das Verfahren zur Messung eines NMR-Signals durch Anlegen einer Mikrowellenimpulssequenz an ein einzelnes, oberflächen nahes ( $<10$  nm tiefes) NV-Zentrum, d.h. ohne Radiofrequenzmanipulation von Kernspins. Die untersuchende Substanz, welche die Zielkernspins enthält, wird mit der Diamantoberfläche in Kontakt gebracht und auf einem konfokalen Mikroskop platziert, welches mit dem System zur Manipulation des Elektronenspins des NV-Zentrums unter einem schwachen ( $\sim 10^1 - 10^3$  G), statischen Magnetfeld mit Mikrowellen ausgestattet ist. Die Präzession der Kernspins erzeugt ein oszillierendes Magnetfeld an der Stelle des NV-Zentrums und je näher der Kernspin am NV-Zentrum ist, desto größer ist das Magnetfeld. Die Beiträge von fernen Kernen können deswegen vernachlässigt werden. Aufgrund statistischer Fluktuationen ist das resultierende magnetische Moment der Kernspins in Nähe des NV Zentrums im Mittel nicht gleich Null,

d.h. eine Nettomagnetisierung ist immer vorhanden, welche mit der Larmor-Frequenz oszilliert und das NMR-Signal erzeugt. Aufgrund des Thermischen Ursprungs wird es als Spinrauschen bezeichnet. Das Detektionsvolumen eines NV Zentrums ist definitionsgemäß das Volumen der Domäne, in welcher sich diejenigen dem NV Zentrum nächsten Kernspins befinden, die 70% zum erfassten Signal beitragen. Physikalisch entspricht es normalerweise einem Volumen von mehreren  $nm^3$ , abhängig von der NV-Tiefe. Daher ist DDNS mit einem einzelnen NV-Zentrum eine Nano-NMR-Technik. Die Anwendung der dynamischen Entkopplungspulssequenz ermöglicht es, dass der NV-Zentrums-Spinzustand eine Phase aufgrund der Wechselwirkung mit den Kernspins, die innerhalb des nanoskopischen Volumens des Materials eingeschlossen sind, aufnimmt. Dynamische Entkopplungsprotokolle bestehen aus sequenziellen Mikrowellenpulsen, die durch Zeitfenster getrennt sind. Wenn die Rauschfrequenz mit den Zeitperioden zwischen den Mikrowellenpulsen in Phase ist, akkumuliert das NV-Zentrum die Phase, andere Frequenzen werden dagegen herausgefiltert. Das NMR-Signal ist die Projektion der erfassten Phase auf die  $\hat{S}_z$ -Komponente des NV-Zentrums-Spins als Funktion der Pulstrennung.

Die Mikrowellenpulse können als Quantengatter auf der Bloch-Kugel betrachtet werden. In der Regel wird der  $|0\rangle \leftrightarrow |-1\rangle$ -Übergang als Qubit verwendet. Unvollkommenheiten der Pulse und Frequenzverstimmungen beeinflussen die Qualität des erfassten Signals. Die geometrische - oder ganz allgemein holonomische - Quantenberechnung hat in den letzten Jahren aufgrund der Robustheit geometrischer Quantengatter gegen diese Arten von Rauschen viel Aufmerksamkeit auf sich gezogen. Ein Vorteil der Verwendung von den nicht-adiabatischen holonomischen Quanten Gatter (HQG) besteht darin, dass ihre Implementierung viel weniger Zeit benötigt als die der dynamischen Gatter. Solche Quantengatter können im Grundzustand des NV-Elektronenspins realisiert werden, wobei  $\{|1\rangle, |-1\rangle\}$  -Zustände als Qubit-Basis und  $|0\rangle$  als Hilfszustand verwendet werden. In dieser Arbeit wurde die Leistung holonomischer Quantengatter (HQG) im Vergleich zu Standardgatteroperationen in Gegenwart verschiedener Arten von Rauschen

untersucht. Wenn die dynamische Entkopplungspulsfolge aus holonomischen Quantengattern besteht, werden die Fehler im Hilfszustand akkumuliert und beeinflussen nicht die Qubit-Menge. Eine solche Wiederbesiedlung führt jedoch zu einer Kompression der Bloch-Kugel, wodurch der Kontrast des NMR-Signals verringert wird. Daher sind HQGs ungeeignet für die NMR-Erfassungstechniken, bei denen eine sequentielle Anwendung einer großen Anzahl von Pulsen erforderlich ist, obwohl ihre Fidelität höher ist als die der dynamischen Gatter.

Durch die Einführung der Wartezeit zwischen zwei aufeinanderfolgenden Implementierungen des Detektionsprotokolls wird die DDNS in ein Schema für die Korrelationsspektroskopie umgewandelt. Die Abklingzeit der Phasenkorrelationen, die bei den beiden Anwendungen von DD-Pulssequenzen erfasst werden, ermöglicht einen Einblick in die Molekulardynamik des auf die Diamantoberfläche aufgetragenen Materials, wie es kürzlich für einfache organische Materialien gezeigt wurde. Interessanterweise ist es eine der wenigen Methoden, die es ermöglicht, die Diffusionsinhomogenität im Nanobereich zu messen. Dies ist beispielsweise bei organischen Molekülen in lebenden Zellmembranen aufgrund des Vorhandenseins von Lipid Rafts (zu deutsch Lipidflößen) möglich. Hier wurde das Korrelationsprotokoll verwendet, um eine Translationsdiffusion der Phospholipide in den künstlichen Zellmembranen als ersten Schritt zur Untersuchung der Ungleichmäßigkeit der Diffusion in räumlich zusammenhängenden Lipidclustern zu untersuchen. Die charakteristische Zeitskala des Diffusionsprozesses ( $D \sim 0,1 - 2 \mu\text{m}^2/\text{s}$ ) ist ideal für das Korrelationsmessschema geeignet, das zu Korrelationszerfall in der Größenordnung von zehn Mikrosekunden führt. Dies ist kürzer als die Relaxationszeit des NV-Centers. Der Durchschnittswert des Translationsdiffusionskoeffizienten wurde mit  $0,17 \pm 0,04 \mu\text{m}^2/\text{s}$  für die halbfeste Lipiddoppelschicht gemessen.

Die Fähigkeit von oberflächennahen NV-Zentren, die im nanoskopischen Detektionsvolumen eingeschlossen sind, zu detektieren, legt die Möglichkeit nahe, die vorhandenen Erfassungsgrenzen in Richtung der Erfassung von

2D-Materialien zu verschieben. Dies würde einen völlig neuen Zweig von Anwendungen in der Elektronik und für Quantencomputer eröffnen, einschließlich der Realisierung eines Raumtemperatur-Quantensimulators. In dieser Arbeit wurde eine Quadrupolresonanzspektroskopie von  $^{11}\text{B}$  ( $I = 3/2$ ) im hexagonalen Bornitrid (hBN) durchgeführt, um diese Anwendungen zu realisieren.

Um möglichst viel Information über das System zu erhalten, sollte jeder Kernspin zum erfassten Signal beitragen. Dies kann durch Hyperpolarisierung der Probe erreicht werden. Die Polarisationsquelle in dieser Arbeit ist ein einzelner Elektronenspin eines NV-Zentrums, der nach jedem Vorgang des Polarisationstransfers optisch repolarisiert werden kann. Der Mechanismus des Polarisationsprotokolls basiert auf der elektronen-nuklearen Doppelresonanz unter der Hartmann-Hahn-Bedingung, wenn also die Rabi-Frequenz der bekleideten Zustände des NV-Spins gleich der Larmor-Frequenz der Ziel-Kernspins ist. Die Geschwindigkeit der Polarisationsübertragung wird durch die Stärke der dipolaren Kopplungen zwischen ihnen gegeben, das heißt je näher der Kernspin ist desto schneller kann er polarisiert werden. Auf diese Weise wurde die Hyperpolarisierung dem Diamanten intrinsischer  $^{13}\text{C}$ -Kernspins erfolgreich realisiert, während die Polarisation von externen Kernen noch immer eine Herausforderung darstellt. In dieser Arbeit wurde die Raumtemperatur-DNP von  $^1\text{H}$  in einer organischen Flüssigkeit (Immersionöl Fluka Analytical 10976) bei 544 G demonstriert. Der Polarisationstransfer vom NV-Zentrum zu den Kernspins wurde als eine Verringerung der  $T_{1\rho}$ -Zerfallszeit beobachtet, wenn das Hartmann-Hahn-Protokoll in Resonanz ein- und ausgeschaltet wurde. Wenn zum Beispiel das NV-Zentrum 7,7 nm tief ist, werden bei jeder Wiederholung der Polarisationssequenz  $150\ \mu\text{s}$  benötigt, um 19% seiner Polarisation auf die Kernspins im Detektionsvolumen zu übertragen. Durch die Einführung der Leerlaufzeiten nach dem Polarisationstransfer konnten wir die feinen Effekte in seiner Dynamik erfassen. Die Polarisationsgeschwindigkeit nahm nämlich mit zunehmender Leerlaufzeit zu. Dies deutet auf eine langsamere molekulare Diffusion in der Nähe der Diamantoberfläche im Vergleich zur Bulk-Flüssigkeit hin, da dies

auf einen Effekt zurückzuführen ist, der dadurch verursacht wird, dass die polarisierten Kernspins in einer Adsorptionsschicht das Erfassungsvolumen verlassen und durch die unpolarisierten Kerne ersetzt werden.

Um jedoch Vorteile zu erzielen, sollte der erzeugte Polarisationsüberschuss durch NMR-Mittel nachgewiesen werden. Aufgrund der molekularen Diffusion in der Flüssigkeit entfernen sich die polarisierten Kernspins aus dem Detektionsvolumen des NV-Zentrums. Daher kann die NMR-Verstärkung nur aus der hyperpolarisierten Feststoffprobe nachgewiesen werden. In dieser Arbeit demonstrieren wir den Polarisationstransfer vom NV-Zentrum zu den  $^{19}\text{F}$  ( $I = 1/2$ ) Kernspins in  $\text{CaF}_2$  unter Verwendung des Hartmann-Hahn-Protokolls. Auch in diesem Fall ist das Signal eine wertvolle Ressource, die aufgrund der Spin-Diffusion und der nuklearen Spin-Relaxation schnell und irreversibel abklingt. Die erzeugte Polarisation muss mehrere Wiederholungen des Detektionsschemas widerstehen, das mehrere zehn Mikrosekunden dauert. Bei DDNS ist diese Zeit durch  $T_2^{\text{nucl}} \sim 10 \mu\text{s}$  begrenzt. Die homonukleare Entkopplung der Kernspins während der Detektion hilft hier nicht weiter, da die Hochfrequenzpulse an den Kernen Resonanzeigenschaften aufweisen, die nicht nur aufgrund des Spinrauschens, sondern auch aufgrund des oszillierenden Hochfrequenzfeldes zur Phasenerfassung führen.

Ein weiterer Ansatz, um das volle Potenzial des hyperpolarisierten Spinsystems auszuschöpfen, ist die Implementierung eines anderen Erfassungsschemas. Es gibt einen kürzlich entwickelten Erkennungsmechanismus, der auf der Erfassung der  $A_{zz}$ -Komponente der Hyperfeinkopplung zwischen dem NV-Zentrum und den Kernspins basiert. Dies bedeutet, dass die Polarisation entlang der  $z$ -Achse beibehalten werden muss. Dies ergibt die zeitlich  $T_1$ -begrenzte Polarisationsabklingzeit, die die untere Grenze von  $\sim 1$  s für  $^{19}\text{F}$  in  $\text{CaF}_2$  hat. In diesem Szenario ermöglicht die Verwendung des Hybridspinregisters, das die Verwendung des Quantenspeichers (intrinsischer Stickstoffkernspin) mit der NV-Erfassung bei hohen ( $\gtrsim 2000$  G) Magnetfeldern kombiniert, sogar die Auflösung der chemischen Verschiebung. Die in dieser Arbeit verwendete Hyperpolarisationsroutine ist nur durch die Stärke des Mikrowellenfeldes begrenzt, das zur Erfüllung der Hartmann-

Hahn-Bedingung für Kernspins erforderlich ist. Die Experimente mit der hyperpolarisierten NMR-Spektroskopie bei hohen Magnetfeldern sind die vielversprechendste Strategie zur Detektion der verbessertes Signal.

## **Gliederung**

Diese Arbeit ist in sechs Kapitel unterteilt.

Kapitel 1 enthält die grundlegende Theorie über das NV-Zentrum: physikalische Eigenschaften und Wachstumsverfahren von Diamanten, die Bildung von NV-Zentren, die Elektronenenergie des Spins, grundlegende Spinmanipulationstechniken und die Beschreibung des experimentellen Aufbaus.

Ein Vergleich zwischen der Leistung von Detektionssequenzen aus Standard- und geometrischen Quantengattern, welche im Grundzustand des NV-Zentrums realisiert werden, ist in Kapitel 2 aufgestellt.

Kapitel 3 demonstriert Experimente zur Messung der lateralen Diffusion von Phospholipiden in künstlichen Zellmembranen mittels Korrelationspektroskopie. In Kapitel 4 werden die experimentellen Ergebnisse der dynamischen Entkopplungsrauschspektroskopie von hexagonalem Bornitrid (hBN) gezeigt.

Kapitel 5 gibt einen Überblick über mögliche Realisierungen der Kernspinpolarisation unter Verwendung des NV-Zentrums in Diamant. Die Dynamik des Polarisationstransfers vom Elektronenspin eines NV-Zentrums auf das Kernspinbad einer organischen Flüssigkeit wird demonstriert.

Ein erster Schritt zum Nachweis von hyperpolarisierten Kernspins in einer festen  $CaF_2$ -Probe wird in Kapitel 6 beschrieben.



# ABBREVIATIONS

- AOM** acousto optical modulator
- APD** avalanche photodiode
- AWG** arbitrary waveform generator
- CPMG** Carr-Purcell-Meiboom-Gill
- CVD** Chemical vapor deposition
- CW** continuous wave
- DD** Dynamical decoupling
- DDNS** dynamical decoupling noise spectroscopy
- DFT** Density functional theory
- DNP** Dynamic nuclear polarization
- DPSS** diode pumped solid state
- EPR** electron paramagnetic resonance
- ES** excited state
- ESLAC** Excited state level anticrossing
- GS** ground state

**GSLAC** Ground state level anticrossing  
**GUV** giant unilamellaer vesicles  
**hBN** hexagonal boron nitride  
**HPHT** High pressure high temperature  
**HQG** holonomic quantum gates  
**ISC** intersystem crossing  
**JT** Jahn-Teller  
**KDD** Knill dynamical decoupling  
**LP** longpass  
**NMR** nuclear magnetic resonance  
**NOVEL** Nuclear spin Orientation Via Electron spin Locking  
**NV** Nitrogen-Vacancy  
**ODMR** optically detected magnetic resonance  
**PBS** polarising beam splitter  
**PCB** printed circuit board  
**RMS** root mean square  
**RWA** rotating wave approximation  
**SLB** supported lipid bilayer  
**SNR** signal-to-noise ratio  
**ZFS** zero field splitting  
**ZPL** zero-phonon line

# CONTENTS

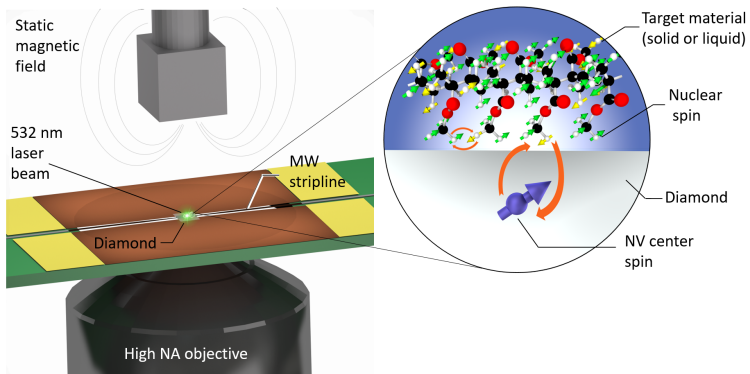
<b>1. Confocal spectroscopy with NV centers in diamond</b>	<b>1</b>
1.1. Diamond as a host material	3
1.1.1. Physical properties	3
1.1.2. Diamond formation and artificial growth	4
1.1.3. Types of diamonds and color centers	5
1.2. Nitrogen-Vacancy center in diamond	6
1.2.1. Formation of NV centers	7
1.2.2. Electronic energy levels	8
1.2.3. Photophysical properties	12
1.2.4. Interaction Hamiltonian	13
1.3. Confocal microscope for nano-NMR	18
1.3.1. Optical path	18
1.3.2. Microwave circuit	20
1.3.3. Sample stage	20
1.4. Spin manipulation techniques	21
1.4.1. Optically Detected Magnetic Resonance	22
1.4.2. Rabi oscillations	24
1.4.3. Quantum gates	26
1.4.4. Relaxation times	28

1.4.5. Dynamical decoupling noise spectroscopy . . . . .	30
1.4.6. NV depth determination . . . . .	36
1.4.7. Correlation protocol . . . . .	38
<b>2. Holonomic non-adiabatic quantum gates realized over the NV center's ground state</b>	<b>39</b>
2.1. Theory . . . . .	41
2.1.1. Holonomy . . . . .	41
2.1.2. Holonomic quantum gates (HQG) with NV centers . . .	42
2.2. The model of one-qubit gate . . . . .	44
2.3. Error scaling with holonomic gates . . . . .	45
2.3.1. The Pauli-X gate . . . . .	46
2.3.2. X-gate using holonomy . . . . .	47
2.3.3. Simulations of gate operations . . . . .	49
2.4. Dynamical decoupling with HQGs . . . . .	52
2.4.1. Error correction . . . . .	54
2.4.2. Nuclear spin polarization . . . . .	55
2.5. Conclusions . . . . .	57
<b>3. Measurement of lateral diffusion of phospholipids in the artificial cell membrane</b>	<b>59</b>
3.1. Measuring Nanoscale Anisotropic Diffusion . . . . .	61
3.2. Dynamics of the lipid bilayer . . . . .	62
3.3. Methods . . . . .	64
3.3.1. Samples modelling the cell membrane . . . . .	64
3.3.2. Setup and diamond sample . . . . .	66
3.4. Measurements of lateral diffusion . . . . .	67
3.4.1. Simulation of NMR signal . . . . .	67
3.4.2. Extraction of the diffusion coefficient . . . . .	68
3.4.3. Correlation measurements of micelles . . . . .	70
3.4.4. Correlation measurements of SLB . . . . .	73
3.5. Conclusions . . . . .	75

<b>4. NMR of hexagonal Boron Nitride</b>	<b>77</b>
4.1. Room-temperature quantum simulator . . . . .	79
4.2. hBN on diamond surface . . . . .	80
4.3. System Hamiltonian and simulations . . . . .	82
4.4. Dynamical decoupling of hBN . . . . .	88
4.5. Conclusions . . . . .	90
<b>5. Hyperpolarization of <math>^1H</math> in solid and liquid samples</b>	<b>91</b>
5.1. Hyperpolarization . . . . .	93
5.1.1. Hyperpolarization . . . . .	93
5.1.2. Conventional hyperpolarization methods . . . . .	96
5.1.3. Hyperpolarization methods with NV's . . . . .	98
5.2. NOVEL on protons . . . . .	107
5.2.1. Resonant $NV^-$ spin cross relaxation to $^1H$ spins in im- mersion oil. . . . .	107
5.2.2. Effect of inhomogeneous couplings and spin-diffusion on the cross-relaxation profile . . . . .	109
5.2.3. Dynamics of $NV^-$ cross-relaxation . . . . .	112
5.2.4. Simulations of $NV^-$ cross-relaxation to proton spins in fluids . . . . .	115
5.2.5. Polarization of PMMA . . . . .	117
5.2.6. Bare diamond measurements . . . . .	119
5.2.7. Methods . . . . .	122
5.3. Conclusions . . . . .	124
<b>6. Coming up detection of hyperpolarized <math>^{19}F</math> in <math>CaF_2</math></b>	<b>125</b>
6.1. Polarization of a solid . . . . .	127
6.2. NOVEL of $^{19}F$ in $CaF_2$ . . . . .	128
6.3. Spin diffusion . . . . .	129
6.4. Polarization distribution . . . . .	131
6.5. Detection of polarization excess . . . . .	134
6.5.1. Polarization strategy . . . . .	134
6.5.2. Nuclear Rabi . . . . .	137

6.5.3. Synchronization of decoupling and detection. . . . .	138
6.6. Conclusions . . . . .	143
<b>List of Figures</b>	<b>145</b>
<b>List of Tables</b>	<b>149</b>
<b>Appendices</b>	<b>149</b>
A. Dynamical and geometrical phases . . . . .	151
B. Calculation of evolution operator in case of non-zero detuning	155
C. Monte Carlo simulations of polarization distribution . . . . .	159
<b>References</b>	<b>161</b>

# CONFOCAL SPECTROSCOPY WITH NV CENTERS IN DIAMOND



Nitrogen-Vacancy (NV) centers are the most studied color defects in diamond owing to their unique optical properties. Such properties as the defect's unlimited photostability at room temperature, long coherence times alongside optical initialization and readout of the spin state make them suitable for a wide variety of applications in sensing and quantum technologies. This introductory chapter contains the basic theory concerning NV centers. In [Section 1.1](#) the relevant physical properties of a diamond, as a host material, are presented. [Section 1.2](#) is devoted to the description of NV centers in diamond, their formation and main features. The details of the experimental setup are given in [Section 1.3](#). The techniques, allowing manipulations of the NV center electron spin and sensing of weak magnetic fields are demonstrated in [Section 1.4](#).

## 1.1. Diamond as a host material

### 1.1.1. Physical properties

Diamond is one of the allotrope forms of carbon, where the atoms are arranged in the so-called diamond cubic order (Figure 1.1). Each carbon atom is connected to the closest four neighbouring atoms via covalent bonds, forming an extremely rigid lattice with tetrahedrally coordinated orbitals with  $sp^3$ -hybridization. A unit cell contains eight atoms with the nearest neighbour distance of about 1.44 Å.

Through such a structure, it is the hardest (10 on the Mohs scale) naturally occurring material known. Hardness measured by the sclerometry method has been measured to be 137 and 167 GPa for the (100) and (111) faces and the compressive strength up to 60 GPa has been reported [1]. Lonsdaleite, with hexagonal carbon lattice, the only material which is simulated to be harder than diamond, has been synthesized in 1966 [2].

Owing to various remarkable properties, diamond is a widely used material in industry. At room temperature and atmospheric pressure, it has density of  $3.52 \text{ g/cm}^3$  [3] and refractive index of  $n = 2.4$ . Because of their incredible hardness diamonds resist scratching, which makes them suitable for gems that are worn daily and for industrial applications, especially for drilling, sawing and polishing of other materials, including other diamonds.

The pure diamond is an insulator with resistivity of  $10^{16} \Omega \cdot \text{cm}$  [4]. At the

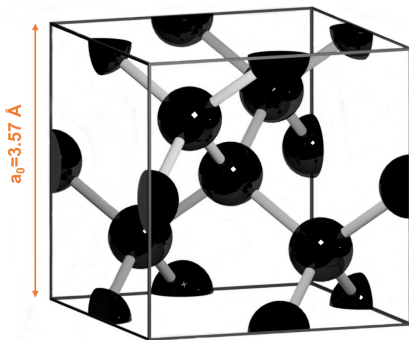


Figure 1.1: Diamond unit cell. Lattice constant  $a_0 = 3.567 \text{ \AA}$ .

same time diamond is an excellent thermal conductor ( $2200 \text{ W} \cdot \text{m}^{-1} \cdot \text{K}^{-1}$ ), has low thermal expansion and low thermo-optic coefficient. These properties result in a very efficient heat dissipation when the diamonds are used as a part of electric circuits. The doping of the diamond with boron turns it into the semiconductor, allowing the production of diamond transistors [5], for example.

Diamond is a promising candidate for high-energy photocatalytic chemistry because of a very wide band gap (5.47 eV at room temperature), diamond is chemically inert and stable [6]. As a result of diamond photoexcitation, highly energetic electrons will be released into solution and mediate the rate of chemical reactions. The low cytotoxicity makes nanodiamonds ideal for bio-sciences [7].

Transparent from deep-ultraviolet to the infrared, isotropic, diamond finds their classical applications in optics in diamond lenses, laser windows and as a part of vacuum windows, Raman lasers [8, 9, 10], etc.

### 1.1.2. Diamond formation and artificial growth

The formation of diamonds requires very high temperatures and pressures (at least  $T > 1000^\circ\text{C}$  and  $P > 5 \text{ GPa}$ ) [11]. In nature such conditions occur in the earth mantle (150 or more kilometres below the surface), where the diamonds are formed as a result of a metasomatic process, when the carbon-containing supercritical fluid melts and reacts with the mantle rocks and diamond crystallizes as a consequence of redox reactions [11]. They also can be formed by the shock of meteorite impact, if the target rock contains carbon.

The two most common production methods of synthetic diamonds are High pressure high temperature (HPHT) and Chemical vapor deposition (CVD). Historically, HPHT method was the first, since it just reproduces the natural formation process. The high-purity carbon turns into diamond under conditions of high heat and great pressure. The reproducible diamond creation was reported for the first time in 1955 [12], where the pressure of  $\sim 10 \text{ GPa}$

at  $\sim 2300^{\circ}\text{C}$  has been applied for the synthesis.

The realization of diamond-based photonic devices requires accurate control of optical design parameters during the growth. CVD technique allows to regulate the properties of the diamond while growing and do not place the restrictions on the size and shape of the material, which can be produced. The method is known since early 50s, by early works in the Soviet Union and the United States on the nucleation growth of diamond by pyrolysis of hydrocarbon gases (such as methane) at the relatively low temperature of  $800^{\circ}\text{C}$  [13]. CVD diamond growth typically occurs under low pressure (1–27 kPa). Varying amounts of gases are supplied into a chamber, where they flow around and react at the substrate (typically a silicon wafer), heated to  $800\text{--}1000^{\circ}\text{C}$ . Desired impurities are added in the gaseous phases at appropriate moments of times. For sensing purposes creation of isotopically purified diamond up to  $\sim 99.99\%$  of  $\text{C}^{12}$  is one of the most preferable modification which reduces the magnetic background.

Natural, synthetic and imitation diamonds (cubic zirconium or silicon carbide) are most commonly distinguished using optical techniques or thermal conductivity measurements.

### 1.1.3. Types of diamonds and color centers

Because the arrangement of atoms in diamond, the material is extremely rigid, only few types of impurities can contaminate it, substituting carbon. In natural diamonds these are mainly limited to boron and nitrogen. Some other imperfections of the lattice are vacancies (missing atoms) and interstitial carbons. All these irregularities of the crystal lattices are called crystallographic defects. The defects that occur around a single lattice point are called point defects.

Pure diamonds are transparent and colourless. A small amount of defects or impurities (about one per million of lattice atoms) can colour diamond in blue (boron), yellow (nitrogen), brown (vacancy cluster), green (GR1 center), purple, pink (NV centers), orange or red [14]. Such defects cause light of only one colour to be transmitted by the part of the crystal, therefore

they are called *colour centers*. Because of the wide band gap, there are more than 500 of such optically active defects [15]. The high Debye temperature of diamond ( $\Theta_0 \sim 2219K$ ) leads to a relatively low phonon population at room temperature, which allow these defect-related electronic states to persist for long times without suffering from phonon-induced relaxation, making them very stable. The diamond consists of two stable isotopes of carbon, with natural abundance  $\sim 98.9\%$  for  $^{12}C$  and  $\sim 1.1\%$  for  $^{13}C$ . Since only  $^{13}C$  possess a spin  $1/2$ , the defects are situated in an area with low magnetic field fluctuations. This leads to quite long coherence times for the color centers with spins and makes the diamond an ideal material for applications in photonics.

According to the optical absorption caused by different impurities, the natural diamonds are divided into type I and type II [3, 16, 17], which are further subdivided into Ia, Ib, IIa and IIb.

*Type I* diamonds contain nitrogen atoms as their main impurity and absorb in both the infrared and ultraviolet region, from 320 nm. They also have a characteristic fluorescence and visible absorption spectrum. *Type Ia* and *Type Ib* contain up to up to 0.3% (3000 ppm) and 0.05% (500ppm) of nitrogen, correspondingly. *Type II* diamonds have no measurable nitrogen impurities, absorb in a different region of the infrared, but have no ultraviolet absorption above 225 nm. Type I have always low and type II mostly high conductivity. The high-conductive type II group is called *Type IIb* (p-type semiconductors) and the low-conductive *Type IIa*.

Over 90% of natural diamonds belong to class I and different types can co-exist within a single stone. As a result, HPHT grown diamonds have mostly type I. The high-purity diamonds, which are needed for problems presented in this thesis, are created by CVD.

## 1.2. Nitrogen-Vacancy center in diamond

The NV center is a point defect in a diamond crystal lattice, which consists of the combination of a substitutional nitrogen atom and vacancy next to it

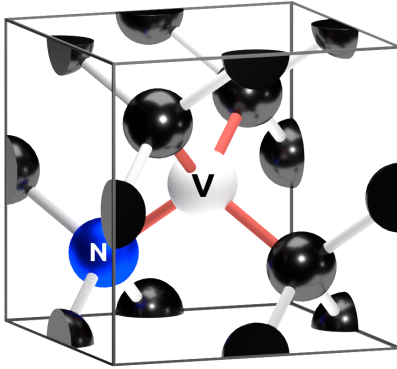


Figure 1.2: Structure of NV center. The red bonds show 4 possible orientations.

(Figure 1.2). The presence of an electron spin opens the way to the numerous applications in biology, quantum computing, and sensing, to mention few [18, 19, 20, 21, 22, 23, 24, 25]. Therefore, it is, probably, one of the most studied defects in diamond (known since 1965 [26, 27]).

Molecular orbitals form the defect with  $C_{3v}$  symmetry [28].  $C_3$  means that the rotation of a center around a symmetry axis by  $\frac{360^\circ}{3}$  does not change its appearance.  $v$  stands for the vertical symmetry plane, which is parallel with the principal axis. The reflection through it generates an identical copy of the original molecule. The symmetry (NV) axis is oriented along four possible crystallographic axes, i.e. there are four possible orientations of NV centers. Each time it can be either N-V or V-N [29].

### 1.2.1. Formation of NV centers

The detailed mechanism of creation of color centers is still not fully understood. The experts disagree on this, but it is commonly assumed, that the diffusing vacancies are trapped by substitutional nitrogen atom, which one usually can find in abundance in Type Ib natural and N-doped CVD diamond, to create an NV center. Therefore, the established recipes for defect creation include implantation of vacancies with subsequent high temperature annealing ( $\sim 900^\circ\text{C}$ ), to make the vacancies mobile. The substitutional nitrogen atom has quite high diffusion activation energy [30], therefore it does not

diffuse together with the vacancy. At the same time some recent studies show that the NV defects are predominantly created directly by irradiation, while simultaneously produced vacancies will form  $V_2$  pairs after annealing [15, 30]. Density functional theory (DFT) calculations show that NV center remains immobile up to  $\sim 1700^\circ\text{C}$  [30].

Thus, the synthetic creation of defects depends on a wide range of parameters and allows to get the NV centers at different depths, concentrations and properties.

Depending on the desired attributes, implantation of the defects can be performed via electron irradiation ( $\sim \text{MeV}$ ) or ion implantation ( $^{15}\text{N}$ ,  $\text{He}_2^+$ ,  $\text{C}^+$ ) [31].

The formation of the NV centers during the CVD growth allows one to control their orientation depending on the orientation of the grown diamond [15]. Usually [100] and [111] orientations are used, since they are commercially more available and provide convenient orientations for the magnetic field alignment.

For the aims pursued in this thesis it was necessary to work with shallow ( $< 10 \text{ nm}$ ) NV centers, therefore, nitrogen irradiation was used for implantation. In the case of implantation energies  $< 10 \text{ keV}$ , the spatial positioning of the N atoms and NV centers lies in the range 5-10 nm [31]. Implanted nitrogen atoms produce simultaneously nitrogen impurities and vacancies.

### 1.2.2. Electronic energy levels

The neutral  $NV^0$  center contains five electrons by the number of unsatisfied bonds. These are three dangling bonds on the carbon atoms bordering the vacancy and two on the nitrogen atom [28]. The center can also capture an extra electron, becoming negatively charged  $NV^-$ . It was discovered by electron paramagnetic resonance (EPR) and hole-burning experiments, that the ground state (GS) of  $NV^-$  is a spin triplet [18], implying that the number of active electrons at the center is even. The coupling to the nitrogen is weaker than coupling to carbons, therefore the active electrons concentrate near carbons [18]. According to some recent studies, a positively charged

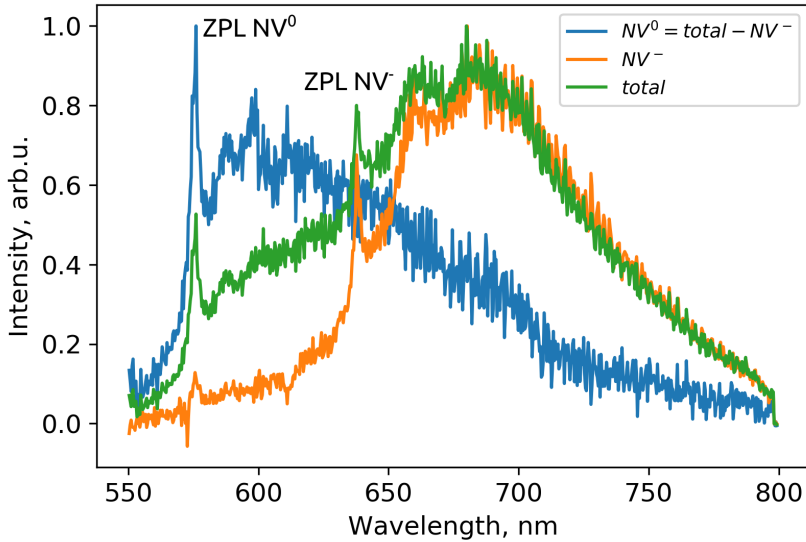


Figure 1.3.: Room-temperature spectra of  $NV^0$  (ZPL 575 nm) and  $NV^-$  (ZPL 637 nm). Experimental data are green and orange lines.  $NV^0$  spectrum is obtained by subtraction. Excitation wavelength 470 nm.  $NV^+$  state is not fluorescent.

$NV^+$  state also exists [28, 32, 33, 34].

The studying of any color center starts from the spectra acquisition. From the spectra one can differentiate the charge states of Nitrogen-Vacancy color center (Figure 1.3) [35, 36]. Optical excitation of the negatively charged NV center on the zero-phonon line (ZPL) at 1.945 eV ( $\sim 22570.8$  K) is well-described by transitions of the electron, when a dynamic Jahn-Teller interaction in the excited state is taken into account [28]. So,  $NV^-$  gives rise to a strong absorption line at 1.945 eV (637 nm). At lower temperature ZPL becomes more pronounced, followed by prominent vibronic side bands.  $NV^0$  with spin 1/2 has a ZPL at 2.156 eV (575 nm). The  $NV^+$  state is non-fluorescent.

The electronic orbitals (Figure 1.4) of the NV centers can be approximated

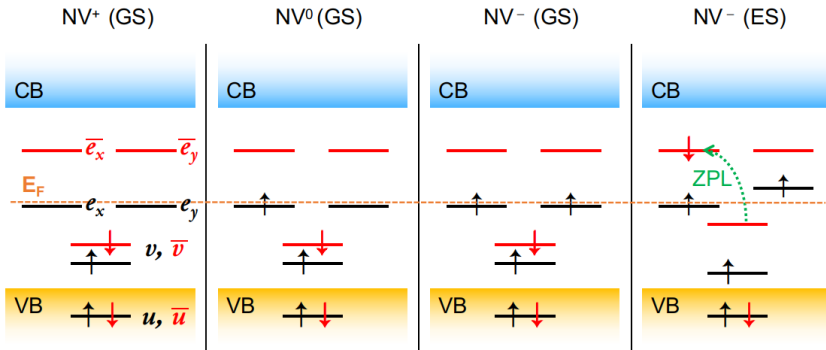


Figure 1.4.: Schematic illustration of spin configurations for different charge states of NV center. Orange dotted horizontal line shows the relative position of the Fermi level  $E_F$ .

applying the group theory to the system with the known symmetry and using DFT calculations [28, 37, 38, 39, 40, 41]. Electrons occupy the energy levels, formed by four molecular orbitals:  $u$ ,  $v$ , and the doubly degenerate  $e_{x,y}$ . In the ground-state configuration, orbitals are filled according to the Pauli exclusion principle and Hund's rules. Two electrons occupying the spin-up and spin-down  $u$  levels are immersed into the valence band. The structure of the excited state (with  $C_{1h}$  symmetry) corresponds to the typical case where the Jahn-Teller (JT) effect (degenerate electronic states couple to vibrational modes of like symmetry) arises [40] and causes symmetry breaking. The ZPL transition (green dashed arrow) occurs between the occupied  $\bar{v}$  and unoccupied  $\bar{e}_{x,y}$  states. The Fermi level of the bulk diamond is denoted by brown horizontal dashed line.

Negatively charged NV center has much more useful properties, than the other charge states, therefore, here and further, the "NV center" will refer to the  $NV^-$ . Taking into account spin-orbit, spin-spin, strain, and Jahn-Teller interactions and complementing them with experimental observation by optical and magnetic-resonance methods, one can get the following term diagrams (Figure 1.5) [28, 37, 41, 42, 43, 44]. These are the eigenstates of the multielectron wave function. The NV center creates spatially localized,

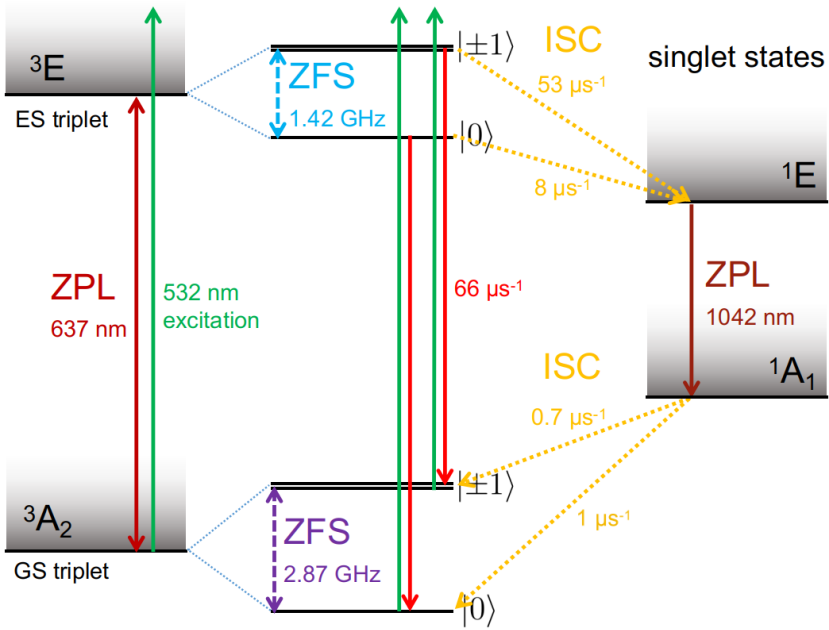


Figure 1.5.: Schematic diagram of the energy levels of negatively charged NV center. Solid and dashed lines indicate radiative and non-radiative transitions, correspondingly.

energetically separated ground and excited states within the bandgap of the diamond. Energy levels ( $^3A_2$ ,  $^3E$ ,  $^1A_1$ ,  $^1E$ ) are named by the irreducible representations of the symmetry groups of triplet and singlet states ( $C_{3v}$ ,  $C_{1h}$ ) [18, 28], i.e. the name represents the symmetry of the energy level. The shaded regions denote the quasicontinua of the vibrational levels, which give rise to the phononic sidebands. The ZPL absorption corresponds to  $^3A_2 \rightarrow ^3E$  transition. The anisotropic dipolar interaction of the two electron spins forming the triplet state averaged over their wave function leads to the zero field splitting (ZFS). The zero field splitting causes a lifting of the degeneracy of the spin sublevels  $m_s = \pm 1, 0$  even in the absence of an external magnetic field.

### 1.2.3. Photophysical properties

Photophysical properties of NV center are related to the behaviour of the defect under the laser illumination.

The spin dynamics of the NV center under optical illumination are driven by radiative transitions between states of the same spin multiplicity as well as a nonradiative intersystem crossing (ISC) between states of different spin multiplicity (see [Figure 1.5](#)).

NV center is not photochemically stable. Under continuous excitation there is a constant charge conversion between neutral and negatively charged states, i.e. they exist simultaneously. The relative concentration strongly depends on the laser intensity and wavelength. Recent studies show that under usual operating conditions the NV exists in an equilibrium of two charge states [70% in the expected negatively charged state ( $NV^-$ ) and 30% in the neutral charged state ( $NV^0$ )] [45]. Time-resolved optical spectroscopy shows that intense irradiation at 514 nm switches the NV to the negative form, but the defect relaxes back to the neutral form under dark conditions [35, 36]. In recent experiments 532 nm laser, with a wavelength within the vibronic absorption band of both the  $NV^-$  and  $NV^0$ , is usually used for excitation because it is commercially more available [46]. The charge stability of shallow NV centers can also be regulated by surface termination [32, 47, 48]. Namely, the desirable state is when all the dangling carbon bonds are terminated by Oxygen [49]. The charge state can be regulated by changing the electrochemical potential around the diamond immersed into the electrolyte solution [50].

To the first order optical excitation is a spin state conserving process. However, spin-orbit (LS) coupling leads to the mixing of triplet and singlet states in the excited state (ES), i.e. in the course of optical excitation the ISC takes place [43].

The different transition rates ([Figure 1.5](#)) lead to the fact, that regardless on the initial state,  $NV^-$  always preferentially decays to  $m_s = 0$  state, which means that NV center can be optically initialized [44, 51, 52, 53]. When being excited from  $m_s = 0$  it relaxes back to this state. However, if the initial

state is  $m_s = \pm 1$ , as a result of ISC it changes the spin state and performs a rather long journey back to the GS. This leads to two very important consequences. The first being that the NV can be polarized under the green laser illumination and spin polarization is dominated by a preferential ISC out of the excited  $m_s = \pm 1$  states instead of a selective decay out of the singlets into the  $m_s = 0$  ground state. The reported degree of polarization reaches 80% (mainly because of the charge state conversion) [54, 55]. Secondly, observing time-resolved photoluminescence one can readout the state of the NV (Figure 1.6) [56, 57]. If the initial state is  $|0\rangle$ , the high initial fluorescence level decays to the steady-state with nonzero population of the singlet state. For  $| - 1 \rangle$  fluorescence decays because of the fast ISC and then recovers to the steady-state. Specifically, optical readout is conducted by comparing the integrated fluorescence (in the first 200 ns) of the spin state to be read out with calibration measurements of the integrated fluorescence corresponding to the spin being prepared in the  $m_s = 0$  and  $\pm 1$  spin states. The integration time window occurs because of the 250 ns lifetime of the singlet state. The readout contrast is reported to be around 30%.

NV center has a magnetic field dependent photoluminescence [58, 59, 60]. The presence of transverse magnetic fields  $B_x$  and  $B_y$  leads to mixing of  $|0\rangle$  and  $|\pm 1\rangle$  levels, which is otherwise suppressed by D. This leads to the reduced rate of photoluminescence.

A large absorption cross-section at the excitation wavelength leads to quantum yield close to unity. Short excited-state lifetime (11.6 ns) and high quantum efficiency for radiative relaxation [18, 61] result in an achievable countrates around 300 kcounts/s [57].

All these properties, together with the stability at room temperature (high Debye temperature), make the NV center extremely suitable for the experiments involving spin manipulation.

#### 1.2.4. Interaction Hamiltonian

The GS fine and hyperfine structures for both nitrogen isotopes can be described by the canonical spin-Hamiltonian of trigonal defects [18, 43, 62].

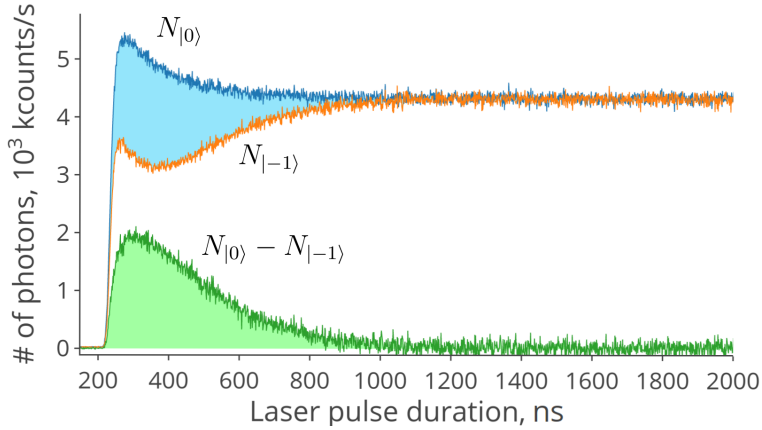


Figure 1.6.: Optical readout of  $NV^-$  spin state. Fluorescence responses for the system initially being in  $|0\rangle$  (blue trace),  $|-1\rangle$  (orange trace) and their difference (green trace). The shaded green (blue) areas represent the signal that allows to discriminate different spin states.

In the total hamiltonian describing NV center in the presence of magnetic, electric and force fields one can single out the following components:

$$\hat{H} = \hat{H}_{ZFS} + \hat{H}_{hf} + \hat{H}_{quad} + \hat{H}_{Zeeman} + \hat{H}_{el+strain}. \quad (1.1)$$

The first three items describe the ground state of defect at zero applied fields.

### Zero field splitting

The fine structure is governed by electron spin dipole-dipole interactions and is described via zero field splitting symmetric traceless tensor  $\mathcal{D}$  [63]:

$$\mathcal{D} = \begin{pmatrix} D_x & 0 & 0 \\ 0 & D_y & 0 \\ 0 & 0 & D_z \end{pmatrix}. \quad (1.2)$$

Then one can show that:

$$\hat{H}_{ZFS} = \hat{S}D\hat{S} = D \left( S_z^2 - \frac{S(S+1)}{3} \right) + E(S_x^2 - S_y^2), \quad (1.3)$$

with  $D = (3/2)D_z$  and  $E = (D_x - D_y)/2$  measurable zero field splitting values. In case of NV center  $D = 2.87$  GHz and  $E \approx 0$  at room temperature [18]. Usually the Hamiltonian is shifted upwards in energy by the amount  $2D/3$ , so that  $\hat{H}_{ZFS} = DS_z^2$  [64]. The use of NV center as a temperature sensor is based on the temperature dependence of  $D$  ( $d\Delta/dT = -2\pi \times 77$  kHz  $K^{-1}$ ) [65] and allows nanometre-scale thermometry in a living cell with nanodiamonds [66].

### Hyperfine coupling

NV center is surrounded by various nuclei, creating the spin bath. The interaction of the electron spin  $\hat{S}$  with nuclear spin  $\hat{I}$  are characterized by the hyperfine coupling tensor, which arises from interactions between magnetic moment of nuclear spin  $\mu_n$  and electron spin  $\mu_e$  [67]. These interactions are the sum of Fermi contact interaction (for the electron in s-state, when the electron wave function is nonzero at the nucleus) and magnetic dipolar interactions of magnetic moments when they are far enough apart. One can always find the principal axes such that the hyperfine tensor is diagonal:

$$\hat{H}_{hf} = \hat{S} \cdot \mathbf{A} \cdot \hat{I} = A_{\parallel} S_z I_z + A_{\perp} (S_x I_x + S_y I_y). \quad (1.4)$$

The first term is equivalent to the addition of extra magnetic field proportional to the z-component of the nuclear spin and causes the splitting of the energy levels to  $2I+1$  lines. It is the inhomogeneous part of dipolar Hamiltonian. The second term allows a simultaneous reversal of electron and nuclear spin, since  $(S_x I_x + S_y I_y) = \frac{1}{2}(S_+ I_- + S_- I_+)$ . This is the so-called flip-flop term and represents a homogeneous part of Hamiltonian, which mixes degenerate Zeeman states and causes line broadening [68].

In this thesis we will focus mostly on the weakly coupled nuclear spins, which are far away from NV center. In this case we can describe the hyperfine interactions with dipolar Hamiltonian [68]:

$$\hat{H}_{dipolar} = \frac{\mu_0}{4\pi r^3} \gamma_e \gamma_n \hbar^2 [3(\hat{S} \cdot e_r)(\hat{I} \cdot e_r) - \hat{S} \cdot \hat{I}]. \quad (1.5)$$

It can be decomposed into six components by how the resulting operators affect the states. For nuclear magnetic resonance (NMR) problems one usually keeps only the first two, that commute with Zeeman part of Hamiltonian, and are usually called *adiabatic* or *secular* part:

$$\hat{H}_{sec} = \frac{\mu_0}{4\pi r^3} \gamma_e \gamma_n \hbar^2 (1 - 3 \cos^2 \theta) \frac{1}{2} [3\hat{S}_z \hat{I}_z - \hat{S} \hat{I}]. \quad (1.6)$$

For the intrinsic  $^{14}\text{N}$   $A_{\perp} = -2.7$  MHz and  $A_{\parallel} = -2.16$  MHz [69, 70],  $^{15}\text{N}$   $A_{\perp} = 3.65$  MHz and  $A_{\parallel} = 3.03$  MHz [70, 71]. In general case hyperfine splitting is  $A_{hfs} = \pm \sqrt{A_{xz}^2 + A_{yz}^2 + A_{zz}^2}$  with the sign determined by the sign of  $A_{zz}$ . The closest  $^{13}\text{C}$  can cause the 130 MHz hyperfine splitting [71, 72].

### Quadrupole coupling

Quadrupole coupling is an electrostatic interaction, that arises for the nuclear spins with  $I > 1/2$ , when the charge distribution inside the nucleus is not spherical. Quadrupole moment of such nucleus couple to the electric field gradient, created by electron. In the general from the quadrupolar Hamiltonian is written as [67, 73]:

$$\hat{H}_Q = \frac{\chi}{4I(2I-1)} (3\hat{I}_z^2 - \hat{I}^2 + \eta(\hat{I}_{xx}^2 - \hat{I}_{yy}^2)), \quad (1.7)$$

where  $\chi = \frac{e^2 q Q}{\hbar}$  is the quadrupole coupling constant (which is a parameter of the substance),  $\eta = \frac{V_{xx} - V_{yy}}{V_{zz}}$  – asymmetry parameter.  $q$  – field gradient, defined as  $V_{zz} = eq$ .  $Q$  – quadrupole moment and  $V$  is an electric field

gradient:

$$V = \begin{bmatrix} V_{xx} & V_{xy} & V_{xz} \\ V_{yx} & V_{yy} & V_{yz} \\ V_{zx} & V_{zy} & V_{zz} \end{bmatrix}. \quad (1.8)$$

One can always find principal axes of potential  $V$ , such that it will have a diagonal form. In the case of axial symmetry by taking the axis to be  $z$ -direction,  $\eta = 0$ .

If the NV center is formed by  $^{14}\text{N}$  isotope with spin  $I=1$ , the interaction is described via nuclear electric quadrupole parameter  $P = -4.96$  MHz [62, 70, 74]:

$$\hat{H}_{quad} = P \left( I_z^2 - \frac{I(I+1)}{3} \right). \quad (1.9)$$

Zeeman splitting

It is worth to point out, that all the aforementioned terms are not affected by the external magnetic field. The application of magnetic field lifts the degeneracy of levels, which correspond to  $m_s = \pm 1$ , and splits the nuclear spin energy levels:

$$\hat{H}_{Zeeman} = g_e \mu_B \mathbf{B} \hat{S} + \gamma_n \mathbf{B} \hat{I}, \quad (1.10)$$

where  $g_e$  is the electronic g-factor ( $g = 2.0028 \pm 0.0003$ );  $\mathbf{B}$  is the external magnetic field,  $\gamma_n$  - nuclear gyromagnetic ratio.

Electric fields and strain

Strain in the crystal lattice results in an effective electric field [75]. Thus, strain (force field) and static electric fields can be treated in the same way. We combine the electric field  $E$  and an applied strain  $\sigma$  to a vector  $\Pi = E + \sigma$ .

The Hamiltonian reads:

$$\hat{H}_{el+strain} = d_{\parallel} \Pi_z S_z^2 - d_{\perp} [\Pi_x (S_x^2 - S_y^2) + \Pi_y (S_x S_y + S_y S_x)], \quad (1.11)$$

where  $d_{\parallel}$  and  $d_{\perp}$  are the components of the ground state electric dipole moment. Transverse electric fields and transverse strain lead to  $E \neq 0$  in the ZFS tensor [43, 62, 64]. Mechanical stress is used in hybrid quantum sensors for electric field measurement [76] and to create the strain mediated coupling to mechanical resonators [77]. This part of Hamiltonian is beyond the subject of this thesis.

### 1.3. Confocal microscope for nano-NMR

The experiments are performed on the confocal scanning microscope supplied by the hardware for the microwave manipulation.

The first scanning confocal microscope was made in 1955 [78]. The principal difference between the fluorescence and optical microscope is the pinhole, which cuts off all the light which comes from outside the focal point. The practical effect of this is that the image comes from a thin section of the sample.

The experimental setup can be divided into three parts: optical, microwave and the software, which controls all the measurements.

#### 1.3.1. Optical path

All the optical components are arranged on the pumped optical table which ensures high stability against vibrations (Figure 1.7). The excitation path starts from the green laser (Laser Quantum diode pumped solid state (DPSS) Gem laser 532 nm 200mW) operating in continuous wave (CW) mode and ends in the sample. The two mirrors bring the beam to the focussing lens, after which it hits the acousto optical modulator (AOM) (Crystal Technology Inc. 3350-199). AOM allows quickly switch the laser on and off within nanoseconds, which is necessary for the NV readout in the pulsed experi-

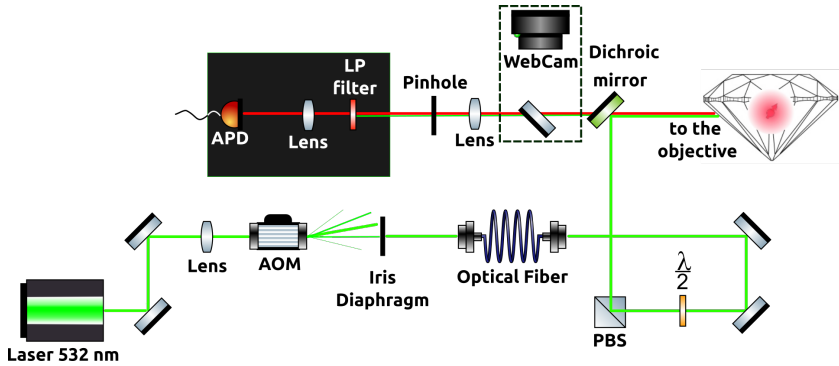


Figure 1.7.: Confocal microscope: optical part of the setup, which consists of excitation (green) and detection (red) paths.

ments. The iris diaphragm next to it blocks all the maxima, except of the first order. Thus, when the AOM is off, no light is coming to the sample. The optical fibre brings the beam into another part of the optical table, where using two mirrors and polarising beam splitter (PBS) the light is directed to the dichroic mirror (reflection band 470-590 nm, transmission band 620-700 nm). The dichroic mirror reflects the beam to the 45° mirror, which brings the beam to the vertical plane. And then the laser hits the objective. The system of two mirrors allows to align the excitation path with respect to the back-reflection. The  $\lambda/2$  plate ensures the right polarisation is coming to the PBS, to avoid the leakage.

The detection path is stretched along the red line, representing the NV's fluorescence in the red region of spectrum. The objective gathers the fluorescence which has been emitted (forwards or backwards, depending on the sample's orientation). The dichroic mirror reflects the green laser, but transmits the fluorescence, which is afterwards collected with the lens and is focused to the pinhole. The 650 nm longpass (LP) filter blocks the rest of the laser lights, which leaked through the dichroic mirror. Then the separated photons are collimated to the avalanche photodiode (APD). The part depicted in the dashed rectangular was used for visualization of hexagonal

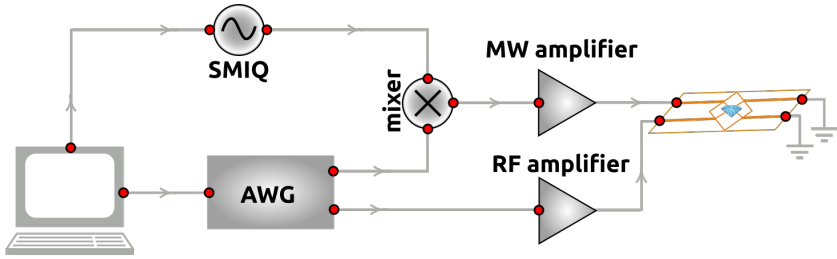


Figure 1.8.: The system for the microwave manipulation of the NV center's electron spin.

boron nitride (hBN) (see [Chapter 4](#)).

The signal from the APD goes to the counts duplicator, where it is distributed to the counting devices: NI-DAQ (for scanning and ODMR) and Swabian Instruments TimeTagger (for pulsed measurements).

### 1.3.2. Microwave circuit

For the spin manipulation, we must be able to apply microwave- and radiofrequency pulses (see next section). The principal scheme of the microwave circuit is depicted in [Figure 1.8](#). All the sequences are loaded to the arbitrary waveform generator (AWG) (Tektronix 5014C), which also triggers the AOM and counters within the loaded sequence. AWG generates only the radiofrequency, therefore to deliver the GHz frequency waves to the sample it is mixed with the SMIQ microwave source. After the amplification the signal goes to the printed circuit board (PCB) board with soldered copper microstructure. The type of microstructure varied in different experiments. At the end the signal is attenuated and grounded.

### 1.3.3. Sample stage

The  $45^\circ$  mirror is located inside a heavy aluminium box, on the top of which one mounts the piezo-scanner (MCL Nano-PDQ350HS nanopositioning stage). The objective (Olympus UPlanSApo 60x, oil immersion,

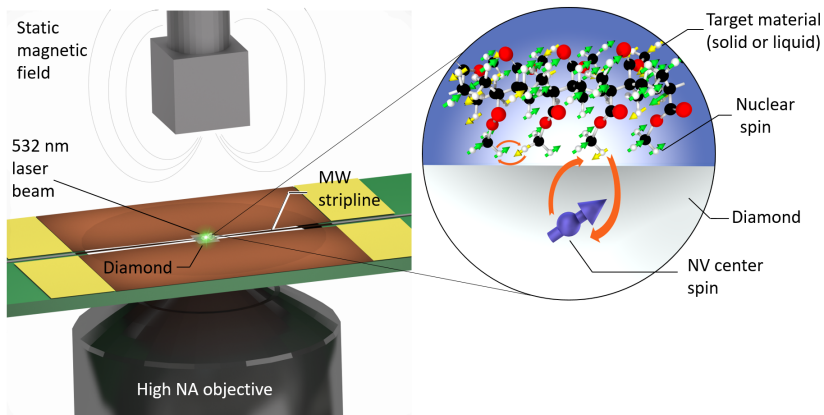


Figure 1.9.: Working geometry for most of the experiments.

NA=1.35) is fixed to the scanner through the adapter. The sample holder is also bound to the aluminium walls, so that when scanning only objective moves. The typical working geometry is when the diamond membrane ( $\sim 30\mu\text{m}$ ) is placed on the copper microstructure, made by electroplating (Figure 1.9). Then the collected fluorescence is emitted backwards. For the enhanced light collection in some experiments nanopillars were used [79]. The magnet is a small nickel cube, which is positioned above the sample. Its position is controlled by mechanical actuators (Newport SMC100 single-axis motor controller) with precision  $10^{-4}$  m.

#### 1.4. Spin manipulation techniques

The spin manipulation techniques are based on the application of resonant MW fields to change the NV center spin state. They are used to determining the relaxation times and performing noise spectroscopy.

The high quantum efficiency allows the photoluminescence measurements in which 300 000 (kilocounts) photons per second can be collected from a single saturated NV center using a standard confocal microscope equipped with a high-numerical aperture objective. The spin manipulation experiments are

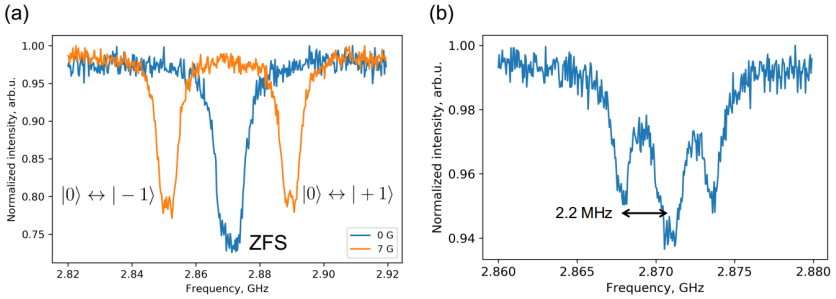


Figure 1.10.: (a) CW ODMR measurements at zero field and at 7 Gauss. The magnetic field is calculated from the position of  $|0\rangle \leftrightarrow |-1\rangle$  and/or  $|0\rangle \leftrightarrow |+1\rangle$  transitions. (b) CW ODMR measured at low microwave power allows to resolve the hyperfine structure. Three lines correspond to  $^{14}\text{N}$ .

performed on unsaturated colour centers with typical value around 150 kc/s. The analysis window of the APD response is 200 ns, which results in 0.03 photon per readout. In turn, the shot noise [80] scales as  $\sqrt{N}$ , therefore the signal-to-noise ratio (SNR) scales as  $N/\sqrt{N} = \sqrt{N}$  [56]. To acquire enough amount of photons and get a valuable SNR one has to perform  $10^4 - 10^6$  readouts (repetitions of pulse sequence). In order to optimize this number one can use single-shot or repetitive readout techniques [81, 82].

#### 1.4.1. Optically Detected Magnetic Resonance

Conventional magnetic resonance methods are restricted to the studying of the ground states of atoms, nuclear spins or molecules and optically detected magnetic resonance (ODMR) is usually used to gain the information about the optically excited states [83, 84]. It is worth noting, that only three of the single quantum emitters in diamond exhibit ODMR [15]. Despite the first ODMR of the NV center was observed in 1988 [85], the history of the confocal microscopy of single NV center starts with its observation in 1977 [86].

In case of NV center ODMR is based on the existence of the optically bright ( $m_s = 0$ ) and dark states ( $m_s = \pm 1$ ). The green laser illumination initializes

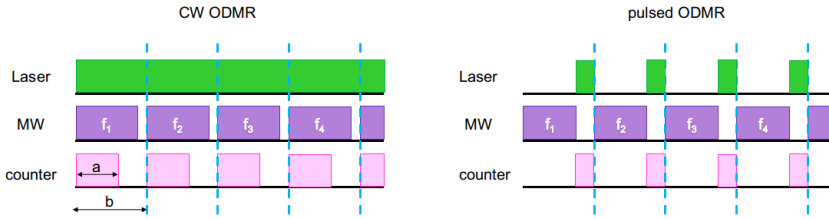


Figure 1.11.: Pulse sequences for CW (left) and pulsed (right) ODMR measurements.

the NV center in the bright state and further application of microwave can bring the center into the dark state, if the frequency is resonant to corresponding transition. That results in the dips in the observed fluorescence intensity (Figure 1.10).

At zero external magnetic field one can observe the lines corresponding to ZFS at GS and ES. Everything, that affects the energies of the magnetic sublevels can be measured by ODMR [87, 88]. This make ODMR useful in fields such as thermometry, electrometry, and of particular importance to this thesis, magnetometry [65]. An application of an external magnetic field induces the Zeeman shifts of the NV center levels and splitting of the ZFS into several lines. This allows reconstruction of the vectorial structure of the magnetic field produced by a sample brought close to the diamond surface [89, 90]. The ultimate photon-shot-noise-limited magnetic-field sensitivity for ac signals of  $f = 20$  kHz is  $0.9 \text{ pT}/\sqrt{Hz}$  [91]. In this thesis ODMR is used to determine the magnitude of the external static magnetic field  $B_0$  and resonance frequency of spin transitions (Figure 1.10(a)).

ODMR can be measured in CW and pulsed modes (Figure 1.11). In CW mode the laser is always on and the MW course perform the sweep of frequencies on the designated range of frequencies, synchronized with the detector (Figure 1.11, left). The value  $a/b$  is called the duty cycle of the counting device. Since the duration of each MW frequency pulse and duty cycle are not properly tuned, CW regime does not show the actual contrast of NV center and is used for determination of transition frequency. In the

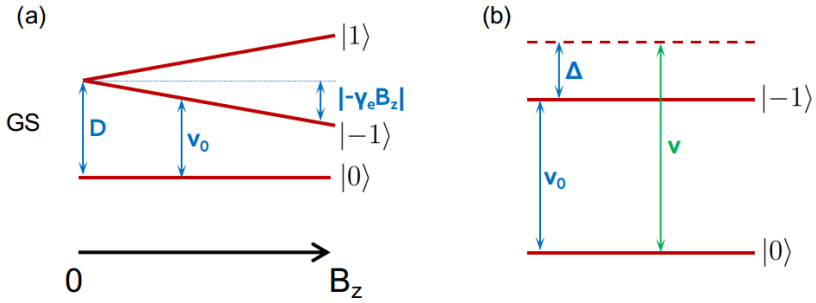


Figure 1.12.: (a) The Zeeman splitting of the GS energy levels of the NV center when the magnetic field is aligned along the quantization axis. (b)  $|0\rangle$  and  $|-1\rangle$  states at some magnetic field strength model a two-level system.

pulsed mode the duration of the MW pulse is tuned to  $\pi$ -pulse (see next subsection). The pulsed ODMR or low field CW ODMR allow to resolve the hyperfine splitting due to intrinsic nitrogen and/or  $^{13}\text{C}$  (Figure 1.10(b)).

#### 1.4.2. Rabi oscillations

Rabi oscillation is the behaviour of a two-level system driven by near-resonant radiation constituting an oscillation of the state population. In this work  $|0\rangle \longleftrightarrow |-1\rangle$  transition represents such a two-level system (Figure 1.12(b)).

Under the static magnetic field  $B_z$  aligned along NV axis the transition frequency is  $\nu_0 = |D - \gamma_e B_z|$ , where  $D$  is the ZFS and  $\gamma_e$  is electron gyromagnetic ratio <sup>1</sup> (Figure 1.12(a)). Defining  $h\nu_0 = \Omega_0$ , without loss of generality we can consider the  $|0\rangle \longleftrightarrow |-1\rangle$  transition as a two-level system. The static part of Hamiltonian is  $\hat{H}_0 = \Omega_0 \hat{S}_z$ . Here and further  $\hat{S}_i$  ( $i = x, y, z$ ) define the spin matrices, corresponding to electron spin  $1/2$ . For the higher spin case see [92].

We want to know the population of the energy levels under continuous microwave irradiation with frequency  $\nu$  applied along x-axis ( $\vec{B} = \{B_1 \sin \omega t, 0, B_z\}$ ). Detuning is defined as  $\Delta = \nu - \nu_0$ . The time-dependent part of Hamiltonian

<sup>1</sup> $D=2.87$  GHz,  $|\gamma_e| = g_e \mu_b / \hbar$ ,  $|\gamma_e / 2\pi| = 2.8025$  MHz/G should be substituted into equation

is then  $\hat{H}_1 = -\gamma_e B_1 \sin \omega t \hat{S}_x$ ,  $\omega = 2\pi\nu$ . For future calculations it is convenient to introduce  $\Omega_1 = -\gamma_e B_1$ . In the experiment in any point inside the diamond the coplanar waveguide or another microstructure creates a  $B_1$  field, which has component, perpendicular to NV axis.

The standard approach to find the solution [67] starts from decomposition of  $\hat{H}_1$  into two counter-rotating terms using the relation:

$$\sin \omega t = \frac{1}{2} [(\sin \omega t \hat{x} + \cos \omega t \hat{y}) + (\sin \omega t \hat{x} - \cos \omega t \hat{y})]. \quad (1.12)$$

Then,

$$\hat{H}_{lab} = \frac{\Omega_0}{2} \hat{S}_z + \frac{\Omega_1}{2} (\sin \omega t \hat{S}_x + \cos \omega t \hat{S}_y) + \frac{\Omega_1}{2} (\sin \omega t \hat{S}_x - \cos \omega t \hat{S}_y). \quad (1.13)$$

It is convenient to go into the frame, rotating along z-axis with frequency  $\omega$ . The corresponding transformation is described via unitary operator  $\hat{U} = e^{i\omega \hat{S}_z t}$  ( $|\psi_{rot}\rangle = \hat{U}|\psi_{lab}\rangle$ ). Using the sandwich formulas:

$$\hat{U} \hat{S}_x \hat{U}^\dagger = \hat{S}_x \cos \omega t - \hat{S}_y \sin \omega t, \quad (1.14)$$

$$\hat{U} \hat{S}_y \hat{U}^\dagger = \hat{S}_y \cos \omega t + \hat{S}_x \sin \omega t. \quad (1.15)$$

The hamiltonian in the rotating frame becomes:

$$\hat{H}_{rot} = \hat{U} \hat{H}_{lab} \hat{U}^\dagger + i\hbar \dot{\hat{U}} \hat{U}^\dagger = \delta\Omega \hat{S}_z - \frac{\Omega_1}{2} \hat{S}_y, \quad (1.16)$$

where  $\delta\Omega = \Omega_0 - \omega$ . Here we used the fact that  $\Omega_1 \ll \omega$  and neglected the fast rotating terms. It is the so-called rotating wave approximation (RWA). The solution of time-dependent Schrödinger equation for  $|\psi\rangle = c_1(t)|0\rangle + c_2(t)|-1\rangle$  results in following expressions for the state populations:

$$P_{|-1\rangle}(t) = \frac{1}{2} \frac{\Omega_1^2/4}{\Omega_R^2} (1 - \cos(\Omega_R t)). \quad (1.17)$$

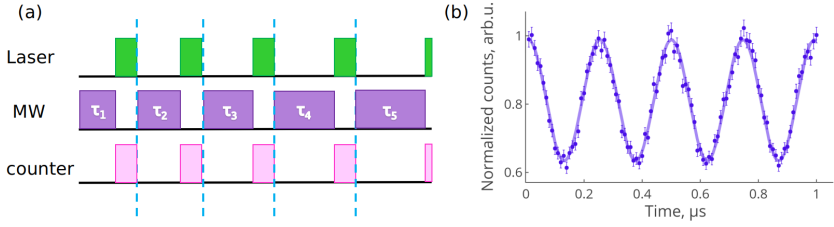


Figure 1.13.: (a) Experimental sequence to measure Rabi oscillations. (b) Rabi oscillations measured on a single shallow NV center. Contrast 36%.

$\Omega_R = \sqrt{\Omega_1^2/4 + \delta\Omega^2}$  is called the Rabi frequency and in the resonant case is equal to  $\Omega_1/2$ . As one can see from Equation (1.17) under the microwave irradiation the state performs periodic oscillations. Figure 1.13(b) shows the measurement of Rabi oscillations in NV center, the counts are normalized to the bright state.

The experimental sequence is depicted in Figure 1.13(a). The resonant MW-pulse following initialization changes the electron spin state, which is read out during the next laser pulse. In the experiment we vary the duration of pulses. As follows from Equation (1.17) at  $\Omega_R\tau = \pi$  the full swap of the state occurs. It is the so-called  $\pi$ -pulse. In the same way one can introduce  $\pi$ -half pulse, which brings the NV center state into the transversal plane of the Bloch's sphere (Figure 1.12(c)).

#### 1.4.3. Quantum gates

The Bloch sphere provides an extremely useful geometrical representation of the state of a spin 1/2 system. We consider states  $m_s = 0$  and  $m_s = -1$  and any normalized superposition can be expressed as follows:

$$|\psi\rangle = \cos\frac{\theta}{2}|0\rangle + \sin\frac{\theta}{2}e^{i\phi}|-1\rangle. \quad (1.18)$$

The parameter  $\theta$  expresses the relative amplitude of the basis states, while  $\phi$  expresses their relative phase. In the Bloch sphere representation, the state

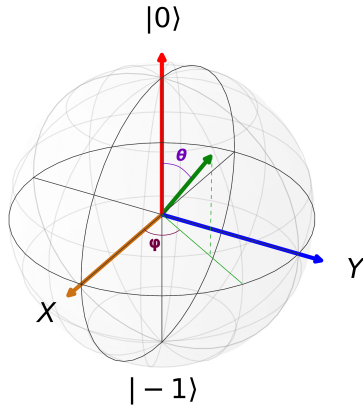


Figure 1.14: Bloch sphere representation of a two-level system.

$|\psi\rangle$  is depicted as a vector pointing from the origin to a point on the surface of the unit sphere (Figure 1.14). Considering any NV transition as a qubit, one can perform quantum logic gates [93]. It can be shown, that *irradiating the qubit with an ac-field with controlled amplitude and phase allows realizing arbitrary single qubit rotations.*

We want to generate the unitary operator that performs arbitrary rotation  $\hat{U} = \cos \theta \hat{\sigma}_x + \sin \theta \hat{\sigma}_y$ . The rotation operator about the axis  $\hat{n} = (\cos \theta, \sin \theta, 0)$  with rotation angle  $\alpha$  is:

$$e^{-i\alpha\hat{n}\cdot\hat{\sigma}} = \cos \alpha \hat{I} + i \sin \alpha (\cos \theta \hat{\sigma}_x + \sin \theta \hat{\sigma}_y). \quad (1.19)$$

Therefore we need a Hamiltonian which is proportional to  $\sim (\cos \theta \sigma_x + \sin \theta \sigma_y)$ . In the experiment we can control the phase of the driving field as well, so that  $H_1 = \gamma_e B_1 \sin(\omega t + \phi) \sigma_x$ . And by changing the relative phase of the pulses, one changes the rotation axis. For example, if we changed the phase of  $B_1$  in the previous section from  $\sin$  to  $\cos$ , in the final Hamiltonian  $\hat{S}_x$  operator would appear. So, the  $90^\circ$  phase shift changes the rotation axis from  $\hat{x}$  to  $\hat{y}$ . The  $\pi$ -pulse along X(Y) axis is called X(Y)-gate.

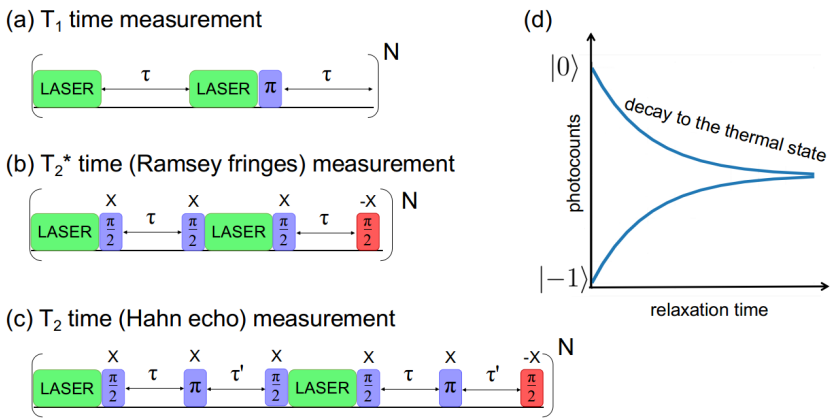


Figure 1.15.: Pulse sequences for  $T_1$  (a),  $T_2^*$  (b) and  $T_2$  (c) time measurements. The resulting signal is schematically depicted in (d).

#### 1.4.4. Relaxation times

Being located in diamond crystal lattice, the NV center is surrounded by various species like  $^{13}\text{C}$  nuclear spins, and other paramagnetic defects, which create fluctuating magnetic fields, the so-called spin noise. If the NV center is prepared in a certain state, the interaction with the environment induces spurious rotations of the state vector on the Bloch sphere, leading to its destruction. Depending on the initial spin state one can introduce longitudinal and transverse relaxation times. The spin relaxation times are a critical figure of merit for various emerging quantum-based applications based on sensing or quantum computation with NV centers.

The longitudinal (or spin-lattice) relaxation time  $T_1$  is the decay constant for the recovery of the  $z$  component of the spin towards its thermal equilibrium value due to interaction with lattice's phonons. In bulk diamond at room temperature, the main contribution to spin-lattice relaxation is a two-phonon Raman process [94]. As follows from ,  $T_1$  processes involve fluctuations at the  $|0\rangle \longleftrightarrow |-1\rangle$  transition frequency, corresponding to rotations about a control vector oriented in the transverse ( $xy$ -) plane of the Bloch sphere.

Therefore, for the shallow NV's the main source of resonant fluctuating magnetic fields can be electrons or ions on a diamond surface [95]. Obviously, different NV centers could have different rates of relaxation.  $T_1$  time depends on the magnetic field and temperature, the characteristic value for the room temperature is 1-10 ms. The pulse sequence for the measurement of longitudinal relaxation of NV center is presented in Figure 1.15(a). After the preparation, the state  $|0\rangle$  decays during the time  $\tau$ . With the subsequent laser pulse we read out the current state and initialize the center back to  $|0\rangle$  for the reference measurement. The  $\pi$ -pulse flips the center state to  $m_s = -1$ , which afterwards decays during the same time  $\tau$ . This procedure is repeated for the set of time intervals. If they are correctly chosen, in the measurement result one will see the decay of bright and dark states of the NV center (Figure 1.15(d)).

Transverse  $T_2$  relaxation time characterizes the decay of the state in the transversal plane of the Bloch sphere. Typically,  $T_2$  is limited by magnetic impurities in the local environment which serve as sources of decoherence (phase acquisition). The surrounding nuclear spins create a slowly-varying magnetic field, causing rotation in the transversal plane. However, it is possible to reduce the effect of the spin bath using dynamic- decoupling techniques (see next section). Because  $T_2$  process involves only the phases of other nuclear spins it is often called "spin-spin" relaxation. NV centers have the longest coherence times reported for any solid-state system at room temperature [96, 97]. The shallow NVs have shorter values than in the bulk diamond [97]. The measurement protocol is a Hahn-echo experiment (Figure 1.15(c)) [98]. The first  $\pi/2$  pulse brings the spin-vector into a transversal plane ( $|\psi\rangle = (|0\rangle + i|-1\rangle)/\sqrt{2}$ ), where it acquires a phase  $\phi$  after an evolution time  $\tau$  ( $|\psi\rangle = (|0\rangle + ie^{i\phi}|-1\rangle)/\sqrt{2}$ ). The  $\pi$  pulse reverts the total effect of fluctuating magnetic fields and this makes the sequence sensitive to AC magnetic fields ( $|\psi\rangle = (-ie^{i\phi}|0\rangle + i|-1\rangle)/\sqrt{2}$ ). After the next free-precession interval  $\tau'$  the state is  $|\psi\rangle = (-ie^{i\phi}|0\rangle + ie^{i\phi'}|-1\rangle)/\sqrt{2}$ . The final  $\pi/2$  or  $-\pi/2$  will project the state to the z-axis for the readout. -X pulse corresponds to  $3\pi/2(-\pi/2)$  phase shift of the MW field. If  $\tau = \tau'$  the measurement result will show the decay with characteristic time  $T_2$

(Figure 1.15(d)). In case of changing  $\tau'$  when keeping first free evolution time constant, one will see the revivals with the envelope corresponding to transverse relaxation time.

Along with  $T_2$  time, one defines the  $T_2^*$  as a pure dephasing time (in NMR it is called free induction decay). The measurement sequence is depicted in (Figure 1.15(b)). Such a measurement scheme is sensitive to DC magnetic fields. As well as  $T_2$ , it is strongly affected by the concentration of  $^{13}\text{C}$  [99]. Following the phenomenological Bloch equations [67] the longitudinal (or transverse) component of the spin magnetization recovers exponentially to an equilibrium magnitude with time constant  $T_1$  (or  $T_2$ ). When the relaxation is dominated by dipolar, quadrupolar or other interactions modulated by molecular motions, the single time constant  $T_1$  (or  $T_2$ ) can be obtained only for two-energy-level spin systems. In contrast, relaxation of spin systems with more than two energy levels can show non-exponential behaviour because of the cross-relaxation. As a result, the process can become bi-exponential [100] or multi-exponential, corresponding to the number of relaxation components. Therefore, the decay curves (Figure 1.15(d)) are usually fitted by stretched exponent,  $f(t) = \exp(-t/T_{1,2}^\beta)$  and  $\beta$  takes the values between 0 and 1. The transverse relaxation time  $T_2$  is related to  $T_1$  and  $T_2^*$  as follows:

$$\frac{1}{T_2} = \frac{1}{2T_1} + \frac{1}{T_2^*}. \quad (1.20)$$

#### 1.4.5. Dynamical decoupling noise spectroscopy

Decoupling means the use of some pulse sequence to average a dipolar coupling. This technique was invented in early 50s of the last century to prolong coherence  $T_2$  times of nuclear spin, and hence, decrease the linewidth of the NMR lines [101]. There are homonuclear and heteronuclear decoupling sequences. Apart from decoupling in NMR one uses also recoupling - the use of some pulse sequence to reintroduce an average dipolar coupling, to measure interatomic distances, for example. Dynamical decoupling (DD) sequences applied to NV center are heteronuclear, since they attenuate the

interactions with various nuclear spins, paramagnetic centers etc. Approximately 10 years ago it became clear, that the sensitivity of shallow NV centers is enough to detect the fluctuating nanoscale magnetic fields, created by the nanoscopic volume of nuclear spins on a diamond surface [102, 103]. The detection volume of single shallow NV is so small, that within it the statistical polarization dominates over the thermal [104]. The presence of the non-zero polarization, fluctuating around a certain value, generates the spin noise on the NV center site, which can be detected using dynamical decoupling. This way to get an NMR signal is called dynamical decoupling noise spectroscopy (DDNS).

Statistical polarization arises from incomplete cancellation of randomly oriented spins [104]. The instantaneous polarization, i.e., the difference  $\Delta N$  between spin-up and spin-down populations, can be either positive or negative and will fluctuate on a time scale that depends on the random flip rate of the spins (for example, due to spin-lattice relaxation). The statistical polarization can be calculated as [105]:

$$SP = \sqrt{\frac{I+1}{3I} \frac{1}{N}}. \quad (1.21)$$

The condition, at which the statistical polarization starts to dominate is given by the number of spins in the system, which is less than the critical number [105]:

$$N_{crit} = \frac{3}{I(I+1)} \left( \frac{k_B T}{\gamma B_0} \right)^2. \quad (1.22)$$

For the spin 1/2 at 300 K and 300 G it corresponds to volume  $\approx 80 \times 10^3 \mu\text{m}^3$ . As the nuclear spins surrounding the NV center precess around  $B_0$  with frequency  $\omega_L$ , their summed dipolar fields effectively create a random magnetic field  $B_{fluct}(t) = B_1(t)\cos(\omega_L t + \epsilon(t))$ , whose amplitude  $B_1(t)$  and phase  $\epsilon(t)$  slowly change with time [106]. Assuming the Gaussian distribution of the random phase [105, 107, 108, 109], the spin noise can be characterized by

two-point correlation function, which is given by  $S(t)$ :

$$S(t) = \langle B_{fluct}(\tau) B_{fluct}(t + \tau) \rangle = \frac{\langle B_{fluct}^2 \rangle}{2\pi} e^{-t/t_c} \cos \omega_L t, \quad (1.23)$$

where  $t_c$  is the correlation time of stochastic fluctuations.

For the equations written in this section the following definition of the fourier transform is used:

$$f(\omega) = \int_{-\infty}^{\infty} e^{i\omega t} f(t) dt, \quad (1.24)$$

$$f(t) = \frac{1}{2\pi} \int_{-\infty}^{\infty} e^{-i\omega t} f(\omega) dt. \quad (1.25)$$

The Fourier transform of the two-point correlation function is the spectral density of noise:

$$S(\omega) = \int_{-\infty}^{\infty} e^{i\omega t} S(t) dt = \langle B_{fluct}^2 \rangle \frac{\omega_c}{\omega_c^2 + (\omega_L - \omega)^2}. \quad (1.26)$$

This noise can be picked up by NV center using DD sequences [102, 109, 110, 111]. They represent a microwave pulse trains and vary in robustness to flip-angle and off-resonance errors [112, 113, 114, 115]. The simplest DD sequence is the Hahn-echo [116]. Among the most used DD protocols one can mention Carr-Purcell-Meiboom-Gill (CPMG) [101], XY4 [117], XY8, XY16, Knill dynamical decoupling (KDD) [108, 112], UDD [118] and continuous DD [119]. Some of them are depicted in [Figure 1.16](#).

To understand the total effect of DD sequence, one should analyse the total phase acquired by NV center. The phase, collected by NV center during the

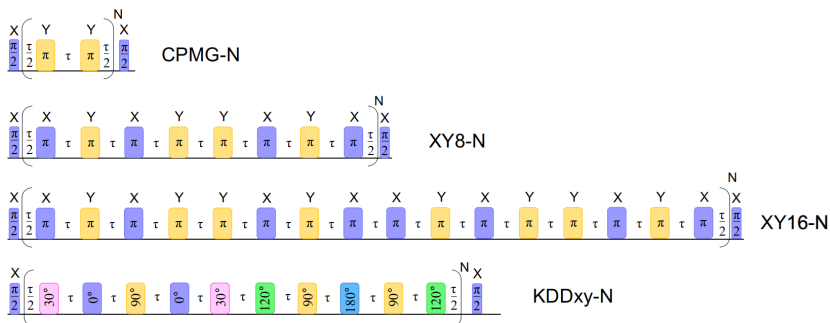


Figure 1.16.: Most commonly used pulse sequences for dynamical decoupling noise spectroscopy.

free evolution time  $t$  between two pulses is:

$$\delta\Phi(t) = \int_0^t \gamma_{NV} B_{fluct}(t) dt. \quad (1.27)$$

If the  $\pi$ -pulses are spaced such as they coincide with the nodes of the fluctuating field (Figure 1.17(a)), the maximal phase accumulates. The noise, which is not in the right phase, will be filtered out. The total phase  $\Delta\Phi$  acquired by NV center is:

$$\Delta\Phi = \int_0^T \gamma_{NV} B_{fluct}(t) f(t, t') dt. \quad (1.28)$$

$f(t, t')$  is the step function which characterizes the pulse sequence (Figure 1.17(b)). It switches between 1 and -1 at the times at which the  $\pi$ -pulses are applied. One can show that the function, describing the measured NV

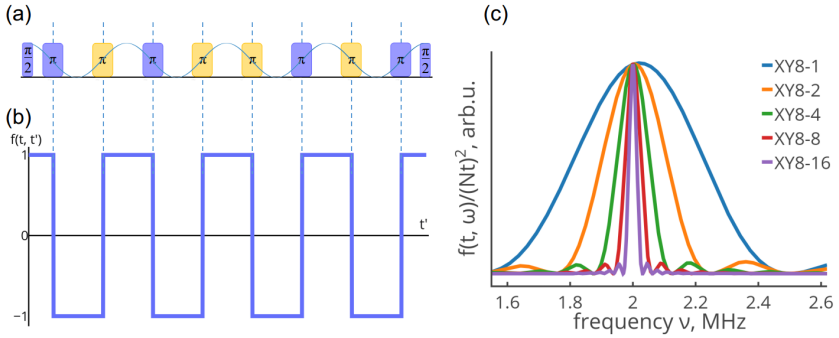


Figure 1.17.: (a) The nodes of the oscillating field coincide with the position of  $\pi$ -pulses of XY8-1 decoupling sequence; (b)  $f(t, t')$  for XY8-1; (c) normalized FFT of  $f(t, t')$ . At free evolution time  $t = 250$  ns the maximum of filter function is located at 2 MHz.

center state will be [108, 109, 120]:

$$W(t) = e^{-\frac{\Delta\phi^2}{2}} = e^{-\chi(t)}, \quad (1.29)$$

$$\chi(t) = \int_0^\infty S(\omega) |f(t, \omega)|^2 d\omega = 2 \int_0^\infty S(\omega) \frac{F(\omega t)}{\omega^2} d\omega. \quad (1.30)$$

$f(t, \omega)$  is the fourier transform of the  $f(t, t')$  (Figure 1.17(c)).  $F(\omega t)$  is the filter function, which encapsulates influence of the pulse sequence on decoherence.

The positions of resonances are given by:

$$t_k = \frac{(2k-1)\pi}{2\omega_L + A_\perp}. \quad (1.31)$$

The typical proton NMR signals ( $W(t)$ ) acquired with DDNS using XY8 sequence are shown in Figure 1.18. The amplitude of  $f(t, \omega)$  scales quadratically with the number of pulsed and free evolution time  $t$ . The linewidth of the filter function is proportional to  $1/Nt$ . The acquired peaks are the convolution of the filter function of the pulse sequence and the spin noise

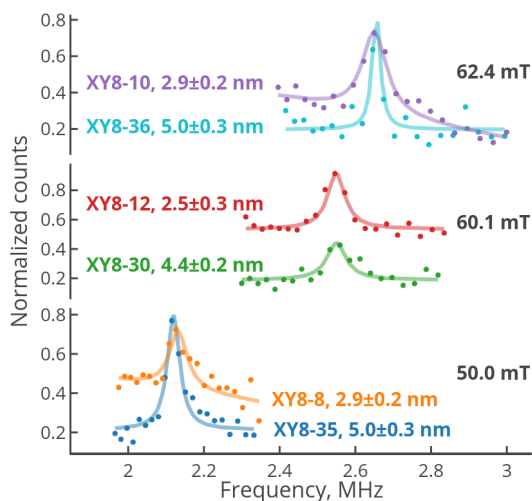


Figure 1.18.: NMR signals from protons in immersion oil acquired with XY8-N pulse sequence.

spectrum created by the spin bath. The linewidth of the noise spectrum is determined by the correlation time of the stochastic fluctuations of the detected AC magnetic field. It is constant for each individual NV center. On the other hand, the width of the filter function depends on the number of pulses, leading to the fact that the detected signal becomes sharper and narrower when increasing  $N$  when measuring the same NV center. Thus, the linewidth and amplitude are determined by these combined effects.

As a side effect, the DD sequences prolong the coherence times [96, 97, 118, 120, 121, 122].

It worth noting, that there are another approaches, which can be used to detect spin noise from statistically polarized spin bath [123].

The closer the spins are, the larger the magnetic field they generate. And at the same time, the smaller the gyromagnetic ratio is, the closer the spins should be. Therefore, the first experimental realization of DDNS was on  $^{13}\text{C}$  [124, 125, 126] (Figure 1.19). Within the next several years various external nuclear spins like  $^1\text{H}$  [23, 127, 128],  $^2\text{H}$  in single protein [129],

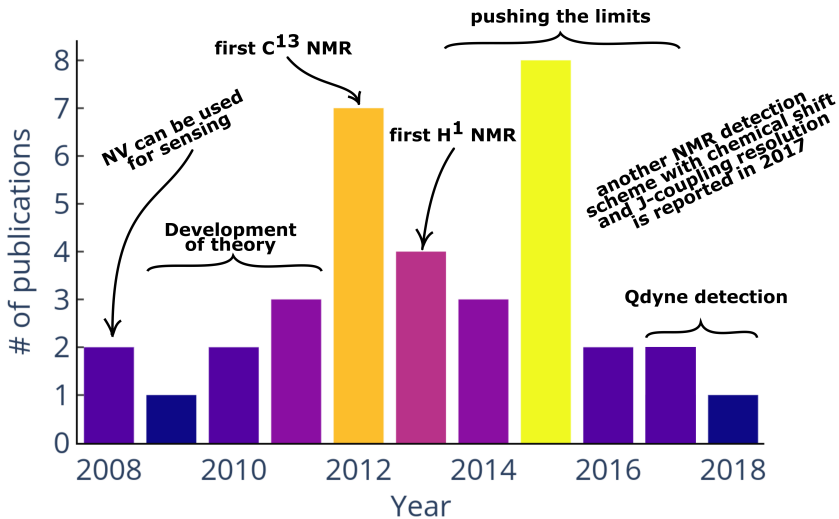


Figure 1.19.: The history of dynamical decoupling with NV centers.

$^{19}F$  and  $^{31}P$  [130],  $^{29}Si$  [131], spin labels in protein [132],  $^{10}B$  and  $^{11}B$  in hBN [133] have been detected. It was found that the pulse imperfections result in acquisition of spurious signals, coming from the harmonics of the filter function [134]. One can use DD sequences for Fourier spectroscopy experiments and detection of hyperfine coupling parameters [135]. And also, there are adaptations of DDNS for ensembles of NV centers [136, 137]. Despite the fact, that DDNS brings the science closer to the nano-NMR, this technique has a one very apparent disadvantage - in the described form it can not resolve the chemical shift. Although the resolution is lower than for standard NMR, there are ways to increase the sensitivity [138]. The most promising of them is via Qdyne detection scheme [139, 140]. However, the general trend is shifted now towards another sensing techniques [141].

#### 1.4.6. NV depth determination

It is always quite useful to know the depth of the NV centers. There are several methods to do that. One of them is to measure the reduction of

$T_1$  time caused by  $Gd^{3+}$  ions [142]. Another, but less precise, is based on simultaneously measured reflected light from the diamond surface and fluorescent light from the NV center and statistical evaluation of both signals [143]. The most precise value one can get analysing the signal acquired with DDNS [116, 127, 128, 144].

The root mean square (RMS) magnetic field, created by nuclear spin at the location of NV center, can, for the one hand, be calculated analytically, and for the other, extracted from the measurements.

The background subtracted noise spectrum is a simple Lorentzian function:

$$S(\nu) = \frac{a}{\pi} \frac{g}{(\nu - \nu_0)^2 + g^2}. \quad (1.32)$$

By optimizing the parameters  $[a, g, \nu_0]$  of  $S(\nu)$  to have the best fit of Equation (1.29) to experimental data, one can calculate  $B_{RMS}$  as:

$$B_{RMS} = \sqrt{2 \int_0^{\infty} S(\nu) d\nu}. \quad (1.33)$$

The factor 2 arises from changing the limits of integration from  $(-\infty, \infty)$  to  $(0, \infty)$ .

The experiments presented in this thesis were performed on [100] oriented diamonds. In this case the NV axis and the nuclear longitudinal axis are both tilted by  $54.7^\circ$  away from the surface normal. The analytical expression for the RMS magnetic field is [116]:

$$B_{RMS} = \frac{1}{8\sqrt{2\pi}} \mu_0 \mu_n \sqrt{\frac{\rho_n}{d^3}}, \quad (1.34)$$

where  $\mu_n$  is a nuclear magneton,  $\rho_n$  uniform nuclear density.  $d$  is the distance from NV to the edge of the proton-filled half space. Equating these two equations one can easily find NV depth  $d$ .

As a calibration sample one uses immersion oil (Fluka Analytical 10976) with  $\rho_{1H} = 5 \times 10^{28} m^{-3}$ .

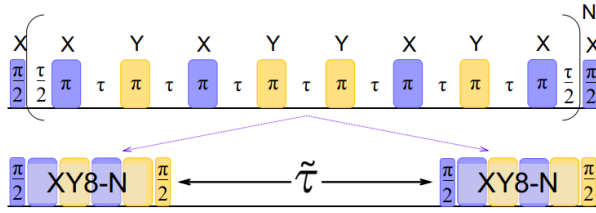


Figure 1.20.: Pulse sequence for the correlation spectroscopy. It consists of two dynamical decoupling blocks, separated by intersequence time  $\tilde{\tau}$ .

#### 1.4.7. Correlation protocol

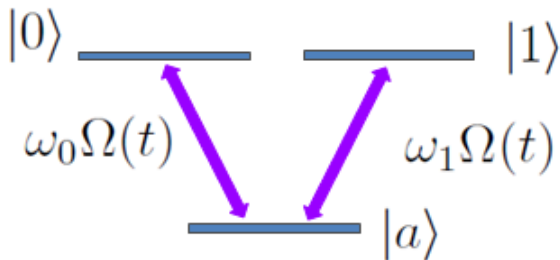
The correlation sequence consists of two dynamical decoupling blocks, separated by intersequence time  $\tilde{\tau}$  [106, 145, 146]. The result of the correlation sequence is the correlations between the phases acquired within the first and the second XY8-N pulse trains.

The detected signal is a sum of phase correlations from  $i$ -th spin in  $j$ -th molecule [106]:

$$\begin{aligned}
 S(\tau, \tilde{\tau}) &\propto \sum_{i,j} \langle \varphi_{i,j}(0), \varphi_{i,j}(\tilde{\tau}) \rangle \\
 &\propto \cos(2\pi\omega_L (2(N \times 8)\tau + \tilde{\tau})) e^{-\frac{2(N \times 8)\tau}{T_2^{NV}}} \sum_{i,j} p_{i,j}(\tilde{\tau}) \exp^{-\tilde{\tau}/T_2^{i,j}} \exp^{-\tilde{\tau}/T_1^{NV}} .
 \end{aligned}
 \tag{1.35}$$

The first multiplier corresponds to the oscillations with the Larmor frequency, the second is the amplitude factor and the expression under the sum sign describes the envelope of the signal.

HOLONOMIC NON-ADIABATIC  
QUANTUM GATES REALIZED  
OVER THE NV CENTER'S  
GROUND STATE



Holonomic quantum computation (HQC) is based on the gate operations, that require adiabatic geometric phase acquisition by quantum states. Due to their fast implementation, and robustness to various noise sources, they could be extremely favorable for quantum computing protocols. Over the last decade Holonomic gates have been experimentally demonstrated in various systems, e.g. molecular ensembles [147], superconducting qubit [148, 149], entangled photons [150] and NV centers in diamond [151, 152, 153, 154, 155]. They also find practical applications in building diamond gyroscopes based on NV center holonomy [21, 24].

This chapter presents a theoretical investigation of the applicability of holonomic non-adiabatic quantum gates (HQG) for quantum sensing based on NV centers in diamond. These gates are realized in the ground state spin manifold of the NV center. A short theoretical introduction is given in [Section 2.1](#). The model for the gate operations is described in [Section 2.2](#). We analyze the effect of various errors (such as pulse errors and non-zero detuning) on the fidelity of Holonomic gates ([Section 2.3](#)), and further study how these errors scale during a repeated application of the gates, as required in DD sequences ([Section 2.4](#)). The simulation results using HQGs are compared with the results obtained from standard gate operations. It is found, that for the case of single qubit HQG, errors are accumulated only on an ancillary level. The population leakage to the ancillary states due to errors results in the compression of the qubit Bloch sphere, and such errors cannot be corrected by unitary actions. Finally, the implementation of adapted NOVEL protocol in a three-level system ([Section 2.4.2](#)) for the nuclear spin polarization using HQG is demonstrated.

## 2.1. Theory

### 2.1.1. Holonomy

Holonomy is an effect that arises in differential geometry when geometrical data is parallel transported around a closed trajectory on a curved surface. A classical example is the parallel transport of a vector around a closed loop A-B-C-A on the surface of a sphere (Figure 2.1) [156]. When the vector returns to the starting point, it finds itself rotated relative to its initial direction, even though it never underwent any local rotation. The rotation is instead a consequence of the curved surface of the sphere. This inability to preserve the geometrical data is a measure for Holonomy. In this example it is the failure to preserve parallel transported geometrical data around a closed loop and is characterized by the rotation angle  $\varphi$  [157].

In quantum mechanics, geometric phase factors [158], both in scalar and matrix forms, are consequences of Holonomies and they reveal the non-trivial curvature of the state space. Holonomy corresponds to the difference between the initial and final quantum states under an adiabatic change of parameters along a closed path in the parameter manifold [159]. In the case of single-qubit Holonomies arise when quantum states evolve around a closed loop on the Bloch sphere.

A cyclic evolution of a non-degenerate quantum system is in general accom-

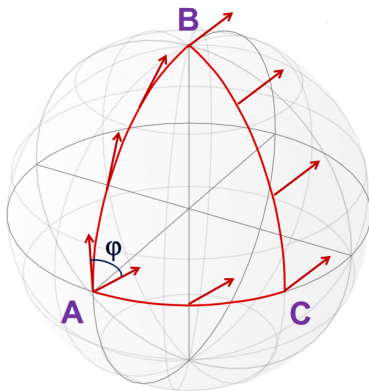


Figure 2.1: Parallel transport of a vector along a closed path on a sphere.

panied by a phase change of its state [148, 158]. The acquired Abelian phase can be divided into two parts: the dynamical phase, which is proportional to the evolution time and the energy of the system, and the geometric phase, which depends only on the path of the system in Hilbert space [158, 160]:

$$|\psi_n(t)\rangle = U(t)|\psi_n(0)\rangle = \exp^{i\beta(t)} \Gamma |\psi_n(0)\rangle. \quad (2.1)$$

Here

$$\exp^{i\beta(t)} = \exp^{-i \int_0^t E_n(t') dt'}, \quad (2.2)$$

$\beta(t)$  is the dynamical phase, where  $E_n(t)$  is the instantaneous eigenvalue of the corresponding eigenstates  $|n(t)\rangle$  of the Hamiltonian at time  $t$ , and

$$\Gamma = P \exp \int_C^i \mathcal{A}(R) dR = T \exp \int_C^f \mathcal{A}(t) dt, \quad (2.3)$$

is the non-abelian geometric phase factor [161], which is the holonomy operator associated with the anti-hermitian connection  $\mathcal{A}$ , in case of a degenerate eigenspace given by

$$\mathcal{A}_{ij}(t) = i \langle i(t) | \frac{d}{dt} | j(t) \rangle. \quad (2.4)$$

$P$  and  $T$  denote the path ordering and time ordering of the exponential around the loop  $C$  in the control manifold.

Here and further the system of units where  $\hbar = 1$  will be used.

### 2.1.2. Holonomic quantum gates (HQG) with NV centers

When no dynamical phase is acquired (or it is controllably removed) by the quantum state, the evolution becomes purely geometric, and allows a faster implementation of quantum gates, regardless of how the loop in parametric manifold is traversed. As the non-Abelian geometric phases are robust to magnetic field and path fluctuations [162], the realization of quantum gates

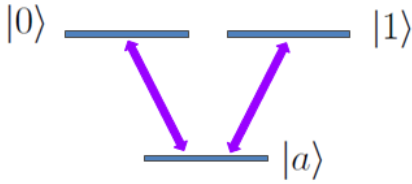


Figure 2.2: 3-level system with degenerate subspace.

using holonomy has apparent noise-resilient features [163] which makes their experimental realization extremely attractive.

Among the several ways used to nullify the dynamical phase in physical systems [164, 165], adiabatic evolution around a closed path is a well studied method. In this scheme, a qubit is realized in a set of degenerate eigenstates of a parameter-dependent Hamiltonian. These states are then adiabatically transported around a loop in the corresponding parametric space. Thus, holonomic quantum gates (HQG) are conventionally based on adiabatic evolution [166]. To perform the nonadiabatic geometric quantum computation one needs to find the path in state space along which the dynamical phase is zero. Particularly, to find a system with degenerate subspace [148].

Apart from quantum computing, quantum gates can also be used in sensing quantum protocols, where nuclear spin manipulations and the applied dynamical control can be illustrated as dynamical paths on the Bloch sphere of the sensor qubit (see Section 1.4.5). Therefore it would be interesting to know whether geometrical quantum gates can make a substantial difference to sensing protocols. Using NV centers in diamond one can combine the advantages of HQG and state dependent optical transitions for applications in sensing and gyroscopy. The three-level system of NV's ground-state triplet allows to generate a non-adiabatic and cyclic state evolution, that results in a purely geometric operation on the degenerate subspace spanned by the computational basis states,  $|0\rangle$  and  $|1\rangle$  (Figure 2.2). The third state,  $|a\rangle$ , acts as an auxiliary state and remains unpopulated after the gate operation [151].

## 2.2. The model of one-qubit gate

Under a permanent magnetic field, the energy levels of the ground state of NV center spin form a V-like configuration ([Figure 2.3\(a\)](#)). For convenience it is worth redefining the state  $|m_s\rangle = 0$  as  $|a\rangle$  and consider  $|m_s\rangle = \pm 1$  as a (qubit) computational basis states  $|0(1)\rangle$ . Another choice of ancillary state can be excited  $|A_2\rangle$  [[153](#), [154](#)]. Transitions  $|a\rangle \leftrightarrow |0(1)\rangle$  can be driven separately by two microwave sources with frequencies  $\nu_0 = D - g\mu_B B_z$  and  $\nu_1 = D + g\mu_B B_z$ . In the rotating frame, the Hamiltonian describing the system-microwave field interactions has the form [[167](#)]:

$$\hat{H}(t) = \Delta_0|0\rangle\langle 0| + \Delta_1|1\rangle\langle 1| + \Omega(t)(\omega_0|a\rangle\langle 0| + \omega_1|a\rangle\langle 1| + h.c.), \quad (2.5)$$

where the rapidly oscillating counter-rotating terms have been neglected (rotating wave approximation). Here  $\Delta_k = 2\pi\nu_k - (E_k - E_a)$  ( $k = 0, 1$ ) are detunings, that can be independently varied.  $\omega_0\Omega(t)$ ,  $\omega_1\Omega(t)$  are the Rabi-frequencies for  $|a\rangle \leftrightarrow |0(1)\rangle$  transitions, correspondingly. The Rabi-weights  $\omega_0$  and  $\omega_1$  should satisfy the condition  $|\omega_0|^2 + |\omega_1|^2 = 1$ . They describe the relative phase and strength of the corresponding transitions.  $\Omega(t)$  is the pulse envelope.

A universal holonomic one-qubit gate can be realized by choosing time independent  $\omega_0$  and  $\omega_1$  over the duration of the pulse pair by tuning the microwave frequencies so that the detunings  $\Delta_0$  and  $\Delta_1$  vanish. Under these conditions, the Hamiltonian reduces to ([Figure 2.3\(b\)](#)):

$$\hat{H}(t) = \Omega(t)(\omega_0|a\rangle\langle 0| + \omega_1|a\rangle\langle 1| + h.c.). \quad (2.6)$$

The system behaves as if it were composed of two degenerate states despite the Zeeman splitting. The dark state  $|d\rangle = -\omega_1|0\rangle + \omega_0|1\rangle$  is decoupled from the bright state  $|b\rangle = -\omega_0^*|0\rangle + \omega_1^*|1\rangle$  by choosing the time-independent  $\omega_0$  and  $\omega_1$  over the duration of the pulse pair. The evolution is reduced to a simple Rabi oscillations between the bright state  $|b\rangle$  and ancillary state  $|a\rangle$

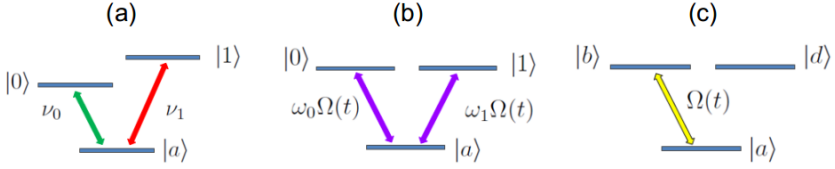


Figure 2.3.: The drawing of the three GS energy levels: (a) under the static magnetic field and (b) with zero detuning, when two MW tones are applied. (c) Rabi oscillations between the bright state  $|b\rangle$  and ancillary state  $|a\rangle$

with frequency  $\Omega(t)$  (Figure 2.3(c)):

$$\hat{H}(t) = \Omega(t)(|b\rangle\langle a| + |a\rangle\langle b|). \quad (2.7)$$

The resulting unitary quantum gate operation acting on the qubit is determined by the holonomy of the loop traced out by the subspace spanned by

$$|\psi_k(t)\rangle = \exp^{-i \int_0^t \hat{H}(t') dt'} |k\rangle = \hat{U}(t, 0)|k\rangle, \quad (2.8)$$

for  $k = 0, 1$  which undergoes cyclic evolution if the pulse pair satisfies the condition  $\int_0^t \Omega(t') dt' = \pi$ .

To be convinced of the holonomicity of  $|0\rangle \rightarrow |a\rangle \rightarrow |1\rangle$  gate see [Appendix A](#). By applying sequentially two  $\pi$  pulse pairs with variable amplitudes and phases, any desired holonomic one- and two-qubit gates can be realized [151, 153, 154, 155, 168].

### 2.3. Error scaling with holonomic gates

There are two qualitatively different sources of errors for holonomic gates. Few are caused by the interaction with the environment - dephasing in the  $[|0\rangle, |a\rangle]$  and  $[|1\rangle, |a\rangle]$  bases. The others originate from the imperfect control of the parameters of the Hamiltonian due to unavoidable instabilities of the

setup. These parameters are associated with the external driving fields used to control the system and are described as classical fields. The non-adiabatic gates can be made resilient to constant mean and relative detunings by employing pulses that are sufficiently short compared to the time scales of the detuning. If the idle time between preparation of the qubit and readout is negligible, the gate will also be resilient to dephasing in the limit of short pulses [163].

Below we have compared the robustness of single qubit holonomic gates over the standard gates in the presence of pulse errors and non-zero detuning for further investigation of the robustness of DD sequences [169].

### 2.3.1. The Pauli-X gate

For comparison let us consider the action of a repetitive  $\hat{X}$  gates. For the qubit evolving under the Hamiltonian  $\hat{H} = \Omega(t)\hat{X}$ , we immediately find the time evolution operator:

$$\hat{U} = e^{-i \int_0^t \hat{H}(t') dt'} = e^{-i \int_0^t \Omega(t') \hat{X} dt'} = e^{-i\theta \hat{X}} = \cos(\theta)\hat{I} - i \sin(\theta)\hat{X}, \quad (2.9)$$

where we denote

$$\int_0^t \Omega(t') dt' = \theta. \quad (2.10)$$

For  $\theta = \pi/2$ , an ideal X-gate is performed, and for the non-ideal case  $\theta = \pi/2 - \varepsilon$ , one can approximate the above mentioned evolution operator by:

$$\hat{U}_{err} = \hat{U}_{ideal} + \varepsilon \hat{I} + o(\varepsilon^2) = \varepsilon \hat{I} - i \hat{X} + o(\varepsilon^2) \quad (2.11)$$

and after  $n$ -iterations we have

$$\hat{U} \approx (-i\hat{X})^n + n\varepsilon(-i\hat{X})^{n-1} + o(\varepsilon^2). \quad (2.12)$$

It means that the error scales linearly with  $n$  and the fidelity of the ideal X-gate deteriorates with increasing  $n$ .

### 2.3.2. X-gate using holonomy

A universal holonomic two-level gate is realized in a three-level system where the qubit levels are coupled to an ancillary state  $|a\rangle$  with varying strengths. The Hamiltonian governing the dynamics is  $H = \Omega(t)(\omega_1|a\rangle\langle 1| + \omega_0|a\rangle\langle 0| + h.c.)$ .

To generate X-gate we set  $\omega_1 = \omega_0 = \frac{1}{\sqrt{2}}$ . The dark and bright states are therefore  $|d\rangle = \frac{1}{\sqrt{2}}(|0\rangle - |1\rangle)$  and  $|b\rangle = \frac{1}{\sqrt{2}}(|0\rangle + |1\rangle)$  correspondingly. For the time evolution operator we get:

$$\hat{U} = |d\rangle\langle d| + \cos(\theta)(|b\rangle\langle b| + |a\rangle\langle a|) + i \sin(\theta)(|a\rangle\langle b| + |b\rangle\langle a|). \quad (2.13)$$

For  $\theta = \pi$  an ideal X gate is performed on the qubit states  $[|0\rangle, |1\rangle]$ :

$$\hat{U} = |d\rangle\langle d| - (|b\rangle\langle b| + |a\rangle\langle a|) = -\hat{X} - |a\rangle\langle a|. \quad (2.14)$$

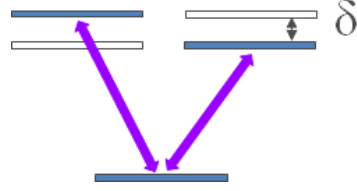
For non-ideal case  $\theta = \pi - \varepsilon$ , the time evolution operator takes the form:

$$\begin{aligned} \hat{U}_{err} &= |d\rangle\langle d| + \cos(\pi - \varepsilon)(|b\rangle\langle b| + |a\rangle\langle a|) + i \sin(\pi - \varepsilon)(|a\rangle\langle b| + |b\rangle\langle a|) \\ &= |d\rangle\langle d| - (|b\rangle\langle b| + |a\rangle\langle a|) + i\varepsilon(|a\rangle\langle b| + |b\rangle\langle a|) + o(\varepsilon^2) \\ &= \hat{U}_{ideal} + i\varepsilon(|a\rangle\langle b| + |b\rangle\langle a|) + o(\varepsilon^2). \end{aligned} \quad (2.15)$$

When it acts on the qubit, errors are accumulated only on ancillary level:

$$\hat{U}_{err}|0\rangle = |1\rangle + \frac{i\varepsilon}{\sqrt{2}}|a\rangle. \quad (2.16)$$

Figure 2.4: The non-zero detuning case



After  $n$  iterations, taking into account that  $\varepsilon \ll 1$ , we find:

$$\begin{aligned}
 [\hat{U}_{err}]^n &= |d\rangle\langle d| + \cos(n(\pi - \varepsilon))(|b\rangle\langle b| + |a\rangle\langle a|) \\
 &\quad + i \sin(n(\pi - \varepsilon))(|a\rangle\langle b| + |b\rangle\langle a|) \\
 &= |d\rangle\langle d| + (-1)^n(|b\rangle\langle b| + |a\rangle\langle a|) - i(-1)^n n\varepsilon(|a\rangle\langle b| + |b\rangle\langle a|).
 \end{aligned} \tag{2.17}$$

The last equation implies that the reduction in the fidelity of repeated operations is not due to the random Bloch vector rotations but due to the loss of purity. Due to this repopulation between the qubit space and the ancillary space, the length of the Bloch sphere reduces during the operation of the gate.

Addition of non-zero detuning leads to the lift of degeneracy (evolution is no more holonomic) and additional errors (Figure 2.4). The corresponding Hamiltonian takes the form:

$$\hat{H}(t) = \Omega(t)(\omega_1|e\rangle\langle 1| + \omega_0|e\rangle\langle 0| + h.c.) + \delta(|1\rangle\langle 1| - |0\rangle\langle 0|). \tag{2.18}$$

Using the first-order perturbation theory we evaluate the evolution operator, which takes the form (for the full derivation see Appendix B):

$$\begin{aligned}
 \hat{U}_{err} &= |d\rangle\langle d| - \gamma[|d\rangle\langle a| + |a\rangle\langle d|] + \gamma^2|a\rangle\langle a| \\
 &\quad - [|b\rangle\langle b| + |a\rangle\langle a| + \gamma(|b\rangle\langle d| + |d\rangle\langle a|)] \\
 &\quad - i\varepsilon[|b\rangle\langle a| + |a\rangle\langle b| + \gamma(|a\rangle\langle d| + |d\rangle\langle b|) + \gamma^2|d\rangle\langle d|].
 \end{aligned} \tag{2.19}$$

If there are no pulse errors:

$$\hat{U}_{err} = |d\rangle\langle d| - \gamma[|d\rangle\langle a| + |a\rangle\langle d|] + \gamma^2|a\rangle\langle a| - [|b\rangle\langle b| + |a\rangle\langle a| + \gamma(|b\rangle\langle d| + |d\rangle\langle a|)], \quad (2.20)$$

where  $\gamma = \delta/\Omega$ .

The next step is analysing the case of random pulse errors in both MW sources. They can be introduced via redefinition of bright and dark states:

$$|d\rangle = -\varepsilon_0\omega_1|0\rangle + \varepsilon_1\omega_0|1\rangle \quad |b\rangle = \varepsilon_0\omega_0^*|0\rangle + \varepsilon_1\omega_1^*|1\rangle \quad (2.21)$$

where  $\varepsilon_0, \varepsilon_1 = 1 \pm \varepsilon$ .

### 2.3.3. Simulations of gate operations

Thus, six cases of the gate operations have been simulated: standard X gate, HQG with pulse errors, HQG with non-zero detuning, HQG with pulse errors and non-zero detuning, HQG with random errors in both MW sources, HQG with non-zero detuning and random errors in two MW sources. The results are presented for the random pulse errors  $|\varepsilon| \leq 0.05\pi$  and/or non-zero detuning  $\gamma = 0.05$  after implementation of 10 X-pulses in [Table 2.1](#) and [Figure 2.5](#).

As one can see from the [Table 2.1](#), the "z" coordinate for standard X gate can strongly differ from the one for HQG. The repopulation between the ancillary level and the qubit space leads to the compression of the Bloch sphere during the HQG operation. Similar results have been obtained in [\[170\]](#).

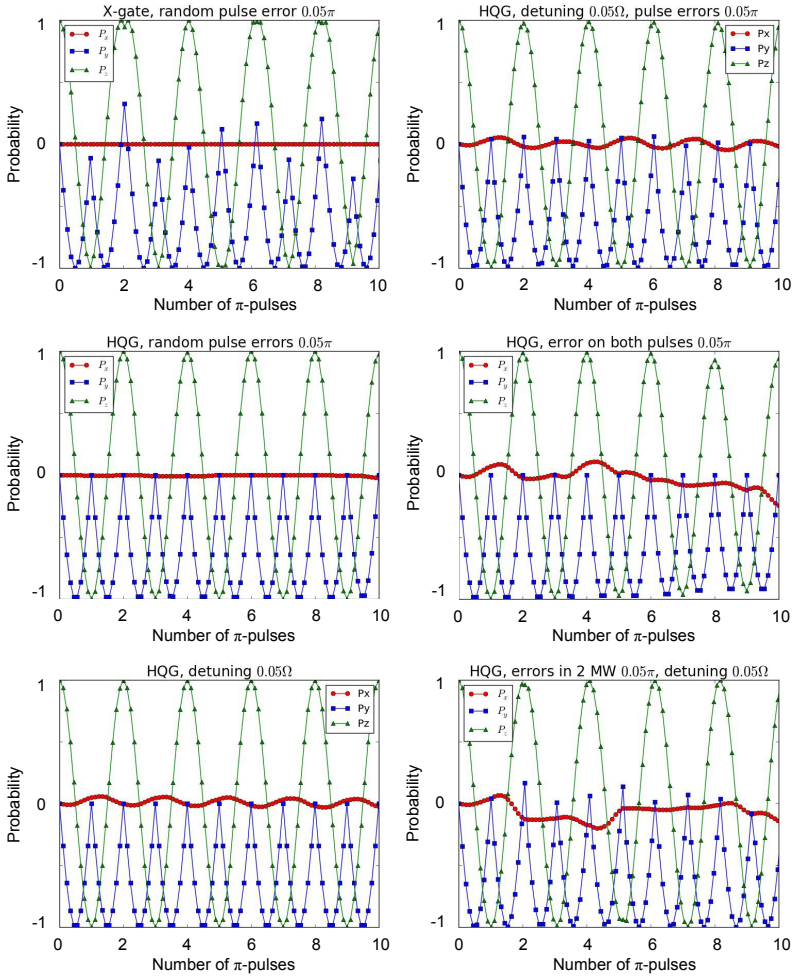


Figure 2.5.:  $\langle S_x \rangle$ ,  $\langle S_y \rangle$  and  $\langle S_z \rangle$  as a function of number of pulses

gate type	type of errors	$\psi_{final}$	$X_{final}$	$Y_{final}$	$Z_{final}$	final length of Bloch sphere
standard X	pulse err-s	0.96 -0.27i	0	0.52	0.85	1
HQXG	detuning	0.0004 -0.9999 0.0125	-0.025	0	0.9997	0.9999
HQXG	pulse err-s	-0.15i -0.99 0.01	-0.02	0	0.98	0.98
HQXG	pulse err-s + detuning	0.002 + 0.024i -0.9 + 0.005i 0.01 + 0.003i	-0.026	0.006	0.999	0.9994
HQXG	2 pulse err-s	0.24i -0.96 0.13	-0.025	0	0.91	0.94
HQXG	2pulse err-s + detuning	0.001 + 0.05i -0.995 + 0.005i 0.08 + 0.002i	-0.16	0.004	0.98	0.997

Table 2.1.: Parameters of the state after 10 X gates. Pulse errors  $|\varepsilon| \leq 0.05\pi$ , detuning  $\gamma = 0.05$ . In case of errors in both MW sources the total error during the gate operation is the same as for pulse error in standard X gate ( $\varepsilon_0, \varepsilon_1 = 1 \pm \varepsilon$ ).

## 2.4. Dynamical decoupling with HQGs

The sensing of nuclear spins with NV centers is usually realized via application of various decoupling sequences (see [Section 1.4.5](#)). We have simulated the well known DD schemes using HQGs and compared them with DD sequences realized through the standard gates. For this reason the interaction of the NV-spin with the single  $I_N = 1/2$  nuclear spin is introduced:

$$H = \Omega(t)(\omega_1|a\rangle\langle 1| + \omega_0|a\rangle\langle 0| + \text{herm.conj.}) \otimes I_2 + J(S_z \otimes I_z \cos(\theta) + S_x \otimes I_x \sin(\theta)) + \omega_L I_1 \otimes I_z. \quad (2.22)$$

Here  $I_2$  and  $I_1$  are unit matrices in 2- and 3-dimensional Hilbert spaces correspondingly,  $\theta$  is the angle between nuclear and NV's spin,  $J = \frac{\mu_0 \gamma_1 \gamma_2 \hbar}{4\pi |r^3|}$ . Evolution operator can be found as  $U = \sum_{k=0}^6 e^{-i\lambda_k(t)t} |\nu_k(t)\rangle\langle \nu_k(t)|$  where  $\lambda_k$  and  $\nu_k$  are instantaneous eigenvalues and eigenvectors of the Hamiltonian. The results of XY8 and CPMG operations were calculated using Python scripts. We evaluated the fidelity  $P = \text{Tr}(\rho_0 \rho(t))$ , where  $\rho_0 = \left[ \frac{|1\rangle+|0\rangle}{\sqrt{2}} \right] \left[ \frac{|1\rangle+|0\rangle}{\sqrt{2}} \right] \otimes I_x$  is the initial state and  $\rho(t)$  is the density matrix of our system after the free evolution for a time  $t$ .

The simulations of the different pulse errors are presented in [Figure 2.6](#). The curves are averaged over 200 runs of the pulse trains, since each time the error is random within the certain range. All sequences contain the same number of  $\pi$ -pulses. The errors in the HQG operation are the random pulse errors in both MW sources (denoted in % of  $\pi$ ).

Firstly, in case of ideal sequences without any errors ([Figure 2.6\(a-d\)](#), red curves) the choice of the gate operations is irrelevant.

In the absence of detuning [Figure 2.6\(a-d\)](#) sensing via HQGs is better: the noise ratio is lower and the peak's magnitude almost does not change when introducing higher errors in comparison to the (a, b). However, in presence of detuning ([Figure 2.6\(e, f\)](#)) detection via holonomic gates is clearly disadvantageous. The population leaks to the ancillary state and the population of the qubit space gradually decreases, which is especially pronounced for CPMG sequence.

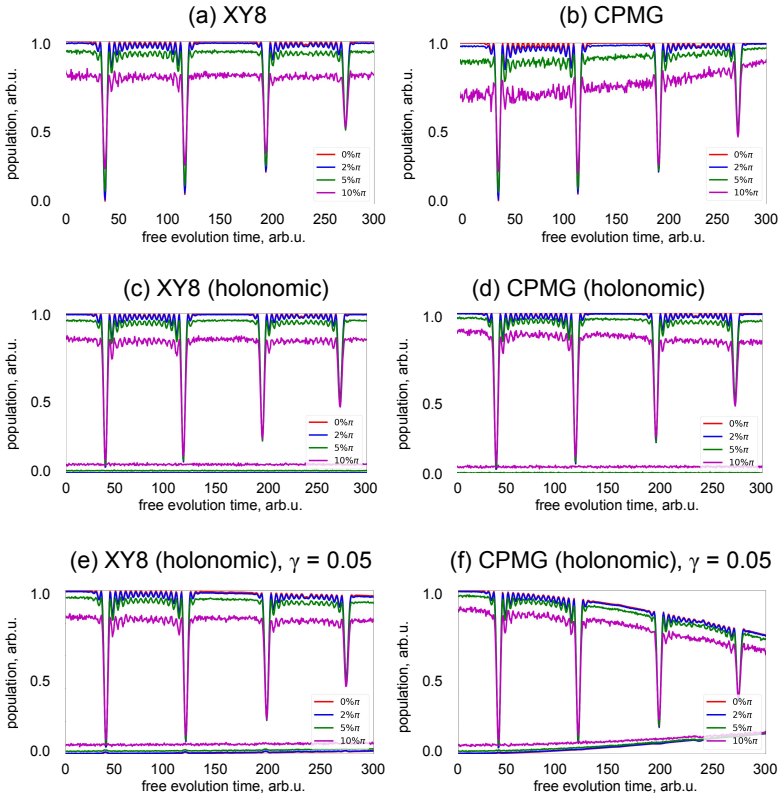


Figure 2.6.: Simulation of the DD sequences with the same number of pulses via standard (a, b) and holonomic (c-f) gate operations in the presence of pulse errors and non-zero detuning. Figures (c-f) show the population of the  $|b\rangle$  and  $|a\rangle$  (horizontal curves) states.

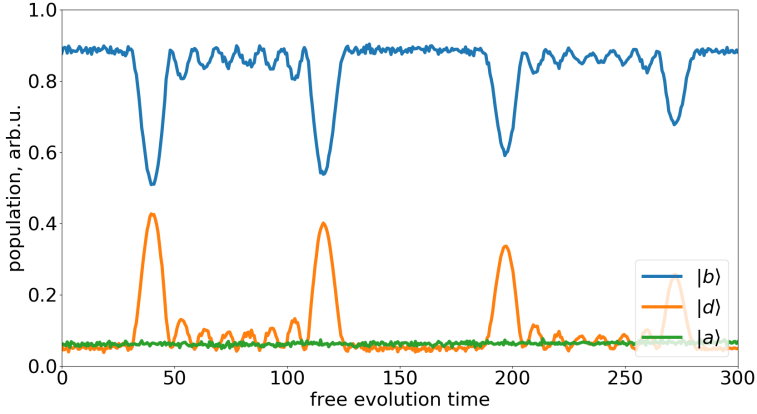


Figure 2.7.: Population of the  $|a\rangle$ ,  $\frac{|0\rangle+|1\rangle}{\sqrt{2}}$  ( $|b\rangle$ ) and  $\frac{|0\rangle-|1\rangle}{\sqrt{2}}$  ( $|d\rangle$ ) as a function of free evolution time for XY8 with HQGs. Pulse errors in both MW sources 10%,  $\gamma = 0.05$

#### 2.4.1. Error correction

The most important problem in the action of HQGs is the leakage of the qubit population to the ancillary state. One of the possible solutions is to transfer the population from the ancillary to the bright state after each DD sequence. It has been realized by the following procedure:

1. Take the partial trace by the nuclear spin subspace
$$\rho'(t) = \sum_{i=0,1} (I_1 \otimes \langle e_i |) \rho (I_1 \otimes |e_i\rangle)$$
2.  $\rho'(t)$  is rewritten in  $|a\rangle, |b\rangle, |d\rangle$  basis
3. Single out part of  $\rho'(t)$  which corresponds to  $|a\rangle$  and  $|b\rangle$
4. Find unitary operator which move all population to the bright state
5. Do inverse transformation to return into  $|a\rangle, |0\rangle, |1\rangle$  basis in 6x6 space

However, this method reduces the sensitivity of the DD sequence. It is clearly seen from the comparison [Figure 2.7](#) with [Figure 2.6\(e\)](#). The error correction did not reduce the population of the ancillary state, and hence decreased the sensitivity.

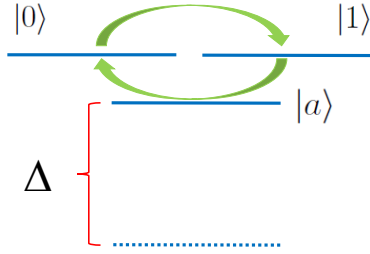


Figure 2.8: NOVEL using HQG

### 2.4.2. Nuclear spin polarization

The ability to actively control the nuclear spin state is essential for quantum computing. The electron spin of the NV center can be used as a source of polarization for surrounding nuclear spins. The polarization transfer can be realized via different mechanisms described in [Section 5.1](#). Among the methods available with the NV center, continuous dynamical decoupling at the Hartmann-Hahn double resonance [171] is the most efficient. The NV center electron spin is brought into the transversal plane and its state is locked and continuously driven along Y axis. The polarization exchange starts when the Rabi frequency of the dressed state of the electron spin becomes equal to the Larmor frequency of the target nuclear spins.

To realize NOVEL [172] in a V-system one needs to introduce sufficiently high detuning  $\Delta$  to the  $|a\rangle$  state ([Figure 2.8](#)) to produce continuous Rabi oscillations between  $|0\rangle$  and  $|1\rangle$ :

$$|0\rangle \rightarrow \alpha|0\rangle + \beta|1\rangle \rightarrow |1\rangle.$$

Recalling  $\omega_0 = \omega_1$  ([Section 2.3.2](#)) and defining  $\omega = \Omega(t)\omega_0 = \Omega(t)\omega_1$ , the Hamiltonian describing these oscillations should have following form:

$$\hat{\mathcal{H}} = \begin{pmatrix} \Delta & \omega & \omega \\ \omega & 0 & 0 \\ \omega & 0 & 0 \end{pmatrix} \otimes I_N, \quad (2.23)$$

where  $I_N$  is the identity matrix in nuclear spin subspace.

In this case the swap between nuclear and NV spin will be observed at

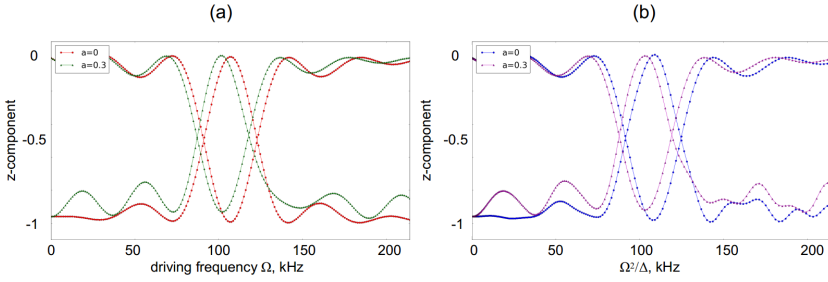


Figure 2.9.: NOVEL for standard (a) and holonomic gates (b). Here  $| - 1 \rangle$  and  $| 1 \rangle$  states of the NV's spin have been used for the swap.

condition  $\omega_L = \omega^2/\Delta$ .

Here we also can introduce fluctuations of detuning as diagonal elements of the Hamiltonian:

$$\mathcal{H}_{HQG} = \begin{pmatrix} \Delta & \omega & \omega \\ \omega & -a\frac{\omega^2}{\Delta} & 0 \\ \omega & 0 & a\frac{\omega^2}{\Delta} \end{pmatrix} \otimes I_N. \quad (2.24)$$

Hamiltonian in Equation (2.24) is equivalent to the following swap operator:

$$\hat{\mathcal{H}}_{standard} = \begin{pmatrix} 0 & 0 & 0 \\ 0 & -a & 1 \\ 0 & 1 & a \end{pmatrix} \otimes I_N. \quad (2.25)$$

The simulations of the swap operation are presented in Figure 2.9. It is worth noting, that for the same values of parameter  $a$  the curves look quite similar.

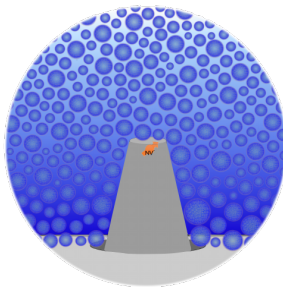
## 2.5. Conclusions

We simulated the performance of HQGs in the ground state spin manifold of the NV center's electron spin, in the presence of systematic errors arising from detuned microwave fields and microwave pulse errors.

Consecutive application of the HQGs leads to the loss of population to the non-computational (ancillary) subspace and effectively reduces the size of the Bloch sphere (in the computational subspace), thereby making it less useful for applications where a repeated application of the gate is required. Thus, despite the fact that absolute fidelity of non-Abelian non-adiabatic geometric operations is higher, the compression of the Bloch sphere during the DDNS with HQGs does not allow to fully benefit from the noise resilience of geometrical operations. However the quantum algorithms usually do not involve as much gate operations as is required for DDNS and therefore the use of HQGs in quantum computation is still valuable.



MEASUREMENT OF LATERAL  
DIFFUSION OF  
PHOSPHOLIPIDS IN THE  
ARTIFICIAL CELL MEMBRANE



The time evolution of proton spins in organic molecules located a few nanometres from the diamond surface could be observed using correlation spectroscopy method as shown in [146]. The sensitivity of such protocols to local spin-dynamics could make NV-microscopy a competitive technique over conventional NMR. This chapter is devoted to the extension of the achieved progress in this field: the measurements of the coefficient of translational diffusion of phospholipids in the artificial cell membranes.

The potential applications and perspectives of using NV centers in bio-sciences are given in [Section 3.1](#). [Section 3.2](#) introduces the types of motions in the phospholipid bilayer. The samples that have been used are presented in [Section 3.3](#). The simulations and experimental results are summarized in [Section 3.4](#).

### 3.1. Measuring Nanoscale Anisotropic Diffusion

Widely used techniques for studying microscopic biological objects have restricted operational conditions. This has narrowed down their potential applications in *in vivo* experiments. Conventional NMR (Nuclear Magnetic Resonance) and MRI (Magnetic Resonance Imaging) have limited resolution even at high magnetic fields ( $> 1$  T). LSM (Laser Scanning Microscopy) requires fluorescence labelling of species. Standard AFM (Atomic Force Microscopy) is not capable to differentiate multiple nuclear species due to a relatively slow scan time, making it sensitive to thermal drifts, while MRFM (Magnetic Resonance Force Microscopy) requires ultra-low temperatures and high vacuum. Hence, all the aforementioned issues highlight the need for a new generation sensing tool, that would provide non-invasive label-free high-resolution detection with nanoscale resolution at low magnetic fields even under ambient conditions.

During the last decade, NV centers in diamond have revolutionized nanoscale biosensing [7, 60, 66, 137, 173, 174]. Due to their high sensitivity, signals arising from multiple nuclear species confined within nanoscopic detection volume could be detected [23, 127, 128, 130, 131]. The detection is realized via DDNS (see Section 1.4.5). A sufficiently long spin life times ( $T_1$  and  $T_2$ ) of the sensor allow for longer pulse-control time required to gain sensitivity for single protein spectroscopy [132, 133]. In addition, the use of a quantum memory (intrinsic nitrogen nuclear spin or  $^{13}\text{C}$ ) at high magnetic fields allows one to achieve resolution to the level of a chemical shift (ppm) [141].

Owing to a vast scope of measurable quantities, the NV-based confocal microscopy has a potential to embody a universal toolbox for bio- and medical applications. Among the various benefits that NV based NMR could offer, one could mention, (i) no fluorescent labelling is needed, (ii) offers a non-invasive method to obtain chemical shift information, (iii) functional at low and high magnetic fields and (iv) operational over wide temperature range at low laser intensities. However, for sensing with DD rather high nuclear spin-density is required. The data acquisition time could be drastically reduced

by working at higher magnetic fields [82], and importantly the detected signal is generated only from nanoscopic sample volumes. Despite the fact that this feature would open the opportunity for the investigation of local nanoscopic processes, nanoscale NMR still needs to prove its unprecedented sensing capabilities.

Cell membranes are structure where compartmentalization into nanoscopic domains is believed to be vital for the functioning of cellular metabolism. The presence of lipid rafts, i.e. regions of the plasma membrane enriched with cholesterol and sphingolipids, results in a nanoscale heterogeneity of diffusion of phospholipids. Consequently diffusion cannot be investigated with standard NMR measurement techniques and FRAP (Fluorescence Recovery After Photobleaching). A recent approach based on the recording of temporal correlations among the interacting nuclear spins [146] allows to study the dynamics of the nuclear spin ensemble within the nanoscopic volume. This makes NV NMR an ideal tool to measure diffusion on nanometer length scales. In this chapter we exploit this method, the so-called correlation spectroscopy with single shallow NV centers, to study the diffusion of phospholipids in the artificial cell membranes which is the first step towards the investigation of non-uniformity of diffusion in spatially contiguous lipid clusters.

### 3.2. Dynamics of the lipid bilayer

Cell membranes are made of phospholipid bilayers with embedded proteins and carbohydrates [175]. It is a site of important biological processes. They control the movement of substances into and out of the cells, flow of chemical or electrical signals between the cells, and are involved in photosynthesis [176]. The lipid and protein molecules are held together mainly by non-covalent interactions. Sugars are attached by covalent bonds to some lipid and protein molecules.

The most common type of phospholipid consists of glycerol (propan-1,2,3-triol) linked to phosphate, choline (hydrophilic head) and two fatty acid

chains (hydrophobic tail). If submerged in water, these molecules will spontaneously associate to form bilayers, with their hydrophobic tails sandwiched between the hydrophobic heads. The characteristic size of such a bilayer is around 3-5nm [177, 178, 179], which lies within the sensitivity range of a single shallow NV center. Therefore, on the one hand, it is an appropriate system to study with NV center. On the other hand, the dynamics of a lipid bilayer is well investigated and it is interesting to probe the abilities and show the potential of the NV-spectroscopy on that.

The lipid bilayer can be regarded as a two-dimensional fluid and most of the lipids and protein molecules can move about in the plane of the membrane. There are many types of motion of phospholipids [180, 181] and they are usually analysed in terms of motional correlation times: characteristic time scales for reorientations. Only the lateral diffusion has a characteristic time which lies within the NV spin sensitivity i.e. is measurable by the correlation protocol.

Lateral diffusion is the Brownian motion of a phospholipid molecule across the membrane within one layer. Inside the cells, it is primarily driven by random nonthermal forces, induced by active proteins. There are a lot of mechanisms constraining lateral diffusion [182, 183]. Due to the numerous biological roles, which include cell signaling, cell adhesion, membrane transport and cell polarization, the rate of lateral diffusion of phospholipids is an object of close examinations. The standard measurement techniques involve NMR [184, 185, 186] and fluorescence [187, 188, 189, 190, 191] methods. Some approaches require fluorescence labelling or other markers.

NV centers allows one to perform the measurements in vivo, without labelling and do the imaging below Rayleigh limit. The high degree of signal localization accuracy allows to study the effect of each biomolecule individually.

In conventional NMR the diffusion coefficient can be extracted from the lineshape. The contribution from a spectral component at a frequency  $\omega$  has

a value of  $T_2$  given by [192]:

$$\frac{1}{T_2} = \frac{\omega^2 \tau_c}{5} + \Delta, \quad (3.1)$$

where  $\Delta$  represents contributions that are independent of vesicle reorientation.  $\tau_c$  is the correlation time of vesicle reorientation, and has two contributions [193, 194]:

$$\frac{1}{\tau_c} = \frac{1}{\tau_R} + \frac{1}{\tau_D} = \frac{3kT}{4\pi\eta r^3} + \frac{6D}{R^2}. \quad (3.2)$$

$1/\tau_R$  is associate with the rate of the vesicle tumbling, and  $1/\tau_D$  originate from the rate of lateral diffusion of the lipid molecules. Thus, the linewidth of the NMR signal is sensitive to the vesicle size: the larger vesicle would increase the linewidth and the smaller ones would decrease. Here some ambiguity may appear when substituting a proper  $r$  to extract  $D$ . In case of measurements with the NV center this does not happen, as we gather the information from the constraint volume and we are insensitive to the vesicle size.

### 3.3. Methods

#### 3.3.1. Samples modelling the cell membrane

For the experiments several model systems, that mimic cell membranes were chosen: micelles, giant unilamellaer vesicles (GUV) and a supported lipid bilayer (SLB). Since all of them were in the liquid phase, the heavy water  $D_2O$  were chosen as a solvent, to ensure that the detecting proton signal comes only from the phospholipids.

Micelles (Figure 3.1) are spherical nanoparticles with a characteristic size of 100-150 nm in diameter. The outer shell is formed by a monolayer of phospholipids and the inner volume is filled by perfluoro-crown-ether. Preparation of the perfluorocarbon (PFC) emulsion is explained in details, for example, here [195]. The nuclear spins providing the strongest NMR

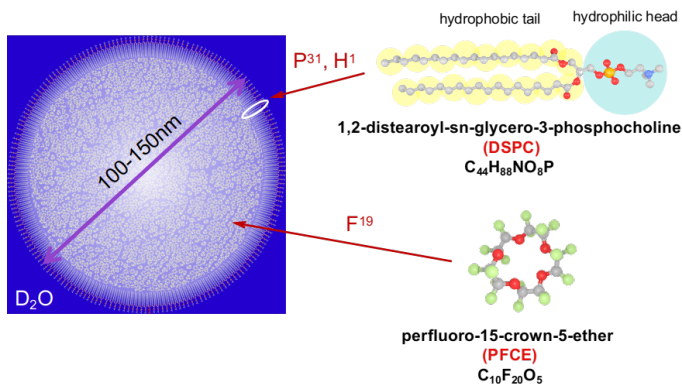


Figure 3.1.: Nanoparticle containing perfluorocarbons (PFC).

signal are  $^1H$ ,  $^{19}F$  and  $^{31}P$ . The  $^{13}C$  is usually not being detected because it is mixed up with the signal from intrinsic carbon in the diamond lattice. The correlation spectroscopy allows to extract the diffusion coefficients of individual nuclear spins. Therefore, it is a good system to compare the motion of different specimen.

GUVs were also candidates in this regard [196, 197, 198]. They are already formed by a bilayer and have a characteristic size from nanometers to tens of microns. However, fluorescent microscope images of labelled GUV showed that they do not sink down and there are a lot of free phospholipids floating around. For our purposes the shell of GUV must be inside the detection volume of at least several NV centers, i.e. they must be brought in a close contact (several nanometers) with the diamond surface. However, even filling them by salts did not result in their aggregation at the bottom, which impeded the experiments with them.

SLBs are popular models of cell membranes with potential biotechnological applications [199]. The creation of the SLB on the diamond surface by vesicle fusion is described in [200, 201, 202]. The general idea is that unilamellar liposomes upon adsorption undergo rupture and form a supported lipid bilayer (SLB) on  $SiO_2$ . It is a very convenient system, since the bilayer can

Figure 3.2: Bilayer boundary on the glass. The diamond membrane was lying approximately in the center of the glass slide. Image size  $80 \times 80 \mu\text{m}$

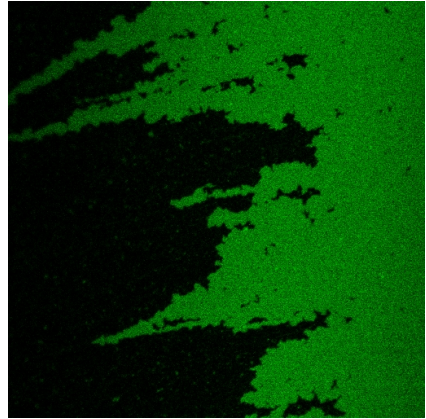
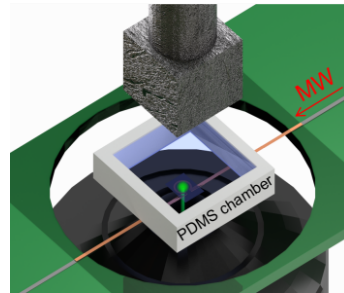


Figure 3.3: PDMS chamber for the experiments with liquid samples.



survive within several weeks and uniformly covers the diamond surface (Figure 3.2).

### 3.3.2. Setup and diamond sample

To perform the experiments we have used approximately  $30 \mu\text{m}$  thick diamond membranes, which were implanted with single shallow NV centers. One diamond sample was textured with nanopillars [79] to decrease the acquisition time of correlation measurements.

To prevent the liquid sample from drying out, PDMS-chambers were used (Figure 3.3).

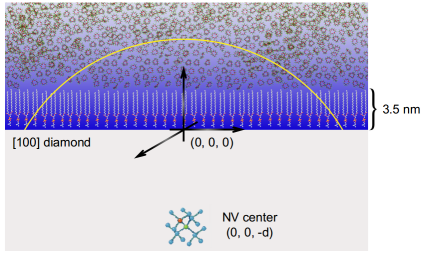


Figure 3.4: The model used for simulations.

## 3.4. Measurements of lateral diffusion

### 3.4.1. Simulation of NMR signal

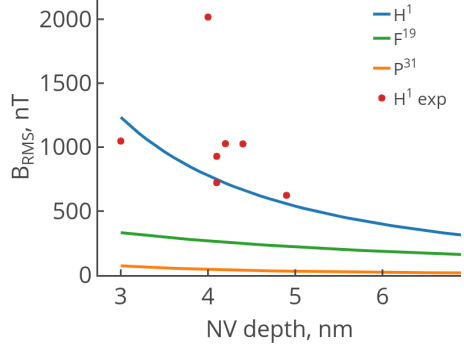
Diffusion can be measured only for those nuclear spins whose signal can be detected. For this reason, we performed numerical calculations of the RMS magnetic field created by nuclear spins at the NV center spin cite.

For the calculations we use the model depicted in [Figure 3.4](#). The NV center inside [100] oriented diamond is located  $d$  nanometers below the surface. Due to the fast isotope exchange reaction [[203](#), [204](#), [205](#)] between heavy water and the adsorbed water layer on the diamond interface, the proton signal can be considered to be originating only from the phospholipids (2 nm length of hydrocarbon chain and 1.5 nm length of hydrophilic part [[206](#)]). The  $^{31}\text{P}$  nuclear spins are situated in the center of the headgroup with the typical area of  $0.71 \text{ nm}^2$  [[207](#), [208](#), [209](#)] and 1.5 nm thickness. The fluorine atoms are located only inside the micelles in perfluoro-crown-ether. Knowing the number of atoms per unit volume, the following nuclear densities can be obtained:  $\rho_{1\text{H}} = 3.5 \times 10^{28} \text{ m}^{-3}$ ,  $\rho_{19\text{F}} = 2.7 \times 10^{28} \text{ m}^{-3}$ ,  $\rho_{31\text{P}} = 9.4 \times 10^{26} \text{ m}^{-3}$ . To calculate the  $B_{RMS}$  one can use the formula for the layer of nuclear spins on the surface of the diamond [[23](#)]:

$$B_{RMS}^2 = \frac{5\pi}{24} \left( \frac{\mu_0}{4\pi} \right)^2 \mu_n^2 \rho_N \left[ \frac{1}{d^3} - \frac{1}{(d+h)^3} \right], \quad (3.3)$$

where  $h$  is the film thickness and  $\rho_N$  is the nuclear density. The numerical simulations are depicted in [Figure 3.5](#) and are in accordance with the ex-

Figure 3.5: Numerical simulations of the  $B_{RMS}$  from nuclear spins in micelles. Red points show the experimental data.



perimental data (red circles). Only the proton signal is strong enough to be detected with shallow NV centers (measurements are  $T_2$  limited). Therefore correlation measurements were performed for  $^1H$ .

### 3.4.2. Extraction of the diffusion coefficient

The movement of phospholipids in the membranes can be considered as a diffusion of particles due to the Brownian motion [210]. Therefore, to measure the diffusion coefficient we can use the correlation protocol (see Section 1.4.7, [145]) and the procedure proposed here [146].

The envelope of the signal can be rewritten as:

$$\sum_j p_j(\tilde{\tau}) \exp^{-\tilde{\tau}/T_2^j} \exp^{-\tilde{\tau}/T_1^{NV}} \approx \exp^{-\tilde{\tau}/T_2} \exp^{-\tilde{\tau}/T_1^{NV}} \int_0^R p(\tilde{\tau}, d) dd. \quad (3.4)$$

It is correct in the framework of the following approximations:

- Molecules are static during XY8-N
- The envelope is constant over time
- The number of spins stays constant over time
- Relaxation rates of nuclear spins are identical

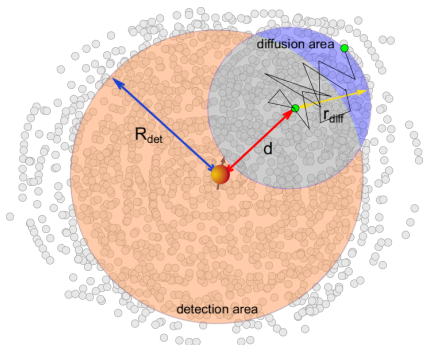


Figure 3.6: Schematic representation of molecular diffusion.  $d$  is the initial distance between the NV center (in the center of the orange circle) and a molecule.

$p(\tilde{\tau}, d)$  is the probability of the molecule (initially located at the distance  $d$  from the center of the detection area) to stay inside the detection volume after time  $\tilde{\tau}$ . The integral in Equation (3.4) represents the total effect from all the molecules. If we look at the slice of the top view of Figure 3.4, for each slice the detection area will be determined by certain radius  $R_{det}$  (Figure 3.6), since the detection volume represents a spherical cup. Therefore,  $p(\tilde{\tau}, d)$  is determined by the ratio between the area created by the overlapping of the detection area by diffusion area and the detection area:

$$p(\tilde{\tau}, d) = \frac{\text{intersection area}}{\text{diffusion area}}. \quad (3.5)$$

Rotational diffusion is several orders of magnitude slower than translational and can therefore be neglected. Therefore, the diffusion area is determined only by the 2D translational diffusion. In this case the diffusion radius over time  $t$  is determined as  $r_d = \sqrt{4D_T t}$ . Coefficient of translational diffusion is  $D_T = kT/6\pi a\eta$ , where  $k$  is the Boltzmann constant,  $T$  is the absolute temperature,  $a$  is the radius of the diffusing particle and  $\eta$  is the solvent viscosity.

The simulated probability of the molecule to stay inside the detection volume as a function of the distance from the center of the detection area and diffusion time is depicted in Figure 3.7(a). For calculations the detection radius was taken to be  $R_{det} = 5$  nm and the coefficient of translational

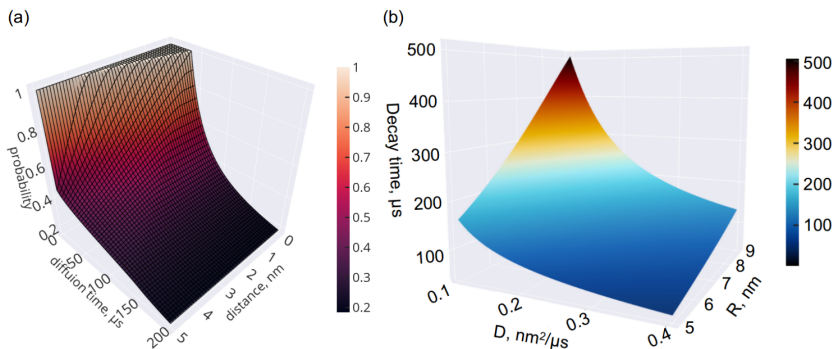


Figure 3.7.: Simulations of the system dynamics. a) Probability of the molecule to stay within the detection volume as a function of time and distance b) Correlation decay time in ns only due to the leaving the detection volume

diffusion was  $D = 0.17 \text{ nm}^2/\mu\text{s}$  (our experimental value).

As the nuclear  $T_2$  and  $T_1^{NV}$ , are much longer than the diffusion time, their effects are negligible over the time scales of interest. Taking into account the small thickness of the layer with respect to the detection volume and the cylindrical symmetry, we calculated the decay time of the correlation measurements for different diffusion coefficients and detection radii (which can be treated as NV depth) [Figure 3.7\(b\)](#). The simulated diffusion coefficient shows that the shallow NV centers are more preferable, as the decay rate of the correlation signal is dominated by the diffusion. So, the effect of molecular diffusion in the correlation signal should emerge at a timescale of few hundred  $\mu\text{s}$ .

### 3.4.3. Correlation measurements of micelles

Since the signal from other nuclear species is too weak to be detected with single shallow NV center, we focused on the proton correlation spectroscopy. Detection of proton signal via DDNS is followed by optimizing the number of repetitions until best contrast (dip) ([Figure 3.8\(a\)](#)) is obtained. It should be

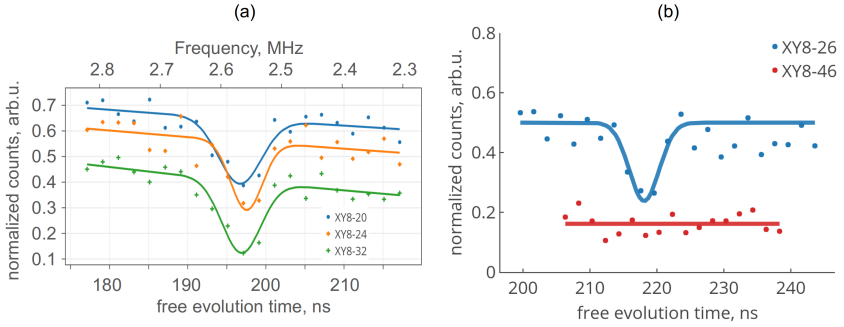


Figure 3.8.: (a) The proton signal detected with the same NV center, applying different number of repetitions of the XY8 dynamical decoupling sequence. (b) Degradation of the sample. No proton signal after 14 days.

noted that after a certain time the proton signal disappeared. In [Figure 3.8\(b\)](#) one can see the measurements which were done at 540G within 2 weeks. After 14 days the proton signal could not be detected any more even with higher order DD sequences.

Having the signal with optimized number of pulses  $N$  one can perform the correlation spectroscopy with  $N/2$  pulse numbers. Assuming that the average  $T_2^{NV}$  time for this sample is  $20.5 \pm 1.6 \mu\text{s}$ , the expected signal contrast is:

$$\exp^{-2(N \times 8)\tau/T_2^{NV}} \approx 0.4 - 4\%. \quad (3.6)$$

It is worth noting that a very small amount of NV centers reveal the correlation signal, i.e. it has a very small likelihood. In experiment the maximal contrast of the detected correlations was 3.9%. These measurements are presented in [Figure 3.9](#). On short 3 – 5  $\mu\text{s}$  timescales ([Figure 3.9\(a\)](#)) one can clearly see the oscillations with the proton Larmor frequency. However, to observe the decay of correlation signal, the intersequence time is increased until the decay of the oscillations could be observed ([Figure 3.9\(b\)](#)). To reduce the total measurement time we had to decrease the number of points, so that one could not see the fast oscillations any more. Therefore, to extract the

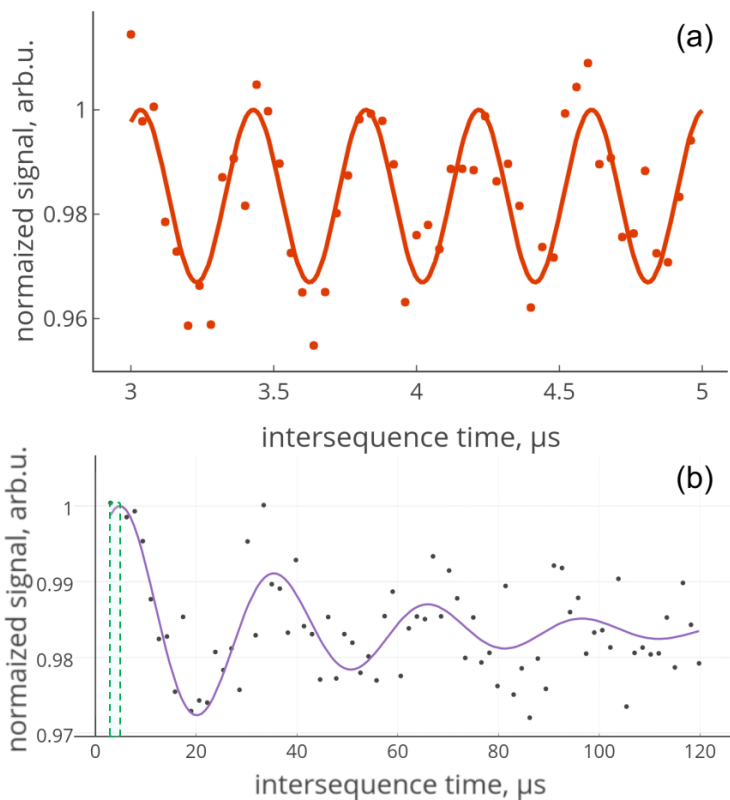


Figure 3.9.: Example of correlation measurements, obtained with XY8-20 at 595.7G applied to 4 nm deep NV center. (a) Oscillations with proton larmor frequency 2.536 MHz. (b) Correlation decay is fitted by decaying cosine with an alias frequency. The range of (a) corresponds to the shaded green rectangle

envelope, the sparse experimental data were fitted by the decaying cosine function oscillating at an alias frequency:

$$S(t) = S_0 \cos(\tilde{\omega}t + \varphi)e^{-\alpha t}. \quad (3.7)$$

The average value of the extracted coefficient of translational diffusion

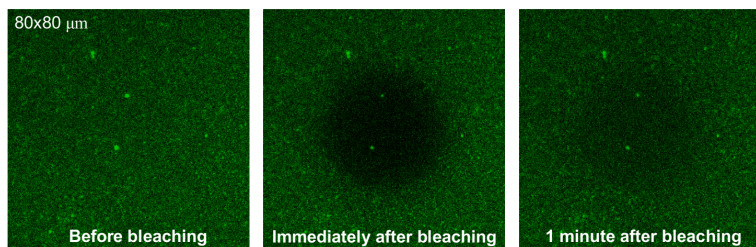


Figure 3.10.: Fluorescence recovery after photobleaching. Frame time 0.78s

is  $D = 0.17 \pm 0.04 \mu\text{m}^2/\text{s}$ . Upon comparison of this result with the literature values in phospholipid monolayers in a similar system ( $C_{40}H_{80}NO_8P$  (L- $\alpha$ -Dipalmitoylphosphatidylcholine), measured by FRAP [211] at room temperature and different surface pressures using surface force balance), suggests that our experimentally obtained  $D$  corresponds to a phase that is intermediate between solid and liquid phase state of the phospholipid monolayer. In our experiment all the measurements were performed under ambient conditions, i.e. the sample was not protected from drying out. We suppose that what may have actually measured the multilayer phospholipid material [206], and not the micelles filled with ether. The next step was to organize the experiment in such a way, that the bio-material would be in a liquid phase and protected from drying inside PDMS chamber.

#### 3.4.4. Correlation measurements of SLB

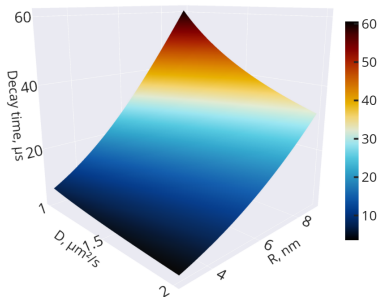
Further experiments were performed on the supported lipid bilayer in the heavy water environment (Figure 3.2). The optimal recipe for the creation of the bilayer by vesicle fusion was:

1. Preparation of the solution with the lipid concentration 0.1 mg/ml in  $H_2O + CaCl_2$
2. Incubation of the  $60\mu\text{l}$  droplet for 45 minutes

material	$D_T, \mu\text{m}^2/\text{s}$	Temperature, $^{\circ}\text{C}$
diamond	$2.022 \pm 0.009$	25
diamond	$1.15 \pm 0.23$	20
glass	$1.89 \pm 0.15$	25
glass	$2.73 \pm 0.42$	30

Table 3.1.: Coefficients of translational diffusion measured with FRAP.

Figure 3.11: Correlation decay time for the range of  $D_T$ , listed in Table 3.1



Basically, the method were taken from [202] and adjusted.

The diffusion coefficient of the bilayer was primarily measured via the fluorescence recovery after photobleaching (FRAP) [189, 190, 212, 213, 214, 215] using the fluorescence microscope (Figure 3.10). The results are summarized in the Table 3.1. The values are higher than for the micelles, as expected. Nevertheless, the calculated correlation decay time lies within the measurable range (Figure 3.11).

The proton NMR signal has been successfully detected. Despite the fact that the FRAP measurements suggest  $D_T$  that should be measurable with correlation spectroscopy, we were unable to observe a decay envelope that matches the measured coefficient of translational diffusion.

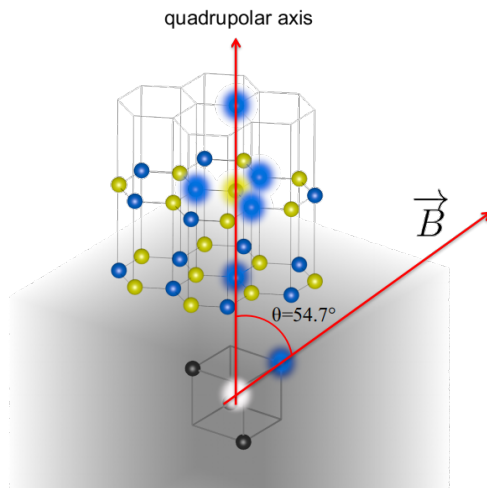
### 3.5. Conclusions

In this chapter we have shown that performing correlation spectroscopy with single shallow NV centers allows us to study the diffusion of phospholipids in an artificial cell membrane. The average value of the coefficient of translational diffusion was measured to be  $D = 0.17 \pm 0.04 \mu\text{m}^2/\text{s}$ . Thus, NV spectroscopy is one of the few methods which could reveal the diffusion heterogeneity on the nanoscale caused by the presence of lipid rafts in the cell membrane, for example.

This approach can provide new ways to investigate the molecular dynamics at nanoscale. The following limitations can be imposed on the processes to be studied. (i) Characteristic timescale of the process should lie within certain range, determined by the correlation decay time of the sensor (NV center). Partially this problem can be solved by using deeper NVs [141]. (ii) The sample must be either chemically attachable to the diamond surface or should at least be in a close contact (couple of nanometers away from the surface).



# NMR OF HEXAGONAL BORON NITRIDE



Two-dimensional (2D) materials open new perspectives for numerous applications in the area of catalysis, electronic, optoelectronic and spintronic devices such as sensors, high performance electrodes, nanocomposites, etc. They also have an enormous potential for electronic industry. Application of a single layer of a 2D material with a regular structure to the diamond implanted with single shallow NV centers can become a prototype of a quantum simulator (QS), since NV center allows detection and manipulation of nuclear spins. Such a realization has a lot of evident advantages like simplicity. This chapter presents the preliminary experiments on the realization of a room-temperature QS on diamond surface using hexagonal Boron Nitride (hBN). This is demonstrated by the detection of an NMR signal from multilayer hBN using DDNS.

The motivation is given in [Section 4.1](#). Main properties of hBN are described in [Section 4.2](#). To predict the location of the corresponding resonant frequencies, simulations of the position of energy levels were made ([Section 4.3](#)). The strongest signal was expected to originate from  $^{11}\text{B}$ . [Section 4.4](#) demonstrates the experimental results.

## 4.1. Room-temperature quantum simulator

Classical numerical simulations of quantum objects become intractable for as few as tens of particles because the tensor multiplication of spin operators leads to exponential scaling of the dimension of the density matrix. Fortunately, the evolution of a quantum object can be calculated even without a quantum computer. It is sufficient to have a controllable quantum system - a so called Quantum Simulator (QS) [216]. It is an ensemble of well-defined qubits that can be initialized, measured, and on which universal quantum gates can be performed. Thus, the simpler quantum device can mimic the evolution of the more complicated one, since they both evolve in accordance with the laws of quantum mechanics. The existing quantum simulators were implemented for solving such problems as Hubbard models [217], quantum phase transitions [218], spin models [219], to mention a few.

Traditionally, the experimental realization of a QS requires low temperature and/or ultra-high vacuum, which is technically complicated. In addition, a QS should be scalable and provide individual control and readout of qubits. Recently, the proposal of the quantum simulator on a diamond surface has been put forward [220]. The accurate fluorine termination of the diamond surface would form a quadratic lattice formed by  $^{19}\text{F}$  atoms. However, from the experimental point of view the even fluorination (C-F bonds only) is not so straightforward. Namely, the appearance of different bonds [47, 221] like triple F, double F, -OF etc.

This chapter presents the primary experiments on the realization of a room-temperature QS on the diamond surface using hexagonal Boron Nitride (hBN), which would have several remarkable benefits.

hBN is a transparent 2D material, which can be mechanically exfoliated onto the diamond surface. This allows the relatively easy creation of an ideal highly ordered pattern of nuclear spins, which is essential from computational reasons.

One of the main characteristics of the QS is the decoherence time, since the evolution should be performed before the state decays. The depolarization

time depends on the internuclear coupling strength:

$$g_{ij} = \frac{\hbar^2 \mu_0 \gamma_i \gamma_j}{4\pi r_{ij}^3}. \quad (4.1)$$

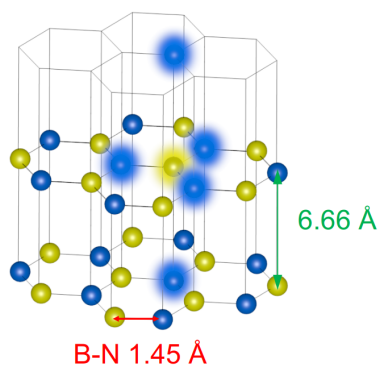
For the rectangular  $^{19}\text{F}$  spin lattice, the coupling strength is 6.8 kHz. When using hBN instead - the internuclear coupling is 9 times weaker ( $^{11}\text{B} - ^{11}\text{B}$  0.78 kHz). This would protect the simulation from decoherence and spin diffusion.

Moreover, the experiments would be carried out at room temperature. The scaling could be regulated by changing the NV depth. From this perspective, no individual control and readout could be achieved, but on the other hand the sensor is located directly next to the quantum system, which is quite reliable and convenient, taking into account that the optical readout of the NV center will not disturb the quantum state.

## 4.2. hBN on diamond surface

hBN has a regular layered hexagonal structure with alternating boron and nitrogen atoms (Figure 4.1). Within each layer, atoms are bound by strong covalent bonds, whereas the layers are held together by weak van der Waals

Figure 4.1: Crystal lattice of hBN. The distance between the nearest boron atoms in plane is 2.51 Å[222].



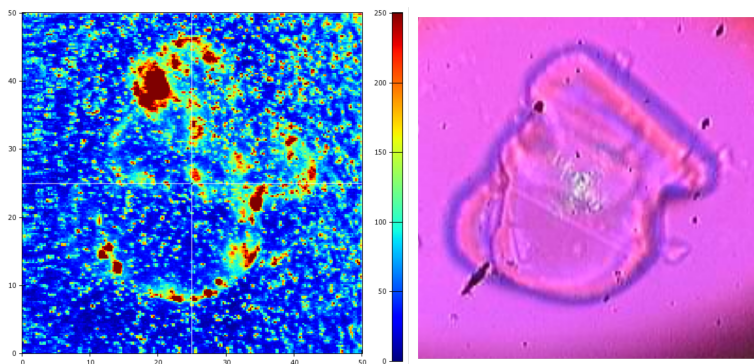


Figure 4.2.: Confocal (left) and web-camera (right) images of the hBN flake.

forces.

The nitrogen nuclear spins are not of much interest, since they are in-

	Nuclear spin, I	Quadrupole coupling constant $\chi$ , MHz	Gyromagnetic ratio $\gamma$ , MHz/T	Natural abundance, %
$^{11}\text{B}$	3/2	2.936	13.66	80.1
$^{10}\text{B}$	3	6.12	4.57	19.9
$^{14}\text{N}$	1	0.132	3.077	99.6
$^{15}\text{N}$	1/2	-	4.316	0.4
$^1\text{H}$	1/2	-	42.576	99.98

Table 4.1.: Isotopic content of hBN and nuclear spin properties [223, 224, 225].  $\gamma_{^1\text{H}}$  is placed into the table for the comparison.

distinguishable from the intrinsic atoms in the diamond lattice. Knowing the material density, distance between atoms and the natural abundance of the boron isotopes one can compute the following nuclear densities:  $\rho_{^{11}\text{B}} = 2.2 \times 10^{28} \text{m}^{-3}$ ,  $\rho_{^{10}\text{B}} = 0.55 \times 10^{28} \text{m}^{-3}$ . The values from Table 4.1 suggest that the NMR signals are expected to be very weak.

Owing to the wide bandgap 5.5 eV hBN is absolutely transparent and in the confocal microscope it could be found with use of the setup configuration when the field of view of the web camera coincides with the confocal image

(Figure 4.2, see also Section 1.3). hBN is applied to the surface by simple exfoliation with scotch tape, similar to graphene.

### 4.3. System Hamiltonian and simulations

Nitrogen is the intrinsic component of the NV center and  $^{10}\text{B}$  has too small gyromagnetic ratio and natural abundance, hence, further we will limit ourselves by considering only the NV- $^{11}\text{B}$  interactions. The Hamiltonian describing the system (Figure 4.3) has the following form (see Section 1.2.4):

$$\hat{\mathcal{H}} = \hat{\mathcal{H}}_{NV} + \hat{\mathcal{H}}_{hf} + \hat{\mathcal{H}}_{Zeeman} + \hat{\mathcal{H}}_Q. \quad (4.2)$$

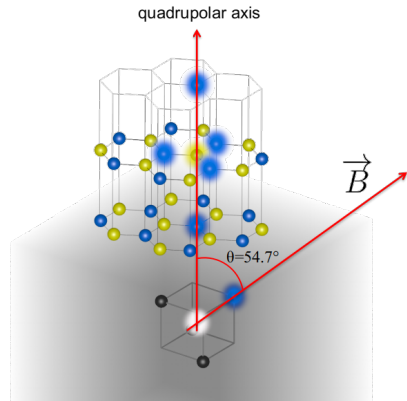
Here  $\hat{\mathcal{H}}_{NV}$  stands for the conventional NV Hamiltonian.  $\hat{\mathcal{H}}_{Zeeman}$  is the Zeeman splitting of the  $^{11}\text{B}$  levels:

$$\hat{\mathcal{H}}_{Zeeman} = \gamma_{^{11}\text{B}} B (I_z \cos \theta + I_x \sin \theta). \quad (4.3)$$

Since the nuclear spin is more than 1/2, the Hamiltonian contains the quadrupole coupling term  $\hat{\mathcal{H}}_Q$  [67, 73]:

$$\hat{\mathcal{H}}_Q = \frac{\chi}{4\hat{I}(2\hat{I}-1)} (3\hat{I}_z^2 - \hat{I}^2 + \eta(\hat{I}_{xx}^2 - \hat{I}_{yy}^2)), \quad (4.4)$$

Figure 4.3: Relative position of the NV axis and quadrupolar axis of the hBN exfoliated to the diamond surface. The angle between them is  $54.7^\circ$  which corresponds to the angle of inclination of NV axis from vertical.



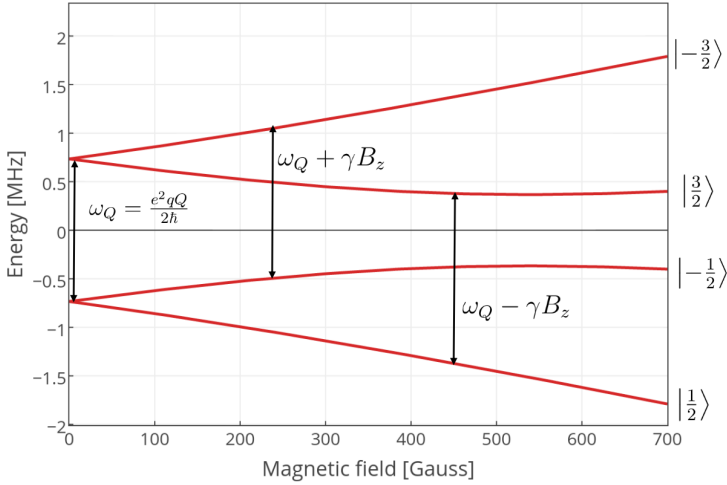


Figure 4.4.: Energy levels of  $^{11}\text{B}$  for  $\theta = 54.7^\circ$  at the magnetic fields, which will be used in the experiment. At this angle two satellite transitions are degenerate, leading to the double signal strength.

where  $\chi = \frac{e^2 q Q}{\hbar}$  is the quadrupole coupling constant (Table 4.1). hBN has an obvious axial symmetry, therefore, taking the symmetry axis to be the z axis (quadrupolar axis in Figure 4.3), the asymmetry parameter is zero,  $\eta = 0$ . In general we are interested in the frequencies of  $^{11}\text{B}$  nuclear spin transitions, which will be required for detection and manipulation. Solving the  $^{11}\text{B}$  part of the Hamiltonian for  $\theta = 54.7^\circ$ , one can find the eigenstates and calculate the transition frequencies at certain magnetic fields (Figure 4.4). Because of the quadrupole coupling there are zero field splitting  $\omega_Q$  and three allowed transitions. The  $| -1/2 \rangle \leftrightarrow | 1/2 \rangle$  transition is called central and  $| \pm 1/2 \rangle \leftrightarrow | \pm 3/2 \rangle$  are satellite transitions [226].

The exfoliation transfer of hBN to the diamond surface (Figure 4.5) can lead to the curving or bending of the hBN flakes. Magnetic field is always aligned along the axis of the NV center. Therefore, local bending of the hBN surface leads to the change of angle  $\theta$  in Equation (4.3) and alters the position of the

Figure 4.5: Local roughness of the surface can lead to the deviations of the angle from  $54.7^\circ$ .

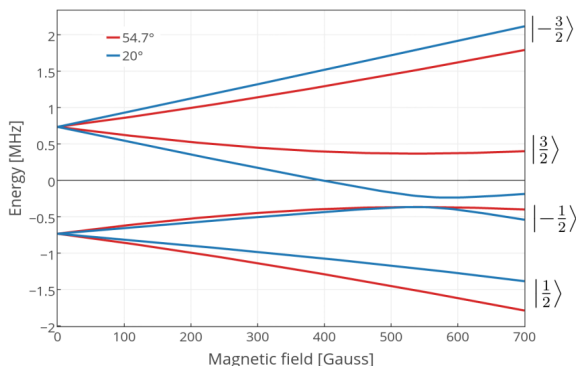
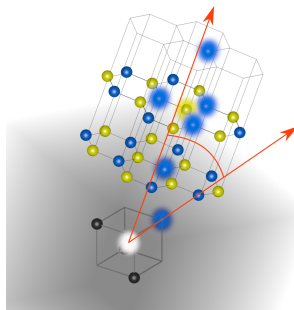


Figure 4.6.: Energy levels of the tilted hBN surface (blue line).

energy levels (Figure 4.6). It turns out that the NMR spectrum is extremely sensitive to local roughness (Figure 4.7). The tilt of the hBN with respect to the diamond surface of  $2^\circ$ , which is equivalent to the 0.35 nm ascent over 10 nm, leads to the splitting of the two (central and satellite) transition into four. Thus, the central transition ( $|1/2\rangle \leftrightarrow |-1/2\rangle$ ) shifts and the forbidden transition ( $|-3/2\rangle \leftrightarrow |3/2\rangle$ ) is driven. The degeneracy is being removed from the satellite transitions.

Such deviations from  $\theta = 54.7^\circ$  were indeed observed experimentally and the simulations (Figure 4.8) have a very good agreement with the data from [133]. It is worth noting that the signal was acquired from 30 nm (45 layers) thick hBN, which means that the signal was 25-55 times weaker than

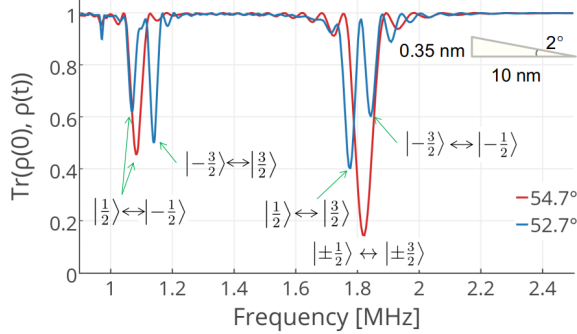


Figure 4.7.: Simulations of NMR signal for XY8-N dynamical decoupling sequence at 500 G when the surface is smooth (red curve) and when it is tilted to 2 degrees (blue curve).

proton signal from immersion oil. The observation of such a weak signal was possible owing to the extremely long coherence times, which provided an opportunity to implement high-repetition-number sequences and measure extremely weak signals.

The ultimate goal is indeed the handling of the single layer of hBN. But first we need to make sure that the NV center with the typical  $T_2$  times around tens of microseconds can sense the material above, i.e. detect an NMR signal with DDNS. For this reason we estimated the signal strength as a function of number of layers. The numerical simulations of the root-mean-square magnetic field as a function of number of layers are shown in [Figure 4.9](#). The saturation occurs at around 20 layers for 7 nm deep NV center. The signal from the monolayer is very weak, therefore in a first step the NMR signal was detected from the bulk material.

The following analytical formulas, describing the magnitude of root mean square magnetic field created by  $^{11}\text{B}$  nuclear spin a bulk material as a function

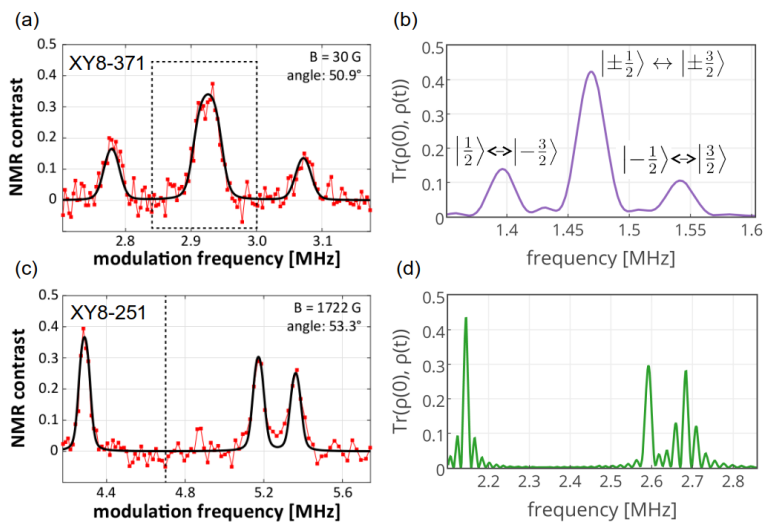
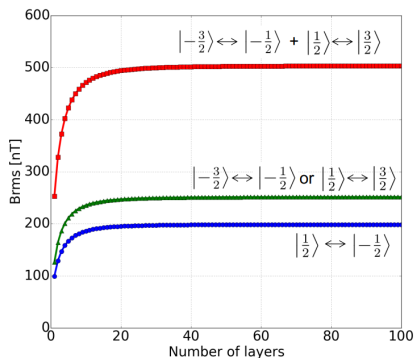


Figure 4.8.: Detection of  $^{11}\text{B}$  using XY8-N dynamical decoupling sequence. (a, c) Literature results from [133] and their simulations (b, d). (a, b)  $B = 30\text{ G}$ , angle  $50.9^\circ$ . (c, d)  $B = 1722\text{ G}$ , angle  $53.3^\circ$ .

Figure 4.9:  $B_{RMS}$  created by  $^{11}\text{B}$  for different numbers of hBN layers. Size of the hBN sheet is  $100 \times 100\text{ nm}$ , NV depth  $7\text{ nm}$ . 100 layers correspond to  $66.6\text{ nm}$  thickness.



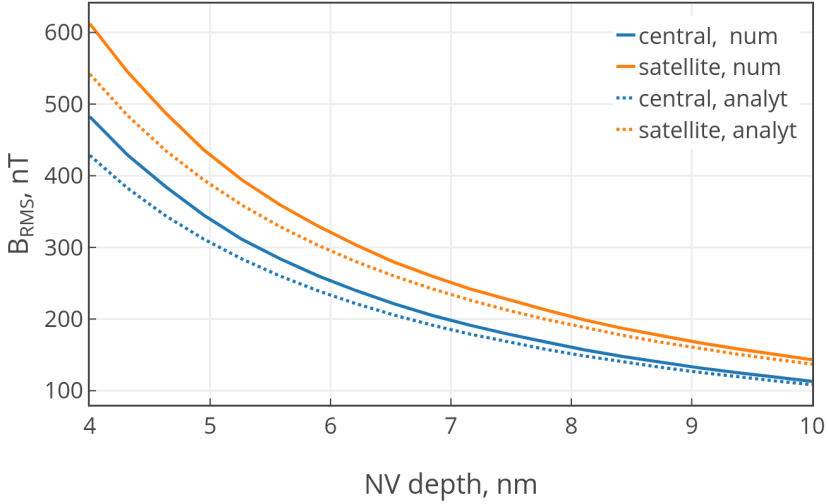


Figure 4.10.:  $B_{RMS}$  as a function of NV depth. Comparison between numerical and analytical simulations. Numerical: 50 layers (33.3 nm) of  $100 \times 100$  nm hBN sheets, analytical: integration over semispace.

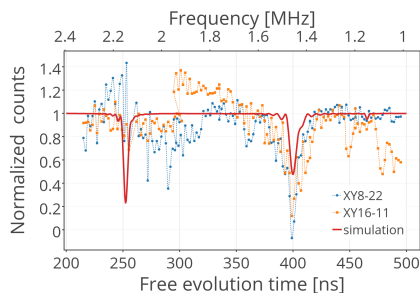
of the NV depth, can be derived:

$$B_{RMS} = \frac{\mu_0}{4\pi} 2\pi\gamma\hbar \sqrt{\frac{0.654\rho}{d^3}} \quad \text{for central transition,} \quad (4.5)$$

$$B_{RMS} = \frac{\mu_0}{4\pi} 2\pi\gamma\hbar \sqrt{\frac{1.048\rho}{d^3}} \quad \text{for satellite transition,} \quad (4.6)$$

where  $d$  is the NV depth,  $\rho$  - nuclear density and  $\gamma$  is the gyromagnetic ratio. In [Figure 4.10](#) the comparison between the numerical and analytical calculations is presented. Taking into account that the satellite transitions are degenerate, their signal strength is twice stronger (red curve [Figure 4.9](#)). The amplitude of the magnetic field is enough to be detected with the single shallow NV center with rather typical  $T_2$  time.

Figure 4.11: NMR signal from hBN at 595.6 G. Combination of six measurement ranges, corresponding to 20 ns free evolution time window. The data are fitted to angle 54.35°.



#### 4.4. Dynamical decoupling of hBN

As it was already mentioned, we began with the detection of  $^{11}\text{B}$  in bulk hBN.

In Figure 4.11 the result of DDNS combined of six measured ranges (each corresponds to 20 ns free evolution time window) is presented. The fitting of the observed dip results in 54.35° angle of inclination, although there is no dip in the second position. The other experimental results also reveal single dips (Figure 4.12). Eventually, no pattern clearly indicating  $^{11}\text{B}$  has been observed.

Figure 4.13 shows all detected NMR signals measured at different magnetic field and frequency ranges. Some frequencies correspond to  $^{13}\text{C}$  and its harmonics [134]. Apart from that, some spurious signals were filtered by XY16 sequence. The shaded regions show where the signals from hBN would have been observed for the range of the angles of inclinations from 49.7° to 59.7°. Despite some peaks were detected at the right positions, we did not succeed in detecting a pattern which would have lead to an unanimous determination of the BN orientation.

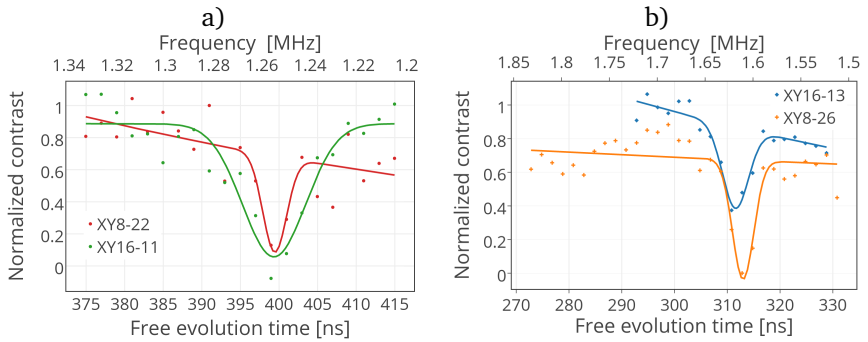


Figure 4.12.: NMR signal from hBN at a) 595.6G b) 700.3G. The dips persist during the measurements with XY8-N and XY16-N dynamical decoupling sequences. This proves that they originate from nuclear species.

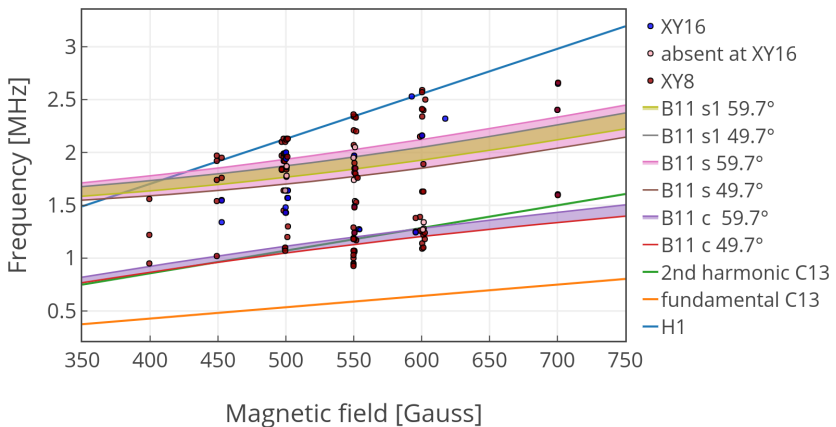


Figure 4.13.: All detected NMR signals. 17 NVs, 2 membrane samples. The letters c and s stand for central and satellite transitions, correspondingly.

## 4.5. Conclusions

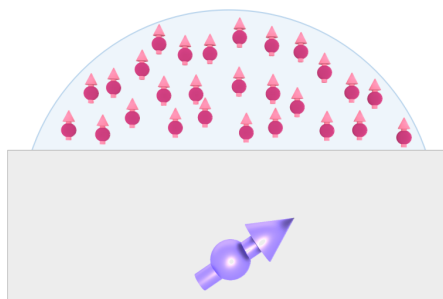
In this chapter experiments on the detection of  $^{11}\text{B}$  in hBN using DDNS with single shallow NV centers have been presented.

The numerical and analytical simulations suggested, that the  $B_{RMS}$  created from 20 layers of material is strong enough to be detected with shallow NV centers. However, the pattern created by several spin transitions corresponding to some tilt angle, which would clearly validate the presence of the sample in contact with the diamond, has not been observed.

CHAPTER

# 5

## HYPERPOLARIZATION OF $^1\text{H}$ IN SOLID AND LIQUID SAMPLES



Nuclear spin hyperpolarization, i.e., the creation of large, nonequilibrium population differences between nuclear spin states, allows one to significantly enhance the signal intensities in NMR experiments. This signal increase is crucial for NMR studies where sensitivity represents a limiting factor, such as the characterization of large (bio)molecular systems. The DNP methods in solids and solutions provide an innovative technological platform for overcoming significant bottlenecks in studying the structure and dynamics of molecular ensembles.

The ability to optically initialize the electronic spin of the NV center in diamond has long been considered a valuable resource to enhance the polarization of neighboring nuclei, but efficient polarization transfer to spin species outside the diamond crystal has proven challenging. In this chapter, the polarization transfer from NV center to external weakly coupled nuclear spins by recording its photoluminescence using NOVEL protocol is demonstrated.

[Section 5.1](#) shows the overview of conventional NMR and NV-based hyperpolarization methods.

[Section 5.2](#) introduces the experimental results of implementation of spin-locking pulse sequence to polarize protons in solid and liquid samples. The changes in  $T_{1\rho}$  time in case of on- and off-resonant locking pulses are shown in [Section 5.2.1](#). [Section 5.2.2](#) elucidates the effect of inhomogeneous couplings of the NV's response shape. The experimental study of the dynamics of the polarization transfer is presented in [Section 5.2.3](#). Slight changes in the cross-relaxation rate as a function of the wait time between successive repetitions of the transfer protocol suggest slower molecular dynamics near the diamond surface compared to that in bulk. This observation is consistent with present models of the microscopic structure of a fluid and can be exploited to estimate the diffusion coefficient near a solid-liquid interface, of importance in colloid science. [Section 5.2.4](#) is devoted to the modelling of observed signals. [Section 5.2.5](#) and [Section 5.2.6](#) presents the polarization of solid sample (PMMA) and water layer on a diamond surface. Experimental details are given in [Section 5.2.7](#).

The main part of this chapter was published in [227].

## 5.1. Hyperpolarization

### 5.1.1. Hyperpolarization

If a nucleus has a spin, it will have an associated magnetic moment:

$$\mu = g \frac{e}{2m_p} I = \gamma I. \quad (5.1)$$

The total magnetic moment of all spins in a substance  $M = \Sigma\mu_i$  is called macroscopic magnetization. When all the magnetic moments are randomly oriented, the macroscopic magnetization is zero (Figure 5.1). If they are preferentially aligned along one axis, the total magnetic moment is nonzero, i.e. there is a polarization excess, which can be detected.

At thermal equilibrium the population distribution over the energy levels obeys the Boltzmann's law (Figure 5.2). Such state is called thermal polarization. For the two-level system the degree of polarization  $p$  is proportional to the difference between the population of energy states  $p = (N_{upper} - N_{lower}) / (N_{upper} + N_{lower})$ . The calculation of the ratio between the numbers of spins at the higher and lower energy levels for 1 Tesla and

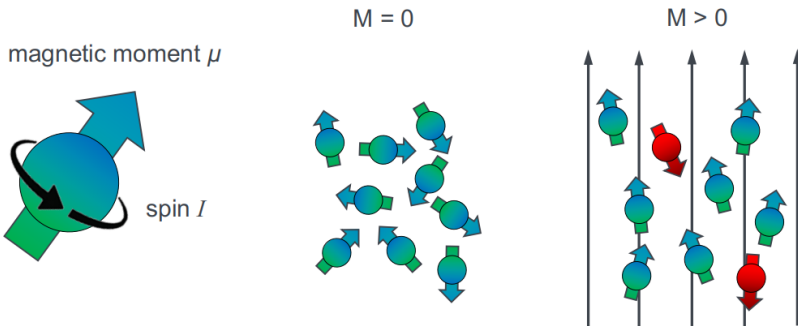


Figure 5.1.: Left. The spin and related magnetic moment. Center. Macroscopic magnetization is zero, since the magnetic moments are randomly oriented. Right. Under the external factors, such as an applied magnetic field, the macroscopic magnetization is nonzero.

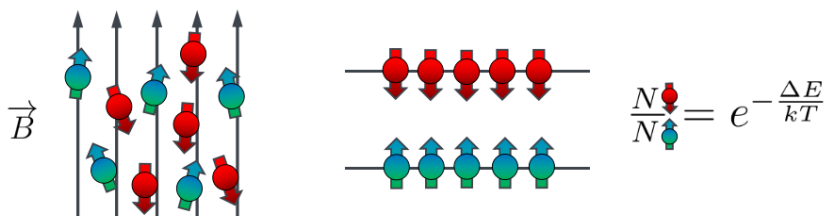


Figure 5.2.: Thermal polarization. At room temperature and in the absence of the magnetic field the energy levels are equally populated.

room temperature (300K) yields:

$$\frac{N_{upper}}{N_{lower}} = e^{-\frac{\Delta E}{kT}} = e^{-\frac{\gamma B}{kT}} = 1 - 6.8 \times 10^{-8}. \quad (5.2)$$

This ratio differs from one only in the eighth decimal place, i.e. the energy levels are equally populated and the macroscopic polarization is almost zero.

If the state, where all the nuclear spins are located in the lower (or upper) energy level (Figure 5.3), is prepared in any way, the substance will have significant magnetic moment. This is the so called hyperpolarized state. Thus, *hyperpolarization* is a process of the preparation of the nuclear spins in the material in a state, which is far beyond thermal equilibrium conditions. The recovery of the Boltzmann's distributions takes place within the  $T_1$  time of nuclear spins.

According to Equation (5.2) the polarization excess can be generated either simply by increasing magnetic field, what is the conventional NMR based on, or by lowering the temperature. To understand the low efficiency of this approaches one can calculate the thermal polarization of the ensemble consisting of 2 million nuclear spins (Figure 5.4). At the magnetic fields used in clinical NMR and higher the amount of spins, contributing to the detected signal, is much less than one percent. It is worth noting, that for this very reason in standard NMR experiments require quite large amount of substance is required. Increasing the sensitivity is one of the driving forces that shifts the NMR spectroscopy in direction of stronger and stronger

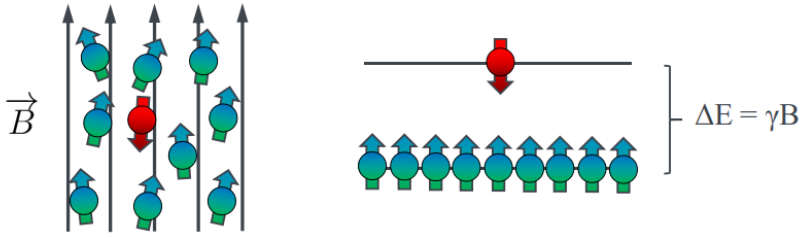


Figure 5.3.: Hyperpolarization. Most of the nuclear spins in a substance are prepared in one state (lower energy level in the picture). It is non-equilibrium state.

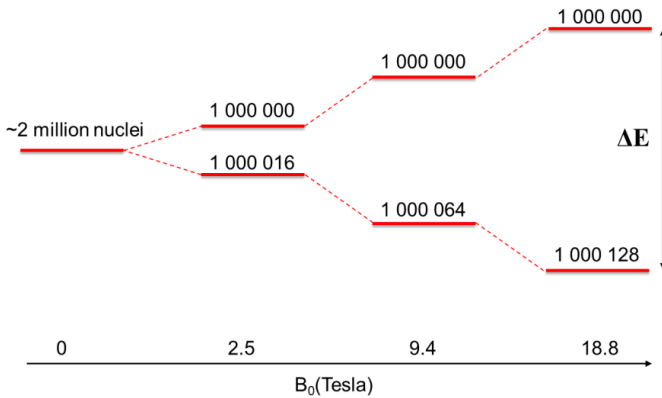


Figure 5.4.: Thermal polarization at high fields. At magnetic fields used for clinical MRI around 2.5 Tesla the signal is generated only from 16 nuclear spins out of 2 millions.

magnetic fields.

Another way to gain the sensitivity is to use hyperpolarization methods. The hyperpolarization of the sample significantly increases the amount of spins, contributing to the detected signal and hence improves the signal-to-noise ratio. The first idea of accumulation of population in one energy level to amplify an NMR signal belongs to Albert Overhauser, who in 1953 suggested transferring the huge polarization of free electrons to the NMR

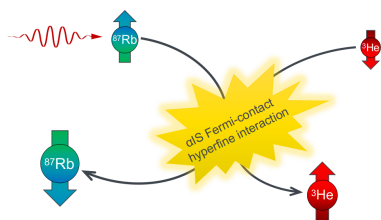


Figure 5.5: Spin exchange optical pumping

active nuclear spins [228]. This hyperpolarization method is called dynamic nuclear polarization (DNP, see the next section) and remains one of the most efficient hyperpolarization techniques available today.

### 5.1.2. Conventional hyperpolarization methods

Depending on the aggregate state of the substance, different approaches to prepare the hyperpolarized state can be implemented.

**Brute-force polarization** is one of the most commonly used signal enhancement methods. In this case the sample is prepolarized at high magnetic field and/or at low temperature and then the detection is carried out at low field ( $< 40$  mT) [229].

**Spin-exchange optical pumping (SEOP)** is a way to create optically induced polarization of noble gases [230]. It works best for inert gases with spin  $1/2$  ( $^3\text{He}$  and  $^{129}\text{Xe}$ ). At first the optical pumping of an alkali metal vapor (e.g. Rb) is performed to generate electron hyperpolarization. Then, the created high electron polarization is transferred to the nuclei of a noble gas through the spin exchange collisions (Figure 5.5). The spin exchange is mediated by Fermi contact hyperfine interactions between the alkali electrons and the spins of the noble gas nuclei. It takes hours to polarize  $^3\text{He}$ , minutes for  $^{129}\text{Xe}$ . The required cell pressures are up to  $\sim 10$  atm.

**Chemically induced polarization** relates to the procedure when the substance is polarized during the mixing with polarizing agent and the subsequent spin-transfer reaction. Parahydrogen or free radicals are usually used as a source of polarization [231, 232]. During the parahydrogen induced polarization (PHIP), the substance is polarized as a result of the isotope

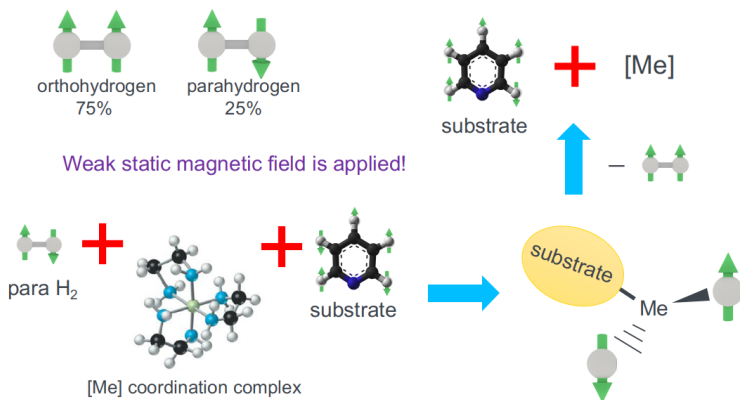


Figure 5.6.: One of the possibilities to create parahydrogen induced polarization in the presence of weak magnetic field.

exchange reaction. One of the possible scenarios is depicted in [Figure 5.6](#) [233]. The temporary association of a substrate and para- $H_2$  via a transition metal center in low magnetic field results in NMR signal amplification without any chemical modification of the hyperpolarized material.

**Dynamic nuclear polarization (DNP)** is based on the polarization transfer from the electron spin bath to adjacent nuclear spins. At the same temperature and magnetic field the polarization of the electron spin reservoir is much higher just due to the larger electron gyromagnetic ratio  $\gamma_e/\gamma_H \approx 660$  ([Equation \(5.2\)](#)). The mechanism that drives the polarization transfer significantly depends on the experimental conditions, such as whether it is done in a solid or liquid state and the source of the unpaired electrons. There are three main experimental approaches: magic-angle spinning (MAS) DNP, Overhauser DNP and dissolution DNP. For MAS DNP and dDNP low temperatures and/or rather moderate field strength ( $\sim 3.4$  T) are required. Recently, the signal from dynamically hyperpolarized protons in water was detected with an ensemble of NV centers in the diamond [234]. TEMPOL radicals were used as a source of unpaired electrons to perform an Overhauser DNP. It worth noting, that one does not have to polarize the sample

using the NV center if the hyperpolarization can be more easily created by other methods.

### 5.1.3. Hyperpolarization methods with NV's

Most of the hyperpolarization techniques are incompatible with *in vivo* NMR experiments. Considering an NV center as an electron spin system, one can perform DNP at room temperature and low magnetic fields. The ability to quickly prepare the NV center in the  $m_s = 0$  using the green laser illumination allows to polarize large amount of nuclear spins over the time range shorter than nuclear  $T_1$  time. Thus, even the smallest lattice imperfection can change the course of the future. One can think about the polarization of the nuclear spins with the NV center and the subsequent detection either with the standard NMR machine [235] or with the same NV center. Being interested in NV-spectroscopy as a stand-alone technique [141], this thesis is focused on the second approach. The shallow NV centers are detecting the statistical polarization (Section 1.4.5), which already constitutes 1% for the detection volume corresponding to  $10^4$  nuclear spins. Therefore, even small improvement of the degree of the polarization can bring us closer to nano-NMR. Another advantage of NV-based hyperpolarization is that the aggregate state of the sample is irrelevant, i.e. any substance can be hyperpolarized. The main idea is to reshape the NV-nuclear spin interaction Hamiltonian so that it will have a dominating flip-flop term, like in the Hyperfine coupling:

$$\text{const} \cdot (I_+ S_- + I_- S_+). \quad (5.3)$$

This will result in the polarization transfer from NV center's electron spin to coupled nuclear spins. At the same time in all cases the duration of the polarization transfer depends on the magnitude of the hyperfine coupling between the NV center and the nuclear spins. The stronger the coupling is, the faster polarization can be transferred. There are several ways to modify the Hamiltonian in such manner. Most of them are based on the microwave

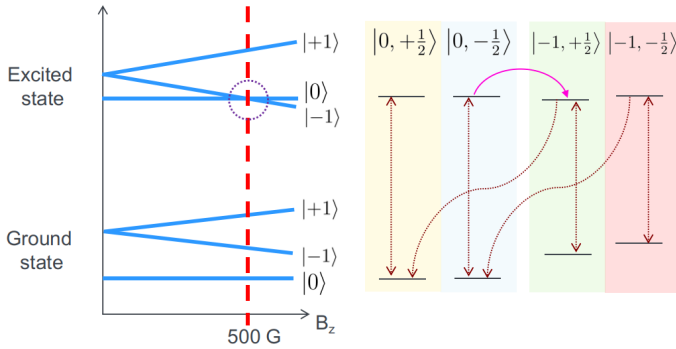


Figure 5.7.: Optical pumping at excited state level anticrossing

manipulation of the NV center, but the simplest approach requires only the laser and certain magnetic field. It is sufficient to tune the magnetic field, bringing NV center either to Excited state level anticrossing (ESLAC) or Ground state level anticrossing (GSLAC).

**Cross-relaxation induced polarization at ESLAC.** To polarize strongly coupled nuclear spins, which are intrinsic to diamond lattice ( $^{14}\text{N}$ ,  $^{15}\text{N}$ ,  $^{13}\text{C}$ ), it is enough to simply tune the static magnetic field to  $\sim 500$  Gauss [236, 237, 238]. Near the ESLAC the  $m_s = |0\rangle$  manifold will approach the  $m_s = |1\rangle$ . When the perpendicular component of the hyperfine coupling mixes the states faster than it decays, the population is pumped towards the state with the higher projection of the nuclear spin (Figure 5.7).

**Cross-relaxation induced polarization at GSLAC.** Similar approach can be applied at GSLAC, tuning the frequency of the NV's transition to the Larmor frequency of the nuclear spins [239, 240, 241]. This method works for the polarization of the external nuclear spins, whose Larmor frequencies lie between 500 kHz and 5 MHz. Due to the features of the GSLAC structure only  $^{14}\text{N}$  containing NV centers are suitable for the external spins' polarization. Among the disadvantages one can mention, the required stability of the magnetic field, since even small oscillations of the magnetic field will slightly detune the frequencies of NV's transition and nuclear Larmor frequencies,

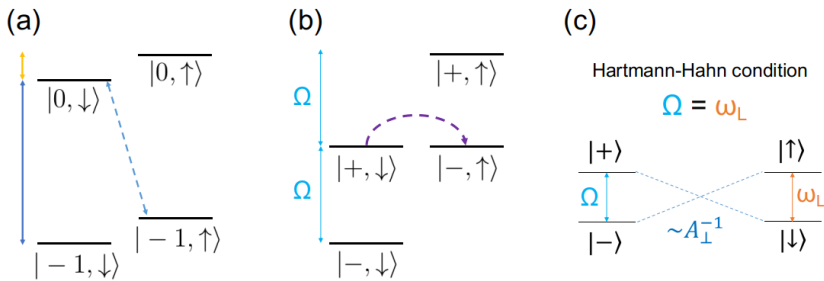


Figure 5.8.: (a) Energy-level diagram of the NV center ground state coupled to single nuclear spin. The blue and yellow arrows indicate the electron and nuclear spin transitions, correspondingly. The dashed arrow shows the suppressed flip-flop transition. (b) The interaction picture when the Hartmann-Hahn condition is fulfilled. (c) Hartmann-Hahn condition.

leading to the interruption of the polarization transfer.

**Nuclear spin Orientation Via Electron spin Locking (NOVEL)** protocol is based on the electron-nuclear double resonance at Hartmann-Hahn condition [172, 242]. The basic principle of this method is to effectively convert the static dipolar field created by NV center in the nuclear spin site into the resonant AC, which would flip the nuclear spin. The theory is described here [171] in details and will be briefly set out below.

Consider the NV center's ground state coupled to the spin half nucleus at magnetic field  $> 0.1$  T. The huge energy mismatch between the electron and nuclear transition energies (Figure 5.8(a)) hampers the mixing of  $|0, \downarrow\rangle$  and  $|-1, \uparrow\rangle$  levels caused by hyperfine coupling. This obstacle can be removed by conversion to the rotating frame. Considering only  $m_s = 0, -1$  manifold, the Hamiltonian from Section 1.2.4 reduces to:

$$H_0 = [D - \gamma_e B_z] S_z + \gamma_N \mathbf{B} \cdot \mathbf{I} + S_z \cdot \mathbf{A}_{\text{hf}} \cdot \mathbf{I}, \quad (5.4)$$

where  $S_z = |-1\rangle\langle -1|$ , because of the electron's triplet state. Continuously driving the electron spin transition with the resonant microwave field  $H_1 =$

$\Omega e^{i\omega_{MW}t}[S_x \otimes \mathbf{1}]$ , in the rotating frame the Hamiltonian takes the form:

$$H_{rot} = \Omega[S_x \otimes \mathbf{1}] + \gamma_N \mathbf{B} \cdot \mathbf{I} + S_z \cdot \mathbf{A}_{hf} \cdot \mathbf{I}. \quad (5.5)$$

Rewriting  $H_{rot}$  in terms of the dressed states  $|\pm\rangle = \frac{|0\rangle \pm |-1\rangle}{\sqrt{2}}$  and using identities:

$$\begin{aligned} S_z &= |-1\rangle\langle -1| - \frac{1}{2}(|+\rangle - |-\rangle)(\langle +| - \langle -|) = \frac{1}{2}(\mathbf{1} - 2\sigma_x), \\ S_x &= \frac{1}{\sqrt{2}}(|+\rangle\langle +| - |-\rangle\langle -|) = \sigma_z, \end{aligned} \quad (5.6)$$

the Hamiltonian in the interaction picture is:

$$H_{int} = \Omega[\sigma_z \otimes \mathbf{1}] + \gamma_N B_{eff} \mathbf{I} - \sigma_x \cdot (A_{\perp} I_x + A_{\parallel} I_z), \quad (5.7)$$

where  $B_{eff} = \mathbf{B} + \frac{1}{2}\mathbf{A}_{hf}$ . The nuclear spin precesses with the Larmor frequency around the effective magnetic field and the energy separation between the dressed states is  $\Omega$  (Figure 5.8(b)) can be varied. Considering the transitions  $|+, \downarrow\rangle \leftrightarrow |-, \uparrow\rangle$  as a two-level system, the energy mismatch between them is  $\delta\Omega = \Omega - \gamma_N B_{eff}$ . Taking the known solution of population of the two-level system with nearly resonant radiation field (see Section 1.4.4 and [243]), the population of the  $|+, \downarrow\rangle$  state is:

$$P_{|+, \downarrow\rangle}(t) = \frac{1}{2} \frac{A_{\perp}^2}{A_{\perp}^2 + \delta\Omega^2} (1 - \cos(\sqrt{A_{\perp}^2 + \delta\Omega^2} t)). \quad (5.8)$$

Thus, if NV center is brought into the transversal plane of the Bloch sphere, in the rotating frame it performs the Rabi oscillations  $|+\rangle \leftrightarrow |-\rangle$ . By adjusting MW amplitude one can match the Rabi frequency of the dressed state of the electron spin to the Larmor frequency of the nuclei at the applied magnetic field leading to  $\delta\Omega = 0$ . This is the so-called Hartmann-Hahn condition (Figure 5.8), which ensures the energy transfer. If the nuclear spin is polarized in  $|\downarrow\rangle$  state, the system will undergo periodic flip-flops  $|+, \downarrow\rangle \leftrightarrow |-, \uparrow\rangle$  and simple maths allow one to calculate the time required

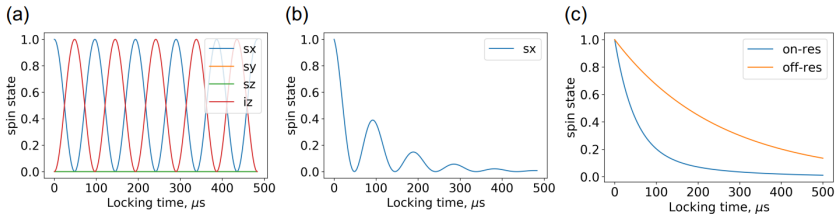


Figure 5.9.: Shape of NOVEL measurements in different cases. (a) One strongly coupled nuclear spins,  $A_{\perp} = 65$ . (b) Strongly coupled nuclear spin  $A_{\perp} = 65$  kHz with relaxation  $T_{1\rho} = 100 \mu\text{s}$ . (c) Relaxation in the presence of the spin bath of weakly coupled nuclear spins. Off-resonant  $T_{1\rho} = 250 \mu\text{s}$ .

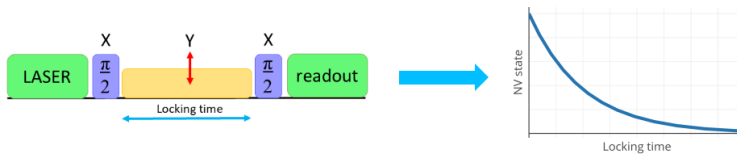


Figure 5.10.: Spin locking pulse sequence.

for the swap:  $t_{\text{swap}} = \pi/A_{\perp}$ .

However, at real experimental conditions the nuclear spins are in the thermally mixed states. Therefore, the NV center oscillates between  $|+\rangle$  and the thermal state (Figure 5.9(a)).

The experimental sequence realizing the described polarization transfer is depicted in Figure 5.10 (left). After the initialization with the green laser, the first  $(\frac{\pi}{2})_X$  pulse brings the electron spin state into the transversal plane of the Bloch sphere. An instantaneous  $90^\circ$  phase shift of the MW driving field locks the polarization along the  $B_1$  field. The subsequent  $(\frac{\pi}{2})_X$  pulse is required to perform the readout. The polarization of the locked state decays with the characteristic time  $T_{1\rho}$  (Figure 5.10, right) and is usually recorded for certain MW amplitude. Thus, the measurement result is the NV state decay as a function of locking time, the so-called  $T_1$  time in the rotating frame -  $T_{1\rho}$  decay [244]. Indeed, in the doubly rotating frame (Figure 5.11):

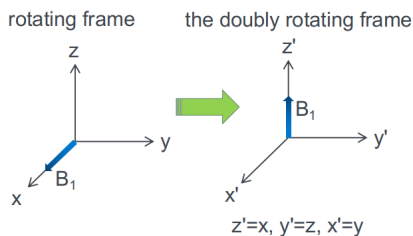


Figure 5.11: Doubly rotating frame

$$\frac{1}{T_{1\rho}} = \frac{d}{dt} \overline{\langle \hat{I}_{z'} \rangle}. \quad (5.9)$$

The NV magnetization undergoes relaxation in the presence of the spin-locking field in the rotating frame, a situation similar to the rotation of longitudinal magnetization around the  $B_0$  field in the laboratory frame. In other words, in the rotating frame, the spin lock field  $B_1$  plays the same role of  $B_0$  as in the laboratory frame.  $T_{1\rho}$  is related to  $T_1$  and  $T_2$  as follows: 1) as the frequency of the spin-locking pulse,  $\omega_1$ , approaches zero,  $T_{1\rho}$  approaches  $T_2$ ; and 2) as  $\omega_1$  approaches the Larmor frequency,  $\omega_0$ ,  $T_{1\rho}$  approaches  $T_1$ . The main mechanisms that contribute to  $T_{1\rho}$  relaxation in liquids are chemical exchange, dipole-dipole interactions, spin spin coupling, diffusion and slow rotational motions of spins on large macromolecules. Relaxation leads to the signal shape presented in Figure 5.9(b).

In the experiments, presented in this chapter, polarization has been transferred to the bath of weakly coupled nuclear spins. Broad distribution of hyperfine couplings reduces the damped cosine to the monotonic decay (Figure 5.9(c), see Section 5.2.2 and Section 5.2.4).

From the practical point of view NOVEL is the most general polarization technique. It does not require the sample to be solid, liquid or gaseous and is applicable at any magnetic fields at the availability of the hardware for demanded frequency range. The main disadvantage of this method is a necessity of a high power stability of the locking pulse, which is defined by the power stability of the microwave amplifier. Refocused NOVEL pulse

protocol is robust against pulse errors at the expense of prolongation of the polarization transfer time [245]. It is composed of  $N$  repetitions of two spin-locking pulses of duration  $(\tau/2)$ , separated by a  $\pi$ -pulse of the same phase.

Since the invention of Hartmann-Hahn double resonance, it was noticed, that it would be particularly useful to have a technique utilizing the fluorescence or phosphorescence of organic molecules to detect optically electron or nuclear spins in nonradiative excited or ground states or to study with the sensitivity of optical detection other phenomena associated with solids such as their acoustic properties, the dynamics of energy transfer, or electron and nuclear spin diffusion. Thus, the first optically detected electron spin locking have been detected for molecules in their excited triplet states by monitoring the microwave-induced modulation of the phosphorescence [246].

Polarization transfer from the NV center to surrounding nuclear spins has been experimentally demonstrated for the intrinsic  $^{13}\text{C}$  and electron spins [171, 247, 248]. NOVEL protocol can be considered as a CW decoupling sequence and can be used for protection of spin coherence [249]. To polarize the nuclear spins with an ensemble of NV centers chirp-modification of the locking pulse can be applied [235, 250]. This is the so-called integrated solid effect (ISE) based on a quasi-adiabatic sweep of the driving field frequency and allows efficient population transfer for a wide range of misalignment angles. Interestingly, NOVEL protocol can also be exploited for sensing phases of water [251].

Changing of the phase of the locking pulse in Figure 5.10 from  $Y$  to  $-Y$  will result in the different direction of the nuclear spin polarization. Therefore, for spectroscopy measurements (characterization of the coupling strength and orientation) an alternating version of the spin-locking sequence is used, which produces the same experimental signal but without polarization of the nuclear bath [171]. Figure 5.12 shows NOVEL measurements of the strongly coupled  $^{13}\text{C}$  surrounded by weaker coupled spins. At  $10\ \mu\text{s}$  time scale the decay is not noticeable. The oscillations do not reach the thermal state because they show the steady state of the strongly coupled nuclear spin. It is being partially polarized during the application of spin-locking pulse

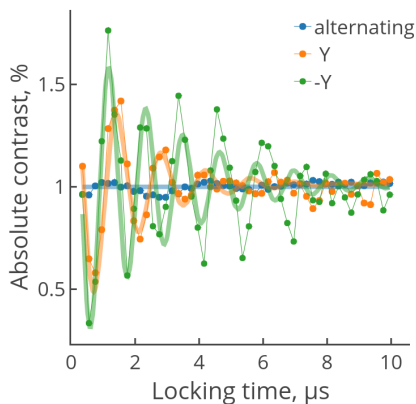


Figure 5.12: NOVEL of strongly coupled  $^{13}\text{C}$  surrounded by bath of weakly coupled  $^{13}\text{C}$  spins. The extracted coupling strength  $A_{\perp}$  is  $715 \pm 69$  kHz for Y and  $865 \pm 54$  kHz for -Y locking pulses.

and polarization does not decay within several repetitions of spin-locking protocol. The alternating pulse sequence does not reveal any polarization transfer.

**Pulsed polarization techniques** are based on pulsed manipulation of NV center's electron spin [93, 105, 252]. They are robust against pulse errors and can be used for polarization of external nuclear spins. However, due to the filter function associated with DDNS-like sequences, the protocols are very narrow-banded in the sense of addressable range of Larmor frequencies. KDDxy-polarizing sequence is illustrated in Figure 5.13(b). As shown in simulation in Figure 5.13(d) there is a narrow range of free evolution times (Larmor frequencies) when the polarization will be transferred. And the higher is the number of pulses, the narrower this frequency window is. Figure 5.13(e) and (f) show the measurement results with decoupling KDDxy and polarizing KDDxy sequences. Thus, both pulse sequences can be used for nuclear spin detection. In principle, any decoupling sequence can be used instead of KDDxy in the round brackets in Figure 5.13(b).

PulsePol sequence [253] is based on the smart Hamiltonian engineering. It is designed in such a way that its average Hamiltonian [254, 255] realizes

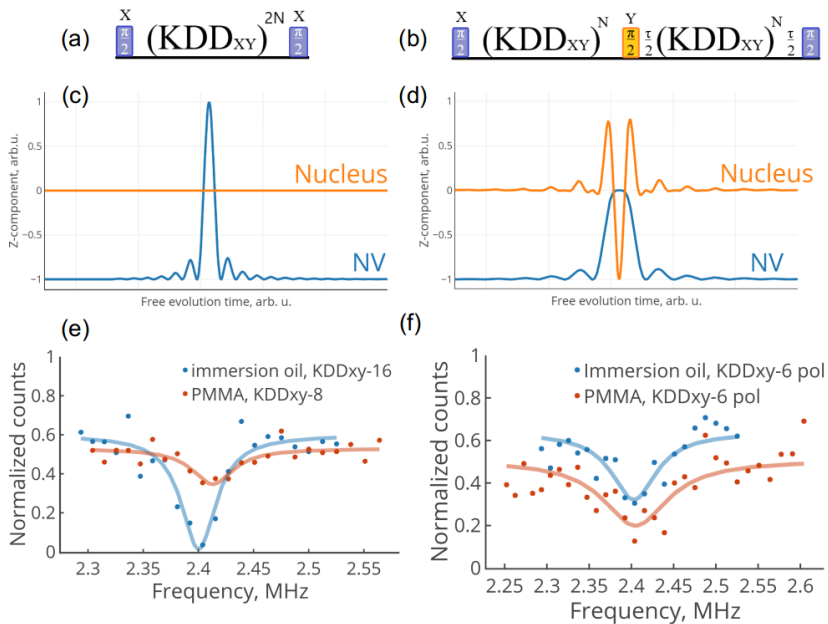


Figure 5.13.: The effect of KDDxy-N DD (a) and KDDxy-N polarizing (b) protocols. The measurements were performed for PMMA and immersion oil. (c) and (d) show the results of simulations. (e) and (f) are the measurement examples.

flip-flops between the NV center and the coupled nuclear spins:

$$H_{avg} = -\frac{\alpha A_x}{4}(I_+ S_- + I_- S_+). \quad (5.10)$$

The resonant condition pulse spacing is not intuitively clear:  $\tau = \frac{n\pi}{\omega_l}$ . The time required for a swap is defined by a  $A_x$  component of hyperfine coupling:

$$t = \frac{4\pi}{\alpha} \frac{1}{A_x}. \quad (5.11)$$

And the required number of repetitions is:

$$N = \frac{t}{2\tau} = \frac{2\omega_I}{3\alpha A_x}. \quad (5.12)$$

## 5.2. NOVEL on protons

### 5.2.1. Resonant $NV^-$ spin cross relaxation to $^1H$ spins in immersion oil.

In general, there are two ways to detect the polarization transfer. The first one is to demonstrate the depolarization of NV centre by recording its photoluminescence and the second is to perform the direct measurements of NMR enhancement. In the experiments we monitored the spin state of the NV center, since the latter approach is quite challenging.

The polarization of the  $NV^-$  center was transferred to  $^1H$  nuclear spins in the immersion oil (Fluka Analytical 10976), which is used to optimally couple the  $NV^-$  fluorescence to the optical objective. After the proton detection using DDNS, the NOVEL signal from individual shallow NVs brought in contact with proton spins in an organic fluid on the diamond surface was recorded. It will be shown later (Section 5.2.3) that the relatively high viscosity of this fluid, and correspondingly its slow molecular diffusion, plays a key role in enabling an efficient polarization transfer.

Figure 5.14(a) shows the typical measurement of  $T_{1\rho}$  in on- and off-resonant cases with respect to proton's Larmor frequency (2.315 MHz) at 54.4 mT. The difference between two curves shows how much polarization is being transferred at each duration of the locking pulse. In Figure 5.14(a) the maximal difference is  $\sim 19\%$  and corresponds to 150  $\mu s$  spin-locking time. Measuring NV state as a function of the mw field amplitude at fixed polarization transfer time (Figure 5.14(b)) one can observe a distinct dip of the same contrast at resonant position.

Another examples of the locking-frequency sweep measurements are shown in Figure 5.15. The contrast of the dip depends on many factors, such as the deviation of the fixed locking time from optimal and the  $NV^-$  individuality. The natural linewidth, defined by the distribution of the Larmor frequen-

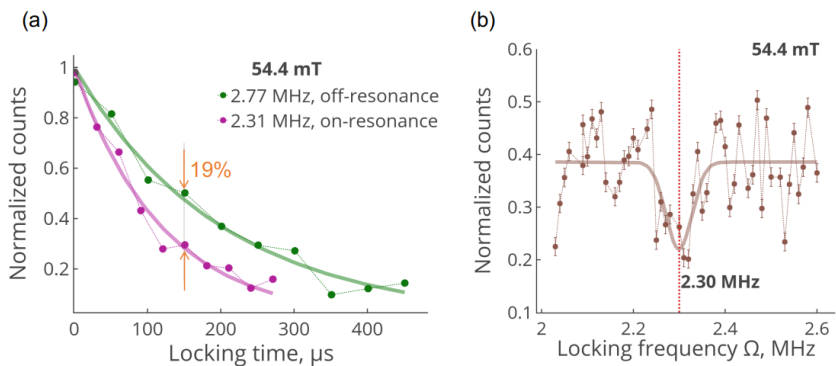


Figure 5.14.: (a) On- and off-resonant measurements of spin locking decay (depth  $7.7 \pm 0.4$  nm). (b) The signal obtained with the same NV center after a NOVEL sequence of fixed spin-locking duration ( $150 \mu\text{s}$ ) and variable microwave amplitude (expressed as the NV spin Rabi frequency). Linewidth 67 kHz, 18.8% contrast

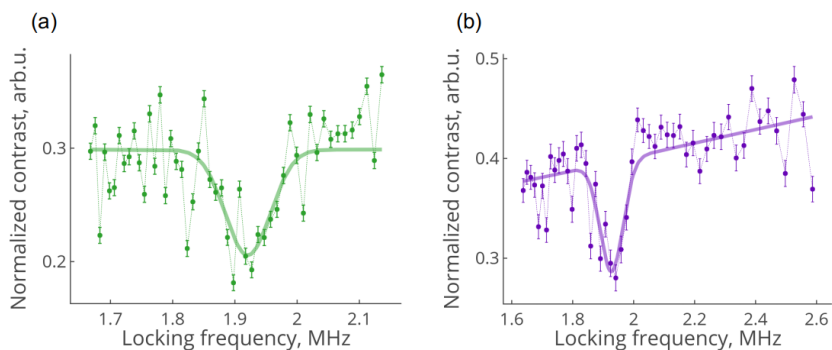


Figure 5.15.: Spin Locking with the amplitude sweep at 450.9 G ( $\omega_{L(^1H)} = 1.92$  MHz). (a) NV depth  $4.8 \pm 0.4$  nm, linewidth 85 kHz, contrast 9.3%. Locking time  $57 \mu\text{s}$ . (b) NV depth  $5.1 \pm 0.4$  nm, linewidth 88 kHz, contrast 11.0%, locking time  $20 \mu\text{s}$ .

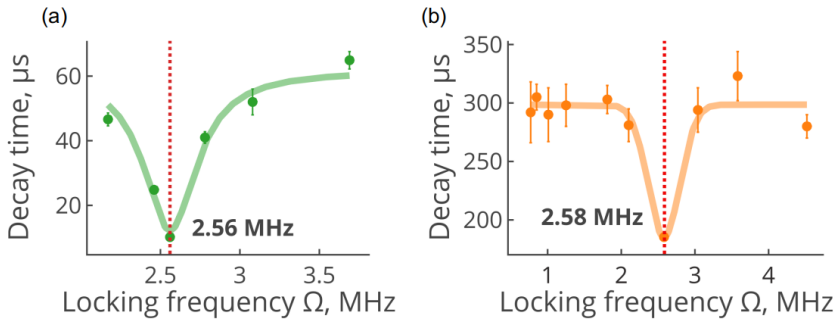


Figure 5.16.:  $NV^-$  spin relaxation time  $T_{1\rho}$  during spin-locking as a function of the Rabi field for two shallow NVs (a)  $2.6 \pm 0.1$  nm (b)  $3.9 \pm 0.2$  nm deep, top, and bottom, respectively. The solid line in (a) and (d) is a Lorentzian fit, whereas the vertical dashed line indicates the  $^1H$  spin resonance frequency at the applied magnetic field 60.2 mT.

cies inside the detection volume (see Section 5.2.2), is broadened by the fluctuations of the MW-power. It is determined by the power stability of the amplifier and usually fluctuates around 80 kHz (see Section 5.2.7).

Measurements of the  $T_{1\rho}$  decay time as a function of locking frequency, reveal greater signals for Rabi frequencies both above and below the proton Zeeman frequency (Figure 5.16, dashed vertical line), thus confirming the resonant nature of the transfer.

We ascribe the distinct dips at the proton Larmor frequencies to the polarisation transfer from the electron spin to the protons. The position of the dip varies with the external magnetic field in accordance with the proton gyromagnetic ratio. Similar results have been published in [256].

### 5.2.2. Effect of inhomogeneous couplings and spin-diffusion on the cross-relaxation profile

In the double rotating frame of the NV, the simple Zeeman coupling between the NV and the nuclear spin bath takes the form of resonant Hartman-Hahn interaction, wherein polarization can be exchanged between different spin

species. The Hamiltonian is simply given by

$$\hat{H} = \sum_{k=1}^N A_{\perp}^k (S^+ I_k^- + S^- I_k^+). \quad (5.13)$$

Due to the inhomogeneity in the hyperfine couplings,  $A_{\perp}^k$ , polarization exchange between the NV spin,  $\hat{S}$  and the nuclear spins  $\hat{I}$  happens at varying timescales,  $\tau_k = \pi/2A_{\perp}^k$ . Such inhomogeneity will lead to the dephasing of the coherent evolution between the spins, due to which the polarization exchange oscillations between the NV and the nuclear spin bath will be completely suppressed, and the NV spin will only lose its polarization continuously with a rate governed by an average coupling strength.

Within the sensing volume of the NV's electron spin, the distribution of the nuclear spins determine the inhomogeneity in their couplings to the NV spin. The average NV's spin polarization dynamics in such a case would be determined by the function

$$P(t) = \int dA_{\perp} G(A_{\perp}) \left( \frac{A_{\perp}^2}{\sqrt{A_{\perp}^2 + \delta\Omega^2}} \right) \sin^2(\sqrt{A_{\perp}^2 + \delta\Omega^2}t), \quad (5.14)$$

where  $G(A_{\perp})$  describes the distribution of coupling strengths  $A_{\perp}$  over the sensing volume and  $\delta\Omega = \omega_s - \omega_I$ , determines the off-resonant condition in polarization exchange. Clearly, such an oscillatory nature of the polarization dynamics gets suppressed for any finite distribution  $G(A_{\perp})$ , and there is only a monotonic loss or gain in polarization. Such quasi-steady state like behavior should not be confused with the diffusion of polarization within the spin-bath as it also leads to a similar behavior. For times much greater than the average interaction strength  $\langle A_{\perp} \rangle$  with the nuclear spin bath i.e.,  $t \gg \frac{1}{\langle A_{\perp} \rangle}$ , the polarization  $P(t)$  of the NV spin shown above reaches an asymptotic value for any continuous distribution  $G(A_{\perp})$ , that could be quite different from its equilibration value. This is directly reflected on the amplitudes of

the  $T_{1\rho}$  dips shown in [Section 5.2.1](#), and given by

$$P(\delta\Omega) = \int dA_{\perp} G(A_{\perp}) \left( \frac{A_{\perp}^2}{\sqrt{A_{\perp}^2 + \delta\Omega^2}} \right). \quad (5.15)$$

For a case of a single proton spin, the above equation corresponds to a Lorentzian distribution and the width of the depolarization ( $T_{1\rho}$  dip) as a function of the MW amplitude is directly given by the coupling strength  $A_{\perp}$ . Whereas in the present case where there is more than one spin in the proton bath occupying a spatially distinct position with respect to the NV electron spin, the width is determined by an average over all the coupling strengths. Due to this inhomogeneity in the couplings the depth of the dip also never reaches its maximum value when compared to the ideal single spin case. Other dominant contribution to the width of  $T_{1\rho}$  dip is the decoherence time of the NV spin. It sets the maximum time for any coherent interaction with external environment and affects both the width and depth of the  $T_{1\rho}$  dips from [Section 5.2.1](#). It leads to broadening of the dip and reduce the depth (contrast) of the dip. To account the role of spin diffusion within the bath, one can approximate this process by including an additional dissipation rate for the proton spins. For higher rates, the NV spin could depolarize much faster even for nonzero detuning  $\delta\Omega$ , caused by power fluctuations. This would effectively broaden the  $T_{1\rho}$  dip. In contrast to effects described above, spin-diffusion would only change the width and does not affect the depth. Thus, the monotonic polarization gain or loss of the NV spin observed in our experiments could arise either due to (i) the fact that inhomogeneous couplings between the NV-electron spin and the nuclear spins have no commensurate frequency to generate any revivals in the polarization exchange as described above or (ii) due to the spin-diffusion effect caused by the inter-nuclear spin coupling that is comparable (if not stronger) to their coupling to the NV- electron spin.

### 5.2.3. Dynamics of $NV^-$ cross-relaxation

Introduction of idle times in the spin-locking protocol (Figure 5.19(a)) allows to study the dynamics of the polarization transfer. All experiments in this section were performed with the same shallow NV center (Figure 5.17).

A direct comparison of the temporal evolution of the  $NV^-$  signal with or without Hartmann-Hahn matching is presented in Figure 5.19(b) (orange and green traces, respectively). In both cases, we observe an exponential decay of the  $NV^-$  spin polarization as a function of locking time, though the on-resonance time constant is considerably shorter, a signature of  $NV^-$  spin cross-relaxation with the proton bath. Calculating the difference between both curves (blue trace in Figure 5.19(b)), we use the slope in the linear response at early times (dotted red line in Figure 5.19(b)) to approximate the cross-polarization time  $T'_{CP} = 120\mu s$ , where the prime highlights the difference with the “true” crosspolarization time  $T_{CP}$  observed in the limit of an infinite wait time  $T_W$  between successive repeats (see below). Assuming for now the difference between the two is not large, we obtain a crude estimate of the distance to the detection volume via the approximate formula [110]:

$$\frac{2\pi}{T'_{CP}} \cong \frac{\mu_0}{4\pi} \frac{\gamma_{NV}\gamma_{1H}\hbar}{r_{\text{eff}}^3} \sqrt{N}, \quad (5.16)$$

where  $N$  is the number of protons within the detection volume,  $\hbar$  is Planck's constant divided by  $2\pi$ , and  $\mu_0$  is the permeability of free space.

The numerical calculation of the  $B_{RMS}$  [116] results in  $N \approx 4 \times 10^4$  (Figure 5.18). Using this value, we get  $r_{\text{eff}} \approx 12$  nm, consistent with the measured  $NV^-$  depth ( $7.7 \pm 0.4$  nm) and estimated detection volume radius ( $r_d \approx 14$  nm, see Figure 5.17).

In stark contrast with prior  $^{13}\text{C}$  NOVEL experiments in diamond [171] (where the  $NV^-$  evolution during the spin-lock time shows successive maxima and minima), the exponential decay observed herein indicates a monotonic, one-directional polarization transfer process. The latter, of course, stems from the broad distribution of  $NV^-$ - $^1\text{H}$  couplings inherent to the

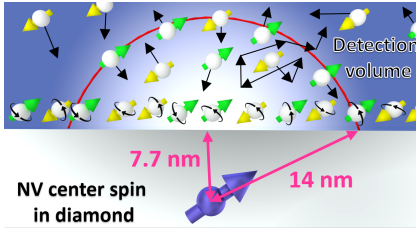


Figure 5.17: NV at a distance  $r_s = 7.7$  nm from the surface effectively interacts with all protons within a distance  $r_d \approx 14$  nm (thus defining the detection volume  $\sim 2(r_d - r_s)^3$ ). This geometry leads to a broad distribution of hyperfine couplings preventing the formation of polarization transfer revivals.

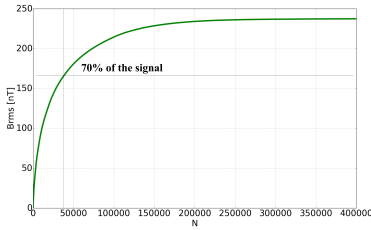


Figure 5.18: The numerical simulation of the  $B_{RMS}$  for the 7.7 nm deep NV center. The total signal is 237 nT. 70% of the total magnetic field, sensed by the NV center, are created by  $\sim 4 \times 10^4$  closest protons located within the spherical cup of 7 nm radius.

present working geometry and, correspondingly, the lack of commensurate frequencies required to produce a “revival” in the polarization transfer. Molecular diffusion during  $T_{CP}$  further contributes to smooth out the  $NV^-$  signal, though we note that a similar exponential decay was seen for protons in PMMA (see Section 5.2.5).

The ability to transfer spin polarization to neighboring protons from a single NV can be further exploited to gather information on the chemical composition [141], nanoscale structure [257, 258], and molecular dynamics [146] near the diamond surface. Of special interest in the case of fluids is how molecules arrange and diffuse near the interface with the solid [259]. Our initial experiments in this direction make use of the protocol in Figure 5.19(a), where we introduce a variable wait time  $T_W$  between successive repetitions of the NOVEL sequence. The rationale is that, because spin diffusion and nuclear spin relaxation within the proton bath are relatively slow, a number of repeats comparable to  $N$  (i.e., the number of protons in the detection volume) is sufficient to locally saturate the proton bath polariza-

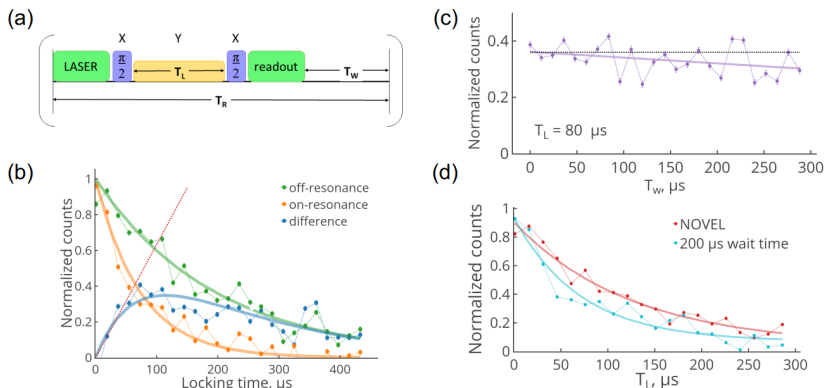


Figure 5.19.: (a) NOVEL protocol featuring a wait time  $T_W$  between successive repeats. (b) The total time of the sequence is fixed to  $450 \mu\text{s}$  - time at which the contrast is 0.  $NV^-$  spin signal after a NOVEL protocol of variable spin-locking time for Rabi frequencies on- and off-resonance relative to the Larmor frequency of protons in immersion oil (orange and green traces, respectively). To determine the cross-polarization time, we take the difference between the two (blue trace); from the inverse of the slope at early times (dashed line), we find  $T'_{CP} = 120 \mu\text{s}$ . (c) NOVEL NV signal as a function of  $T_W$  for a fixed spin-locking time  $T_L = 80 \mu\text{s}$ . (d) Same as in (c) but as a function of  $T_L$  for a wait time  $T_W \approx 200 \mu\text{s}$  (cyan) and zero wait time  $T_W \approx 0$  (red) traces, respectively. In all cases, the magnetic field is 54.4 mT; all other conditions are the same as those in Figure 2.

tion. Since  $N$  is much smaller than the number of repeats needed to attain a reasonable signal-to-noise (SNR) ratio (of order  $10^6$  per data point), a polarization transfer blockade takes place unless molecules physically diffuse in and out of this volume on a faster time scale. Indeed, we find for protons in oil that the signal amplitude after a NOVEL sequence of fixed spin-locking time ( $80 \mu\text{s}$ ) tends to decrease as  $T_W$  grows (Figure 5.19(c)); along the same lines, we observe comparatively faster cross-relaxation after the addition of a fixed wait time of  $200 \mu\text{s}$  (Figure 5.19(d)), thus hinting at diffusion processes out of the detection volume with characteristic times longer than  $T_{CP}$ .

#### 5.2.4. Simulations of $NV^-$ cross-relaxation to proton spins in fluids

To interpret these observations on a more quantitative basis, we model the polarization transfer process through a set of coupled master equations describing the flow of polarization from the NV to protons within the detection volume (which we describe as a single unit block interacting with the NV via an effective coupling of amplitude  $T_{CP}^{-1}$ ). Defining  $T_R$  as the time separating two successive repeats, we write:

$$\frac{dP^{NV}}{dt} = \frac{f(t)}{T_p^{NV}}(1 - P^{NV}) - \frac{P^{NV}}{T_{SL}^{NV}} - \frac{g(t)}{T_{CP}}(P^{NV} - P^H), \quad (5.17)$$

$$\frac{dP^H}{dt} = -\frac{P^H}{T_{SL}^H} - \frac{P^H}{T_D^H} + \frac{g(t)}{NT_{CP}}(P^{NV} - P^H). \quad (5.18)$$

Here,  $P^{NV}$  ( $P^H$ ) denotes the  $NV^-$  ( $^1H$ ) spin polarization (within the detection volume),  $T_{SL}^{NV}$  ( $T_{SL}^H$ ) is the  $NV^-$  ( $^1H$ ) spin-lattice relaxation time,  $T_D$  is the characteristic time a molecule spends within the detection volume, and  $T_p^{NV}$  denotes the NV spin pumping time under optical excitation;  $f(t)$  ( $g(t)$ ) is a step function (of period  $T_R$ ) equal to 1 when the laser (mw) is on and 0 otherwise. We would like to note that the contribution from  $T_{SL}$  is always on, independent of the applied MW field. Therefore, this term does not contain the step function.

To numerically solve the above set of equations, we assume  $T_{SL}^H \approx 1s \gg T_D^H$ , i.e., the decay of proton polarization in the detection volume is dominated by molecular diffusion. As the NV spin polarization happens on a time scale  $T_p^{NV} \sim 1\mu s$ , which is much shorter than any other time scale, the full polarization of the NV spin is reached almost instantaneously prior to the NOVEL transfer and wait time. Assuming  $g(t) = 1$  during the transfer time, one can easily solve the above equations to obtain a closed form solution for the NV polarization, given by

$$P^{NV}(t) = \frac{1}{\Gamma} e^{-\frac{(\gamma_D + \gamma_{SL} + 2\gamma_C)t}{2}} \left[ (\gamma_D + \gamma_{SL}) \sinh\left(\frac{\Gamma t}{2}\right) + \Gamma \cosh\left(\frac{\Gamma t}{2}\right) \right], \quad (5.19)$$

where  $\gamma_D = \frac{1}{T_D^H}$ ,  $\gamma_{SL} = \frac{1}{T_{SL}^{NV}}$ ,  $\gamma_C = \frac{1}{T_{CP}}$ ,  $\Gamma = \sqrt{(\gamma_D + \gamma_{SL})^2 + 2\gamma_C^2}$ .

For simplicity, we further assume that the  $NV^-$  spin-lattice relaxation time  $T_{SL}^{NV} = 250 \mu\text{s}$  is given by the off-resonance  $NV^-$  spin relaxation time  $T_{1\rho}^{\text{off}}$  (see Figure 5.19(b)). With these approximations, we interpret the observations in Figure 5.19(c, d) as the result of slow molecular diffusion dynamics near the surface, i.e.,  $T_D^H > T_{CP}$ .

By assuming  $T_{CP} = 120 \mu\text{s}$ , we find the experimentally observed contrast for  $T_D^H \gtrsim 170 \mu\text{s}$  (Figure 5.20). Interestingly, this value exceeds the time that molecules spend within the detection volume,  $(r_d - r_s)^2/D_M^b \approx 60 \mu\text{s}$ , calculated when assuming that the self-diffusion coefficient of bulk oil,  $D_M^b \approx 0.3 \text{ nm}^2/\mu\text{s}$ , remains unchanged near the surface. Our results suggest, therefore, that the dynamics of oil molecules is slower close to the solid-liquid interface, a notion consistent with theoretical models [259, 260, 261] and recent experimental observations [146, 262].

In applications aimed at the hyperpolarization of target fluids [241, 263], an interesting question is the set of conditions,  $T_{CP}$ ,  $T_D$ , and  $T_R$ , required to optimize the polarization transfer. In Figure 5.21, we analyze the  $NV^-$  spin cross-relaxation contrast by calculating the polarization gain by the proton spin when the  $NV^-$  spin is driven at on- and off-resonance conditions. For Figure 5.21(c), we have fixed the cross-polarization time  $T_{CP}$  and varied the wait time  $T_W$  and diffusion time  $T_D$ . We find the most efficient cross-polarization when  $T_D \approx T_R > T_{CP}$ , and it remains constant for any further increases in  $T_R$ . However, at faster diffusion rates ( $T_D \ll T_{CP}$ ), the cross-polarization rate averages to zero, thereby reducing the transfer efficiency for any  $T_R$ . Hence, regardless of the repetition rate, high diffusive fluids such as water cannot be polarized efficiently through this technique without the formation of a near-surface layer featuring sufficiently slow molecular dynamics.

The discussion above can be formally extended to nuclear spins in solids if  $T_D^H$  is replaced by the spin diffusion time  $T_S^H \approx (r_d - r_s)^2/D_S$ , where  $D_S \approx (\mu_0/4\pi)(0.1\gamma_H^2\hbar/r_{H-H})$  is the spin diffusion coefficient [264] and  $r_{H-H}$  is the internuclear distance. This process, however, is inherently slow:

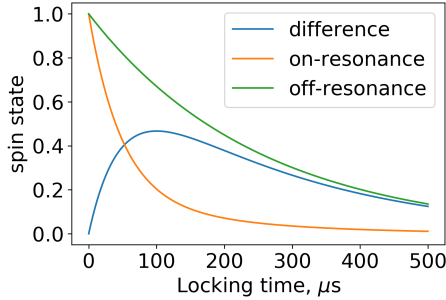


Figure 5.20.: Plot of Equation (5.19), for  $T_{CP} = 120\mu s$ ,  $T_{SL}^{NV} = 250\mu s$ ,  $T_D^H = 170\mu s$ . We show the polarization decay of the NV spin obtained from the Equation (5.19). For long times the polarization loss to the spin-bath dominates and the overall equilibration rate of the NV center is determined by  $\gamma$ , on the other hand for short times the oscillatory function appears to induce additional loss, due to the exchange of polarization with the target nuclear spin ensemble. The two competing effects results in the shortening of the equilibration rate over short time scales and attains its natural dissipation rate on longer time scales.

Even for strongly coupled nuclear systems such as protons, we calculate  $D_S \approx 2 \times 10^{-4} nm^2/\mu s$ , orders of magnitude smaller than the self-diffusion coefficient of most fluids. The rapid polarization of neighboring nuclei thus prevents further transfer, the so-called "blockade", hence leading to negligible NOVEL contrast. Naturally, the contrast can be made nonzero by periodically cycling the sign of the starting NV-spin, though at the expense of a net polarization gain in the nuclear spin reservoir. By the same token, nonzero contrast is expected in the limit of exceptionally short nuclear spin-lattice relaxation times, precisely the condition throughout our NOVEL transfer experiments to protons in a PMMA film.

### 5.2.5. Polarization of PMMA

PMMA is a solid proton-containing sample, transparent in the visible range of the spectrum and at 532 nm has a transmission value of  $T=92\%$  [265].

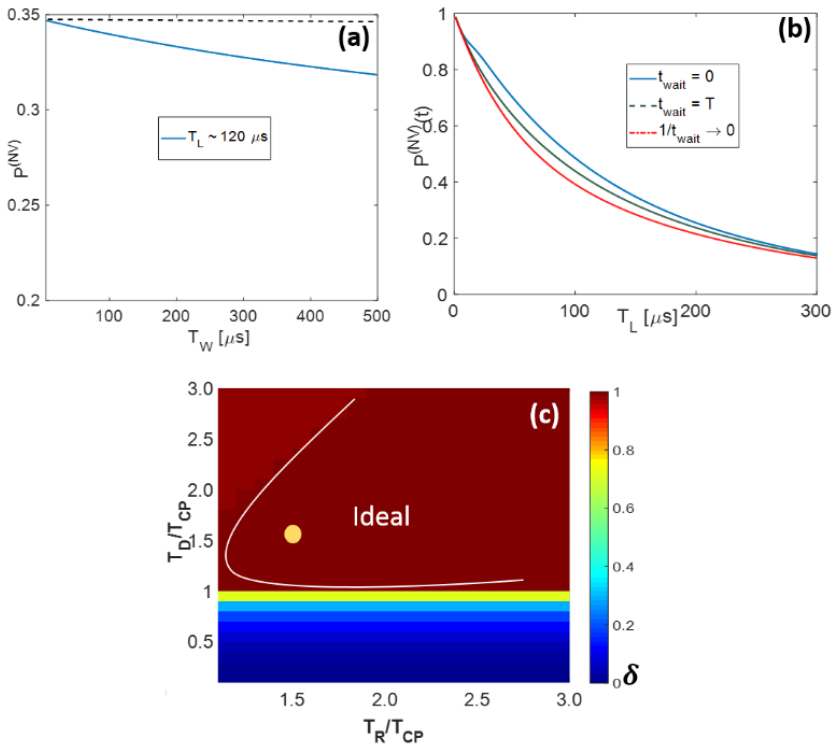


Figure 5.21.: Modelling  $NV^-$  cross-relaxation to proton spin in fluids. (a) Calculated NOVEL signal for a fixed spin-locking duration as a function of the wait  $T_W$  between repeats. (b) Same as in (a) but as a function of the spin-locking time for a short ( $1 \mu\text{s}$ ) and a long ( $200 \mu\text{s}$ ) wait time between repeats (blue and orange traces, respectively). For reference, the plot also includes the ideal response in the limit of infinite wait time (red trace). (c) Calculated contrast (see eq 4) as a function of the repetition and diffusion times,  $T_R$  and  $T_D$ , respectively.

Multiphoton absorption in the infrared or visible range can lead to the thermal decomposition of material [266, 267]. This process requires high peak powers, which can be produced by picosecond and femtosecond pulsed lasers [268]. For pulse durations longer than picoseconds, the multiphoton effects reduce dramatically. The probability of multiphoton absorption for nanosecond laser pulses is almost negligible. However, the ablation of PMMA in the visible spectrum at  $\lambda = 532$  nm can be explained through a photomechanical mechanism [269]. Mechanical stresses caused by laser irradiation of polymers can strongly influence laser ablation of these materials. The mechanical stresses created during laser irradiation can be caused by thermoelastic stresses emerging from thermal expansion [270, 271]. As the laser pulse heats a surface layer, it generates thermoelastic stress pulses in directions perpendicular to the surface, one propagating into the medium and one towards the free surface.

As a result, the overheating of the material in the absorbing region leads to photothermal decomposition and almost to the fragmentation of the acrylic polymeric material into species due to bond breaking. The dominant volatile product of thermal degradation of PMMA is Methylmethacrylate (monomer) [272].

In our measurements the laser power before the objective was  $78 \mu W$ , yielding  $4.7$  mJ/s power in the focused spot, which is in several orders of magnitude [266, 268] lower than that is required for laser ablation. However, the observed reduction of off-resonance  $T_{1\rho}$  with the time (Figure 5.22(a, c)) can be attributed to electron spin noise, arising either from the free radicals in the sample or from some unpaired electrons on the surface, appeared during the process of thermal decomposition. At the same time, the dips corresponding to the resonance polarization transfer to  $^1H$  nuclear spins are still observable (Figure 5.22(b, d), Figure 5.23).

#### 5.2.6. Bare diamond measurements

Taking into account the existence of the water layer on a diamond surface, it was interesting to make a reference measurements of relaxation times of

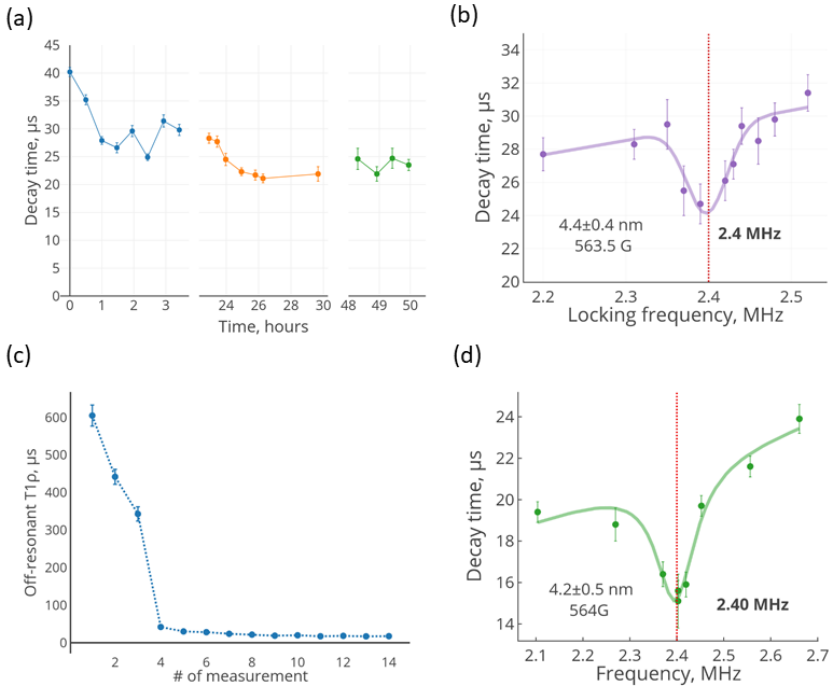


Figure 5.22.:  $T_{1\rho}$  measurements of 2 NV centers with PMMA on the diamond surface. The plots in the left column (a, c) are the off-resonance  $T_{1\rho}$  data in the chronological order. In (a) we started the monitoring of the  $T_{1\rho}$  much later. The initial  $T_{1\rho}$  is not known. The dip in (b) is measured between 3rd and 24th hours. In (d) the  $T_{1\rho}$  is measured between points number 7 and 11.

NV centers with no substances applied.

These measurements were done for the same NV center (depth  $5.9 \pm 0.7$  nm) at 537.9 G. Figure 5.24(a) shows the  $T_1$  time in air and the comparison of off-resonant  $T_{1\rho}$  times for the bare diamond and with immersion oil on the surface. As a rule,  $T_1$  times are significantly longer than the  $T_{1\rho}$ . The application of the oil to the diamond surface does not change the  $T_{1\rho}$  in comparison with PMMA.

The NOVEL measurements with the amplitude sweep of the spin-locking

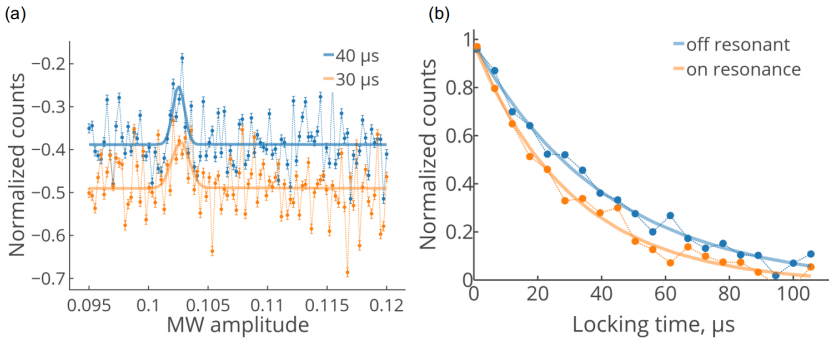


Figure 5.23.: (a) Results of the NOVEL protocol measured with the amplitude sweep of the spin-locking pulse for 2 different fixed spin-locking times (40 and 30  $\mu\text{s}$ ). (b)  $T_{1\rho}$  measurements with off- and on-resonant locking. Extracted values are  $42 \pm 4 \mu\text{s}$  and  $30.8 \pm 2.7 \mu\text{s}$  correspondingly. Magnetic field 498.1 G, NV depth is  $5.9 \pm 0.5 \text{ nm}$ .

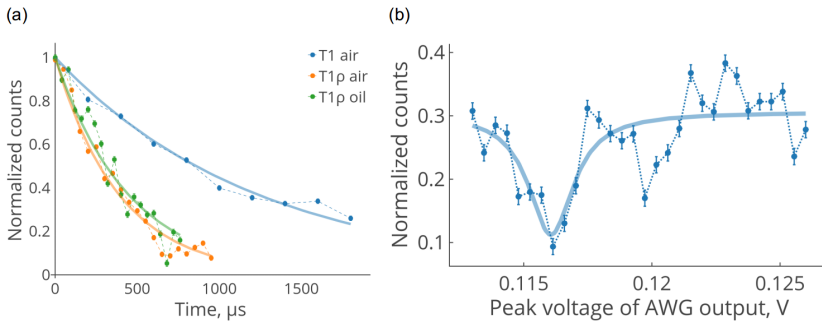


Figure 5.24.: Bare diamond measurements. Magnetic field 537.9 G, NV depth  $5.9 \pm 0.7 \text{ nm}$ . (a)  $T_1$ ,  $T_{1\rho}$  of the same NV center in air and oil.  $T_1 = 1240 \pm 40 \mu\text{s}$  in the air, while the relaxation times in the rotating frame ( $T_{1\rho}$ ) are:  $T_{1\rho}$  air off-resonance =  $390 \pm 14 \mu\text{s}$ ,  $T_{1\rho}$  oil off-resonance =  $448 \pm 24 \mu\text{s}$ . (b) NOVEL with the amplitude sweep. Duration of the locking pulse is 410  $\mu\text{s}$ . At the applied magnetic field, the proton Larmor frequency is 2.29 MHz. The dip we see lies between 0.114V and 0.118V output voltage of the AWG, which correspond to 2.12 and 2.34 MHz Rabi frequency. We attribute it to the polarization of the water layer on the diamond surface.

pulse are presented in Figure 5.24(b). Surprisingly, there is a dip which is located at the position of the proton Larmor frequency and can be attributed to the polarization of protons in the water layer.

### 5.2.7. Methods

**Diamond membrane.** All the experiments in this chapter were done with the same diamond membrane.  $T_2$  times up to  $\sim 180 \mu\text{s}$  were observed for the NV centers confined within 2-8 nm of depth at the sample area.

For the creation of the NV centers we used the procedure described in [273]. It consists of three parts: growth of the boron-doped layer, implantation and etching.

**The growth of the boron-doped layer.** An epitaxial boron-doped layer of diamond was grown by microwave-assisted chemical vapour deposition (CVD) method. Boron acceptor concentration was above  $10^{20} \text{ cm}^{-2}$  and the thickness of the  $p+$  layer was  $\sim 6$  nm. Then, the post-growth annealing at  $800^\circ\text{C}$  in UHV was performed to stimulate out-diffusion of atomic hydrogen, which could accumulate in the sub-surface layer of the diamond during the CVD growth.

**Implantation** ( $^{15}\text{N}$  at 5 keV energy, an average dose of  $5 \times 10^9 \text{ cm}^{-2}$ ) were done at room temperature at an incident angle below  $3^\circ$ , leading to the channelling effect [49]. The projected depth was calculated to be  $\sim 20$  nm below the surface – much below the thickness of the sacrificial  $p+$  layer. Then, the sample was annealed at  $950^\circ\text{C}$  for 2 h in high vacuum and cleaned by boiling in 3 acids ( $\text{H}_2\text{SO}_4$ ,  $\text{HNO}_3$ ,  $\text{HClO}_4$ ).

**$p+$  etching.**  $\sim 8$  nm of diamond were removed by reactive ion etching (RIE) in  $\text{O}_2$ . The final treatment was surface finishing using oxygen radicals produced by remote inductively coupled plasma for etching the RIE induced surface damage (see [49] as well).

**Power stability of the amplifier.** The errors of the locking pulse are mostly from the power instability of the amplifier. To determine this, we measured the Rabi frequency during 20 minutes, every second reading out the photocounts from the counter. Then we fitted the data corresponding to

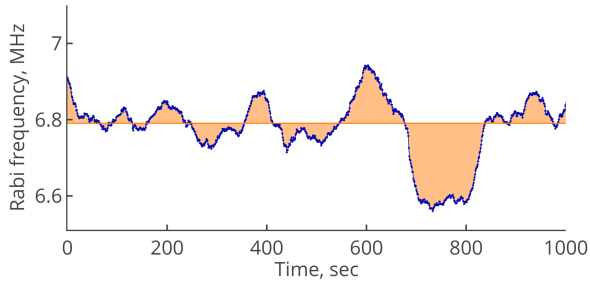


Figure 5.25.: Measurement of quasi-instantaneous Rabi frequency over time. It demonstrates the power stability of the amplifier.  $V_{pp} = 0.5$  V. Each data point was averaged over 60 s.

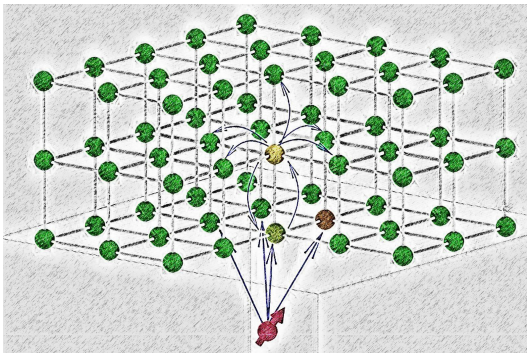
the first 60 seconds, then from 2nd second to 61st and so on (Figure 5.25). The result is the average instant Rabi frequency as a function of time. The standard deviation of the frequency fluctuations is 1.1% which leads to the 77kHz jittering around the average value.

### 5.3. Conclusions

In summary, we demonstrated microwave-assisted cross-polarization from optically pumped shallow NVs to protons in an organic fluid on the diamond surface. By studying the polarization transfer efficiency as a function of the repetition rate, we obtained an estimate for the effective time an oil molecule spends within the detection volume. The corresponding near-surface diffusion coefficient  $D_M^s \lesssim 0.1 \text{ nm}^2/\mu\text{s}$  substantially lower than in bulk ( $D_M^b \lesssim 0.3 \text{ nm}^2/\mu\text{s}$ ), thus supporting the notion of slower molecular dynamics near the solid surface.

Extension of these studies to properly prepared surfaces and other target fluids could be performed to directly measure the spin diffusion coefficients in solids [264] and directly probe the “no-slip” condition at the surface, a notion often invoked but notoriously difficult to verify experimentally [259, 260, 261]. Alternatively, polarizing external spins can be a key element in various quantum information protocols using solid state spins, such as in simulating strongly interacting spin systems that can be controlled and readout through single quantum probes [220], and for studies on the foundational aspects of quantum thermodynamics. Also, the ability to polarize nuclear spins within a confined volume is relevant for nano-NMR, since the study of molecular proteins and membrane systems *in vivo* represents a considerable challenge for structural biology [274, 275]. Integrating an NV center inside a microfluidic device [263], spin-locking technique can be used to polarize liquids for a subsequent detection via conventional NMR.

COMING UP DETECTION OF  
HYPERPOLARIZED  $^{19}\text{F}$  IN  
 $\text{CaF}_2$



To establish DNP-enhanced nano-NMR with single shallow NV centers as a stand-alone competitive technique, it is necessary to develop a polarization-detection scheme involving single NV center and understand its constraints. This chapter shows the preliminary experiments in this direction. Due to the molecular diffusion in the liquids, such studies are restricted to solids. However, the spin diffusion creates some obstacles for solids. In our experiments  $CaF_2$  was chosen as a solid sample due the high amount of  $^{19}F$  spins with large gyromagnetic ratio (Section 6.1). In addition to that, calcium fluoride does not affect the coherence properties of shallow NV centers. Section 6.2 contains the results of the Hartmann-Hahn polarization experiments which confirm that  $^{19}F$  in  $CaF_2$  can be easily polarized. The theory of spin diffusion presented in Section 6.3. Polarization distribution was modelled for different polarization rates using Monte Carlo method in Section 6.4. Its analysis allowed us to propose a detection method based on the polarization of the detection volume to some extent and subsequent dynamical decoupling of nuclear spins (Section 6.5).

## 6.1. Polarization of a solid

The absence of molecular diffusion in a solid should lead to a possibility of creation of enough amount of polarization excess for the subsequent detection of NMR enhancement with NV center. However, as we know from the previous chapter, not all the solids are appropriate for such measurements (Section 5.2.5), i.e. do not change the NV's relaxation times. Moreover, the sample should consist of a huge number of nuclear spins with large gyromagnetic ratio. Otherwise it will not be possible to make the reference measurements and prove the presence of a material on the diamond surface.  $^1\text{H}$  has the largest gyromagnetic ratio ( $\gamma_{^1\text{H}} = 42.58 \text{ MHz/T}$ ) among the nuclear spins and organic solids form a big class of potential substances. They are made mostly of hydrogen, but not resistant to laser illumination and will inevitably reduce the  $T_1$  time. The second largest  $\gamma$  is possessed by  $^{19}\text{F}$  ( $\gamma_{^{19}\text{F}} = 40.05 \text{ MHz/T}$ ). In recent work [137] the ability to sense a several nanometer thick patches of  $\text{CaF}_2$  using an ensemble of NV centers has been shown. Thus, calcium fluoride has been chosen for experiments on the detection of the polarization enhancement.

$\text{CaF}_2$  is an ionic crystal with the fluorite structure, insoluble neither in water, nor in organic solvents. The unit cell of the material is most easily described as a simple cubic lattice formed by the  $\text{F}^-$  ions where a  $\text{Ca}^{2+}$  ion is contained in every second cube. The distance between fluorine atoms is  $2.7255 \text{ \AA}$  (half of the lattice constant) [276, 277]. This corresponds to  $5.25 \text{ kHz}$  interfluorine coupling constant. It equals to NV- $^{19}\text{F}$  coupling at the distance of  $2.42 \text{ nm}$ . The nuclear density can be easily calculated to be  $\rho_{^{19}\text{F}} = 4.905 \times 10^{28} \text{ m}^{-3}$ .

Figure 6.1 shows the NMR signals from  $50 \text{ nm}$  thick layer of  $\text{CaF}_2$  detected with two different NV centers at  $\sim 450 \text{ G}$ . The weaker dips correspond to hydrogen in the water which has been encapsulated between the diamond and salt during the evaporation procedure. It worth noting that NMR of this water can reveal the effect of the liquid confinement on the signal linewidth.

Another important point was to check the effect of the material on the relaxation times of single shallow NV centers. Off-resonant  $T_{1\rho}$  times measured

Figure 6.1: Two  $^{19}\text{F}$  NMR signals from 50 nm thick layer of  $\text{CaF}_2$  acquired with XY16 DD sequences applied to two different NV centers. Depth determined by fluorine nuclear density:  $5.5 \pm 0.6$  nm for blue trace and  $4.8 \pm 0.5$  nm for orange.

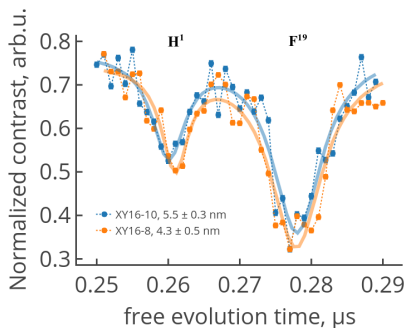
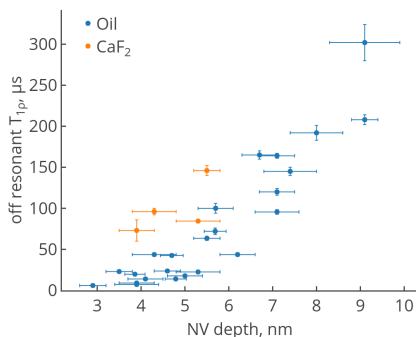


Figure 6.2: Off-resonant  $T_{1\rho}$  times measured for the same NV centers with immersion oil or  $\text{CaF}_2$  applied to the diamond surface.



for different NV centers with immersion oil or  $\text{CaF}_2$  on the diamond surface are presented in Figure 6.2. Interestingly, calcium fluoride slightly increases the relaxation times in comparison with immersion oil or another liquids [278].

Thus, the ability to detect fluorine nuclei and sustainability of relaxation times to the presence of the material on the surface is convincing confirmation of a good choice of the material.

## 6.2. NOVEL of $^{19}\text{F}$ in $\text{CaF}_2$

Applying the NOVEL protocol to the NV center with a 50 nm thick layer of  $\text{CaF}_2$  above it, one can easily get results similar to those of Section 5.2.1, confirming the ability of resonant polarization transfer from NV center to

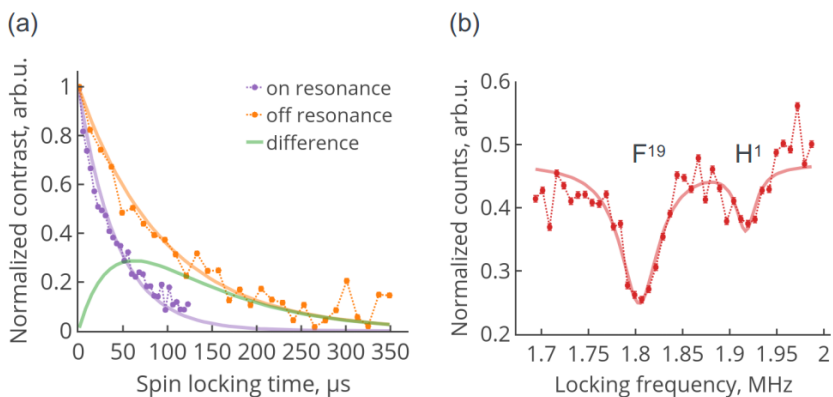


Figure 6.3.: Response of the NV center to the NOVEL sequence applied to the  $^{19}\text{F}$ . Thickness of  $\text{CaF}_2$  50 nm. Depth of the NV  $4.3 \pm 0.5$  nm. Magnetic field 450.3 G. (a)  $T_{1\rho}$  measurements. Off-resonance  $96 \pm 4 \mu\text{s}$ , on-resonance  $42.3 \pm 1.3 \mu\text{s}$ . Max contrast 28.8%. (b) NOVEL with the frequency sweep of the locking pulse. FWHM 49.5 kHz and 25.0 kHz. The contrast of  $^{19}\text{F}$  dip is 19.1%. Spin-locking time  $60 \mu\text{s}$ .

$^{19}\text{F}$  nuclear spins.

Typical outcomes of application of the spin-locking protocol are presented in Figure 6.3. Figure 6.3(a) shows on- and off- resonant  $T_{1\rho}$  measurements with clear contrast. The measurement with the amplitude sweep of the spin-locking pulse is depicted in Figure 6.3(b). The smaller dip corresponds to the polarization of hydrogen in encapsulated water.

### 6.3. Spin diffusion

$\text{CaF}_2$  is a solid and can easily be polarized, nevertheless there is a process of polarization loss which will hinder the detection of the NMR enhancement with NV center.

Spin diffusion is a transfer of spin polarization induced by dipolar interactions among the like nuclear spins. The concept was introduced by Bloembergen in 1949 [279].

The process obeys the diffusion equation, relatively slow and its really direct measurements are not possible [68, 279]. In case of nuclear spins with  $I = 1/2$  for  $p = P_{-\frac{1}{2}} - P_{\frac{1}{2}}$  one can write:

$$\frac{\partial p}{\partial t} = D \Delta p. \quad (6.1)$$

If we confine ourselves to account for flip-flop transitions of the nearest neighbors, the diffusion constant  $D$  is given by [68, 280]:

$$D = Wa^2 \approx \frac{a^2}{30T_2}, \quad (6.2)$$

where  $W$  is the probability for a simultaneous transition between neighboring nuclear spins and  $a$  is the lattice constant. For the cubic crystal  $W \approx (30 \times T_2)^{-1}$  as a result of averaging over all directions [280].

In most cases spin diffusion is not directly measured. NMR methods are based on the creation of the polarization excess in some parts of the sample (magnetization grating, for example) and the subsequent detection of the residual polarization after some diffusion time. Proton spin diffusion is widely used to obtain various structural information [281, 282, 283] and determine domain sizes [284] in heterogeneous organic solids and biomolecules.

The suppression of nuclear spin diffusion is relevant for solid state quantum computing and can be performed via the application of a nonuniform magnetic field [285, 286].

Spin diffusion coefficients in  $CaF_2$  along the [001] direction are  $710 \pm 50 \text{ nm}^2/\text{s}$  for Zeeman order [287, 288] and  $2900 \pm 300 \text{ nm}^2/\text{s}$  for dipolar order [289] (Figure 6.4). It is  $\sim 423$  times slower than molecular diffusion in the bulk immersion oil. Thus, for the 5 nm detection volume it takes around 32 ms for polarization to reach the border after being generated.

In the context of this work the spin diffusion is relevant for several reasons. It transfers the polarization excess from the interface to the bulk material, which is crucial for conventional NMR detection methods. Strong dipole-

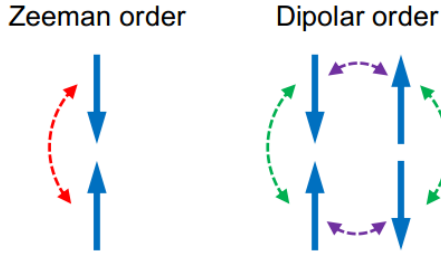


Figure 6.4.: Diffusion of Zeeman order is the flip-flop between two spins (red arrows). Diffusion of dipolar order is realized by two possibilities, when two pairs of spins turn over simultaneously (either two green or two violet flips).

dipole interactions between nuclear spins result in a fast propagation of polarization so that the polarization blockade does not occur. As a consequence, during the detection with an NV center it should be suppressed. Thus, despite the spin diffusion is shorter than the molecular diffusion, it should not be underestimated.

## 6.4. Polarization distribution

To optimize the measurement protocol depicted in [Figure 6.5](#), which consist of  $N$  polarization cycles with the subsequent detection of hyperpolarization we need to know the polarization distribution over time  $p(\vec{r}, t)$ . It is determined by  $T_1^{nucl}$ , spin diffusion coefficient and cross-polarization time.

Ideally, one should find the solution of the following equation [[279](#), [280](#)]:

$$\frac{\partial p(\vec{r}, t)}{\partial t} = D \Delta p(\vec{r}, t) - \frac{p(\vec{r}, t)}{T_1^{nucl}} + \frac{p(\vec{r}, t)}{T_{CP}(\vec{r}, t)}, \quad (6.3)$$

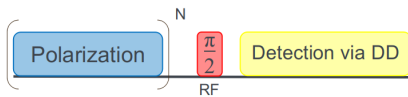


Figure 6.5: Polarization enhanced sensing scheme.

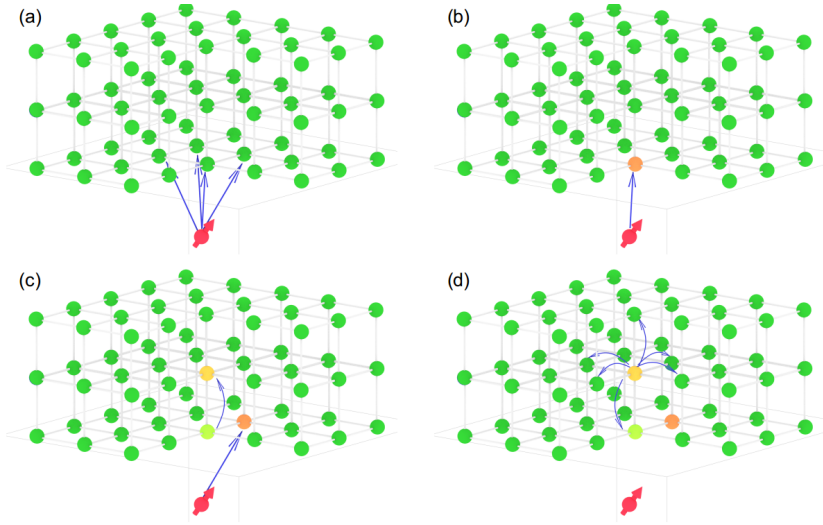


Figure 6.6.: The model of polarization dynamics in the presence of the spin diffusion. (a) At starting point in time the substance is not polarized. During the application of NOVEL protocol NV center (red spin) can transfer a part of its polarization to four nearest nuclear spins with equal probability. (b) One nuclear spin is partially polarized. (c) During the next implementation of Hartmann-Hahn sequence polarized spin transfers the polarization to the neighbor due to the dipolar interactions. NV center polarizes another nearest spin. (d) The process of polarization propagation continues in a diffusive manner.

where the influence of spin-lattice relaxation ( $T_1^{nucl}$ ) and cross-polarization to the nuclear spins ( $T_{CP}(\vec{r}, t)$ ) are taken into account.

Equation (6.3) is quite complicated to solve analytically since  $T_{CP}(\vec{r}, t)$  is a time-spatial variable [290]. There are several ways to find a numerical solution [291, 292], but for our purposes simple Monte Carlo simulations are sufficient.

They can be modelled in the following manner. There is an NV center located under the cubic lattice, formed by fluorine atoms. During the first NOVEL cycle ( $N=1$  in Figure 6.8(a)) part of NV's polarization can be transferred to

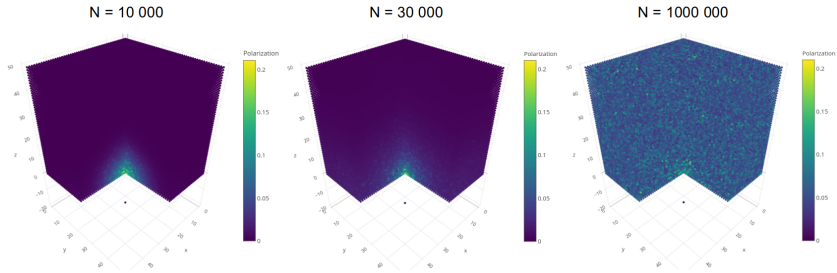


Figure 6.7.: Simulations of the polarization distribution inside a cell of  $50 \times 50 \times 50$  atoms after different amount of polarization cycles  $N$ . At  $N = 10^4$  (left) the polarization did not reach the borders of the cube and exponentially decays with the distance from NV. When  $N = 3 \times 10^4$  (center) the boundary conditions come into play, which then lead to the accumulation of the polarization inside a confined volume over time (right).

one of several closest nuclear spins (four nuclear spins marked by arrows in Figure 6.6(a)). This nuclear spin is randomly chosen (Figure 6.6(b)). After the second implementation of NOVEL protocol NV will polarize another nuclear spin, but the polarization of the previously polarized spin will diffuse to random nearest neighbor (Figure 6.6(c, d)).

Applying this reasoning one can obtain the total polarization within the detection volume after certain amount of polarization transfer steps or determine the conditions for the steady state, for example. Figure 6.7 shows the simulations of the polarization distribution inside a cell of  $50 \times 50 \times 50$  atoms after different number of polarization cycles  $N$ . The details are described in Appendix C. At  $N = 10^4$  the polarization did not reach the borders of the cube and exponentially decays with the distance from NV. When  $N = 3 \times 10^4$  the boundary conditions come into play, which then lead to the accumulation of the polarization inside a confined volume over time.

Depending on the pumping rate (how much polarization is being transferred) the polarization excess can either continuously diffuse out of the detection volume or a steady state can be generated. In case of shallow NV centers the pumping rate is slower than the spin diffusion in  $CaF_2$  which

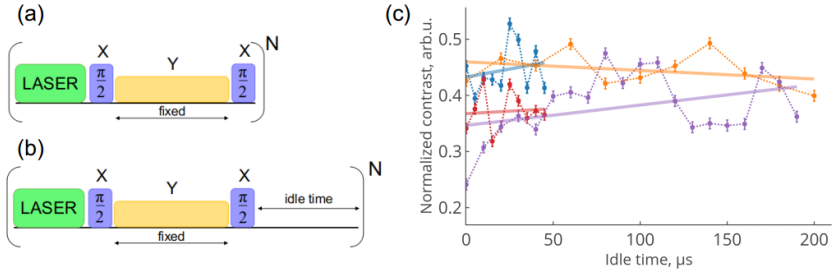


Figure 6.8.: (a) NOVEL pulse sequence. (b) NOVEL with idle times. (c) Measurement with  $N = 10^6$  repetitions of the protocol depicted in (b). Magnetic field = 449.5 G. NV depth  $5.3 \pm 0.5$  nm. On- and off-resonant contrast 20%. Spin-locking time is  $31 \mu\text{s}$  for blue and orange data points,  $42.8 \mu\text{s}$  for red and purple.

leads to the fast dissipation of polarization. It is confirmed by the measurements depicted in Figure 6.8(c). Here the PROPI protocol with different idle times has been applied to the same NV center (Figure 6.8(b)) [250]. It was repeated  $N = 10^6$  times for each idle time one by one. In other words, for a certain time window the sequence was repeated one million times. Then the idle time has been increased and the sequence was repeated  $N$  times, and so on. Such a huge amount of repetitions was chosen beforehand to approximate the saturating condition. If it was the case, the contrast would decrease with increasing the idle time. However, due to the fast propagation of the polarization over the sample the signals remain the same.

## 6.5. Detection of polarization excess

### 6.5.1. Polarization strategy

To optimize the hyperpolarization strategy we need to minimize the leakage of polarization due to the spin diffusion.

One of the simplest approaches is the cancellation of spin diffusion by confining the size of the sample. Then the polarization will be growing strong. However, this is efficient if only the volume is small, i.e. the time required

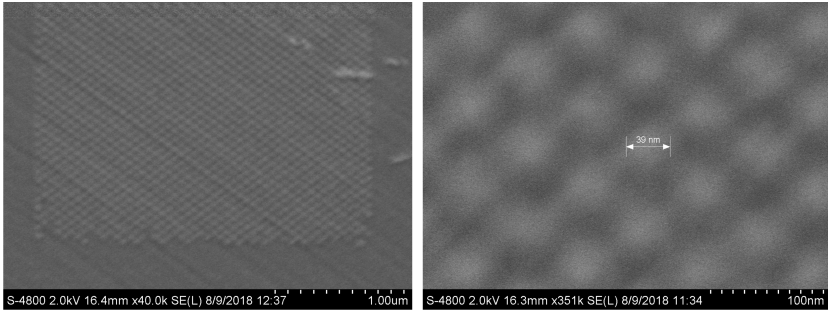


Figure 6.9.: SEM images of  $CaF_2$  patches. The characteristic size of cuboids is around  $40\text{ nm} \times 40\text{ nm} \times 2\text{ nm}$ . The arrow length on the right image is 39 nm. Thanks to Dr. Rainer Stöhr for the images.

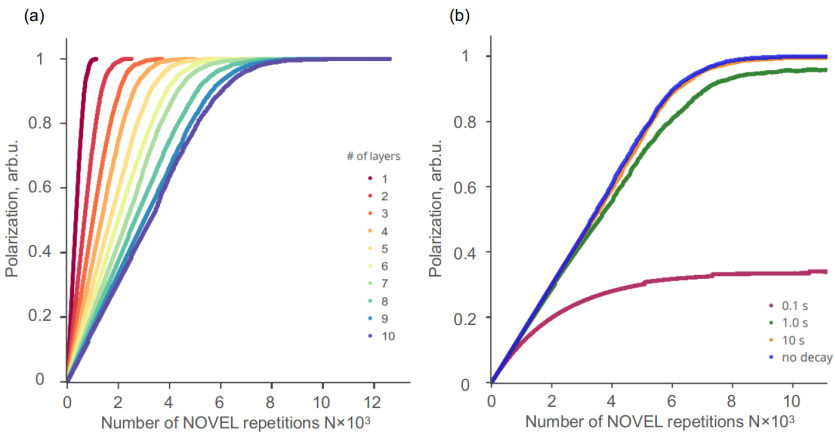


Figure 6.10.: Simulation of nuclear spin polarization as a function of number of repetitions of NOVEL sequence for  $10 \times 10$  atom ( $2.7\text{ nm} \times 2.7\text{ nm}$ ) sheets of fluorine atoms. (a) Imaginary case with infinite nuclear  $T_1$  time. The thickness varies from 1 to 10 layers. (b) Impact of nuclear  $T_1$  time.  $N = 1000$  repetitions correspond to  $44.5\text{ ms}$  polarization time.

for the total polarization is comparable to the readout time. [Figure 6.10](#) shows the nuclear spin polarization as a function of repetitions of NOVEL protocol for different number of fluorine layers. For single  $10 \times 10$  atoms sheet of squared fluorine lattice it takes only  $\sim 45$  ms to polarize the whole volume. From the experimental point of view it is quite complicated for at least two reasons. Firstly, it is challenging to create a pattern made of nanoscopic islands of a substance. The smallest  $CaF_2$  patches on the surface of a diamond produced by lithography are depicted in [Figure 6.9](#). Secondly, the probability to find a nano-sized cube of material exactly above the NV center is quite small.

The steady state is not always achievable due to the inefficient polarization pumping rate and the spatial distribution of polarization will be limited by nuclear  $T_1$  time. Depending on the purity of the crystal spin-lattice relaxation times of the fluorine nuclear spins can vary from several seconds to several minutes at room temperature and several tesla [[279](#), [287](#), [288](#), [289](#), [293](#), [294](#), [295](#)]. For our estimations we can use the lower limit in the order of  $T_1 = 1$  s, then the  $T_1$  limited diffusion radius is  $r = \sqrt{T_1 D} \approx 30$  nm. Simulations show, that there is another promising way. The detection volume can be polarized to some extent and then the enhanced signal can be quickly read out. One will have to adjust the number of polarization repetitions because of the statistical polarization.

We consider the 5 nm deep NV center. Its detection volume (70% of spins contributing to the detected signal) contains 12707 nuclear spins, which create statistical polarization of 1% ([Equation \(1.21\)](#)). Obviously, one should optimize the experiments so that the created polarization exceeds the statistical polarization.

For example, to have at least one spin with 10% polarization on the border of the detection volume ([Figure 6.11](#)) one have to apply  $N = 14952$  repetitions of the sequence in [Figure 6.8\(a\)](#), each time transferring 15% of polarization. Taking spin-locking time to be  $40 \mu s$ , within  $\approx 700$  ms the polarization inside the detection volume will reach 8.4%. Since the one repetition of DD detection protocol takes  $\sim 11 \mu s$ , the proposed concept is quite feasible.

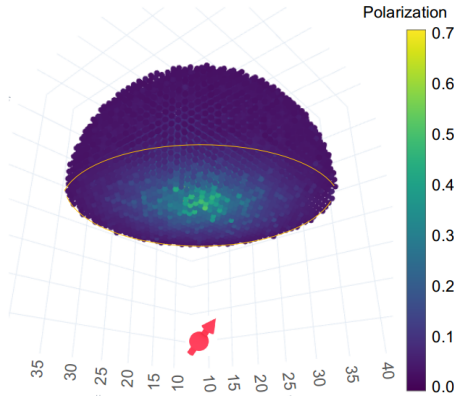


Figure 6.11.: Polarization of the detection volume when at least one nuclear spin on the boundary reaches the 10% polarization.

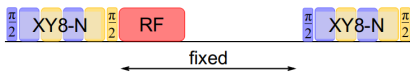


Figure 6.12: Sequence to measure the nuclear Rabi oscillations.

### 6.5.2. Nuclear Rabi

Active control of the nuclear spins is unavoidable during the detection because at least one radiofrequency  $\pi$ -half pulse is required to bring the polarization to the transversal plane for the readout via DDNS. In this scenario the polarization lifetime will be limited by  $T_2^*$ , which is in the order of tens of microseconds [294]. To prolong this time one will have to apply homonuclear decoupling protocols on the nuclear spins. Therefore, we need to measure nuclear Rabi oscillations.

The only way to measure the nuclear Rabi with single shallow NV center is to apply a modified correlation protocol (Section 1.4.7) depicted in Figure 6.12. Here the radiofrequency field, which changes the phase of nuclear spins, is applied within the fixed intersequence time.

However, before applying sequence in Figure 6.12 it is reasonable to measure the correlation signal itself, since correlation decay time in a solid sample is limited by nuclear  $T_2^*$ .

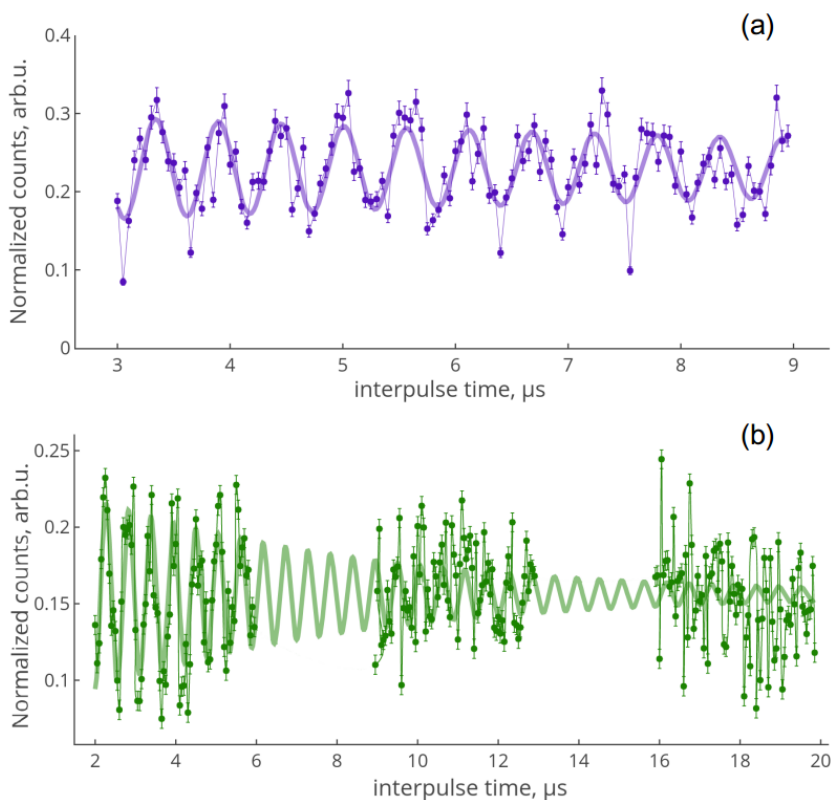


Figure 6.13.: Long correlation measurements. Fast oscillations correspond to 1.8 MHz  $^{19}\text{F}$  Larmor frequency. (a) XY16-4,  $T_2^* = 11.2 \mu\text{s}$ . (b) XY16-5,  $T_2^* = 6.8 \mu\text{s}$ .

The correlation measurements are shown in [Figure 6.13](#). The extracted  $T_2^*$  times are in the order of  $10 \mu\text{s}$ , which implies that the synchronization of DDNS with homonuclear decoupling is obligatory.

### 6.5.3. Synchronization of decoupling and detection.

In this subsection the problem concerning the detection of polarization with single shallow NV center will be discussed.

In conventional NMR there is a class of measurement pulse sequences, which decouple the same nuclear spins from each other: perform the so-called homonuclear decoupling. They can be CW-like as frequency switched Lee-Goldburg [296, 297, 298] or pulsed [299, 300].

We need to apply them simultaneously with the DDNS to prolong the polarization decay time. However, the homonuclear decoupling consist of radiofrequency pulses of the same frequency as the Larmor frequency of the nuclear spins. Therefore NV center will inevitably acquire the phase not only due to precessing spins, but also due to applied RF field. One have to design the pulse sequence where parallel decoupling of NV center from environment and homonuclear decoupling of nuclear spins will result in the cancellation of RF part of phase and acquisition of only of actual signal.

We are going to try to synchronize the XY8-N detection scheme with the one of the homonuclear decoupling sequences.

Intuitively the simplest approach would be to use some continuous decoupling technique with the possibility to inverse the phase of the radiofrequency field to cancel its contribution to NMR signal acquired with NV center. The frequency-switched Lee-Goldburg (FSLG) sequence fulfils this criterion [298].

Lee-Goldburg (LG) condition is realized when the effective field  $B_{\text{eff}}$  makes a magic angle  $\theta = 54.7^\circ$  with the static magnetic field  $B_0$  (Figure 6.14) [297]. If this effective field is sufficiently larger than the local field in the solid, locking of the nuclear spins along the LG axis results in the attenuation of the dipolar interactions in the rotating frame. Since the effective field is (Figure 6.14):

$$B_{\text{eff}} = \left[ B_0 - \frac{\omega}{\gamma} \right] \vec{z} + B_1 \vec{i}, \quad (6.4)$$

a condition on the LG frequency is:

$$\tan \theta = \frac{B_1}{B_0 - \omega_{LG}/\gamma} \implies \omega_{LG} = \gamma \left( B_0 - \frac{B_1}{\tan \theta} \right), \quad (6.5)$$

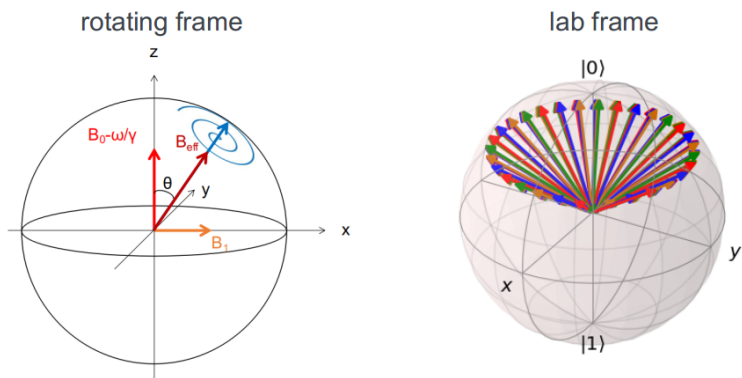


Figure 6.14.: Lee-Goldburg condition. At sufficiently large effective field  $B_{\text{eff}}$  the locking of the spin polarization along the magic angle  $\theta = \arccos(1/\sqrt{3}) \approx 54.7^\circ$  results in the effective decoupling of the nuclear spins. In the laboratory frame the polarization rotates with the frequency of the applied  $B_1$  field.

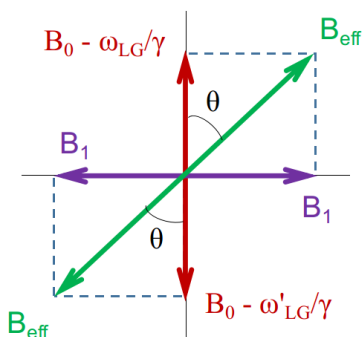


Figure 6.15: 2 Lee-Goldburg conditions.

where  $\gamma$  is the nuclear gyromagnetic ratio. For the  $\text{CaF}_2$  crystals the magnitude of the AC field around 5.2 Gauss is enough [297]. Then, for  $^{19}\text{F}$  at 450 G the difference between the  $\omega_{\text{Larmor}}$  and  $\omega_{\text{LG}}$  is  $\sim 0.8\%$  ( $\sim 14.7$  kHz).

In the FSLG scheme, the frequency of the RF irradiation is switched rapidly between the two Lee-Goldburg conditions (Figure 6.15). The simple math

gives us the second frequency:

$$\omega'_{LG} = \gamma \left( B_0 + \frac{B_1}{\tan \theta} \right), \quad (6.6)$$

which is also very close to the Larmor frequency of the nuclear spins.

In this scenario during the Lee-Goldburg decoupling the phase will be acquired due to the component of the polarization in the transversal plane, which oscillates with  $\omega_{LG}$  and the interpulse time should also vary within a sequence. The characteristic polarization decay time will be close to  $T_{1\rho}^{nucl}$ . The possibility to change the frequency of the  $B_1$  field gives us the room for changing the phase of the LG field to  $\pi$ . [Figure 6.16](#) demonstrates that the  $180^\circ$ -phase shift in the mid of the dynamical decoupling sequence eliminates the acquired phase. Thus, to cancel out the  $B_1$  contribution to the phase acquired by NV center, the basic block of the detection protocol with homonuclear decoupling should consist of four sections: LG decoupling at  $\omega_{LG}$ , LG decoupling at  $\omega'_{LG}$ ,  $\pi$ -shifted LG decoupling at  $\omega_{LG}$  and  $\pi$ -shifted LG decoupling at  $\omega'_{LG}$ . To bring the polarization from one LG state to another we need to use  $\pi$ -pulse, to avoid the unwanted evolution. At this moment it is important to set the limits to the magnitude of the driving field. If the RF field is too strong, the Rabi frequency of the nuclear spins will approach to their Larmor frequencies (1.802 MHz at 450 G), which will lead to violation of the secular approximation ([Figure 6.17](#)).

The possible polarization detection scheme would look similar to presented in [Figure 6.18](#). The main problem appears at the end of the nuclear  $\pi$ -pulse, when the frequency and phase of the LG field should be shifted. This phase shift implies the re-calibration of the rotating frame, i.e. the polarization always follows radiofrequency  $B_1$  field by default and they are always collinear and in phase.

Therefore, the experiments should be continued at high fields, which give the possibility to readout the information stored in the nuclear spin memory [82]. The experimental scheme would be the same as in [141], but with a preceding polarization part.

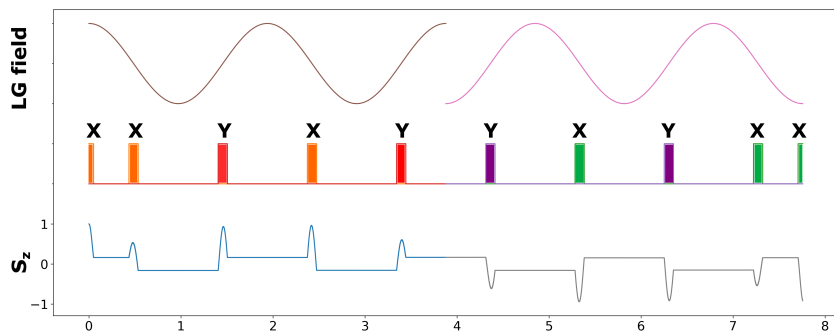


Figure 6.16.: Effect of the phase shift of the Lee-Goldburg field in the mid of the detection sequence on the acquired phase.  $S_z$  is the vertical component of the NV center spin.

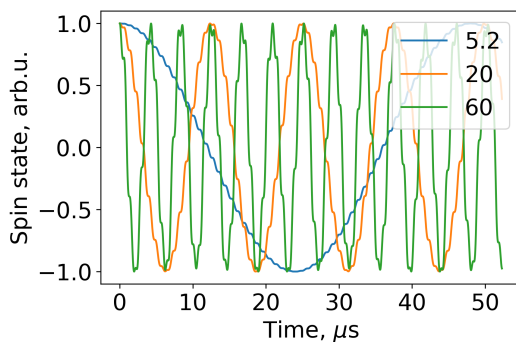


Figure 6.17.: Violation of the secular approximation at strong driving fields. The Legend shows the magnetic field in Gauss.

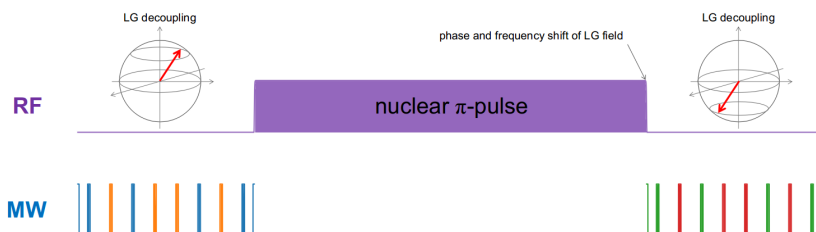


Figure 6.18.: Proposed detection scheme.

## 6.6. Conclusions

This chapter presented a strategy to measure the enhanced signal from hyperpolarized nuclear spins in solid using the NOVEL protocol applied to single shallow NV center. The suggested approach can also be implemented for other sensing techniques [141].

We have analysed a variety of boundary conditions. As a rule, the suitable samples must have a high nuclear spin density to create a large effective coupling strength with the NV center. This leads to a high, in comparison with the polarization speed, spin diffusion rate. According to the proposed scheme, this problem can be solved by quick polarization of a small part of the volume and subsequent homonuclear decoupling of nuclear spins during the detection. Future work will involve the design of the compatible with the readout pulse sequence.

To detect the nuclear spin polarization via dynamical decoupling, one should bring the nuclear spin to the transversal plane, where the decay will be limited by  $T_2^* \approx 10 \mu s$ . In principle, as long as we are not using organic materials, the experiments can be carried out at the low temperature to increase the nuclear coherence times [279, 295, 301].

The local hyperpolarization of solids can be useful for studying the decay of multiple quantum coherence intensities [293].



# LIST OF FIGURES

1.1. Diamond unit cell . . . . .	3
1.2. Structure of NV center . . . . .	7
1.3. NV spectra . . . . .	9
1.4. Spin configurations . . . . .	10
1.5. Energy level scheme . . . . .	11
1.6. Optical readout of NV state . . . . .	14
1.7. Confocal microscope . . . . .	19
1.8. Microwave part of the setup . . . . .	20
1.9. Setup . . . . .	21
1.10. ODMR measurements . . . . .	22
1.11. Pulse sequence for ODMR measurement . . . . .	23
1.12. Zeeman splitting of the GS . . . . .	24
1.13. Rabi oscillations . . . . .	26
1.14. Bloch sphere . . . . .	27
1.15. Pulse sequences for $T_1$ , $T_2$ and $T_2^*$ . . . . .	28
1.16. DD pulse sequences . . . . .	33
1.17. DD explanation . . . . .	34
1.18. Proton NMR . . . . .	35
1.19. DD evolution . . . . .	36

1.20. Correlation protocol . . . . .	38
2.1. Holonomy . . . . .	41
2.2. 3-level system with degenerate subspace. . . . .	43
2.3. The model of one-qubit gate . . . . .	45
2.4. The non-zero detuning case . . . . .	48
2.5. $\langle S_x \rangle$ , $\langle S_y \rangle$ and $\langle S_z \rangle$ as a function of number of pulses . . . . .	50
2.6. DD sequences with different errors . . . . .	53
2.7. Population of the states with error correction . . . . .	54
2.8. NOVEL using HQG . . . . .	55
2.9. NOVEL for standard (a) and holonomic gates (b). . . . .	56
3.1. Nanoparticle containing perfluorocarbons (PFC). . . . .	65
3.2. Bilayer boundary on the glass . . . . .	66
3.3. PDMS chamber . . . . .	66
3.4. The model used for simulations. . . . .	67
3.5. Simulations of the $B_{RMS}$ from micelles . . . . .	68
3.6. Model to calculate the correlation decay . . . . .	69
3.7. Simulations of the system dynamics . . . . .	70
3.8. NMR of micelles . . . . .	71
3.9. Example of correlation measurements . . . . .	72
3.10. FRAP . . . . .	73
3.11. Correlation decay time for bilayer . . . . .	74
4.1. Crystall lattice of hBN . . . . .	80
4.2. Confocal image of hBN . . . . .	81
4.3. hBN on the diamond surface . . . . .	82
4.4. Energy levels of $^{11}B$ for $\theta = 54.7^\circ$ . . . . .	83
4.5. Local roughness of the surface . . . . .	84
4.6. Energy levels of the tilted surface . . . . .	84
4.7. XY8 signal, inclination $2^\circ$ . . . . .	85
4.8. Simulations of the literature results . . . . .	86
4.9. $B_{RMS}$ for different number of layers . . . . .	86

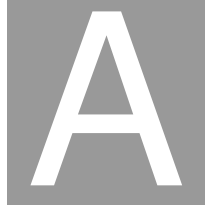
4.10.	$B_{RMS}$ as a function of NV depth . . . . .	87
4.11.	NMR signal from hBN at 595.6 G . . . . .	88
4.12.	NMR signal from hBN . . . . .	89
4.13.	All detected NMR signals from hBN . . . . .	89
5.1.	Macroscopic magnetization . . . . .	93
5.2.	Thermal polarization . . . . .	94
5.3.	Hyperpolarized state . . . . .	95
5.4.	Thermal polarization at high fields . . . . .	95
5.5.	Spin exchange optical pumping . . . . .	96
5.6.	Parahydrogen induced polarization . . . . .	97
5.7.	optical pumping at ESLAC . . . . .	99
5.8.	Hartmann-Hahn condition . . . . .	100
5.9.	NOVEL signal shapes . . . . .	102
5.10.	Spin locking sequence . . . . .	102
5.11.	Doubly rotating frame . . . . .	103
5.12.	NOVEL of $^{13}C$ . . . . .	105
5.13.	KDDxy polarizing sequence . . . . .	106
5.14.	$T_{1\rho}$ measurements . . . . .	108
5.15.	Amplitude sweep measurements . . . . .	108
5.16.	$T_{1\rho}$ as a function of locking field . . . . .	109
5.17.	Model of the near-surface dynamics . . . . .	113
5.18.	Numerical simulations of the detection volume . . . . .	113
5.19.	Dynamics of $NV^-$ cross-relaxation . . . . .	114
5.20.	Polarization decay simulations . . . . .	117
5.21.	Modelling $NV^-$ cross-relaxation to proton spin in fluids . . . . .	118
5.22.	PMMA polarization . . . . .	120
5.23.	NOVEL on PMMA . . . . .	121
5.24.	Polarization of water layer . . . . .	121
5.25.	Power stability of the amplifier . . . . .	123
6.1.	$^{19}F$ NMR with XY16 . . . . .	128
6.2.	Off-resonant $T_{1\rho}$ of $CaF_2$ . . . . .	128

6.3.	NOVEL $^{19}\text{F}$ . . . . .	129
6.4.	Zeeman and Dipolar order of spin diffusion . . . . .	131
6.5.	Polarization enhanced sensing scheme. . . . .	131
6.6.	Spin diffusion . . . . .	132
6.7.	MC simulations for low pumping rate . . . . .	133
6.8.	Measurements with $10^6$ repetitions . . . . .	134
6.9.	$\text{CaF}_2$ patches . . . . .	135
6.10.	Polarization inside a closed volume . . . . .	135
6.11.	Polarization of the detection volume . . . . .	137
6.12.	Sequence to measure the nuclear Rabi oscillations. . . . .	137
6.13.	Correlation spectroscopy of $\text{CaF}_2$ . . . . .	138
6.14.	Lee-Goldburg condition . . . . .	140
6.15.	2 Lee-Goldburg conditions . . . . .	140
6.16.	Effect of the phase shift . . . . .	142
6.17.	Violation of the secular approximation . . . . .	142
6.18.	Proposed detection scheme . . . . .	142

# LIST OF TABLES

2.1. Parameters of the state after 10 X gates . . . . .	51
3.1. Coefficients of translational diffusion measured with FRAP. . .	74
4.1. hBN characteristics . . . . .	81





# DYNAMICAL AND GEOMETRICAL PHASES

We can explicitly calculate dynamical and geometrical phases and show that the former equals to zero. For dynamical phase we get:

$$\hat{H}(t)|\psi_i(t)\rangle = E(t)|\psi_i(t)\rangle \quad (\text{A.1})$$

where  $E(t)$  is the instantaneous eigenvalue for the instantaneous eigenvector  $|\psi_i(t)\rangle$ .

$$\begin{aligned} E_n(t) &= \langle\psi_n(t)|\hat{H}(t)|\psi_n(t)\rangle = \langle n|e^{i\int_0^t \hat{H}(t')dt'} \hat{H}(t) e^{-i\int_0^t \hat{H}(t')dt'} |n\rangle = \\ &= \langle n|\hat{H}(t)|n\rangle = \\ &= \Omega(t)[\omega_1\langle n|e\rangle\langle 1|n\rangle + \omega_0\langle n|e\rangle\langle 0|n\rangle + \omega_1^*\langle n|1\rangle\langle e|n\rangle + \omega_0^*\langle n|0\rangle\langle e|n\rangle] \\ &= 0 \end{aligned} \quad (\text{A.2})$$

for  $n = 0, 1$ . Consequently,

$$e^{i\beta(t)} = e^{-i \int_0^t \hat{H}(t') dt'} = 1 \quad (\text{A.3})$$

And the evolution is purely geometric since  $\langle \psi_k(t) | \hat{H}(t) | \psi_l(t) \rangle = \langle k | \hat{H}(t) | l \rangle = 0$  for  $t = [0, \tau]$ . To get the non-abelian geometric phase one needs to calculate the following operator:

$$\mathcal{A}_{ij}(t) = i \langle \psi_i(t) | \frac{d}{dt} | \psi_j(t) \rangle \quad (\text{A.4})$$

Physically,  $\psi_1(t)$  represents the dark state and  $\psi_2(t)$  describes the Rabi oscillations between the bright and excited states:

$$\psi_1(t) = \hat{U}(t) |d\rangle = |d\rangle \quad (\text{A.5})$$

$$\psi_2(t) = e^{i\theta(t)} \hat{U}(t) |b\rangle = e^{i\theta(t)} [\cos(\theta(t)) |b\rangle - i \sin(\theta(t)) |e\rangle] \quad (\text{A.6})$$

Here  $\int_0^t \Omega(t') dt' = \theta(t)$  and the global phase factor  $e^{i\theta(t)}$  has been inserted to ensure that  $\psi_2(\tau) = \psi_2(0)$ . The only one matrix element which is not equal to zero is:

$$\begin{aligned} \mathcal{A}_{22}(t) &= i \langle \psi_2(t) | \frac{d}{dt} | \psi_2(t) \rangle = \\ &= i e^{-i\theta(t)} [\cos \theta \langle b | + i \sin \theta \langle e |] e^{i\theta(t)} i \theta'(t) (|b\rangle (\cos \theta - \sin \theta) - i |e\rangle (\cos \theta - \sin \theta)) \\ &= -\theta'(t) = -\Omega(t) \quad (\text{A.7}) \end{aligned}$$

Thus,

$$\mathcal{A} = \begin{bmatrix} 0 & 0 \\ 0 & -\Omega(t) \end{bmatrix} \quad (\text{A.8})$$

As a result we get the following holonomy operator:

$$\Gamma = T e^{i \int_0^t \mathcal{A}(t') dt'} \tag{A.9}$$



# CALCULATION OF EVOLUTION OPERATOR IN CASE OF NON-ZERO DETUNING

For the considered  $\hat{X}$  gate  $|1\rangle\langle 1| - |0\rangle\langle 0| = -(|b\rangle\langle d| + |d\rangle\langle b|)$  and we can rewrite the Hamiltonian in the following form:

$$\hat{H}(t) = \Omega(t)(|e\rangle\langle b| + |b\rangle\langle e|) - \delta(|b\rangle\langle d| + |d\rangle\langle b|) \quad (\text{B.1})$$

$$= \hat{H}_0(t) + \lambda V(t) \quad (\text{B.2})$$

$\lambda = 1$  for the full perturbation.

To calculate the evolution operator we use the first-order perturbation theory:

$$\hat{H}_0(t)|n^{(0)}\rangle = E_n^{(0)}|n^{(0)}\rangle \quad (\text{B.3})$$

$$\hat{H}(t)|n\rangle = E_n|n\rangle \quad (\text{B.4})$$

$$|n\rangle = |n^{(0)}\rangle + |n^{(1)}\rangle \quad (\text{B.5})$$

$$|n^{(1)}\rangle = \sum_{k \neq n} \frac{\langle k^{(0)}|V(t)|n^{(0)}\rangle}{E_n^{(0)} - E_k^{(0)}} |k^{(0)}\rangle \quad (\text{B.6})$$

where  $|k^{(0)}\rangle$  is the orthogonal complement of  $|n^{(0)}\rangle$ .

$$E_n = E_n^{(0)} + E_n^{(1)} = E_n^{(0)} + \langle n^{(0)}|V(t)|n^{(0)}\rangle \quad (\text{B.7})$$

$$\hat{U}(t) = \sum_{k=1}^3 e^{-iE_k t} |k\rangle \langle k| \quad (\text{B.8})$$

Instantaneous eigenstates of the unperturbed Hamiltonian are:

$$|1^{(0)}\rangle = |d\rangle \quad |2^{(0)}\rangle = \frac{|b\rangle + |a\rangle}{\sqrt{2}} \quad |3^{(0)}\rangle = \frac{|b\rangle - |a\rangle}{\sqrt{2}} \quad (\text{B.9})$$

$$E_1^{(1)}, E_2^{(1)}, E_3^{(1)} = 0 \quad (\text{B.10})$$

It means that the eigenvalues of  $\hat{H}_0(t)$  and the Hamiltonian with perturbation are equal. For  $|1^{(0)}\rangle$  orthogonal complements are  $|2^{(0)}\rangle$  and  $|3^{(0)}\rangle$ , for  $|2^{(0)}\rangle$  -  $|1^{(0)}\rangle$ ,  $|3^{(0)}\rangle$ , for  $|3^{(0)}\rangle$  -  $|1^{(0)}\rangle$ ,  $|2^{(0)}\rangle$ . The corresponding eigenvalues are  $E_1^{(0)} = 0$ ,  $E_2^{(0)} = \Omega(t)$ ,  $E_3^{(0)} = -\Omega(t)$ .

$$|1^{(1)}\rangle = \frac{\langle 2^{(0)}|V(t)|1^{(0)}\rangle}{E_1^{(0)} - E_2^{(0)}} |2^{(0)}\rangle + \frac{\langle 3^{(0)}|V(t)|1^{(0)}\rangle}{E_1^{(0)} - E_3^{(0)}} |3^{(0)}\rangle = -\frac{\delta}{\Omega} |a\rangle \quad (\text{B.11})$$

$$|2^{(1)}\rangle = \frac{\delta}{\sqrt{2}\Omega} |d\rangle \quad (\text{B.12})$$

$$|3^{(1)}\rangle = -\frac{\delta}{\sqrt{2}\Omega} |d\rangle \quad (\text{B.13})$$

and for the eigenvalues of  $\hat{H}(t)$  we get:

$$|1\rangle = |d\rangle - \frac{\delta}{\Omega}|a\rangle \quad (\text{B.14})$$

$$|2\rangle = \frac{|b\rangle + |a\rangle}{\sqrt{2}} + \frac{\delta}{\sqrt{2}\Omega}|d\rangle \quad (\text{B.15})$$

$$|3\rangle = \frac{|b\rangle - |a\rangle}{\sqrt{2}} - \frac{\delta}{\sqrt{2}\Omega}|d\rangle \quad (\text{B.16})$$

After the calculation of all inner products and taking into account pulse errors, the final evolution operator takes the form:

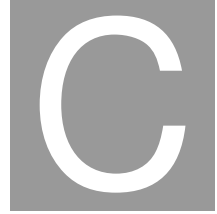
$$\begin{aligned} \hat{U}_{err} = & |d\rangle\langle d| - \gamma[|d\rangle\langle a| + |a\rangle\langle d|] + \gamma^2|a\rangle\langle a| \\ & - [ |b\rangle\langle b| + |a\rangle\langle a| + \gamma(|b\rangle\langle d| + |d\rangle\langle a|) ] \\ & - i\varepsilon[ |b\rangle\langle a| + |a\rangle\langle b| + \gamma(|a\rangle\langle d| + |d\rangle\langle b|) + \gamma^2|d\rangle\langle d| ] \end{aligned} \quad (\text{B.17})$$

If there is only non-zero detuning:

$$\begin{aligned} \hat{U}_{err} = & |d\rangle\langle d| - \gamma[|d\rangle\langle a| + |a\rangle\langle d|] + \gamma^2|a\rangle\langle a| \\ & - [ |b\rangle\langle b| + |a\rangle\langle a| + \gamma(|b\rangle\langle d| + |d\rangle\langle a|) ] \end{aligned} \quad (\text{B.18})$$

where  $\gamma = \delta/\Omega$ .





# MONTE CARLO SIMULATIONS OF POLARIZATION DISTRIBUTION

The  $^{19}\text{F}$  atoms are arranged in a cubic lattice, where  $a$  is the lattice constant. The NV center is placed  $d$  nanometers below the grid. Then, the distance from NV to 4 closest nuclear spins is  $r = \sqrt{d^2 + a^2/2}$ . In the simulations polarization could be transferred to 1 of 16 nearest nuclear spins with equal probability.

The depth was taken to be 5 nanometers. We restricted  $T_1$  time by 1 second. Assuming that the sequence is  $[[\text{laser} = 4.5 \mu\text{s}][\text{pi}/2 = 40 \text{ ns}][\text{spin locking} = 40 \mu\text{s}]] \times M$  (for  $M$  repetitions) for 5 nm deep NV center, there are 44.54  $\mu\text{s}$  for the spin diffusion and 40  $\mu\text{s}$  for the cross-polarization.

The frequency of flip-flops between two adjacent nuclear spins is [68]:

$$\omega = \frac{E_S - E_T}{\hbar} = \frac{\gamma^2 \hbar}{2r^3} (1 - 3 \cos^2 \theta) \quad (\text{C.1})$$

Then the swap time Equation (C.1) is:

$$t_{flip-flop} = \frac{2\pi a^3}{\gamma_{19F}^2 \hbar} \quad (C.2)$$

Which means that  $t_{flip-flop} = 600 \mu s$ . Therefore, the fraction of polarization which one nuclear spin can transfer to another one within one cycle of the sequence is  $p_{nuclear} = 0.23$ .

For the amount of the polarization released from NV center we took the experimental value  $p_{SL} = 0.15$ , which was transferred to one of 20 nearest nuclear spins.

# REFERENCES

- [1] V. S. Roberto Bini, “Materials Under Extreme Conditions: Molecular Crystals at High Pressure,” in. IMPERIAL COLLEGE PRESS, 2014, ch. 4.4.1 Diamonds, p. 102 (cit. on p. 3).
- [2] C. Frondel, U. Marvin, “Lonsdaleite, a Hexagonal Polymorph of Diamond,” *Nature*, vol. 214, pp. 587–589, 1967 (cit. on p. 3).
- [3] R. Mykolajewycz, J. Kalnajs, A. Smakula, “High-Precision Density Determination of Natural Diamonds,” *J. Appl. Phys.*, 1964 (cit. on pp. 3, 6).
- [4] J. Manca, M. Nesladek, M. Neelen, C. Quaeys, L. De Schepper, W. De Ceuninck, “High electrical resistivity of CVD-diamond,” *Microelectron. Reliab.*, vol. 39, pp. 269–273, 1999 (cit. on p. 3).
- [5] M. Geis, “Diamond Transistor Performance and Fabrication,” *Proc. IEEE*, vol. 79, no. 5, pp. 669–676, 1991 (cit. on p. 4).
- [6] C. E. Nebel, “A source of energetic electrons,” *Nat. Mater.*, vol. 12, pp. 780–781, 2013 (cit. on p. 4).
- [7] T. Rendler, J. Neburkova, O. Zemek, J. Kotek, A. Zappe, Z. Chu, P. Cigler, J. Wrachtrup, “Optical imaging of localized chemical events using programmable diamond quantum nanosensors,” *Nat. Commun.*, vol. 8, p. 14701, 2017 (cit. on pp. 4, 61).
- [8] R. Mildren, A. Sabella, “Highly efficient diamond Raman laser,” *Opt. Lett.*, vol. 34, no. 18, pp. 2811–2813, 2009 (cit. on p. 4).
- [9] E. Granados, D. J. Spence, R. P. Mildren, “Deep ultraviolet diamond Raman laser,” *Opt. Express*, vol. 19, no. 11, pp. 10857–63, 2011 (cit. on p. 4).

- [10] P. Latawiec, V. Venkataraman, M. Burek, B. Hausmann, I. Bulu, M. Lončar, “On-chip diamond Raman laser,” *Optica*, vol. 2, no. 11, pp. 924–928, 2015 (cit. on p. 4).
- [11] S. Shirey, P. Cartigny, D. J. Frost, S. Keshav, F. Nestola, P. Nimis, D. G. Pearson, N. V. Sobolev, M. J. Walter, “Diamonds and the Geology of Mantle Carbon,” *Rev. Mineral. Geochem.*, vol. 75, pp. 355–421, 2013 (cit. on p. 4).
- [12] F. Bundy, H. Hall, H. Strong, R. Wentorf Jun., “Man-Made Diamonds,” *Nature*, vol. 176, pp. 51–55, 1955 (cit. on p. 4).
- [13] H. O. Pierson, “Handbook of Carbon, Graphite, Diamonds and Fullerenes: Processing, Properties and Applications,” in: Noyes Publications, 1993, ch. 13. CVD Diamond (cit. on p. 5).
- [14] J. Shigley, C. Breeding, “Optical Defects in Diamond: A Quick Reference Chart,” *Gems and Gemology*, vol. 49, no. 2, pp. 107–111, Summer 2013 (cit. on p. 5).
- [15] T. Schröder, S. Mouradian, J. Zheng, M. Trusheim, M. Walsh, E. Chen, L. Li, I. Bazn, D. Englund, “Quantum nanophotonics in diamond,” *J. Opt. Soc. Am. B*, vol. 33, no. 4, B65–B83, 2016 (cit. on pp. 6, 8, 22).
- [16] R. Robertson, J. Fox, A. Martin, “Two types of diamond,” *Phil. Trans. Roy. Soc. (London) A*, vol. 232, pp. 463–535, 1934 (cit. on p. 6).
- [17] J. Walker, “Optical absorption and luminescence in diamond,” *Rep. Prog. Phys.*, vol. 42, pp. 1605–1659, 1979 (cit. on p. 6).
- [18] F. Jelezko, J. Wrachtrup, “Single defect centres in diamond: A review,” *Phys. Status Solidi*, vol. 203, no. 13, pp. 3207–3225, 2006 (cit. on pp. 7, 8, 11, 13, 15).
- [19] R. Schirhagl, K. Chang, M. Loretz, C. L. Degen, “Nitrogen-Vacancy Centers in Diamond: Nanoscale Sensors for Physics and Biology,” *Annu. Rev. Phys. Chem.*, vol. 65, no. 1, pp. 83–105, 2014 (cit. on p. 7).
- [20] L. G. Hanson, “Is quantum mechanics necessary for understanding magnetic resonance?” *Concepts Magn. Reson. A*, vol. 32, no. 5, pp. 329–340, 2008 (cit. on p. 7).
- [21] M. P. Ledbetter, K. Jensen, R. Fischer, A. Jarmola, D. Budker, “Gyroscopes based on nitrogen-vacancy centers in diamond,” *Phys. Rev. A*, vol. 86, no. 5, pp. 1–5, 2012 (cit. on pp. 7, 40).

- [22] L. Rondin, J.-P. Tetienne, T. Hingant, J.-F. Roch, P. Maletinsky, V. Jacques, “Magnetometry with nitrogen-vacancy defects in diamond,” *Rep. Prog. Phys.*, vol. 77, no. 5, p. 056 503, 2014 (cit. on p. 7).
- [23] D. Rugar, H. J. Mamin, M. Sherwood, M. Kim, C. Rettner, K. Ohno, D. Awschalom, “Proton magnetic resonance imaging with a nitrogen-vacancy spin sensor,” *Nat. Nanotechnol.*, vol. 10, pp. 120–124, 2015 (cit. on pp. 7, 35, 61, 67).
- [24] D. MacLaurin, M. Doherty, L. Hollenberg, A. Martin, “Measurable quantum geometric phase from a rotating single spin,” *Phys. Rev. Lett.*, vol. 108, no. 24, pp. 1–5, 2012 (cit. on pp. 7, 40).
- [25] P. Hemmer, “Toward Molecular-Scale MRI,” *Science*, vol. 529, pp. 529–530, 2013 (cit. on p. 7).
- [26] L. du Preez, “Electron paramagnetic resonance and optical investigations of defect centers in diamond,” PhD thesis, University of the Witwatersrand, 1965 (cit. on p. 7).
- [27] G. Davies, M. Hamer, “Optical studies of the 1.945 eV vibronic band in diamond,” *Proc. R. Soc. Lond. A*, vol. 348, pp. 285–298, 1976 (cit. on p. 7).
- [28] A. Lenef, S. Rand, “Electronic structure of the N-V center in diamond: Theory,” *Phys. Rev. B*, vol. 53, no. 20, pp. 13 441–13 455, 1996 (cit. on pp. 7–11).
- [29] J. Michl, T. Teraji, S. Zaiser, I. Jakobi, G. Waldherr, F. Dolde, P. Neumann, M. W. Doherty, N. B. Manson, J. Isoya, J. Wrachtrup, “Perfect alignment and preferential orientation of nitrogen-vacancy centers during chemical vapor deposition diamond growth on (111) surfaces,” *Appl. Phys. Lett.*, vol. 104, p. 102 407, 2014 (cit. on p. 7).
- [30] P. Deák, B. Aradi, M. Kaviani, T. Frauenheim, A. Gali, “Formation of NV centers in diamond: A theoretical study based on calculated transitions and migration of nitrogen and vacancy related defects,” *Phys. Rev. B*, vol. 89, p. 075 203, 2014 (cit. on pp. 7, 8).
- [31] F. Fávoro de Oliveira, “Forefront engineering of nitrogen-vacancy centers in diamond for quantum technologies,” PhD thesis, University of Stuttgart, 2017 (cit. on p. 8).

- [32] M. V. Hauf, B. Grotz, B. Naydenov, M. Dankerl, S. Pezzagna, J. Meijer, F. Jelezko, J. Wrachtrup, M. Stutzmann, F. Reinhard, J. A. Garrido, “Chemical control of the charge state of nitrogen-vacancy centers in diamond,” *Phys. Rev. B*, vol. 83, 081304(R), 2011 (cit. on pp. 9, 12).
- [33] C. Schreyvogel, V. Polyakov, S. Burk, H. Fedder, A. Denisenko, F. Fávoro de Oliveira, R. Wunderlich, J. Meijer, V. Zuerbig, J. Wrachtrup, C. E. Nebel, “Active and fast charge-state switching of single NV centres in diamond by in-plane Al-Schottky junctions,” *Beilstein J. Nanotechnol.*, vol. 7, pp. 1727–1735, 2016 (cit. on p. 9).
- [34] M. Pfender, “Mitigating the noise of a quantum sensor in single-spin nuclear magnetic resonance,” PhD thesis, University of Stuttgart, 2018 (cit. on p. 9).
- [35] N. Manson, J. Harrison, “Photo-ionization of the nitrogen-vacancy center in diamond,” *Diam. Relat. Mater.*, vol. 14, pp. 1705–1710, 2005 (cit. on pp. 9, 12).
- [36] T. Gaebel, M. Domhan, C. Wittmann, I. Popa, F. Jelezko, J. Rabeau, A. Green-tree, S. Praver, E. Trajtkov, P. Hemmer, J. Wrachtrup, “Photochromism in single nitrogen-vacancy defect in diamond,” *Appl. Phys. B*, vol. 82, no. 2, pp. 243–246, 2006 (cit. on pp. 9, 12).
- [37] N. Manson, J. P. Harrison, M. J. Sellars, “Nitrogen-vacancy center in diamond: Model of the electronic structure and associated dynamics,” *Phys. Rev. B*, vol. 74, p. 104303, 2006 (cit. on p. 10).
- [38] F. M. Hossain, M. W. Doherty, H. F. Wilson, L. C. L. Hollenberg, “Ab Initio Electronic and Optical Properties of the N-V<sup>-</sup> Center in Diamond,” *Phys. Rev. Lett.*, vol. 101, p. 226403, 2008 (cit. on p. 10).
- [39] Y. Ma, M. Rohlfing, A. Gali, “Excited states of the negatively charged nitrogen-vacancy color center in diamond,” *Phys. Rev. B*, vol. 81, p. 041204, 2010 (cit. on p. 10).
- [40] J. Zhang, C. Z. Wang, Z. Z. Zhu, V. V. Dobrovitski, “Vibrational modes and lattice distortion of a nitrogen-vacancy center in diamond from first-principles calculations,” *Phys. Rev. B*, vol. 84, no. 3, pp. 1–12, 2011 (cit. on p. 10).
- [41] J. R. Maze, A. Gali, E. Togan, Y. Chu, A. Trifonov, E. Kaxiras, M. D. Lukin, “Properties of nitrogen-vacancy centers in diamond: The group theoretic approach,” *New J. Phys.*, vol. 13, 2011 (cit. on p. 10).

- [42] L. J. Rogers, R. L. McMurtrie, M. J. Sellars, N. B. Manson, "Time-averaging within the excited state of the nitrogen-vacancy centre in diamond," *New J. Phys.*, vol. 11, 2009 (cit. on p. 10).
- [43] M. Doherty, F. Dolde, H. Fedder, F. Jelezko, J. Wrachtrup, N. Manson, L. Hollenberg, "Theory of the ground-state spin of the NV<sup>-</sup> center in diamond," *Phys. Rev. B*, vol. 85, p. 205 203, 2012 (cit. on pp. 10, 12, 13, 18).
- [44] M. L. Goldman, M. W. Doherty, A. Sipahigil, N. Y. Yao, S. D. Bennett, N. B. Manson, A. Kubanek, M. D. Lukin, "State-selective intersystem crossing in nitrogen-vacancy centers," *Phys. Rev. B*, vol. 91, p. 165 201, 2015 (cit. on pp. 10, 12).
- [45] G. Waldherr, J. Beck, M. Steiner, P. Neumann, A. Gali, T. Frauenheim, F. Jelezko, J. Wrachtrup, "Dark States of Single Nitrogen-Vacancy Centers in Diamond Unraveled by Single Shot NMR," *Phys. Rev. Lett.*, vol. 106, p. 157 601, 2011 (cit. on p. 12).
- [46] X. Chen, C. Zou, Z. Gong, C. Dong, G. Guo, F. Sun, "Subdiffraction optical manipulation of the charge state of nitrogen vacancy center in diamond," *Light Sci. Appl.*, vol. 4, e230, 2015 (cit. on p. 12).
- [47] S. Cui, E. L. Hu, "Increased negatively charged nitrogen-vacancy centers in fluorinated diamond," *Appl. Phys. Lett.*, vol. 103, no. 5, 2013 (cit. on pp. 12, 79).
- [48] C. I. Pakes, J. A. Garrido, H. Kawarada, "Diamond surface conductivity: Properties, devices, and sensors," *MRS Bulletin*, vol. 39, no. 06, pp. 542–548, 2014 (cit. on p. 12).
- [49] F. Fávoro de Oliveira, S. A. Momenzadeh, Y. Wang, M. Konuma, M. Markham, A. M. Edmonds, A. Denisenko, J. Wrachtrup, "Effect of low-damage inductively coupled plasma on shallow nitrogen-vacancy centers in diamond," *Appl. Phys. Lett.*, vol. 107, no. 7, p. 073 107, 2015 (cit. on pp. 12, 122).
- [50] S. Karaveli, O. Gaathon, A. Wolcott, R. Sakakibara, D. Peterka, J. S. Owen, R. Yuste, D. R. Englund, "Electrochemical potential control of charge state and fluorescence of nitrogen vacancy centers in nanodiamonds," *PNAS*, vol. 113, no. 15, pp. 3938–3943, 2016 (cit. on p. 12).
- [51] L. Robledo, H. Bernien, T. van der Sar, R. Hanson, "Spin dynamics in the optical cycle of single nitrogen-vacancy centres in diamond," *New J. Phys.*, vol. 13, p. 025 013, 2011 (cit. on p. 12).

- [52] J.-P. Tetienne, L. Rondin, P. Spinicelli, M. Chipaux, T. Debuisschert, J.-F. Roch, V. Jacques, “Magnetic-field-dependent photodynamics of single NV defects in diamond: an application to qualitative all-optical magnetic imaging,” *New J. Phys.*, vol. 14, p. 103 033, 2012 (cit. on p. 12).
- [53] M. L. Goldman, A. Sipahigil, M. W. Doherty, N. Y. Yao, S. D. Bennett, M. Markham, D. J. Twitchen, N. B. Manson, A. Kubanek, M. D. Lukin, “Phonon-Induced Population Dynamics and Intersystem Crossing in Nitrogen-Vacancy Centers,” *Phys. Rev. Lett.*, vol. 114, p. 145 502, 2015 (cit. on p. 12).
- [54] J. Harrison, M. Sellars, N. Manson, “Optical spin polarisation of the N-V centre in diamond,” *J. Lumin.*, vol. 107, pp. 245–248, 2004 (cit. on p. 13).
- [55] D. Pagliero, A. Laraoui, J. Henshaw, C. Meriles, “Recursive polarization of nuclear spins in diamond at arbitrary magnetic fields,” *Appl. Phys. Lett.*, vol. 105, p. 242 402, 2014 (cit. on p. 13).
- [56] M. Steiner, P. Neumann, J. Beck, F. Jelezko, J. Wrachtrup, “Universal enhancement of the optical readout fidelity of single electron spins at nitrogen-vacancy centers in diamond,” *Phys. Rev. B*, vol. 81, p. 035 205, 2010 (cit. on pp. 13, 22).
- [57] D. Hopper, H. Shulevitz, L. Bassett, “Spin Readout Techniques of the Nitrogen-Vacancy Center in Diamond,” *Micromachines*, vol. 9, p. 437, 2018 (cit. on p. 13).
- [58] M. S. Grinolds, P. Maletinsky, S. Hong, M. D. Lukin, R. L. Walsworth, A. Yacoby, “Quantum control of proximal spins using nanoscale magnetic resonance imaging,” *Nat. Phys.*, vol. 7, no. 9, pp. 687–692, 2011 (cit. on p. 13).
- [59] F. Dolde, “The nitrogen vacancy center in internal and external fields,” PhD thesis, University of Stuttgart, 2014 (cit. on p. 13).
- [60] D. R. Glenn, K. Lee, H. Park, R. Weissleder, A. Yacoby, M. D. Lukin, H. Lee, R. L. Walsworth, C. B. Connolly, “Single-cell magnetic imaging using a quantum diamond microscope,” *Nat. Methods*, vol. 12, no. May, pp. 1–5, 2015 (cit. on pp. 13, 61).
- [61] A. T. Collins, M. F. Thomaz, M. I. B. Jorge, “Luminescence decay time of the 1.945 eV centre in type Ib diamond,” *J. Phys. Condens. Matter*, vol. 16, no. 11, pp. 2177–2181, 1983 (cit. on p. 13).

- [62] M. W. Doherty, N. B. Manson, P. Delaney, F. Jelezko, J. Wrachtrup, L. C. L. Hollenberg, “The nitrogen-vacancy colour centre in diamond,” *Phys. Rep.*, vol. 528, no. 1, pp. 1–45, 2013 (cit. on pp. 13, 17, 18).
- [63] J. Loubser, J. van Wyk, “Electron spin resonance in the study of diamond,” *Rep. Prog. Phys.*, vol. 41, p. 1201, 1978 (cit. on p. 14).
- [64] P. Neumann, “Towards a room temperature solid state quantum processor — The nitrogen-vacancy center in diamond,” PhD thesis, University of Stuttgart, 2011 (cit. on pp. 15, 18).
- [65] H. Clevenson, M. Trusheim, C. Teale, T. Schröder, D. Braje, D. Englund, “Broadband magnetometry and temperature sensing with a light-trapping diamond waveguide,” *Nat. Phys.*, vol. 11, pp. 393–397, 2015 (cit. on pp. 15, 23).
- [66] G. Kucsko, P. Maurer, N. Yao, M. Kubo, H. Noh, P. Lo, H. Park, M. Lukin, “Nanometre-scale thermometry in a living cell.,” *Nature*, vol. 500, no. 7460, pp. 54–58, 2013 (cit. on pp. 15, 61).
- [67] C. P. Slichter, *Principles of Magnetic Resonance*, Third Enlarged and Updated Edition, M. Cardona, P. Fulde, K. von Klitzing, H.-J. Queisser, Eds., ser. Springer Series in Solid-State Sciences 1. Springer-Verlag Berlin Heidelberg New York, 1989 (cit. on pp. 15, 16, 25, 30, 82).
- [68] A. Abragam, *The Principles of Nuclear Magnetism*. Oxford: Clarendon Press, 1961 (cit. on pp. 15, 16, 130, 159).
- [69] X.-F. He, N. Manson, P. Fisk, “Paramagnetic resonance of photoexcited N-V defects in diamond. II. Hyperfine interaction with the  $N^{14}$  nucleus,” *Phys. Rev. B*, vol. 47, no. 14, pp. 8816–8822, 1993 (cit. on p. 16).
- [70] S. Sangtawesin, C. McLellan, B. Myers, A. Bleszynski Jayich, D. Awschalom, J. Petta, “Hyperfine-enhanced gyromagnetic ratio of a nuclear spin in diamond,” *New J. Phys.*, vol. 18, p. 083 016, 2016 (cit. on pp. 16, 17).
- [71] B. Smeltzer, L. Childress, A. Gali, “ $^{13}\text{C}$  Hyperfine interactions in the nitrogen-vacancy centre in diamond,” *New J. Phys.*, vol. 13, 2011 (cit. on p. 16).
- [72] A. Dréau, J. Maze, M. Lesik, J. Roch, V. Jacques, “High-resolution spectroscopy of single NV defects coupled with nearby  $^{13}\text{C}$  nuclear spins in diamond,” *Phys. Rev. B*, vol. 85, no. 13, pp. 1–7, 2012 (cit. on p. 16).

- [73] J. A. S. Smith, “Nuclear Quadrupole Resonance Spectroscopy,” *Journal of Chemical Education*, vol. 48, no. 1, pp. 39–48, 1971 (cit. on pp. 16, 82).
- [74] C. Shin, M. Butler, H.-J. Wang, C. Avalos, S. Seltzer, R.-B. Liu, A. Pines, V. Bajaj, “Optically detected nuclear quadrupolar interaction of  $^{14}\text{N}$  in nitrogen-vacancy centers in diamond,” *Phys. Rev. B*, vol. 89, p. 205 202, 2014 (cit. on p. 17).
- [75] P. Udvarhelyi, V. Shkolnikov, A. Gali, G. Burkard, A. Pályi, “Spin-strain interaction in nitrogen-vacancy centers in diamond,” *Phys. Rev. B*, vol. 98, p. 075 201, 2018 (cit. on p. 17).
- [76] J. Cai, F. Jelezko, M. Plenio, “Hybrid sensors based on colour centres in diamond and piezoactive layers,” *Nat. Commun.*, vol. 5, p. 4065, 2014 (cit. on p. 18).
- [77] P. Ovartchaiyapong, K. Lee, B. Myers, A. Bleszynski Jayich, “Dynamic strain-mediated coupling of a single diamond spin to a mechanical resonator,” *Nat. Commun.*, vol. 5, p. 4429, 2014 (cit. on p. 18).
- [78] M. Minsky, “Memoir on Inventing the Confocal Scanning Microscope,” *Scanning*, vol. 10, pp. 128–138, 1988 (cit. on p. 18).
- [79] S. Momenzadeh, R. J. Stöhr, F. Favaro de Oliveira, A. Brunner, A. Denisenko, S. Yang, F. Reinhard, J. Wrachtrup, “Nanoengineered diamond waveguide as a robust bright platform for nanomagnetometry using shallow nitrogen vacancy centers,” *Nano Lett.*, vol. 15, no. 1, pp. 165–169, 2015 (cit. on pp. 21, 66).
- [80] M. Fox, *Quantum Optics an Introduction*, ser. Oxford Master series in atomic, optical and laser physics. Oxford University Press, 2006 (cit. on p. 22).
- [81] L. Jiang, J. S. Hodges, J. R. Maze, P. Maurer, J. M. Taylor, D. G. Cory, P. R. Hemmer, R. L. Walsworth, A. Yacoby, A. S. Zibrov, M. D. Lukin, “Repetitive Readout of a Single Electronic Spin via Quantum Logic with Nuclear Spin Ancillae,” *Science*, vol. 326, no. 5950, pp. 267–272, 2009 (cit. on p. 22).
- [82] P. Neumann, J. Beck, M. Steiner, F. Rempp, H. Fedder, P. R. Hemmer, J. Wrachtrup, F. Jelezko, “Single-shot readout of a single nuclear spin,” *Science*, vol. 329, no. 5991, pp. 542–544, 2010 (cit. on pp. 22, 62, 141).
- [83] J. Davies, “Optically-detected magnetic resonance and its applications,” *Contemp. Phys.*, vol. 17, no. 3, pp. 275–294, 1976 (cit. on p. 22).

- [84] J. Wrachtrup, C. von Borczyskowski, J. Bernard, M. Orrit, R. Brown, "Optical-Detection of Magnetic-Resonance in a Single Molecule," *Nature*, vol. 363, no. 6426, pp. 244–245, 1993 (cit. on p. 22).
- [85] E. van Oort, N. Manson, M. Glasbeek, "Optically Detected Spin Coherence of the Diamond N-V Center in Its Triplet Ground-State," *J. Phys. Condens. Matter*, vol. 21, no. 23, pp. 4385–4391, 1988 (cit. on p. 22).
- [86] A. Gruber, A. Dräbenstedt, C. Tietz, L. Fleury, J. Wrachtrup, C. von Borczyskowski, "Scanning Confocal Optical Microscopy and Magnetic Resonance on Single Defect Centers," *Science*, vol. 276, no. 5321, pp. 2012–2014, 1997 (cit. on p. 22).
- [87] P. Kehayias, M. Mrózek, V. Acosta, A. Jarmola, D. Rudnicki, R. Folman, W. Gawlik, D. Budker, "Microwave saturation spectroscopy of nitrogen-vacancy ensembles in diamond," *Phys. Rev. B*, vol. 89, no. 24, pp. 1–8, 2014 (cit. on p. 23).
- [88] R. R. Fu, B. P. Weiss, E. A. Lima, R. J. Harrison, X.-N. Bai, S. J. Desch, D. S. Ebel, C. Suavet, H. Wang, D. Glenn, D. Le Sage, T. Kasama, R. L. Walsworth, A. T. Kuan, "Paleomagnetism. Solar nebula magnetic fields recorded in the Semarkona meteorite.," *Science*, vol. 346, no. 6213, pp. 1089–92, 2014 (cit. on p. 23).
- [89] M. Chipaux, A. Tallaire, J. Achard, S. Pezzagna, J. Meijer, V. Jacques, J. F. Roch, T. Debuisschert, "Magnetic imaging with an ensemble of Nitrogen Vacancy centers in diamond," *Eur. Phys. J. D*, vol. 69, p. 166, 2015 (cit. on p. 23).
- [90] S. Hong, M. S. Grinolds, L. M. Pham, D. Le Sage, L. Luan, R. L. Walsworth, A. Yacoby, "Nanoscale magnetometry with NV centers in diamond," *MRS Bulletin*, vol. 38, no. 02, pp. 155–161, 2013 (cit. on p. 23).
- [91] T. Wolf, P. Neumann, K. Nakamura, H. Sumiya, T. Ohshima, J. Isoya, J. Wrachtrup, "Subpicotesla diamond magnetometry," *Phys. Rev. X*, vol. 5, no. 4, pp. 1–10, 2015 (cit. on p. 23).
- [92] P. London, P. Balasubramanian, B. Naydenov, L. P. McGuinness, F. Jelezko, "Strong driving of a single spin using arbitrarily polarized fields," *Phys. Rev. A*, vol. 90, no. 1, pp. 1–9, 2014 (cit. on p. 24).

- [93] T. Taminiau, J. Cramer, T. van der Sar, V. Dobrovitski, R. Hanson, “Universal control and error correction in multi-qubit spin registers in diamond,” *Nat. Nanotechnol.*, vol. 9, no. 3, pp. 171–6, 2014 (cit. on pp. 27, 105).
- [94] A. Jarmola, V. Acosta, K. Jensen, S. Chemerisov, D. Budker, “Temperature- and magnetic-field-dependent longitudinal spin relaxation in nitrogen-vacancy ensembles in diamond,” *Phys. Rev. Lett.*, vol. 108, no. 19, pp. 1–5, 2012 (cit. on p. 28).
- [95] A. O. Sushkov, N. Chisholm, I. Lovchinsky, M. Kubo, P. K. Lo, S. D. Bennett, D. Hunger, A. Akimov, R. L. Walsworth, H. Park, M. D. Lukin, “All-Optical Sensing of a Single-Molecule Electron Spin,” *Nano Lett.*, vol. 14, no. 11, pp. 6443–6448, 2014 (cit. on p. 29).
- [96] N. Bar-Gill, L. Pham, A. Jarmola, D. Budker, R. Walsworth, “Solid-state electronic spin coherence time approaching one second.,” *Nat Commun*, vol. 4, p. 1743, 2013 (cit. on pp. 29, 35).
- [97] T. Rosskopf, A. Dussaux, K. Ohashi, M. Loretz, R. Schirhagl, H. Watanabe, S. Shikata, K. M. Itoh, C. L. Degen, “Investigation of surface magnetic noise by shallow spins in diamond,” *Phys. Rev. Lett.*, vol. 112, no. 14, pp. 1–5, 2014 (cit. on pp. 29, 35).
- [98] E. Hahn, “Spin echoes,” *Phys. Rev.*, vol. 80, no. 4, pp. 580–594, 1950 (cit. on p. 29).
- [99] P. Jamonneau, M. Lesik, J. Tetienne, I. Alvizu, L. Mayer, A. Dréau, S. Kosen, J.-F. Roch, S. Pezzagna, J. Meijer, T. Teraji, Y. Kubo, P. Bertet, J. Maze, V. Jacques, “Competition between electric field and magnetic field noise in the decoherence of a single spin in diamond,” *Phys. Rev. B*, vol. 93, p. 024305, 2016 (cit. on p. 30).
- [100] M. Zdanowska-Frączek, W. Medycki, “ $^{35}\text{Cl}$  nqr and  $^{19}\text{F}$  nmr relaxation studies of  $\text{CClF}_2$  group dynamics in  $\text{N}(\text{CH}_3)_4\text{H}(\text{ClF}_2\text{CCOO})_2$ ,” *Solid State Nucl. Magn. Reson.*, vol. 6, pp. 141–146, 1996 (cit. on p. 30).
- [101] S. Meiboom, D. Gill, “Modified Spin-Echo Method for Measuring Nuclear Relaxation Times,” *Rev. Sci. Instrum.*, vol. 29, no. 8, pp. 688–691, 1958 (cit. on pp. 30, 32).

- [102] J. M. Taylor, P. Cappellaro, L. Childress, L. Jiang, D. Budker, P. R. Hemmer, A. Yacoby, R. Walsworth, M. D. Lukin, “High-sensitivity diamond magnetometer with nanoscale resolution,” *Nat. Phys.*, vol. 4, no. 10, pp. 810–816, 2008 (cit. on pp. 31, 32).
- [103] L. Hall, J. Cole, C. Hill, L. Hollenberg, “Sensing of Fluctuating Nanoscale Magnetic Fields Using Nitrogen-Vacancy Centers in Diamond,” *Phys. Rev. Lett.*, vol. 103, no. 22, pp. 1–4, 2009 (cit. on p. 31).
- [104] C. Degen, M. Poggio, H. Mamin, D. Rugar, “Role of Spin Noise in the Detection of Nanoscale Ensembles of Nuclear Spins,” *Phys. Rev. Lett.*, vol. 99, p. 250 601, 2007 (cit. on p. 31).
- [105] T. Staudacher, “Nuclear magnetic resonance spectroscopy on a (5-nanometre)<sup>3</sup> sample volume,” PhD thesis, University of Stuttgart, 2013 (cit. on pp. 31, 105).
- [106] A. Laraoui, J. S. Hodges, C. A. Ryan, C. A. Meriles, “Diamond nitrogen-vacancy center as a probe of random fluctuations in a nuclear spin ensemble,” *Phys. Rev. B*, vol. 84, no. 10, 2011 (cit. on pp. 31, 38).
- [107] L. Viola, E. Knill, S. Lloyd, “Dynamical Decoupling of Open Quantum Systems,” *Phys. Rev. Lett.*, vol. 82, no. 12, pp. 2417–2421, 1999 (cit. on p. 31).
- [108] Ł. Cywiński, R. Lutchyn, C. Nave, S. Das Sarma, “How to enhance dephasing time in superconducting qubits,” *Phys. Rev. B*, vol. 77, no. 17, p. 174 509, 2008 (cit. on pp. 31, 32, 34).
- [109] T. Yuge, S. Sasaki, Y. Hirayama, “Measurement of the noise spectrum using a multiple-pulse sequence,” *Phys. Rev. Lett.*, vol. 107, no. 17, pp. 1–4, 2011 (cit. on pp. 31, 32, 34).
- [110] C. A. Meriles, L. Jiang, G. Goldstein, J. S. Hodges, J. Maze, M. D. Lukin, P. Cappellaro, “Imaging mesoscopic nuclear spin noise with a diamond magnetometer,” *J. Chem. Phys.*, vol. 133, no. 12, pp. 1–8, 2010 (cit. on pp. 32, 112).
- [111] B. Naydenov, F. Dolde, L. Hall, C. Shin, H. Fedder, L. Hollenberg, F. Jelezko, J. Wrachtrup, “Dynamical Decoupling of a single electron spin at room temperature,” *Phys. Rev. B*, vol. 83, 081201(R), 2011 (cit. on p. 32).

- [112] A. M. Souza, G. A. Álvarez, D. Suter, “Robust dynamical decoupling for quantum computing and quantum memory,” *Phys. Rev. Lett.*, vol. 106, p. 240 501, 2011 (cit. on p. 32).
- [113] A. Souza, G. Álvarez, D. Suter, “Effects of time-reversal symmetry in dynamical decoupling,” *Phys. Rev. A*, vol. 85, no. 3, p. 032 306, 2012 (cit. on p. 32).
- [114] Z.-H. Wang, G. de Lange, D. Risté, R. Hanson, V. V. Dobrovitski, “Comparison of dynamical decoupling protocols for a nitrogen-vacancy center in diamond,” *Phys. Rev. B*, vol. 85, no. Cdd, p. 155 204, 2012 (cit. on p. 32).
- [115] M. Ali Ahmed, G. Álvarez, D. Suter, “Robustness of dynamical decoupling sequences,” *Phys. Rev. A*, vol. 87, no. 4, pp. 3–8, 2013 (cit. on p. 32).
- [116] H. J. Mamin, M. Kim, M. Sherwood, C. Rettner, K. Ohno, D. Awschalom, D. Rugar, “Nanoscale nuclear magnetic resonance with a nitrogen-vacancy spin sensor,” *Science*, vol. 339, no. 6119, pp. 557–560, 2013 (cit. on pp. 32, 37, 112).
- [117] A. Maudsley, “Modified Carr-Purcell-Meiboom-Gill sequence for NMR fourier imaging applications,” *J. Magn. Reson.*, vol. 69, no. 3, pp. 488–491, 1986 (cit. on p. 32).
- [118] C. Ryan, J. Hodges, D. Cory, “Robust decoupling techniques to extend quantum coherence in diamond,” *Phys. Rev. Lett.*, vol. 105, no. 20, pp. 1–4, 2010 (cit. on pp. 32, 35).
- [119] M. Hirose, C. Aiello, P. Cappellaro, “Continuous dynamical decoupling magnetometry,” *Phys. Rev. A*, vol. 86, no. 6, pp. 1–5, 2012 (cit. on p. 32).
- [120] J. Medford, L. Cywiński, C. Barthel, C. M. Marcus, M. P. Hanson, A. C. Gossard, “Scaling of Dynamical Decoupling for Spin Qubits,” *Phys. Rev. Lett.*, vol. 108, no. 8, p. 086 802, 2012 (cit. on pp. 34, 35).
- [121] N. Bar-Gill, L. Pham, C. Belthangady, D. Le Sage, P. Cappellaro, J. Maze, M. Lukin, A. Yacoby, R. Walsworth, “Suppression of spin-bath dynamics for improved coherence of multi-spin-qubit systems,” *Nat. Commun.*, vol. 3, p. 858, 2012 (cit. on p. 35).

- [122] Y. Romach, C. Müller, T. Unden, L. Rogers, T. Isoda, K. Itoh, M. Markham, A. Stacey, J. Meijer, S. Pezzagna, B. Naydenov, L. McGuinness, N. Bar-Gill, F. Jelezko, “Spectroscopy of surface-induced noise using shallow spins in diamond,” *Phys. Rev. Lett.*, vol. 114, p. 017601, 2015 (cit. on p. 35).
- [123] W. Rose, H. Haas, A. Q. Chen, N. Jeon, L. J. Lauhon, D. G. Cory, R. Budakian, “High-Resolution Nanoscale Solid-State Nuclear Magnetic Resonance Spectroscopy,” *Phys. Rev. X*, vol. 8, p. 011030, 2018 (cit. on p. 35).
- [124] T. H. Taminiau, J. J. T. Wagenaar, T. van der Sar, F. Jelezko, V. V. Dobrovitski, R. Hanson, “Detection and Control of Individual Nuclear Spins Using a Weakly Coupled Electron Spin,” *Phys. Rev. Lett.*, vol. 109, no. 13, p. 137602, 2012 (cit. on p. 35).
- [125] N. Zhao, J. Honert, B. Schmid, M. Klas, J. Isoya, M. Markham, D. Twitchen, F. Jelezko, R.-B. Liu, H. Fedder, J. Wrachtrup, “Sensing single remote nuclear spins,” *Nat. Nanotechnol.*, vol. 7, no. 10, pp. 657–662, 2012 (cit. on p. 35).
- [126] F. Shi, X. Kong, P. Wang, F. Kong, N. Zhao, R.-B. Liu, J. Du, “Sensing and atomic-scale structure analysis of single nuclear-spin clusters in diamond,” *Nat. Phys.*, vol. 10, no. 1, pp. 21–25, 2013 (cit. on p. 35).
- [127] T. Staudacher, F. Shi, S. Pezzagna, J. Meijer, J. Du, C. A. Meriles, F. Reinhard, J. Wrachtrup, “Nuclear Magnetic Resonance Spectroscopy on a (5-Nanometer)<sup>3</sup> Sample Volume,” *Science*, vol. 339, no. 6119, pp. 561–563, 2013 (cit. on pp. 35, 37, 61).
- [128] M. Loretz, S. Pezzagna, J. Meijer, C. L. Degen, “Nanoscale nuclear magnetic resonance with a 1.9-nm-deep nitrogen-vacancy sensor,” *Appl. Phys. Lett.*, vol. 104, no. 3, pp. 1–5, 2014 (cit. on pp. 35, 37, 61).
- [129] I. Lovchinsky, A. Sushkov, E. Urbach, N. de Leon, S. Choi, K. De Greve, R. Evans, R. Gertner, E. Bersin, C. Müller, L. McGuinness, F. Jelezko, R. Walsworth, H. Park, M. Lukin, “Nuclear magnetic resonance detection and spectroscopy of single proteins using quantum logic,” *Science*, 2016 (cit. on p. 35).
- [130] S. DeVience, L. Pham, I. Lovchinsky, A. Sushkov, N. Bar-Gill, C. Belthangady, F. Casola, M. Corbett, H. Zhang, M. Lukin, H. Park, A. Yacoby, R. Walsworth, “Nanoscale nmr spectroscopy and imaging of multiple nuclear species,” *Nat. Nanotechnol.*, vol. 10, pp. 129–134, 2015 (cit. on pp. 36, 61).

- [131] C. Müller, X. Kong, J.-M. Cai, K. Melentijević, A. Stacey, M. Markham, D. Twitchen, J. Isoya, S. Pezzagna, J. Meijer, J. F. Du, M. B. Plenio, B. Naydenov, L. P. McGuinness, F. Jelezko, “Nuclear magnetic resonance spectroscopy with single spin sensitivity,” *Nat. Commun.*, vol. 5, p. 4703, 2014 (cit. on pp. 36, 61).
- [132] F. Shi, Q. Zhang, P. Wang, H. Sun, J. Wang, X. Rong, M. Chen, C. Ju, F. Reinhard, H. Chen, J. Wrachtrup, J. Wang, J. Du, “Single-protein spin resonance spectroscopy under ambient conditions,” *Science*, vol. 347, no. 6226, pp. 1135–1138, 2015 (cit. on pp. 36, 61).
- [133] I. Lovchinsky, J. D. Sanchez-Yamagishi, E. Urbach, S. Choi, S. Fang, T. Andersen, K. Watanabe, T. Taniguchi, A. Bylinskii, E. Kaxiras, P. Kim, H. Park, M. D. Lukin, “Nanoscale magnetic resonance spectroscopy of an atomically thin material using a single spin qubit,” *Science*, vol. 2538, 2016 (cit. on pp. 36, 61, 84, 86).
- [134] M. Loretz, J. Boss, T. Roskopf, H. Mamin, D. Rugar, C. Degen, “Spurious Harmonic Response of Multipulse Quantum Sensing Sequences,” *Phys. Rev. X*, vol. 5, no. 2, p. 021 009, 2015 (cit. on pp. 36, 88).
- [135] J. M. Boss, K. Chang, J. Armijo, K. Cujia, T. Roskopf, J. R. Maze, C. L. Degen, “One- and Two-Dimensional Nuclear Magnetic Resonance Spectroscopy with a Diamond Quantum Sensor,” *Phys. Rev. Lett.*, vol. 116, p. 197 601, 2016 (cit. on p. 36).
- [136] D. Farfurnik, A. Jarmola, L. M. Pham, Z. H. Wang, V. V. Dobrovitski, R. L. Walsworth, D. Budker, N. Bar-Gill, “Optimizing a dynamical decoupling protocol for solid-state electronic spin ensembles in diamond,” *Phys. Rev. B*, vol. 92, no. 6, p. 060 301, 2015 (cit. on p. 36).
- [137] F. Ziem, M. Garsi, H. Fedder, J. Wrachtrup, “Quantitative nanoscale MRI with a wide field of view,” (cit. on pp. 36, 61, 127).
- [138] L. Trifunovic, F. L. Pedrocchi, S. Hoffman, P. Maletinsky, A. Yacoby, D. Loss, “High-efficiency resonant amplification of weak magnetic fields for single spin magnetometry at room temperature,” *Nat. Nanotechnol.*, vol. 10, no. May, pp. 541–546, 2015 (cit. on p. 36).
- [139] I. Schwartz, J. Roskopf, S. Schmitt, B. Tratzmiller, Q. Chen, L. P. McGuinness, F. Jelezko, M. B. Plenio, “Blueprint for nanoscale NMR,” *Sci. Rep.*, vol. 9, no. 6938, pp. 1–11, 2019 (cit. on p. 36).

- [140] D. Glenn, D. Bucher, J. Lee, M. Lukin, H. Park, R. Walsworth, “High-resolution magnetic resonance spectroscopy using a solid-state spin sensor,” *Nature*, vol. 555, pp. 351–354, 2018 (cit. on p. 36).
- [141] N. Aslam, M. Pfender, P. Neumann, R. Reuter, A. Zappe, F. Fávoro de Oliveira, A. Denisenko, H. Sumiya, S. Onoda, J. Isoya, J. Wrachtrup, “Nanoscale nuclear magnetic resonance with chemical resolution,” *Science (New York, N.Y.)*, vol. 357, no. 6346, pp. 67–71, 2017 (cit. on pp. 36, 61, 75, 98, 113, 141, 143).
- [142] S. Steinert, F. Ziem, L. T. Hall, A. Zappe, M. Schweikert, N. Götz, A. Aird, G. Balasubramanian, L. Hollenberg, J. Wrachtrup, “Magnetic spin imaging under ambient conditions with sub-cellular resolution,” *Nat. Commun.*, vol. 4, p. 1607, 2013 (cit. on p. 37).
- [143] A. Haussler, P. Heller, L. McGuinness, B. Naydenov, F. Jelezko, “Optical depth localization of nitrogen-vacancy centers in diamond with nanometer accuracy,” *Opt. Express*, vol. 22, no. 24, p. 29 986, 2014 (cit. on p. 37).
- [144] L. M. Pham, S. J. DeVience, F. Casola, I. Lovchinsky, A. O. Sushkov, E. Bersin, J. Lee, E. Urbach, P. Cappellaro, H. Park, A. Yacoby, M. D. Lukin, R. L. Walsworth, “NMR Technique for Determining the Depth of Shallow Nitrogen-Vacancy Centers in Diamond,” vol. 045425, pp. 1–14, 2015 (cit. on p. 37).
- [145] A. Laraoui, F. Dolde, C. Burk, F. Reinhard, J. Wrachtrup, C. Meriles, “High-resolution correlation spectroscopy of  $^{13}\text{C}$  spins near a nitrogen-vacancy centre in diamond,” *Nat. Commun.*, vol. 4, p. 1651, 2013 (cit. on pp. 38, 68).
- [146] T. Staudacher, N. Raatz, S. Pezzagna, J. Meijer, F. Reinhard, C. A. Meriles, J. Wrachtrup, “Probing molecular dynamics at the nanoscale via an individual paramagnetic centre,” *Nat. Commun.*, vol. 6, p. 8527, 2015 (cit. on pp. 38, 60, 62, 68, 113, 116).
- [147] G. Feng, G. Xu, G. Long, “Experimental realization of nonadiabatic holonomic quantum computation,” *Phys. Rev. Lett.*, vol. 110, no. 19, pp. 1–5, 2013 (cit. on p. 40).
- [148] A. Abdumalikov Jr, J. Fink, K. Juliusson, M. Pechal, S. Berger, A. Wallraff, S. Filipp, “Experimental realization of non-Abelian non-adiabatic geometric gates,” *Nature*, vol. 496, no. 7446, pp. 482–5, 2013 (cit. on pp. 40, 42, 43).

- [149] Z.-Y. Xue, J. Zhou, Z. D. Wang, “Universal holonomic quantum gates in decoherence-free subspace on superconducting circuits,” *Phys. Rev. A*, vol. 92, p. 022320, 2015 (cit. on p. 40).
- [150] J. C. Loredó, M. A. Broome, D. H. Smith, A. G. White, “Observation of Entanglement-Dependent Two-Particle Holonomic Phase,” *Phys. Rev. Lett.*, vol. 112, no. 14, p. 143603, 2014 (cit. on p. 40).
- [151] S. Arroyo-Camejo, A. Lazareiev, S. W. Hell, G. Balasubramanian, “Room temperature high-fidelity holonomic single-qubit gate on a solid-state spin,” *Nat. Commun.*, vol. 5, p. 4870, 2014 (cit. on pp. 40, 43, 45).
- [152] C. Zu, W. Wang, L. He, W. Zhang, C. Dai, F. Wang, L. Duan, “Experimental realization of universal geometric quantum gates with solid-state spins,” *Nature*, vol. 514, no. 7520, pp. 72–75, 2014 (cit. on p. 40).
- [153] B. B. Zhou, P. C. Jerger, V. O. Shkolnikov, F. J. Heremans, G. Burkard, D. D. Awschalom, “Holonomic Quantum Control by Coherent Optical Excitation in Diamond,” *Phys. Rev. Lett.*, vol. 119, no. 14, pp. 1–6, 2017 (cit. on pp. 40, 44, 45).
- [154] Y. Sekiguchi, N. Niikura, R. Kuroiwa, H. Kano, H. Kosaka, “Optical holonomic single quantum gates with a geometric spin under a zero field,” *Nat. Photonics*, vol. 11, no. 5, pp. 209–214, 2017 (cit. on pp. 40, 44, 45).
- [155] K. Nagata, K. Kuramitani, Y. Sekiguchi, H. Kosaka, “Universal holonomic quantum gates over geometric spin qubits with polarised microwaves,” *Nat. Commun.*, vol. 9, no. 1, 2018 (cit. on pp. 40, 45).
- [156] E. Sjöqvist, “A new phase in quantum computation,” *Physics*, vol. 1, 2008 (cit. on p. 41).
- [157] D. Töyrä, “Fidelity of geometric and holonomic quantum gates for spin systems for spin systems,” no. April, p. 53, 2014 (cit. on p. 41).
- [158] M. V. Berry, “Quantal Phase Factors Accompanying Adiabatic Changes,” *Proc. Roy. Soc. A*, vol. 392, no. 1802, pp. 45–57, 1984 (cit. on pp. 41, 42).
- [159] Y. Aharonov, J. Anandan, “Phase change during a cyclic quantum evolution,” *Phys. Rev. Lett.*, vol. 58, pp. 1593–1596, 1987 (cit. on p. 41).
- [160] V. Karimipour, N. Majd, “Exact solutions for a universal set of quantum gates on a family of isospectral spin chains,” *Phys. Rev. A*, vol. 72, no. 5, pp. 1–5, 2005 (cit. on p. 42).

- [161] J. Anandan, “Non-adiabatic non-abelian geometric phase,” *Phys. Lett. A*, vol. 133, pp. 171–175, 1988 (cit. on p. 42).
- [162] M. Kowarsky, L. Hollenberg, A. Martin, “The non-Abelian geometric phase in the diamond nitrogen-vacancy center,” vol. 042116, no. 2, p. 5, 2014 (cit. on p. 42).
- [163] M. Johansson, E. Sjöqvist, L. M. Andersson, M. Ericsson, B. Hessmo, K. Singh, D. M. Tong, “Robustness of nonadiabatic holonomic gates,” *Phys. Rev. A*, vol. 86, no. 6, pp. 1–10, 2012 (cit. on pp. 43, 46).
- [164] Y. Ota, M. Bando, Y. Kondo, M. Nakahara, “Implementation of holonomic quantum gates by an isospectral deformation of an Ising dimer chain,” *Phys. Rev. A*, vol. 78, no. 5, p. 052315, 2008 (cit. on p. 43).
- [165] Z. T. Liang, Y. X. Du, W. Huang, Z. Y. Xue, H. Yan, “Nonadiabatic holonomic quantum computation in decoherence-free subspaces with trapped ions,” *Phys. Rev. A*, vol. 89, no. 6, pp. 1–5, 2014 (cit. on p. 43).
- [166] V. S. Malinovsky, S. Rudin, “Adiabatic holonomic quantum gates for a single qubit,” *Phys. Scr.*, vol. T160, no. T160, p. 014029, 2014 (cit. on p. 43).
- [167] E. Sjöqvist, D. M. Tong, L. Mauritz Andersson, B. Hessmo, M. Johansson, K. Singh, “Non-adiabatic holonomic quantum computation,” *New J. Phys.*, vol. 14, no. 10, p. 103035, 2012 (cit. on p. 44).
- [168] G.-A. Yan, J.-X. Chen, H. Lu, “Room temperature high-fidelity non-adiabatic holonomic quantum computation on solid-state spins in Nitrogen-Vacancy centers,” pp. 1–6, 2017 (cit. on p. 45).
- [169] M. Ahmed, A. Ahmed, “Dynamical Decoupling using NMR for Quantum Computing,” 2013 (cit. on p. 46).
- [170] S.-B. Zheng, C.-P. Yang, F. Nori, “Comparison of the sensitivity to systematic errors between nonadiabatic non-Abelian geometric gates and their dynamical counterparts,” *Phys. Rev. A*, vol. 93, no. 3, p. 032313, 2016 (cit. on p. 49).
- [171] P. London, J. Scheuer, J. M. Cai, I. Schwarz, a. Retzker, M. B. Plenio, M. Katagiri, T. Teraji, S. Koizumi, J. Isoya, R. Fischer, L. P. McGuinness, B. Naydenov, F. Jelezko, “Detecting and polarizing nuclear spins with double resonance on a single electron spin,” *Phys. Rev. Lett.*, vol. 111, no. 6, pp. 1–5, 2013 (cit. on pp. 55, 100, 104, 112).

- [172] A. Henstra, P. Dirksen, J. Schmidt, W. Wenckebach, “Nuclear Spin Orientation via Electron Spin Locking (NOVEL),” *J. Magn. Reson.*, vol. 77, pp. 389–393, 1988 (cit. on pp. 55, 100).
- [173] A. Schrand, H. Huang, C. Carlson, J. Schlager, E. Osawa, S. Hussain, L. Dai, “Are Diamond Nanoparticles Cytotoxic?” *J. Phys. Chem. B.*, vol. 111, pp. 2–7, 2007 (cit. on p. 61).
- [174] P. Neumann, I. Jakobi, F. Dolde, C. Burk, R. Reuter, G. Waldherr, J. Honert, T. Wolf, A. Brunner, J. Shim, D. Suter, H. Sumiya, J. Isoya, J. Wrachtrup, “High-Precision Nanoscale Temperature Sensing Using Single Defects in Diamond,” *Nano Lett.*, vol. 13, pp. 2738–2742, 2013 (cit. on p. 61).
- [175] H. Watson, “Biological membranes,” *Essays Biochem.*, vol. 59, pp. 43–70, 2015 (cit. on p. 62).
- [176] B. S. Brown, *Biological Membranes*, 1996, p. 44 (cit. on p. 62).
- [177] J. Ranck, L. Mateu, D. Sadler, A. Tardieu, T. Gulik-Krzywicki, V. Luzzati, “Order-disorder conformational transitions of the hydrocarbon chains of lipids,” *J. Mol. Biol.*, vol. 85, pp. 249–277, 1974 (cit. on p. 63).
- [178] T. Gulik-Krzywicki, “Structural studies of the associations between biological membrane components,” *Biochim. Biophys. Acta*, vol. 415, pp. 1–28, 1975 (cit. on p. 63).
- [179] Y. Tahara, Y. Fujiyoshi, “A New Method to Measure Bilayer Thickness: Cryo-electron Microscopy of Frozen Hydrated Liposomes and Image Simulation,” *Micron*, vol. 25, pp. 141–149, 1994 (cit. on p. 63).
- [180] K. Gawrisch, “The structure of biological membranes, second edition,” in P. Yeagle, Ed. CRC Press, 2005, ch. 4. The Dynamics of Membrane Lipids, pp. 147–171 (cit. on p. 63).
- [181] A. C. Woodka, P. D. Butler, L. Porcar, B. Farago, M. Nagao, “Lipid Bilayers and Membrane Dynamics: Insight into Thickness Fluctuations,” *Phys. Rev. Lett.*, vol. 109, no. 5, p. 058 102, 2012 (cit. on p. 63).
- [182] T. V. Ratto, M. L. Longo, “Obstructed diffusion in phase-separated supported lipid bilayers: a combined atomic force microscopy and fluorescence recovery after photobleaching approach,” *Biophys. J.*, vol. 83, no. 6, pp. 3380–3392, 2002 (cit. on p. 63).

- [183] Y. Hosaka, K. Yasuda, R. Okamoto, S. Komura, "Lateral diffusion induced by active proteins in a biomembrane," *Phys. Rev. E*, vol. 95, p. 052407, 2017 (cit. on p. 63).
- [184] M. Edidin, "Rotational and Translational Diffusion in Membrane," 1974 (cit. on p. 63).
- [185] A.-L. Kuo, C. Wade, "Lipid lateral diffusion by pulsed nuclear magnetic resonance.," *Biochemistry*, vol. 18, pp. 2300–2308, 1979 (cit. on p. 63).
- [186] G. Sorland, D. Aksnes, L. Gjerdåker, "A pulsed field gradient spin-echo method for diffusion measurements in the presence of internal gradients," *J. Magn. Reson.*, vol. 137, no. 2, pp. 397–401, 1999 (cit. on p. 63).
- [187] Y. Chen, B. C. Lagerholm, B. Yang, K. Jacobson, "Methods to measure the lateral diffusion of membrane lipids and proteins," *Methods*, vol. 39, no. 2, pp. 147–153, 2006 (cit. on p. 63).
- [188] D. Marguet, P.-F. Lenne, H. Rigneault, H.-T. He, "Dynamics in the plasma membrane: how to combine fluidity and order," *The EMBO Journal*, vol. 25, no. 15, pp. 3446–3457, 2006 (cit. on p. 63).
- [189] P. Jönsson, M. P. Jonsson, J. O. Tegenfeldt, F. Höök, "A method improving the accuracy of fluorescence recovery after photobleaching analysis.," *Biophys J*, vol. 95, no. 11, pp. 5334–5348, 2008 (cit. on pp. 63, 74).
- [190] D. Soumpasis, "Theoretical analysis of fluorescence photobleaching recovery experiments," *Biophys. J.*, vol. 41, no. 1, pp. 95–97, 1983 (cit. on pp. 63, 74).
- [191] N. Dadashvand, L. A. Williams, C. M. Othon, "Heterogeneous rotational diffusion of a fluorescent probe in lipid monolayers," *Structural Dynamics*, vol. 1, no. 5, 2014 (cit. on p. 63).
- [192] A. J. Deese, E. A. Dratz, L. Hymel, S. Fleischer, "Proton NMR  $T_1$ ,  $T_2$ , and  $T_{1\rho}$  relaxation studies of native and reconstituted sarcoplasmic reticulum and phospholipid vesicles," *Biophys. J.*, vol. 37, no. 1, pp. 207–216, 1982 (cit. on p. 64).
- [193] M. Bloom, E. Burnell, M. Valic, G. Weeks, "Nuclear magnetic resonance line shapes in lipid bilayer model membranes.," *Chem. Phys. Lipids*, vol. 14, pp. 107–112, 1975 (cit. on p. 64).

- [194] M. Bloom, E. Burnell, A. MacKay, C. Nichol, M. Valic, G. Weeks, "Fatty acyl chain order in lecithin model membranes determined from proton magnetic resonance.," *Biochemistry*, vol. 17, no. 26, pp. 5750–5762, 1978 (cit. on p. 64).
- [195] U. Fogel, Z. Ding, H. Hardung, S. Jander, G. Reichmann, C. Jacoby, R. Schubert, J. Schrader, "In vivo monitoring of inflammation after cardiac and cerebral ischemia by fluorine magnetic resonance imaging," *Circulation*, vol. 118, no. 2, pp. 140–148, 2008 (cit. on p. 64).
- [196] R. Dimova, S. Aranda, N. Bezlyepkina, V. Nikolov, K. A. Riske, R. Lipowsky, "A practical guide to giant vesicles. Probing the membrane nanoregime via optical microscopy," *J. Phys.: Condens. Matter*, vol. 18, pp. 1151–1176, 2006 (cit. on p. 65).
- [197] D. Needham, T. McIntosh, E. Evans, "Thermomechanical and transition properties of dimyristoylphosphatidylcholine/cholesterol bilayers.," *Biochemistry*, vol. 27, pp. 4668–4673, 1988 (cit. on p. 65).
- [198] P. Walde, K. Cosentino, H. Engel, P. Stano, "Giant Vesicles: Preparations and Applications," *Chembiochem*, vol. 11, no. 7, pp. 848–865, 2010 (cit. on p. 65).
- [199] R. Richter, A. Mukhopadhyay, A. Brisson, "Pathways of lipid vesicle deposition on solid surfaces: a combined QCM-D and AFM study," *Biophys. J.*, vol. 85, no. 5, pp. 3035–47, 2003 (cit. on p. 65).
- [200] P. S. Cremer, S. G. Boxer, "Formation and Spreading of Lipid Bilayers on Planar Glass Supports," *J. Phys. Chem. B*, vol. 103, no. 13, pp. 2554–2559, 1999 (cit. on p. 65).
- [201] E. Reimhult, B. Kasemo, F. Höök, "Rupture pathway of phosphatidylcholine liposomes on silicon dioxide," *Int. J. Mol. Sci.*, vol. 10, no. 4, pp. 1683–1696, 2009 (cit. on p. 65).
- [202] S. Kaufmann, D. A. Simpson, L. T. Hall, V. Perunicic, P. Senn, S. Steinert, L. P. McGuinness, B. C. Johnson, T. Ohshima, F. Caruso, J. Wrachtrup, R. E. Scholten, P. Mulvaney, L. Hollenberg, "Detection of atomic spin labels in a lipid bilayer using a single-spin nanodiamond probe.," *Proc. Natl. Acad. Sci. U.S.A.*, vol. 110, no. 27, pp. 10894–8, 2013 (cit. on pp. 65, 74).

- [203] A. Narten, "Thermodynamic Effects of Mixing Light and Heavy Water," *J. Chem. Phys.*, vol. 41, no. 5, p. 1318, 1964 (cit. on p. 67).
- [204] M. Kakiuchi, "Distribution of isotopic water molecules,  $H_2O$ ,  $HDO$ , and  $D_2O$ , in vapor and liquid phases in pure water and aqueous solution systems," *Geochim. Cosmochim. Acta*, vol. 64, no. 9, pp. 1485–1492, 2000 (cit. on p. 67).
- [205] V. Goncharuk, A. Kavitskaya, I. Romanyukina, O. Loboda, "Revealing water's secrets: deuterium depleted water," *Chem. Cent. J.*, vol. 7, p. 103, 2013 (cit. on p. 67).
- [206] A. Tikhonov, V. Asadchikov, Y. Volkov, B. Roshchin, I. Monakhov, I. Smirnov, "Kinetics of the formation of a phospholipid multilayer on a silica sol surface," *JETP Letters*, vol. 104, no. 12, pp. 873–879, 2016 (cit. on pp. 67, 73).
- [207] [Online]. Available: <http://www.liposomes.org/2009/01/number-of-lipid-molecules-per-liposome.html> (cit. on p. 67).
- [208] B. A. Lewis, D. M. Engelman, "Lipid bilayer thickness varies linearly with acyl chain length in fluid phosphatidylcholine vesicles," *J. Mol. Biol.*, vol. 166, no. 2, pp. 211–217, 1983 (cit. on p. 67).
- [209] N. Kučerka, M. P. Nieh, J. Katsaras, "Fluid phase lipid areas and bilayer thicknesses of commonly used phosphatidylcholines as a function of temperature," *Biochim. Biophys. Acta*, vol. 1808, no. 11, pp. 2761–2771, 2011 (cit. on p. 67).
- [210] P. G. Saffman, M. Delbruck, "Brownian motion in biological membranes," *Proc Natl Acad Sci USA*, vol. 72, no. 8, pp. 3111–3113, 1975 (cit. on p. 68).
- [211] R. Peters, K. Beck, "Translational diffusion in phospholipid monolayers measured by fluorescence microphotolysis," *Proc. Natl. Acad. Sci. U.S.A.*, vol. 80, no. 23, pp. 7183–7187, 1983 (cit. on p. 73).
- [212] D. Axelrod, D. E. Koppel, J. Schlessinger, E. Elson, W. Webb, "Mobility measurement by analysis of fluorescence photobleaching recovery kinetics," *Biophys. J.*, vol. 16, no. 9, pp. 1055–1069, 1976 (cit. on p. 74).
- [213] N. Öncan, M. Player, A. Macdonald, "Determination of Diffusion Coefficients of Fluorescently Labelled Molecules in Lipid Membranes Using Confocal Scanning Laser," *Z. Naturforsch.*, vol. 59a, pp. 683–688, 2004 (cit. on p. 74).

- [214] S. Seiffert, W. Oppermann, “Systematic evaluation of FRAP experiments performed in a confocal laser scanning microscope,” *J. Microsc.*, vol. 220, pp. 20–30, 2005 (cit. on p. 74).
- [215] L. Renner, T. Osaki, S. Chiantia, P. Schwille, T. Pompe, C. Werner, “Supported lipid bilayers on spacious and pH-responsive polymer cushions with varied hydrophilicity,” *J. Phys. Chem. B*, vol. 112, no. 20, pp. 6373–6378, 2008 (cit. on p. 74).
- [216] I. M. Georgescu, S. Ashhab, F. Nori, “Quantum simulation,” *Rev. Mod. Phys.*, vol. 86, no. 1, pp. 153–185, 2014 (cit. on p. 79).
- [217] M. Greiner, O. Mandel, T. Esslinger, T. Hänsch, I. Bloch, “Quantum phase transition from a superfluid to a Mott insulator in a gas of ultracold atoms,” *Nature*, vol. 415, pp. 39–44, 2002 (cit. on p. 79).
- [218] A. Friedenauer, H. Schmitz, J. T. Glueckert, D. Porras, T. Schaetz, “Simulating a quantum magnet with trapped ions,” *Nat. Phys.*, vol. 4, no. 757, pp. 1–5, 2008 (cit. on p. 79).
- [219] J. W. Britton, B. C. Sawyer, A. C. Keith, C.-C. J. Wang, J. K. Freericks, H. Uys, M. J. Biercuk, J. J. Bollinger, “Engineered two-dimensional Ising interactions in a trapped-ion quantum simulator with hundreds of spins,” *Nature*, vol. 484, no. 7395, pp. 489–492, 2012 (cit. on p. 79).
- [220] J. Cai, A. Retzker, F. Jelezko, M. Plenio, “A large-scale quantum simulator on a diamond surface at room temperature,” *Nat. Phys.*, vol. 9, no. 1, pp. 1–6, 2013 (cit. on pp. 79, 124).
- [221] K. J. Rietwyk, S. L. Wong, L. Cao, K. M. Odonnell, L. Ley, A. T. S. Wee, C. I. Pakes, “Work function and electron affinity of the fluorine-terminated (100) diamond surface,” *Appl. Phys. Lett.*, vol. 102, no. 9, 2013 (cit. on p. 79).
- [222] M. I. Petrescu, M.-G. Balint, “Structure and properties modification in boron nitride. Part 1: Direct polymorphic transformations mechanisms,” *U.P.B Sci. Bull.*, vol. 69, no. 1, pp. 35–42, 2007 (cit. on p. 80).
- [223] P. M. Geffroy, F. Mabilat, C. Bessada, J. Coutures, D. Massiot, “High Resolution NMR of BN and BN Precursors: a Combined  $^{11}\text{B}$  and  $^{14}\text{N}$  Approach,” *Mater. Sci. Forum*, vol. 325-326, pp. 319–324, 2000 (cit. on p. 81).

- [224] G. Jeschke, W. Hoffbauer, M. Jansen, "A comprehensive NMR study of cubic and hexagonal boron nitride," *Solid State Nucl. Magn. Reson.*, vol. 12, no. 1, pp. 1–7, 1998 (cit. on p. 81).
- [225] J. Akitt, "Quadrupole relaxation of boron-11 and boron-10 nuclei," *J. Magn. Reson.*, vol. 3, pp. 411–414, 1970 (cit. on p. 81).
- [226] C. Connor, J. Chang, A. Pines, "Aluminum and boron nuclear quadrupole resonance with a direct current superconducting quantum interference device," *J. Chem. Phys.*, vol. 93, no. 11, pp. 7639–7646, 1990 (cit. on p. 83).
- [227] F. Shagieva, S. Zaiser, P. Neumann, D. B. R. Dasari, R. Stöhr, A. Denisenko, R. Reuter, C. A. Meriles, J. Wrachtrup, "Microwave-Assisted Cross-Polarization of Nuclear Spin Ensembles from Optically Pumped Nitrogen-Vacancy Centers in Diamond," *Nano Lett.*, vol. 18, pp. 3731–3737, 2018 (cit. on p. 92).
- [228] A. Overhauser, "Polarization of Nuclei in Metals," *Phys. Rev.*, vol. 92, no. 2, pp. 411–415, 1953 (cit. on p. 96).
- [229] M. E. Halse, "Perspectives for hyperpolarisation in compact NMR," *Trends Anal. Chem.*, vol. 83, pp. 76–83, 2016 (cit. on p. 96).
- [230] B. M. Goodson, "Nuclear Magnetic Resonance of Laser-Polarized Noble Gases in Molecules, Materials, and Organisms," *J. Magn. Reson.*, vol. 155, pp. 157–216, 2002 (cit. on p. 96).
- [231] M. L. Truong, F. Shi, P. He, B. Yuan, K. N. Plunkett, A. M. Coffey, R. V. Shchepin, D. A. Barskiy, K. V. Kovtunov, I. V. Koptuyug, K. W. Waddell, B. M. Goodson, E. Y. Chekmenev, "Irreversible catalyst activation enables hyperpolarization and water solubility for NMR signal amplification by reversible exchange," *J. Phys. Chem. B*, vol. 118, no. 48, pp. 13 882–13 889, 2014 (cit. on p. 96).
- [232] P. J. Rayner, S. B. Duckett, "Signal Amplification by Reversible Exchange (SABRE): From Discovery to Diagnosis," *Angewandte Chemie - International Edition*, vol. 57, no. 23, pp. 6742–6753, 2018 (cit. on p. 96).
- [233] R. W. Adams, J. A. Aguilar, K. D. Atkinson, M. J. Cowley, P. I. Elliott, S. B. Duckett, G. G. Green, I. G. Khazal, J. Lopez-Serrano, D. C. Williamson, "Reversible interactions with para-hydrogen enhance NMR sensitivity by polarization transfer," *Science*, vol. 323, no. 5922, pp. 1708–1711, 2009 (cit. on p. 97).

- [234] D.B. Bucher, D.R. Glenn, H. Park, M.D. Lukin, R.L. Walsworth, “Hyperpolarization-enhanced NMR spectroscopy with femtomole sensitivity using quantum defects in diamond,” 2018 (cit. on p. 97).
- [235] J. Scheuer, I. Schwartz, Q. Chen, D. Schulze-Sünninghausen, P. Carl, P. Höfer, A. Retzker, H. Sumiya, J. Isoya, B. Luy, M. Plenio, B. Naydenov, F. Jelezko, “Optically induced dynamic nuclear spin polarisation in diamond,” *New J. Phys*, vol. 18, p. 013 040, 2016 (cit. on pp. 98, 104).
- [236] V. Jacques, P. Neumann, J. Beck, M. Markham, D. Twitchen, J. Meijer, F. Kaiser, G. Balasubramanian, F. Jelezko, J. Wrachtrup, “Dynamic polarization of single nuclear spins by optical pumping of nitrogen-vacancy color centers in diamond at room temperature,” *Phys. Rev. Lett.*, vol. 102, no. 5, pp. 7–10, 2009 (cit. on p. 99).
- [237] R. Fischer, A. Jarmola, P. Kehayias, D. Budker, “Optical polarization of nuclear ensembles in diamond,” *Phys. Rev. B*, vol. 87, no. 12, pp. 1–7, 2013 (cit. on p. 99).
- [238] F. Poggiali, P. Cappellaro, N. Fabbri, “Measurement of the excited-state transverse hyperfine coupling in NV centers via dynamic nuclear polarization,” *Phys. Rev. B*, vol. 95, no. 19, pp. 1–8, 2017 (cit. on p. 99).
- [239] D. A. Broadway, J. D. A. Wood, L. T. Hall, A. Stacey, M. Markham, D. A. Simpson, J.-P. Tetienne, L. C. L. Hollenberg, “Anticrossing Spin Dynamics of Diamond Nitrogen-Vacancy Centers and All-Optical Low-Frequency Magnetometry,” *Phys. Rev. Appl*, vol. 6, p. 064 001, 2016 (cit. on p. 99).
- [240] J. D. Wood, J. P. Tetienne, D. A. Broadway, L. T. Hall, D. A. Simpson, A. Stacey, L. C. Hollenberg, “Microwave-free nuclear magnetic resonance at molecular scales,” *Nat. Commun.*, vol. 8, no. May, pp. 1–6, 2017 (cit. on p. 99).
- [241] D. A. Broadway, J. P. Tetienne, A. Stacey, J. D. Wood, D. A. Simpson, L. T. Hall, L. C. Hollenberg, “Quantum probe hyperpolarisation of molecular nuclear spins,” *Nat. Commun.*, vol. 9, no. 1, pp. 1–8, 2018 (cit. on pp. 99, 116).
- [242] S. Hartmann, E. Hahn, “Nuclear Double Resonance in the Rotating Frame,” *Phys. Rev.*, vol. 128, no. 5, pp. 2042–2053, 1962 (cit. on p. 100).
- [243] D. A. Steck, *Quantum and Atom Optics*. 2016 (cit. on p. 101).
- [244] R. Reddy, “ $T_{1\rho}$  imaging : Techniques and basis for image contrast,” *Proc. Intl. Soc. Mag. Reson. Med.*, vol. 18, 2010 (cit. on p. 102).

- [245] Y. Hovav, B. Naydenov, F. Jelezko, N. Bar-Gill, “Low-Field Nuclear Polarization Using Nitrogen Vacancy Centers in Diamonds,” *Phys. Rev. Lett.*, vol. 120, p. 060 405, 2018 (cit. on p. 104).
- [246] C. B. Harris, R. L. Schlupp, H. Schuch, “Optically detected electron spin locking and rotary echo trains in molecular excited states,” *Phys. Rev. Lett.*, vol. 30, no. 21, pp. 1019–1022, 1973 (cit. on p. 104).
- [247] A. Laraoui, C. A. Meriles, “Approach to dark spin cooling in a diamond nanocrystal,” *ACS Nano*, vol. 7, no. 4, pp. 3403–3410, 2013 (cit. on p. 104).
- [248] C. Belthangady, N. Bar-Gill, L. M. Pham, K. Arai, D. Le Sage, P. Cappellaro, R. L. Walsworth, “Dressed-State Resonant Coupling between Bright and Dark Spins in Diamond,” *Phys. Rev. Lett.*, vol. 110, no. 15, p. 157 601, 2013 (cit. on p. 104).
- [249] G.-Q. Liu, Q.-Q. Jiang, Y.-C. Chang, D.-Q. Liu, W.-X. Li, C.-Z. Gu, H. C. Po, W.-X. Zhang, N. Zhao, X.-Y. Pan, “Protection of centre spin coherence by dynamic nuclear spin polarization in diamond,” *Nanoscale*, vol. 6, no. 17, pp. 10 134–10 139, 2014 (cit. on p. 104).
- [250] J. Scheuer, I. Schwartz, M. Samuel, Q. Chen, M. B. Plenio, B. Naydenov, F. Jelezko, “Robust techniques for polarization and detection of nuclear spin ensembles,” *Phys. Rev. B*, vol. 96, p. 174 436, 2017 (cit. on pp. 104, 134).
- [251] P. Fernández-Acebal, M. Plenio, “Sensing phases of water via nitrogen-vacancy centres in diamond,” *Sci. Rep.*, vol. 8, p. 13 543, 2018 (cit. on p. 104).
- [252] S. Zaiser, “A single electron sensor assisted by a quantum coprocessor,” PhD thesis, University of Stuttgart, 2019 (cit. on p. 105).
- [253] I. Schwartz, J. Scheuer, B. Tratzmiller, S. Müller, Q. Chen, I. Dhand, Z.-Y. Wang, C. Müller, B. Naydenov, F. Jelezko, M. Plenio, “Robust optical polarization of nuclear spin baths using Hamiltonian engineering of nitrogen-vacancy center quantum dynamics,” *Sci. Adv.*, vol. 4, no. 8, pp. 1–7, 2018 (cit. on p. 105).
- [254] A. Brinkmann, “Introduction to average Hamiltonian theory. I. Basics,” *Concepts Magn. Reson. Part A Bridg. Educ. Res.*, vol. 45A, no. 6, 2016 (cit. on p. 105).

- [255] S. A. Moiseev, V. A. Skrebnev, “Short-cycle pulse sequence for dynamical decoupling of local fields and dipole-dipole interactions,” *Phys. Rev. A*, vol. 91, no. 2, pp. 10–13, 2015 (cit. on p. 105).
- [256] P. Fernández-Acebal, O. Rosolio, J. Scheuer, C. Müller, S. Müller, S. Schmitt, L. McGuinness, I. Schwarz, Q. Chen, A. Retzker, B. Naydenov, F. Jelezko, M. Plenio, “Toward Hyperpolarization of Oil Molecules via Single Nitrogen Vacancy Centers in Diamond,” *Nano Lett.*, vol. 18, no. 3, pp. 1882–1887, 2018 (cit. on p. 109).
- [257] A. Laraoui, D. Pagliero, C. A. Meriles, “Imaging nuclear spins weakly coupled to a probe paramagnetic center,” *Phys. Rev. B*, vol. 91, no. 20, pp. 1–7, 2015 (cit. on p. 113).
- [258] A. Ajoy, U. Bissbort, M. Lukin, R. Walsworth, P. Cappellaro, “Atomic-scale nuclear spin imaging using quantum-assisted sensors in diamond,” *Phys. Rev. X*, vol. 5, no. 1, pp. 1–19, 2015 (cit. on p. 113).
- [259] P. Thompson, S. Troian, “A general boundary condition for liquid flow at solid surfaces,” *Nature*, vol. 389, pp. 360–362, 1997 (cit. on pp. 113, 116, 124).
- [260] E. Kätelhön, R. Compton, “Understanding nano-impacts: Impact times and near-wall hindered diffusion,” *Chem. Sci.*, vol. 5, pp. 4592–4598, 2014 (cit. on pp. 116, 124).
- [261] S. Eloul, R. Compton, “General Model of Hindered Diffusion,” *J. Phys. Chem. Lett.*, vol. 7, pp. 4317–4321, 2016 (cit. on pp. 116, 124).
- [262] D. Ortiz-Young, H.-C. Chiu, S. Kim, K. Voitchovsky, E. Riedo, “The interplay between apparent viscosity and wettability in nanoconfined water,” *Nat. Commun.*, vol. 4, no. 2482, 2013 (cit. on p. 116).
- [263] D. Abrams, M. E. Trusheim, D. R. Englund, M. D. Shattuck, C. a. Meriles, “Dynamic nuclear spin polarization of liquids and gases in contact with nanostructured diamond,” *Nano Lett.*, vol. 14, no. 5, pp. 2471–2478, 2014 (cit. on pp. 116, 124).
- [264] I. Lowe, S. Gade, “Density-Matrix Derivation of the Spin-Diffusion Equation,” *Phys. Rev.*, vol. 156, no. 3, p. 817, 1967 (cit. on pp. 116, 124).

- [265] A. Bettiol, T. Sum, J. Kan, F. Watt, "Fabrication of micro-optical components in polymer using proton beam micro-machining and modification," *Nucl. Instrum. Methods B*, vol. 210, pp. 250–255, 2003 (cit. on p. 117).
- [266] H. Bennett, A. Guenther, D. Milam, B. Newnam, M. Soileau, "In laser induced damage in optical materials: 1987," in. NBS Spec. Pub.: 756; ASTM: Washington, 1988, ch. Zyung, T.; Kim, H.; Postlewaite J.C.; Dlott, D.D. Ultrafast Imaging of Optical Damage in PMMA. Pp. 98–104 (cit. on p. 119).
- [267] R. Srinivasan, "Ablation of polymers and biological tissue by ultraviolet lasers.," *Science*, vol. 234, no. 4776, pp. 559–565, 1986 (cit. on p. 119).
- [268] J. Bhawalkar, G. He, P. Prasad, "Nonlinear multiphoton process in organic and polymeric materials," *Rep. Prog. Phys.*, vol. 59, no. 9, pp. 1041–1070, 1996 (cit. on p. 119).
- [269] E. Spyratou, M. Makropoulou, A. A. Serafetinides, "Study of visible and mid-infrared laser ablation mechanism of PMMA and intraocular lenses: Experimental and theoretical results," *Lasers Med. Sci.*, vol. 23, no. 2, pp. 179–188, 2008 (cit. on p. 119).
- [270] R. Srinivasan, B. Braren, K. Casey, "Nature of "incubation pulses" in the ultraviolet laser ablation of poly methylmethacrylate," *J. Appl. Phys.*, vol. 68, p. 1842, 1990 (cit. on p. 119).
- [271] D. Hare, J. Franken, D. Dlott, "Coherent Raman measurements of polymer thin-film pressure and temperature during picosecond laser ablation," *J. Appl. Phys.*, vol. 77, p. 5950, 1995 (cit. on p. 119).
- [272] G. Zhiming, K. Tsyoshi, H. Dongyan, N. Masahiro, "Kinetics of thermal degradation of poly(methyl methacrylate) studied with the assistance of the fractional conversion at the maximum reaction rate," *Polym. Degrad. Stab.*, vol. 84, no. 3, pp. 399–403, 2004 (cit. on p. 119).
- [273] F. Fávaro de Oliveira, D. Antonov, Y. Wang, P. Neumann, S. A. Momenzadeh, T. Häußermann, A. Pasquarelli, A. Denisenko, J. Wrachtrup, "Tailoring spin defects in diamond by lattice charging," *Nat. Commun.*, vol. 8, no. 15409, pp. 1–8, 2017 (cit. on p. 122).
- [274] C.-Y. Cheng, S. Han, "Dynamic Nuclear Polarization Methods in Solids and Solutions to Explore Membrane Proteins and Membrane Systems," *Annu. Rev. Phys. Chem.*, vol. 64, pp. 507–532, 2013 (cit. on p. 124).

- [275] E. Daviso, G. J. Janssen, A. Alia, G. Jeschke, J. Matysik, M. Tessari, “A 10 000-fold nuclear hyperpolarization of a membrane protein in the liquid phase via a solid-state mechanism,” *J. Am. Chem. Soc.*, vol. 133, no. 42, pp. 16 754–16 757, 2011 (cit. on p. 124).
- [276] J. H. Burnett, Z. H. Levine, E. L. Shirley, J. H. Bruning, “Symmetry of spatial-dispersion-induced birefringence and its implications for  $CaF_2$  ultraviolet optics,” *J. Microlith., Microfab., Microsyst.*, vol. 1, no. 3, pp. 213–224, 2002 (cit. on p. 127).
- [277] M. Huisinga, “Ultraviolet photoelectron spectroscopy and electron stimulated desorption from  $CaF_2$ ,” PhD thesis, Free University of Berlin, 1999 (cit. on p. 127).
- [278] M. Kim, H. Mamin, M. Sherwood, K. Ohno, D. Awschalom, D. Rugar, “Decoherence of Near-Surface Nitrogen-Vacancy Centers Due to Electric Field Noise,” *Phys. Rev. Lett.*, vol. 115, no. 8, pp. 1–5, 2015 (cit. on p. 128).
- [279] N. Bloembergen, “On the interaction of nuclear spins in a crystalline lattice,” *Physica*, vol. 15, no. 3-4, pp. 386–426, 1949 (cit. on pp. 129–131, 136, 143).
- [280] G. Khutsishvili, “Spin diffusion,” *Sov. Phys. Usp.*, vol. 8, no. 5, pp. 743–769, 1966 (cit. on pp. 130, 131).
- [281] K. Kumashiro, K. Schmidt-Rohr, O. Murphy, K. Ouellette, W. Cramer, L. Thompson, “A Novel Tool for Probing Membrane Protein Structure: Solid-State NMR with Proton Spin Diffusion and X-Nucleus Detection,” *J. Am. Chem. Soc.*, vol. 120, no. 20, pp. 5043–5051, 1998 (cit. on p. 130).
- [282] G. J. Gallagher, M. Hong, L. K. Thompson, “Solid-state NMR spin diffusion for measurement of membrane-bound peptide structure: Gramicidin A,” *Biochemistry*, vol. 43, no. 24, pp. 7899–7906, 2004 (cit. on p. 130).
- [283] B. Elena, L. Emsley, “Powder crystallography by proton solid-state NMR spectroscopy,” *J. Am. Chem. Soc.*, vol. 127, no. 25, pp. 9140–9146, 2005 (cit. on p. 130).
- [284] Q. Chen, K. Schmidt-Rohr, “Measurement of the local  $^1H$  spin-diffusion coefficient in polymers,” *Solid State Nucl. Magn. Reson.*, vol. 29, no. 1-3, pp. 142–152, 2006 (cit. on p. 130).

- [285] G. Berman, B. Chernobrod, V. Gorshkov, “Spin diffusion and relaxation in a nonuniform magnetic field,” *Phys. Rev. B*, vol. 71, p. 184 409, 2005 (cit. on p. 130).
- [286] G. Berman, B. Chernobrod, V. Gorshkov, V. Tsifrinovich, “Spin diffusion and relaxation in solid state spin quantum computer,” *Phys. Lett. A*, vol. 352, pp. 107–114, 2006 (cit. on p. 130).
- [287] G. Leppelmeier, J. Jeener, “Measurement of the Nuclear Spin Diffusion Coefficient in  $CaF_2$ ,” *Phys. Rev.*, vol. 175, no. 2, pp. 498–502, 1968 (cit. on pp. 130, 136).
- [288] W. Zhang, D. Cory, “First Direct Measurement of the Spin Diffusion Rate in a Homogeneous Solid,” *Phys. Rev. Lett.*, vol. 80, no. 6, pp. 1324–1327, 1998 (cit. on pp. 130, 136).
- [289] G. S. Boutis, D. Greenbaum, H. Cho, D. G. Cory, C. Ramanathan, “Spin diffusion of correlated two-spin states in a dielectric crystal,” *Phys. Rev. Lett.*, vol. 92, no. 13, pp. 3–6, 2004 (cit. on pp. 130, 136).
- [290] T. T. P. Cheung, “Spin diffusion in NMR in solids,” *Phys. Rev. B*, vol. 23, no. 3, pp. 1404–1418, 1981 (cit. on p. 132).
- [291] A. Karabanov, D. Wiśniewski, I. Lesanovsky, W. Köckenberger, “Dynamic Nuclear Polarization as Kinetically Constrained Diffusion,” *Phys. Rev. Lett.*, vol. 115, p. 020 404, 2015 (cit. on p. 132).
- [292] D. Wiśniewski, A. Karabanov, I. Lesanovsky, W. Köckenberger, “Solid effect DNP polarization dynamics in a system of many spins,” *J. Magn. Reson.*, vol. 264, pp. 30–38, 2016 (cit. on p. 132).
- [293] H. Cho, P. Cappellaro, D. G. Cory, C. Ramanathan, “Decay of highly correlated spin states in a dipolar-coupled solid: NMR study of  $CaF_2$ ,” *Phys. Rev. B*, vol. 74, no. 22, pp. 1–7, 2006 (cit. on pp. 136, 143).
- [294] E. Sorte, B. Fine, B. Saam, “Long-time behavior of nuclear spin decays in various lattices,” *Phys. Rev. B*, vol. 83, p. 064 302, 2011 (cit. on pp. 136, 137).
- [295] S. B. Saun, S. Won, S. Kwon, S. Lee, “NMR spin-lattice relaxation time  $T_1$  of thin films obtained by magnetic resonance force microscopy,” *J. Magn. Reson.*, vol. 254, pp. 71–74, 2015 (cit. on pp. 136, 143).

- [296] A. Redfield, "Nuclear Magnetic Resonance Saturation and Rotary Saturation in Solids," *Phys. Rev.*, vol. 98, no. 6, pp. 1787–1809, 1955 (cit. on p. 139).
- [297] M. Lee, W. Goldburg, "Nuclear-Magnetic-Resonance Line Narrowing by a Rotating RF Field," *Phys. Rev.*, vol. 140, no. 4A, pp. 1261–1271, 1965 (cit. on pp. 139, 140).
- [298] A. Bielecki, A. Kolbert, M. Levitt, "Frequency-switched pulse sequences: Homonuclear decoupling and dilute spin NMR in solids," *Chem. Phys. Lett.*, vol. 155, no. 4,5, pp. 341–346, 1989 (cit. on p. 139).
- [299] J. Waugh, L. Huber, U. Haeberlen, "Approach to high-resolution NMR in solids," *Phys. Rev. Lett.*, vol. 20, no. 5, pp. 180–182, 1968 (cit. on p. 139).
- [300] G. Sharma, T. Gaebel, E. Rej, D. Reilly, S. Economou, E. Barnes, "Enhancement of nuclear spin coherence times by driving dynamic nuclear polarization at defectcenters in solids," 2019 (cit. on p. 139).
- [301] B. Meier, J. Kohlrautz, J. Haase, "Eigenmodes in the Long-Time Behavior of a Coupled Spin System Measured with Nuclear Magnetic Resonance," *Phys. Rev. Lett.*, vol. 108, p. 177 602, 2012 (cit. on p. 143).

# ACKNOWLEDGEMENTS

I wish to express my gratitude to Prof. Jörg Wrachtrup who provided me excellent ideas for research projects.

I am thankful to Prof. Peter Michler and Prof. Maria Daghofer for agreeing to be the second reviewer and the chairwoman on my defense.

I would like to thank the International Max Planck Research School for Condensed Matter Science for the financial support of the first 2.5 years of my PhD and Dr. Hans-Georg Libuda who helped to get on with formalities and documents.

Prof. Carlos Meriles deserves special thanks for being my distant online supervisor.

I am grateful to Dr. Philipp Neumann, for giving me the idea to start experiments on hyperpolarization, to Dr. Durga Dasari, for supervising my theoretical project and for helping me later on with formulas and to Dr. Ya Wang, from whom I inherited the experimental setup.

I thank the colleagues, who helped me in the lab: Ingmar Jakobi, Dr. Roman Kolesov, Dr. Sen Yang, Dr. Kangwei Xia. Special thanks to Dr. Ilja Gerhardt for rescuing my piezo-scanner from the custom office in Köln.

I would like to thank Dr. Sebastian Zaiser, Dr. Nabeel Aslam, Dr. Matthias Pfender, Dr. Thomas Häberle, Dr. Dominik Schmid-Lorch, Dr. Vadim Vorobev, Dr. Boris Yavkin, Dr. Torsten Rendler and Matthias Niethammer for fruitful

discussions. I am grateful to Jochen Scheuer for explaining me how Qudi is programmed.

I would like to thank also all the people who produced the diamond membranes for me and helped me with the samples preparations: Dr. Andrej Denisenko, Dr. Rainer Stöhr, Dr. Rolf Reuter, Dr. Felipe Favaro de Oliveira, Dr. Amit Finkler, Dr. Andrea Zappe.

I appreciate Jonas Meinel's and Dr. Durga Dasari's proof-reading of my thesis. Special thanks for the schwäbisch-bayerisches language check of my German summary to Dr. Dominik Schmid-Lorch, Jacob Steiner, Jonas Meinel and for the linguistic review of the English text to Dr. Jacob Henshaw.

Many thanks go to Stephan Hirschmann, for the technical support, Claudia Unger and Britta Lenz, for helping with the orders and with all the documents, Mrs. Ivanka Spajic, for keeping our institute clean and for preparing delicious snacks at 16 o'clock during several years.

I am grateful to Dr. Ali Momenzadeh, Dr. Rolf Reuter, Dr. Dominik Schmid-Lorch and Dr. Artem Aerov for teaching me not to give up no matter what, for their support and inspiration.

# ERKLÄRUNG DER SELBSTSTÄNDIGKEIT

Hiermit erkläre ich, diese Arbeit selbstständig verfasst und nur die als Quellen angegebenen Hilfsmittel verwendet zu haben.

Ich habe mich nicht anderweitig um einen Dokortitel beworben und besitze keinen dementsprechenden Titel.

Ich erkläre die Kenntnisnahme der dem Verfahren zugrundeliegenden Promotionsordnung der Fäkultät 8 der Universität Stuttgart vom 22. Februar 2016.

Stuttgart, 6. Juni 2019

Farida Shagieva